Max-Planck-Institut für Astrophysik

Parametric Studies of Hydrodynamic Instabilities in the Supernova Core by Two- and Three-Dimensional Simulations

Leonhard Scheck

Vollständiger Abdruck der von der Fakultät für Physik der Technischen Universität München zur Erlangung des akademischen Grades eines

Doktors der Naturwissenschaften

genehmigten Dissertation.

Vorsitzender:	Univ.-Prof. Dr. Lothar Oberauer
Prüfer der Dissertation:	
	1. Priv.-Doz. Dr. Hans-Thomas Janka
	2. Univ.-Prof. Dr. Andrzej J. Buras

Die Dissertation wurde am 05.09.2006 bei der Technischen Universität München eingereicht
und durch die Fakultät für Physik am 29.11.2006 angenommen.

Contents

1 Introduction **5**
1.1 The explosion mechanism . . . 6
  1.1.1 Core collapse . . . 6
  1.1.2 Prompt explosions . . . 7
  1.1.3 Delayed explosions . . . 7
1.2 The anisotropy of core collapse supernovae . . . 8
  1.2.1 Evidence for anisotropy . . . 8
  1.2.2 Possible origins . . . 9
1.3 Neutron star kicks . . . 10
  1.3.1 The neutron star velocity distribution . . . 10
  1.3.2 Neutron star kick mechanisms . . . 11
1.4 Aims of this thesis . . . 12

2 Computational approach and numerical methods **15**
2.1 Hydrodynamics and gravity . . . 15
2.2 Neutrino transport and neutrino source terms . . . 18
2.3 Numerical grid . . . 19
2.4 Boundary conditions . . . 21
  2.4.1 Hydrodynamics . . . 21
  2.4.2 Neutrinos . . . 21
  2.4.3 Moving the inner boundary to a different mass shell . . . 23

3 Explosion anisotropy in two dimensions **25**
3.1 Preliminaries . . . 25
  3.1.1 Initial models and initial perturbations . . . 25
  3.1.2 Overview of the simulations . . . 27
  3.1.3 Definitions and approximations for post-processing the simulations . . . 28
3.2 Two representative models . . . 34
  3.2.1 The character of the flow . . . 34
  3.2.2 Acceleration and recoil of the neutron star . . . 37
  3.2.3 Possible origin of the low-order modes . . . 40
  3.2.4 Comparison with previous works . . . 41
  3.2.5 Sensitivity to the seed perturbations . . . 44
3.3 Dependence on the initial model and the core luminosity . . . 47
3.4 The effects of rotation . . . 49
  3.4.1 Evolution of the rotation rate . . . 50
  3.4.2 Morphology . . . 50
  3.4.3 Energetics . . . 54
  3.4.4 Neutron star recoil . . . 54
3.5 Robustness and long-time evolution of the neutron star recoils . . . 55
  3.5.1 Anisotropic neutrino emission . . . 55

3.5.2 Inertial mass of the neutron star . . . 56
3.5.3 Neutron star contraction and gravitational potential . . . 57
3.5.4 Long-time evolution of the neutron star kicks . . . 58
3.6 Implications for the neutron star velocity distribution . . . 59

4 The origin of the global anisotropy 63
4.1 Hydrodynamic instabilities . . . 64
4.1.1 Linear and non-linear convective growth of perturbations . . . 64
4.1.2 The advective-acoustic cycle . . . 65
4.2 Simulations . . . 67
4.2.1 A model without neutrinos . . . 67
4.2.2 Models with suppressed convection . . . 70
4.2.3 Models with typical explosion energies . . . 75
4.3 Interpretation of the linear phase . . . 76
4.3.1 Measuring oscillation period and cycle efficiency . . . 76
4.3.2 Identification of the instability mechanism . . . 79
4.4 Interpretation of the non-linear phase . . . 82
4.4.1 AAC triggers convection . . . 82
4.4.2 Explosion vs. non-explosion . . . 83
4.4.3 The AAC as an alternative to convection . . . 86

5 Three-dimensional effects 87
5.1 Model parameters . . . 88
5.1.1 Initial models and boundary conditions . . . 88
5.1.2 Numerical grid . . . 88
5.1.3 Additional 2D simulations . . . 89
5.2 Non-rotating models . . . 89
5.2.1 Evolution of global quantities . . . 89
5.2.2 Convective overturn . . . 94
5.2.3 Neutrino-driven outflows . . . 100
5.2.4 Global anisotropy and neutron star kicks . . . 104
5.3 A rotating model . . . 113
5.3.1 Missing polar downflows . . . 113
5.3.2 Anisotropic, neutrino-driven outflows . . . 116
5.3.3 Explosion anisotropy and downflow distribution . . . 118
5.3.4 Neutron star kick . . . 122
5.3.5 Spin-kick alignment? . . . 124

6 Summary and conclusions 127

A Neutrino transport 137
A.1 Transport equation . . . 137
A.2 Neutrino distribution function . . . 139
A.3 Optical depth . . . 140
A.4 Source terms . . . 142

B Explosion energy 149

C Hydrodynamics in an accelerated frame of reference 155

1

Introduction

About two times per century a massive star dies in our Milky Way. Instead of passing away silently, these stars die in spectacular explosions — supernovae. In the first seconds of such an extremely violent event, more energy is set free than was radiated away by the star during its whole life. Only a small part of this energy is released in the form of electromagnetic radiation, but this amount already suffices for the explosion to outshine even its parent galaxy. For this reason supernovae have been noticed since the beginnings of astronomical observations. Reports of strange stars that appear for some time and vanish again can be found in records of Chinese astronomers more than 2000 years ago. Supernova observations appear also in early Korean, Japanese, Arabic and European records. Two of the first "modern" astronomers were fortunate to witness such rare[1] events, Tycho Brahe in 1572 and Johannes Kepler in 1604.

With the advent of modern astronomical instruments it became possible to study the spectra of supernovae. This allowed Minkowski (1941) to distinguish two classes of supernovae, a classification that is still in use today: The spectra of Type II supernovae show strong Balmer hydrogen lines near maximum brightness, whereas the spectra of Type I supernovae show no signs of hydrogen. The absolute peak magnitude and the shape of the lightcurve also differ for the two classes. Differences in the spectra and the light curve behaviour within the two classes led to subclassifications. The early spectra of Type Ia supernova show lines of silicon, in contrast to types Ib and Ic, which do not. Type Ib and Ic supernovae differ in the presence or absence of helium lines, respectively. The lightcurve of Type II-L supernovae declines linearly after maximum light, whereas Type II-P supernova are characterised by a plateau phase in the light curve.

This purely phenomenological classification does not involve any theoretical understanding of the underlying explosion mechanism that could explain the observed differences. A first hint that there are actually two fundamentally different mechanisms at work came from the identification of the environments, in which the supernovae occurred. Type Ia supernovae show no tendency to occur in a certain galaxy type, nor in a certain location within the galaxy. In contrast, Type II, Type Ib, and Type Ic supernovae are observed only in spiral galaxies, and most of them occur in regions with a high star formation rate, i.e., in spiral arms and H II regions. This points to the possibility that the progenitors of Type Ia supernovae are old, low-mass stars and that supernovae of the other classes originate from younger, short-lived, massive stars. Currently the generally agreed upon interpretation is that Type Ia supernovae are thermonuclear explosions of white dwarfs, which do not leave any compact remnant behind. All other types are thought to arise from the collapse of a massive star's core, which triggers an explosion that disrupts the outer layer of the star and leads to the formation of a neutron star or even a black hole. The various subclasses differ in the presence of hydrogen and helium layers at the moment of explosion. The stars can have stripped these outer stellar layers by stellar wind loss or mass transfer in binary star systems. The processes taking place in the first seconds of such a "core collapse supernova", which are still not well-understood, are the subject this work.

---

[1] Only supernovae occurring in the Milky Way could be observed by early astronomers. Using modern instruments, nowadays more than 100 supernovae per year are detected in remote galaxies.

1.1 The explosion mechanism

In 1934, Baade & Zwicky realized that enormous amounts of gravitational binding energy must be released, when the core of an ordinary star collapses to a neutron star. They suggested that this energy powers the supernova explosion of the dying star. The existence of extremely compact neutron stars had been proposed by Landau only two years before (after the discovery of the neutron by Chadwick in 1932), but such objects were found only some decades later, when periodic radio signals were detected from pulsars, rotating neutron stars with strong magnetic fields. Yet, the process itself, i.e. the mechanism leading to the explosion and the formation of a neutron star, is still not completely understood after more than seventy years of research.

1.1.1 Core collapse

There is, however, some agreement about the processes taking place right before the onset of the explosion (see Bethe 1990 for a more detailed description). Near the end of their lives, stars with main sequence masses of more than about $8\,M_\odot$ have gone through several burning phases and have developed an onion-shell like structure. For main sequence masses larger than about $10\,M_\odot$ the core of such a progenitor star consists of iron-group elements (mostly ^{56}Fe and ^{56}Ni), which are the most tightly bound elements and consequently cannot release further energy by nuclear burning. This core is surrounded by shells of lighter nuclei – around the iron core there is Si/S, and further out O/Ne/Mg, C/O, He, and finally H (the latter two shells may have been lost due to stellar winds or mass transfer in binary systems). At the surface of the iron core, silicon burning still takes place and adds mass to the core. Inevitably the core approaches the Chandrasekhar mass limit (about $1.4\,M_\odot$) above which the self-gravity of the core cannot be balanced by the pressure of the degenerate, relativistic electron gas any more. Finally, electron captures and the endothermic photo-disintegration of heavy nuclei, two effects that reduce the pressure, trigger the collapse of the iron core when its mass is close to this limit of stability. The core, the radius of which is initially several thousand kilometres, collapses within about 0.1 s (which is on the order of the free-fall time scale) and forms a "proto-neutron star", the pre-stage of the final neutron star with a radius of only $\sim 50\,\mathrm{km}$.

The gravitational binding energy released during the collapse is converted into internal energy of the core. Initially, neutrinos produced by electron captures are able to escape unhindered and transport energy out of the collapsing core efficiently. However, the mean free path for neutrinos decreases during the collapse, as the density increases. Once the density has become sufficiently high ($\rho \approx 10^{12}\,\mathrm{g/cm^3}$) the time scale for the neutrinos to diffuse out of the core becomes larger than the collapse time scale and thus the neutrinos are "trapped" inside the core. For this reason most of the gravitational binding energy remains stored in the core during collapse and leaks out only later (and more slowly – on a time scale of about 10 s) in the form of neutrinos. The latter diffuse from the dense neutron star interior towards the outer layers and are finally able to escape. The energy- and neutrino-type dependent radius, at which the transition from diffusion to free streaming occurs, is called "neutrinosphere". The total energy that is released (i.e. the maximum energy that can be radiated away by neutrinos) is several 10^{53} erg. The collapse is stopped in the centre of the core, when supranuclear densities are reached and repulsive nuclear forces prevent a further compression of the matter. The infalling matter is decelerated abruptly, overshoots the equilibrium density and rebounds ("core bounce"), thereby generating pressure waves that steepen to a outward propagating shock wave with an energy of several 10^{51} erg.

1.1.2 Prompt explosions

Initially, it was thought that the shock wave could reach the outer layers of the star and make them unbound. However, it soon turned out that such a "prompt explosion mechanism" does not work, because the shock wave experiences a severe energy loss on its way outwards. There are two reasons for this: Firstly, the matter overrun by the shock after its formation consists of iron group nuclei, which are dissociated at the shock. In this endothermic process the shock loses 8.8 MeV per nucleon or about 17×10^{51} erg per $M_\odot$. And secondly, the outward moving shock reaches regions with lower density and also the postshock density decreases. After a few milliseconds the density has become low enough to allow neutrinos to escape from the postshock region. This leads to a strong "neutrino burst" that cools the postshock matter rapidly and extracts a significant amount of energy from the shock wave. As a consequence, the shock stalls only milliseconds after core bounce and becomes a slowly moving accretion shock (i.e. the postshock velocity turns negative). The shock reaches a radius of 100–200 km and recedes again. Therefore a different mechanism must drive the explosion.

1.1.3 Delayed explosions

In 1966 Colgate & White speculated about the possibility, that the absorption of neutrinos in the outer stellar layers might deposit enough energy to trigger an explosion. Although their model was too simplistic and did not include a real neutrino transport, their basic idea seemed quite promising and stimulated other studies: After core bounce there is a huge reservoir of energy in the core, from which energy leaks out slowly in form of neutrinos. If only a small fraction of this energy was re-absorbed, it would suffice to power an explosion with the canonical energy of 10^{51} erg known from observations.

As the models were improved with time, those who hoped that such a "neutrino heating" could prevent the supernova shock from stalling shortly after its formation were disappointed. However, Wilson (1985) discovered that the stalled shock could be "revived" by neutrino heating on a much longer time scale (several 100 ms). This so-called "delayed explosion" scenario is still considered to be the most promising way to trigger an explosion. This explosion mechanism leads to unbound matter because neutrinos deposit energy in a "gain layer" below the shock, mainly due to neutrino absorption by free protons and neutrons. In the one-dimensional simulations (i.e. simulations, for which spherical symmetry was assumed) of Wilson (1985) and Bethe & Wilson (1985), this persistent deposition of energy increases the shock radius, and finally leads to an explosion. However, in the two decades after this pioneering work most of the new one-dimensional (1D) simulations with progressively improved transport treatment (and including also relativistic effects) failed to produce explosions. Nowadays there is growing consensus that the neutrino-driven explosion mechanism of core collapse supernovae does not work in spherical symmetry, at least for progenitors more massive than about $10\,M_\odot$. None of the recent one-dimensional state-of-the-art simulations with detailed descriptions of the neutrino transport develops an explosion (Rampp & Janka 2000; Liebendörfer et al. 2001; Liebendörfer et al. 2005; Thompson et al. 2003; Buras et al. 2003, 2006a,b). Only for the least massive stars experiencing a core collapse (those whose cores contain O/Ne/Mg instead of iron group elements) explosions in spherical symmetry turned out to be possible (Kitaura et al. 2006).

Yet, when two-dimensional simulations (i.e. simulations, for which axisymmetry was assumed) became feasible, multi-dimensional effects were recognised to be helpful. In these simulations small seed perturbations grow by hydrodynamic instabilities to large amplitudes and affect the evolution significantly. In particular, it has been shown that convection is able to develop below the stalled supernova shock and can increase the efficiency of neutrino-heating significantly (Herant et al. 1994; Burrows et al. 1995; Janka & Müller 1996). Current 2D simulations are considerably closer to the explosion threshold than models in spherical symmetry (Buras et al. 2003, 2006a,b), and a successful explosion has been reported for an $11.2\,M_\odot$ progenitor (Buras et al. 2006b). Despite these encouraging results, it still has to be shown that the "convectively supported delayed explosion mechanism" works robustly, i.e. that it is able to produce explosions for a wide range of parameters and not only for certain progenitor models. Nevertheless, this mechanism is still the most promising way to explain supernova explosions. Current 2D models are on the verge of exploding, but at the moment, it is not clear what is missing (see Buras et al. 2003). It may be that improvements in the EoS, the treatment of neutrino transport or the weak interaction rates of neutrinos are needed. It could also be that multidimensional effects were not modelled correctly due to the restriction to two dimensions, the assumed initial conditions, or shortcomings of the applied numerical methods. It is even possible that rotation and hydromagnetic effects have to be taken into account, although at the moment it is believed that they will change the picture only for special cases.

1.2 The anisotropy of core collapse supernovae

However the final, robust explosion mechanism works in detail, it will also have to explain why core collapse supernovae are non-spherical. There is mounting evidence that these explosions develop a pronounced global anisotropy, and several explanations for this behaviour have been proposed.

1.2.1 Evidence for anisotropy

The best example for an anisotropic explosion is the nearest supernova observed in the last centuries, Supernova 1987A, which is located in the Large Magellanic Cloud. Already soon after the explosion, it was recognised that the lightcurve could only be explained if radioactive nickel was mixed outward into the hydrogen envelope (Woosley et al. 1988). When the ejecta became optically thin in the infrared, the velocity distributions of iron group elements could be deduced from infrared lines and provided further evidence for large-scale mixing of the ejecta (Colgan et al. 1994; Haas et al. 1990). Furthermore, the red/blue asymmetry of some of the lines pointed towards a global asymmetry (Haas et al. 1990; Jennings et al. 1993). Nowadays, the non-spherical, prolate distribution of the ejecta (Fig. 1.1) can be directly imaged with the Hubble Space Telescope (Wang et al. 2002). Also anisotropic ejecta distributions of other, older, supernova remnants have been imaged directly, e.g. Cassiopeia A (Hwang et al. 2004) or Puppis A, which seems to be an almost one-sided explosion (Winkler & Petre 2006).

For many other supernovae that are not spatially resolved, information about the anisotropy could be obtained by spectropolarimetry (Leonard et al. 2006; Wang et al. 2003, 2001, and

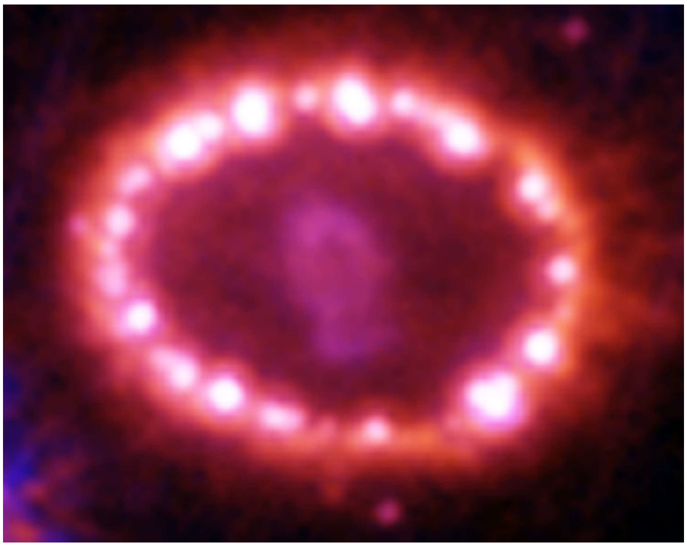

Figure 1.1: Optical image of supernova 1987A taken by the Hubble Space Telescope in 2003. The ring-like structure is thought to be caused by the collision of the supernova shock with matter that has been stripped by the progenitor star in an anisotropic stellar wind more than 10 000 years prior to the collapse. The supernova ejecta are visible in the centre of the ring and show a pronounced prolate deformation. *Credit: NASA, P. Challis, R. Kirshner (Harvard-Smithsonian Center for Astrophysics) and B. Sugerman (STScI)*

references therein). The observed polarisation of light of typically 1–2 percent translate into axis ratios of up to 3 : 1 (assuming a prolate, spheroidal shape of the photosphere) and indicate that global anisotropies are a common feature of many core-collapse supernovae. Interestingly, the deeper one can look into the expanding and increasingly transparent supernova ejecta, the higher is the asymmetry inferred from the observed polarisation. This indicates that the origin of the anisotropy seems to be intrinsically linked to the mechanism of the explosion.

1.2.2 Possible origins

Various kinds of hydrodynamic instabilities may be responsible for the global anisotropy of the ejecta that seems to be present already soon after the onset of the explosion. The first instability that has been recognised to be important is convection. Inside the neutron star convection can enhance the core neutrino luminosity (see e.g. Keil et al. 1996; Buras et al. 2006b) and is therefore of interest for the explosion mechanism, but leads only to anisotropy on relatively small angular scales.

More relevant concerning global modes is a second convectively unstable region, the gain layer. Here the neutrino heating is stronger for smaller radii than near the shock and therefore flow with a negative radial derivative of entropy establishes, a situation which is convectively unstable. Perturbations grow with a local growth rate of at most (for small-scale perturbations) the Brunt-Väisäla frequency, which attains values of up to $\sim 1000\,\mathrm{s}^{-1}$. However, considering only local stability is not sufficient in this case, as we are mainly interested in modes comparable to the size of the whole unstable region. The first study of global stability related to this problem was performed by Chandrasekhar (1961), who investigated volume-filling convection in a fluid sphere by means of a linear perturbation analysis. Chandrasekhar found the dipole or $l = 1$ mode (in terms of an expansion in spherical harmonics Y_l^m) to be the most unstable. In fact, Woodward et al. (2003) and Kuhlen et al. (2003) demonstrated with three-dimensional hydrodynamic simulations that the $l = 1$ mode dominates the convection in red giant and main sequence stars, respectively. However, Foglizzo et al. (2006b) studied a problem that resembles the stalled shock phase in supernovae more closely, taking also into account the limited radial thickness of the convectively unstable layer below the shock and the transport of matter out of the unstable region (as it settles onto the neutron star). The latter process turns out to have a stabilising effect and can hamper the growth of convection significantly. In particular, the lowest modes are convectively unstable only if the ratio of the convective growth time scale to the "advection time" (i.e. the time required by the matter to cross the unstable layer) is sufficiently small. Foglizzo et al. (2006b) estimate that this may not be the case in general and propose that instabilities different from convection may be responsible for the occurrence of low (dipolar or quadrupolar) modes.

The so-called "advective-acoustic cycle" (Foglizzo & Tagger 2000; Foglizzo 2001, 2002), is a promising candidate for such an instability. It is based on the production of sound waves by the advection (i.e. transport by fluid motion) of entropy and vorticity perturbations from the shock to the neutron star. These sound waves rise and hit the supernova shock, thereby producing new entropy and vorticity perturbations. By means of linear stability analysis, Galletti & Foglizzo (2005) and Foglizzo et al. (2006a) showed that these processes result in an amplifying feedback loop for non-radial perturbations in the stalled accretion shock phase of core collapse supernovae. Highest growth rates are found for the lowest modes (in particular $l = 1$). Global instabilities different from convection are also found in the non-linear regime by hydrodynamic simulations. Blondin et al. (2003) discovered in 2D hydrodynamic simulations that the adiabatic accretion flow below a standing shock develops a non-radial, oscillatory instability (which they termed "standing accretion shock instability" or SASI), dominated by the $l = 1$ or $l = 2$ modes. Similar results were found in simulations with neutrino cooling and heating terms (Blondin & Mezzacappa 2006; Ohnishi et al. 2006). The nature of this instability mechanism is still a matter of debate. While Ohnishi et al. (2006) regard the advective-acoustic cycle as the cause of the low mode oscillations, Blondin & Mezzacappa (2006) argue that a different kind of instability, which is purely acoustic and does not involve advection, is at work in their simulations.

Due to strong simplifications (in particular boundary and initial conditions are taken from a stationary flow solution), these simulations cannot be regarded as accurate models for the situation in supernova cores. The lack of more detailed simulations that could allow to assess the impact of instabilities like the advective-acoustic cycle in the non-stationary flow around a forming neutron star was an important motivation to perform the simulations we present in this work — in particular, as in addition such simulations could provide new insights about another process, that is not well-understood, the acceleration of neutron stars during their birth.

1.3 Neutron star kicks

The high velocities of neutron stars is a topic closely related to the anisotropy of core collapse supernovae. Observations suggest that neutron stars receive a strong "kick" during their formation in the supernova, possibly linked to an anisotropic explosion. In the following we give an overview of observations and possible kick mechanisms.

1.3.1 The neutron star velocity distribution

Neutron stars move with space velocities much higher than those of their progenitors (e.g. Cordes et al. 1993; Lyne & Lorimer 1994; Hansen & Phinney 1997; Zou et al. 2005; Chatterjee et al. 2005). In the most extreme cases the velocities can exceed 1000 km/s. For instance, Chatterjee & Cordes (2002) deduced a pulsar velocity of ~ 1600 km/s for the neutron star in the Guitar

Nebula using radio observations, and Winkler & Petre (2006) measured the velocity of the neutron star in Puppis A directly (using X-ray observations) and found a value of 1500 km/s. However, in general pulsars are slower than these extreme cases, and the presence of pulsars in globular clusters (with small escape velocities) shows that in many cases the neutron star birth velocity must in fact be very small. Efforts to determine the birth velocity distribution function of neutron stars agree in the finding that the average velocity is several 100 km/s. However, claims of a bimodality of the pulsar velocity distribution are still controversial. While some authors have obtained evidence for a low- and a high-velocity component of the distribution function (Cordes & Chernoff 1998; Fryer et al. 1998; Arzoumanian et al. 2002; Brisken et al. 2003), others have found that a simple Maxwellian fit works best (Hansen & Phinney 1997; Hobbs et al. 2005).

1.3.2 Neutron star kick mechanisms

The disruption of binary star systems, in which one star explodes as a supernova and leaves a neutron star behind, does not lead to sufficiently high velocities, and also the orbital parameters of many binary systems imply an intrinsic acceleration mechanism of the pulsars, probably linked to their creation (see Lai 2001; Lai et al. 2001 for reviews). Quite a number of explanations have been suggested, mostly involving anisotropic mass ejection in the supernova explosion or anisotropic neutrino emission of the cooling, nascent neutron star.

The latter suggestion, i.e. a “neutrino rocket engine” that boosts neutron stars to big velocities makes use of the fact that the huge reservoir of gravitational binding energy released during the collapse of the stellar core is mostly carried away by neutrinos. Creating a global emission anisotropy of these neutrinos of even only 1% — which is sufficient to obtain a NS recoil of about $300\,\mathrm{km\,s^{-1}}$ —, however, turned out to be very difficult. Most ideas refer to unknown neutrino properties (e.g., Fuller et al. 2003; Fryer & Kusenko 2006 and refs. therein) and/or require the presence of a very strong magnetic field with a large dipole component (instead of being randomly structured and variable with time) in the newly formed NS (e.g. Arras & Lai 1999a,b; Socrates et al. 2005). Such assumptions are not generally accepted and are not the result of self-consistent calculations but put into the models “by hand”.

The other possibility — i.e. a “hydrodynamic kick mechanism”, in which the momentum of the anisotropic ejecta is balanced by a recoil of the neutron star — might be supported by the fact that some pulsars seem to propagate in a direction opposite to mass distribution asymmetries of their associated supernova remnants (see, e.g. Winkler & Petre 2006). However, clear observational evidence is still missing. Herant (1995) has shown that in principle a hydrodynamic kick mechanism can produce neutron star velocities of the required magnitude in strongly anisotropic, (in the most extreme cases one-sided i.e., dipole-dominated) explosions.

Yet, so far only simulations started from the assumption that a considerable dipolar asymmetry was already present in the pre-collapse iron core gave rise to a large anisotropy of the supernova explosion and yielded high neutron star velocities of $\sim 500\,\mathrm{km/s}$ (Burrows & Hayes 1996). The origin of such big pre-collapse perturbations, however, is not clear (Murphy et al. 2004). Simulations, in which the initial perturbations were not that extreme (see e.g. Janka & Müller 1994), were not dominated by low modes and consequently the neutron star recoil velocities remained rather small. In this situation it seems to be worthwhile to investigate whether the latter result still holds true when simulations are performed with improved methods and new data regarding the neutrino luminosity of nascent neutron stars is taken into account.

1.4 Aims of this thesis

The main goal of this work is an investigation of hydrodynamic instabilities in the supernova core during the onset of the explosion. In particular, we are interested in the question, whether such instabilities can lead to a global anisotropy of the explosion without the aid of special initial conditions (such as macroscopic asymmetries in the star before gravitational collapse, extremely rapid rotation or extraordinary strong magnetic fields in the progenitor star). Furthermore, we would like to know whether large recoil velocities as observed for many young pulsars can result from anisotropic mass ejection in the explosion. To this end we present a comprehensive 2D study of supernova dynamics that can be considered as a significant improvement and extension of the earlier calculations of Janka & Müller (1996) with respect to the treatment of neutrino transport, the assumed characteristics of the neutrino emission from the neutron star core, the inclusion of rotation, the spatial resolution, and the covered evolutionary time of the supernova explosions.

Apart from determining the magnitude of the explosion anisotropy we aim also at investigating its origin. In particular we will try to find out, whether hydrodynamic instabilities different from convection are able to grow sufficiently fast in the non-stationary postshock flow to have an significant influence on the explosion, and to what extent these instabilities are responsible for the formation of global modes. Neither the linear studies of Foglizzo et al. (2006a) (for which a stationary background flow was assumed) nor the 2D hydrodynamic simulations of Blondin et al. (2003); Blondin & Mezzacappa (2006); Ohnishi et al. (2006) (for which initial and boundary conditions were taken from a stationary solution) can answer these questions. Yet, there is still no concensus on a more fundamental question, which we also want to investigate: What is the nature of the non-convective instability present in the above mentioned 2D simulations – is the instability mechanism related to the advective-acoustic cycle, a purely acoustic cycle (as advocated by Blondin & Mezzacappa) or something else? In this work we will present a series of 2D simulations that are able to address these questions.

And finally we would like to study how 3D effects change the evolution and morphology of our supernova models. We will present the first 3D simulations using high-resolution, shock-capturing methods and demonstrate that also in three dimensions global modes are able to develop. Due to the enormous computational costs of 3D simulations it is still not feasible to perform full parameter studies in 3D. However, already the few 3D simulations we were able to compute allow some insight concerning the differences between 2D and 3D models.

We use a simple and fast, yet sufficiently accurate neutrino transport scheme for the transparent and semi-transparent regimes that allows us to study fundamental aspects of the still poorly understood interaction between hydrodynamic instabilities and neutrino heating for a large number of 2D models and even several 3D models. This scheme may not be accurate enough to answer the question whether neutrino heating is viable to drive supernova explosions or not. However, this is not a goal of this work either. In fact we do not attempt to follow the transport of neutrinos seamlessly from the optically thick core of the proto-neutron star into the optically thin regime. Instead, we treat the fluxes and spectra of the neutrinos emitted from the core of the nascent neutron star as a boundary condition, and explore the explosion dynamics in dependence of systematic variations, limited by fundamental constraints of the neutrino emission properties of the nascent neutron star. Our models are therefore parametric studies and based on the assumption that the convectively supported neutrino-heating mechanism (Herant et al. 1994; Burrows et al. 1995; Janka & Müller 1996) works.

We proceed by summarising our numerical algorithms and computational approach in Chapter 2. In Chapter 3 we will discuss about 80 2D Models and their dependence on different initial and boundary conditions. The topic of Chapter 4 is a more detailed investigation on the nature of non-convective instabilities, which are studied by means of a further series of 2D simulations. In Chapter 5 our 3D simulations are discussed and compared to the corresponding 2D simulations. Chapter 6, finally, contains our conclusions. Appendix A presents a detailed description of our neutrino transport scheme, in Appendix B we analyse the explosion energetics of the neutrino-driven supernovae in our simulations and in Appendix C we discuss the solution of the hydrodynamics equations in an accelerated frame of reference. Parts of the present work were already presented in the publications of Scheck et al. (2004, 2006).

2

Computational approach and numerical methods

2.1 Hydrodynamics and gravity

The matter taking part in the processes we intend to study can be regarded as an ideal fluid (Müller 1998), as viscosity and heat conduction have been shown to be negligible (except in shock waves). Therefore the flow is ruled by the following conservation laws for mass, momentum (the inviscious, compressible Euler equation) and energy,

$$\frac{\partial \rho}{\partial t} + \mathrm{div}\,(\rho \vec{v}) = 0, \tag{2.1}$$

$$\frac{\partial}{\partial t}(\rho \vec{v}) + \mathrm{div}\,[\rho\,(\vec{v} \otimes \vec{v})] + \mathrm{grad}\,p = -\rho\,\mathrm{grad}\,\Phi + \vec{Q}_{\mathrm{M}}, \tag{2.2}$$

$$\frac{\partial}{\partial t}(\rho E) + \mathrm{div}\,[(\rho E + p)\vec{v}\,] = -\rho\,\vec{v} \cdot \mathrm{grad}\,\Phi + Q_{\mathrm{E}} + \vec{v} \cdot \vec{Q}_{\mathrm{M}}. \tag{2.3}$$

Here ρ is the density, $\vec{v}$ the fluid velocity, p the pressure, $E = v^2/2 + \epsilon$ the specific total energy, ϵ the specific internal energy, and Φ the gravitational potential. The momentum and energy source terms due to neutrinos, $\vec{Q}_{\mathrm{M}}$ and Q_{E}, are discussed in Appendix A. In order to solve the set of equations (2.1)–(2.3), an equation of state (EoS), e.g. a relation between pressure, density and temperature has to be specified. In general this relation depends also on the composition of the matter, i.e. on the mass fractions X_i or number fractions Y_i of nuclei and nucleons. Therefore one has to take into account the evolution of the abundance for each species according to a conservation equation,

$$\frac{\partial \rho X_i}{\partial t} + \mathrm{div}\,(\rho X_i \vec{v}) = R_i. \tag{2.4}$$

Here R_i denotes the source term due to nuclear reactions. In the case of nuclear statistic equilibrium (NSE) the composition is determined by temperature, density and only one additional variable, e.g. the electron fraction Y_e. Thus instead of computing the rates R_i for each species one has to determine the source term only for Y_e, whose evolution is determined by

$$\frac{\partial \rho Y_e}{\partial t} + \mathrm{div}\,(\rho Y_e \vec{v}) = Q_{\mathrm{N}}. \tag{2.5}$$

Here Q_N is the source term caused by neutrino absorption and emission (see Appendix A). Yet, also in case of NSE Eqn. (2.4) has to be solved for each species (with $R_i = 0$) in order to distinguish compositional changes due to mixing (which do not affect the internal energy) from those caused by nuclear reactions that lead to changes in the internal energy and therefore result in an additional source term in Eqn. (2.3).

In spherical coordinates (r, θ, ϕ) and omitting source terms due to neutrino processes and nuclear reactions (which are treated separately in an operator splitting procedure), equations (2.1)–(2.4) read

$$\partial_t \rho + \frac{1}{r^2}\partial_r(r^2[\rho v_r]) + \frac{1}{r\sin\theta}\partial_\theta(\sin\theta[\rho v_\theta]) + \frac{1}{r\sin\theta}\partial_\phi[\rho v_\phi] = 0, \tag{2.6}$$

$$\begin{aligned}\partial_t(\rho v_r) + \frac{1}{r^2}\partial_r(r^2[\rho v_r^2]) + \frac{1}{r\sin\theta}\partial_\theta(\sin\theta[\rho v_r v_\theta]) + \frac{1}{r\sin\theta}\partial_\phi[\rho v_r v_\phi]&\\ + \left\{-\frac{\rho v_\theta^2}{r} - \frac{\rho v_\phi^2}{r}\right\} + \partial_r p \quad &= \quad -\rho\partial_r\Phi,\end{aligned} \tag{2.7}$$

$$\begin{aligned}\partial_t(\rho v_\theta) + \frac{1}{r^2}\partial_r(r^2[\rho v_\theta v_r]) + \frac{1}{r\sin\theta}\partial_\theta(\sin\theta[\rho v_\theta^2]) + \frac{1}{r\sin\theta}\partial_\phi[\rho v_\theta v_\phi]&\\ + \left\{\frac{\rho v_\theta v_r}{r} - \frac{\rho v_\phi^2 \cos\theta}{r\sin\theta}\right\} + \frac{1}{r}\partial_\theta p \quad &= \quad -\rho\frac{\partial_\theta\Phi}{r},\end{aligned} \tag{2.8}$$

$$\begin{aligned}\partial_t(\rho v_\phi) + \frac{1}{r^2}\partial_r(r^2[\rho v_\phi v_r]) + \frac{1}{r\sin\theta}\partial_\theta(\sin\theta[\rho v_\theta v_\phi]) + \frac{1}{r\sin\theta}\partial_\phi[\rho v_\phi^2]&\\ + \left\{\frac{\rho v_\phi v_r}{r} + \frac{\rho v_\phi v_\theta \cos\theta}{r\sin\theta}\right\} + \frac{1}{r\sin\theta}\partial_\phi p \quad &= \quad -\rho\frac{\partial_\phi\Phi}{r\sin\theta},\end{aligned} \tag{2.9}$$

$$\begin{aligned}&\partial_t(\rho E) + \frac{1}{r^2}\partial_r(r^2[\rho v_r(E+p)]) + \frac{1}{r\sin\theta}\partial_\theta(\sin\theta[\rho v_\theta(E+p)]) + \frac{1}{r\sin\theta}\partial_\phi[\rho v_\phi(E+p)]\\ &\quad = -\rho\left(v_r\partial_r\Phi + v_\theta\frac{\partial_\theta\Phi}{r} + v_\phi\frac{\partial_\phi\Phi}{r\sin\theta}\right),\end{aligned} \tag{2.10}$$

$$\partial_t\rho X_i + \frac{1}{r^2}\partial_r(r^2[\rho X_i v_r]) + \frac{1}{r\sin\theta}\partial_\theta(\sin\theta[\rho X_i v_\theta]) + \frac{1}{r\sin\theta}\partial_\phi[\rho X_i v_\phi] = 0. \tag{2.11}$$

The terms in curly braces are fictitious forces that are caused by the fact that in general curvilinear coordinates (and in particular in spherical geometry) the directions of the base unit vectors vary in space.

Adopting the dimensional splitting procedure of Strang (1968), we do not solve Eqns. (2.6)–(2.11) simultaneously, but in *directional sweeps*. That is, in a first step (the radial sweep) we neglect all terms with θ- or ϕ-derivatives and fictitious forces acting in θ- or ϕ-directions, so that the non-radial components of the flow are just advected, but do not feel any forces. Analogously, in the second and the third step we consider only forces in the $\theta-$ and the ϕ-direction, respectively.

For two-dimensional simulations it is sufficient to perform only the $r-$ and $\theta-$-sweeps, if the velocity in ϕ-direction is zero, i.e. for non-rotating models. If, however, rotation is included, one has to account for the changes of ρv_ϕ due to fictitious forces (which guarantee that the specific angular momentum of a mass element is conserved). In 3D these forces act during the ϕ-sweep. As we want to avoid to perform the ϕ-sweep also in 2D simulations, we distribute the fictitious forces in Eq. (2.9) over the first two sweeps, i.e. for ρv_ϕ we take into account additional source terms $\rho v_\phi v_r / r$ and $\rho v_\phi v_\theta \cot\phi / r$ in the r- and the θ-sweep, respectively.

The equations to be solved in one sweep are the one-dimensional hydrodynamic equations (with some additional factors accounting for the geometry) plus two advection equations for the lateral components (i.e. the flow perpendicular to the current sweep direction). For instance, in the radial sweep the following set of equations has to be solved:

$$\frac{\partial U}{\partial t} + \frac{\partial (AF)}{\partial V} + \frac{\partial H}{\partial r} = G, \tag{2.12}$$

where

$$U = \begin{pmatrix} \rho \\ \rho u \\ \rho v \\ \rho w \\ \rho E \\ \rho X_i \end{pmatrix}, \quad F(U) = \begin{pmatrix} \rho u \\ \rho u^2 \\ \rho v u \\ \rho w u \\ u(\rho E + p) \\ \rho u X_i \end{pmatrix}, \quad H(U) = \begin{pmatrix} 0 \\ p \\ 0 \\ 0 \\ 0 \\ 0 \end{pmatrix}, \quad G = \begin{pmatrix} 0 \\ \rho g \\ 0 \\ 0 \\ \rho u g \\ 0 \end{pmatrix}. \tag{2.13}$$

Here U are the conserved quantities, $F(U)$ is the flux function, $V(r) = \frac{4\pi}{3} r^3$, and $A(r) = 4\pi r^2$.

Conservation laws like (2.12) can be solved accurately using finite volume methods. In such approaches the fluxes $F(U)$ at the interfaces of the numerical grid cells are computed and used to update the cell-averaged values of the conserved quantities, U. In one dimension the update step for a cell i can be written as

$$U_i(t^n) = U_i(t^{n-1}) + \frac{t^n - t^{n-1}}{V_i} \left(A_{i-1/2} F_{i-1/2} - A_{i+1/2} F_{i+1/2} \right), \tag{2.14}$$

where $F_{i\pm 1/2}$ and $A_{i\pm 1/2}$ are the fluxes and areas of the left and the right cell interface, respectively, and V_i is the cell volume. This procedure guarantees that the physically conserved quantities are also numerically conserved, which is important for a correct treatment of shock waves and in particular to avoid unphysical shock velocities (LeVeque 1998).

In a special class of finite volume methods, the Godunov type schemes, the fluxes at the cell interfaces are computed solving a local Riemann problem, and thus taking the non-linearity in the equations explicitely into account. For the calculations discussed in this work we use an improved version of the original Godunov method, the Piecewise-Parabolic Method (PPM) of Colella & Woodward (1984), which is a "high-resolution shock-capturing" (HRSC) scheme. The ability of PPM to achieve high accuracy with a relatively low number of grid cells and to avoid that shock waves become more than a few cells wide ("shock capturing") is based on a rather complicated reconstruction of the hydrodynamic state within the grid cells, which is discussed in detail in Colella & Woodward (1984). The implementation we are using is basically the same as described in Kifonidis et al. (2003). It consists of a hydrodynamics module which is based on the direct Eulerian version of PPM (augmented by the HLLE solver of Einfeldt 1988 to avoid the odd-even-decoupling instability, which is discussed in Kifonidis et al. 2003), and a module that computes the source terms for energy and lepton number which enter the hydrodynamic equations due to neutrino absorption, scattering, and emission processes (see Sect. 2.2).

The equation of state used for our simulations is that of Janka & Müller (1996). It includes contributions by photons, electrons and positrons of arbitrary degeneracy and relativity, and non-degenerate neutrons, protons, α's and a representative nucleus of the iron group (in our case this nucleus is chosen to be ^{54}Mn) in NSE. In contrast to Kifonidis et al. (2003, 2006) we do not follow explosive nucleosynthesis in this work. This allows us to save a considerable amount of computer time, which is mandatory for carrying out an extended parameter study like the one presented here.

Following Kifonidis et al. (2003), we include relativistic corrections in our otherwise Newtonian code by replacing the "spherical part" of the gravitational potential of the 2D mass distribution by the "effective relativistic potential" of Rampp & Janka (2002) (for details, see Marek et al. 2006). For describing the gravity of the central "point mass" (i.e., the mass enclosed by the inner boundary) we use the baryonic mass where Eq. (53) in Rampp & Janka (2002) requires the gravitational mass. This turned out to yield very good agreement with the improved version of the effective relativistic potential developed by Marek et al. (2006).

2.2 Neutrino transport and neutrino source terms

The original code version of Kifonidis et al. (2003) made use of a simple light-bulb approximation (Janka & Müller 1996) in which luminosities of neutrinos and antineutrinos of all flavours were imposed at the inner boundary (which is usually below the neutrinospheres) and kept constant with radius. These luminosities were typically *not* chosen to give accurate values for the fluxes prevailing below the neutrinospheric layers, but their choice was guided by the asymptotic luminosities that emerge from the contracting and accreting nascent neutron star at *large* radii. This was necessary in order to cope with the main problem of a light-bulb approach, namely that it neglects changes of the neutrino fluxes and spectra that result from the interactions of neutrinos with the stellar matter, thus ignoring, for example, the contributions of the neutrino emission from accreted matter to the neutrino luminosity.

In this work we considerably improve upon this former approach by explicitly including these effects. We achieve this by abandoning the light bulb in favour of a gray, characteristics-based scheme, which can approximate neutrino transport in the transparent and semi-transparent regimes. The approach is not particularly suitable to handle also the regime of very large optical depths, τ. Therefore we still do our simulations with an inner grid boundary at $\tau \approx 10 \dots 100$. However, the luminosities prescribed there have no relation to those used in the older light-bulb calculations. We have chosen them to reproduce qualitatively the evolution of the luminosities in a Lagrangian mass shell below the neutrinospheres as obtained in recent Boltzmann transport calculations. More details will be given in Sect. 2.4.2.

The transport scheme itself solves the zeroth order moment equation of the Boltzmann transport equation in spherical symmetry in the form

$$\frac{\partial}{\partial t} L + c_{\mathrm{eff}} \frac{\partial}{\partial r} L = 4\pi\, r^2\, c_{\mathrm{eff}}\, Q_\nu^+ - \kappa c L. \tag{2.15}$$

Here $L(r,t)$ stands for the neutrino number flux or the neutrino luminosity, Q_ν^+ is the neutrino number or energy production rate per unit volume (which is equal to the corresponding loss rate of the stellar medium), and κ is the corresponding absorptivity. The "effective speed" of the neutrino propagation, c_{eff}, is governed by diffusion at high densities and reaches the speed of light, c, at large radii and low optical depths. Equation (2.15) has been derived under the assumption that $\partial_t c_{\mathrm{eff}} = 0$. It can be solved analytically, when Q_ν^+, κ and c_{eff} are assumed to be constant within each cell of the numerical grid. For c_{eff} a functional form in dependence of τ is adopted, which fits the results of detailed transport simulations in neutron star "atmospheres".

The neutrino-matter interaction rates are calculated using the assumption that the spectra have Fermi-Dirac form. Charged-current processes with neutrons (n) and protons (p),

$$\nu_{\mathrm{e}} + \mathrm{n} \rightleftharpoons \mathrm{p} + \mathrm{e}^-, \tag{2.16}$$

$$\bar{\nu}_{\mathrm{e}} + \mathrm{p} \rightleftharpoons \mathrm{n} + \mathrm{e}^+, \tag{2.17}$$

thermal electron-positron ($\mathrm{e}^{\pm}$) pair creation and annihilation,

$$\mathrm{e}^{+}+\mathrm{e}^{-} \rightleftharpoons \nu_i+\bar{\nu}_i \quad (i=\mathrm{e},\mu,\tau), \tag{2.18}$$

and neutrino scattering off nuclei (A), nucleons, and electrons and positrons,

$$\nu_i+\mathrm{A} \rightleftharpoons \nu_i+\mathrm{A}, \tag{2.19}$$

$$\nu_i+\left\{\begin{array}{c}\mathrm{n}\\ \mathrm{p}\end{array}\right\} \rightleftharpoons \nu_i+\left\{\begin{array}{c}\mathrm{n}\\ \mathrm{p}\end{array}\right\}, \tag{2.20}$$

$$\nu_i+\mathrm{e}^{\pm} \rightleftharpoons \nu_i+\mathrm{e}^{\pm}, \tag{2.21}$$

are taken into account.

We solve Eq. (2.15) for neutrino number and energy transport separately for neutrinos and antineutrinos of all flavours (e,μ,τ). This allows us to adopt a non-equilibrium description of the transport in the sense that the spectral form is assumed to be Fermi-Dirac, but the neutrino temperatures T_{ν_i} are not necessarily equal to the gas temperature T. Solving two transport equations for neutrino number and energy, we therefore can determine locally neutrino number and energy densities and thus the spectral temperatures T_{ν_i} from the mean neutrino energies. A detailed description of our approximative solution of the non-equilibrium transport problem and the exact expressions for the employed interaction kernels can be found in Appendix A. While giving qualitatively similar results as Boltzmann-solvers in spherical symmetry (cf. Sect. 3.2.4), the computational cost of this approximative transport scheme is two orders of magnitude lower.

Equation (2.15) describes the neutrino transport in the radial direction only. Transport in the lateral direction is ignored in our two-dimensional simulations, but lateral variations of the neutrino quantities are allowed for by applying the radial transport solver independently on different radial "rays" corresponding to the different angular (i.e. lateral in 2D) directions of our polar grid.

2.3 Numerical grid

The hydrodynamic equations are solved on a spherical grid with coordinates (r,θ,ϕ). We denote $\theta=0$ as "north pole" and $\theta=\pi$ as "south pole". The interfaces of the grid cells are located at

$$\begin{aligned}
r_{i\pm\frac{1}{2}} &= R_{\mathrm{ib}}{}^{(i\pm\frac{1}{2}-\frac{1}{2})\cdot\alpha}, \quad i=1\ldots N_r\\
\theta_{j\pm\frac{1}{2}} &= \theta_0+(j\pm\frac{1}{2}-\frac{1}{2})\cdot\Delta\theta, \quad j=1,\ldots,N_\theta\\
\phi_{k\pm\frac{1}{2}} &= (k\pm\frac{1}{2}-\frac{1}{2})\cdot\Delta\phi, \quad k=1,\ldots,N_\phi
\end{aligned}$$

where α is typically chosen such that the outermost zone ends at $R_{\mathrm{ob}}\approx 2\cdot 10^9\,\mathrm{cm}$, which is usually sufficient to prevent the supernova shock to run off the grid in the first second after core bounce.

The inner boundary is placed within the forming neutron star after core bounce, at a *Lagrangian* mass shell somewhat below the electron neutrinosphere. The spacing of the zones near and below the neutrinospheres is chosen such that variations of the optical depth per zone remain smaller than a few. The baryonic matter of the neutron star interior to the inner boundary, M_{core} (which is typically $\sim 1.1\,M_\odot$), is removed and its gravitational attraction is taken into account by assuming a point mass at $r = 0$ (see Sect. 2.1). In the course of the simulation the grid contracts radially, mimicking the contraction of the neutron star (see Sect. 2.4.1).

The resolution in the second and third dimension is given by $\Delta\theta = \theta_{tot}/N_\theta$ (where $\theta_{tot} = \pi - 2\theta_0$) and $\Delta\phi = 2\pi/N_\phi$, respectively. Here N_θ and N_ϕ denote the number of zones in latitudinal and longitudinal directions, respectively. The total solid angle covered by the grid is called Ω_{tot}. Unless noted otherwise, the calculations presented in the following are carried out in a full sphere, i.e. $\theta_0 = 0$. In 2D the angular resolution is chosen such that square-shaped cells are obtained in the convective region, i.e. $\Delta r \approx r\Delta\theta$. Typically 400 radial and 180 lateral zones (i.e. $\Delta\theta = 1^\circ$) are used. In 3D the significantly higher computational cost forced us to increase the angular zone size to $\Delta\theta = \Delta\phi = 2^\circ$–$4^\circ$.

The spherical grid is well-suited to represent the approximately spherical symmetric regions in our simulations, in particular the neutron star and the strong density gradient at its surface. An accurate representation of the latter region on a Cartesian grid would require significantly higher resolution and would therefore be computationally much more expensive. However, the spherical grid has the disadvantage of having a non-uniform angular resolution. For equidistant zone interfaces in latitudinal and longitudinal direction, the numerical zones near the poles occupy much smaller solid angles than those near the equator. This has an influence on the local growth rate of instabilities (see Sect. 5.2.1).

Furthermore, in 3D additional problems arise due to the fact that, in contrast to the equatorial region, the zones near the poles are not roughly rectangular but rather strongly deformed. The poles pose singularities in the sense that the zone interfaces coinciding with the polar axis have zero area. Therefore the flux of matter through these interfaces must be zero, which means that reflecting boundary conditions have to be applied at the polar axis. The reflection of a fluid element with a lateral momentum p_{lat} at this axis leads to a fluid element with momentum $-p_{lat}$, i.e. $-2p_{lat}$ is added to the total momentum of the fluid on the grid. Thus the total momentum is not a strictly conserved quantity any more. If the grid includes the polar axis, i.e. $\theta_0 = 0$, then at least the z-component of the total grid momentum is conserved because right at the axis the lateral momentum has no z-component. Note that in 2D also the x- and y-components are conserved because the x- and y-momentum of every zone is zero due to the assumed axisymmetry.

Since we are also interested in neutron star kicks, we need to point out that the use of the inner boundary condition (enclosing the neutron star "core") implies that the neutron star is attached to the centre of our computational grid. It is therefore not free to move relative to the ejecta during the simulation (unless special measures are taken, see below). This is tantamount to assuming that the neutron star has an infinite *inertial* mass. Two implications result from this approximation: A potential hydrodynamic feedback of a displacement of the neutron star relative to the ejecta is neglected, and the neutron star recoil velocity has to be determined indirectly in a post-processing step by making use of the assumption of total momentum conservation (see Sect. 3.1.3).

The relative motion between neutron star and ejecta can, however, be accounted for during a simulation by "wagging the dog", i.e. by assuming that instead of the neutron star the ejecta move coherently in the opposite direction of the neutron star's recoil velocity. This can be achieved technically by applying a Galilei transformation to the gas on the computational grid after every time step. To accomplish this for several of our computed models (Table 3.3), we assume that the frame of reference connected with the neutron star core is (in a first approximation) an inertial frame (see Appendix C for a justification of this assumption). We then evaluate for every time step n the change of the total linear momentum of the matter on the grid, $\Delta\vec{P}^n_{\mathrm{grid}}$. By virtue of momentum conservation this must be equal to the change of the momentum of the neutron star core. In case the core mass is constant, this gives

$$\Delta \vec{P}^{n}_{\mathrm{grid}} = -M^{n}_{\mathrm{core}}\, \Delta \vec{v}^{\,n}_{\mathrm{core}}. \tag{2.22}$$

Hence, after the time step, the core should move with a velocity that has changed by $\Delta \vec{v}^{\,n}_{\mathrm{core}}$. Changing the frame of reference instead, we perform a Galilei transformation by adding $-\Delta \vec{v}^{\,n}_{\mathrm{core}}$ to the gas velocities in all zones of the grid. In the new inertial frame the neutron star core remains at rest and centred at $r = 0$. Simulations including this procedure will be used to investigate potential deficiencies of our standard assumption that the NS has an infinite inertial mass and takes up momentum without starting to move (see Sects. 3.2.2 and 3.5).

2.4 Boundary conditions

2.4.1 Hydrodynamics

The boundary conditions for the hydrodynamics equations are defined similar to those in Kifonidis et al. (2003). Reflecting conditions are imposed at the lateral boundaries at $\theta = 0$ and $\theta = \pi$, while transmitting (i.e. zero gradient) boundary conditions are employed at the outer radial boundary. For the 3D simulations, periodic boundary conditions have to be used in ϕ-direction.

The inner boundary, which is located at the Lagrangian mass coordinate where we cut our initial (i.e. immediate post-bounce) models, is taken to be impenetrable. The contraction of this mass shell (and hence of the neutron star core) is mimicked by moving the inner boundary of our Eulerian grid from its initial radius, $R^{\mathrm{i}}_{\mathrm{ib}}$, inwards to a final radius $R^{\mathrm{f}}_{\mathrm{ib}}$ according to the expression

$$R_{\mathrm{ib}}(t) = \frac{R^{\mathrm{i}}_{\mathrm{ib}}}{1 + (1 - \exp(-t/t_{\mathrm{ib}}))\,(R^{\mathrm{i}}_{\mathrm{ib}}/R^{\mathrm{f}}_{\mathrm{ib}} - 1)} \tag{2.23}$$

of Janka & Müller (1996). The parameter $R^{\mathrm{i}}_{\mathrm{ib}}$ is typically in the range $55\,\mathrm{km} < R^{\mathrm{i}}_{\mathrm{ib}} < 85\,\mathrm{km}$.

For $R^{\mathrm{f}}_{\mathrm{ib}}$ and t_{ib} we use two alternative prescriptions: In what we henceforth will call the "standard boundary contraction case", we set $R^{\mathrm{f}}_{\mathrm{ib}} = 15\,\mathrm{km}$ and $t_{\mathrm{ib}} = t_L$, where the time scale t_L is connected to the luminosity decay and will be defined in Sect. 2.4.2. In the second prescription, the so-called "rapid boundary contraction case", we set $R^{\mathrm{f}}_{\mathrm{ib}} = 10.5\,\mathrm{km}$ and $t_{\mathrm{ib}} = 0.25\,\mathrm{s}$.

Figure 2.1 compares both prescriptions with each other and with data from a supernova simulation with the nuclear equation of state of Lattimer & Swesty (1991) and with Boltzmann neutrino transport (Buras et al. 2003) for one of our initial models. In this figure, we show also the contraction used for one of the 3D models, which is even somewhat faster than the "rapid" contraction.

The standard boundary contraction results in a larger final radius and a slower contraction of the neutron star. The rapid boundary contraction gives results which are almost indistinguishable from the Boltzmann calculation, and might therefore be considered as more realistic. The standard case has practical advantages, though, because it allows for larger time steps and thus reduces the computational cost of a simulation. Unless noted otherwise, the simulations are performed for the standard contraction of the inner boundary.

2.4.2 Neutrinos

The boundary conditions for the neutrino properties at the inner grid boundary are chosen to be *isotropic*. We impose luminosities for neutrinos and antineutrinos of all three flavours which

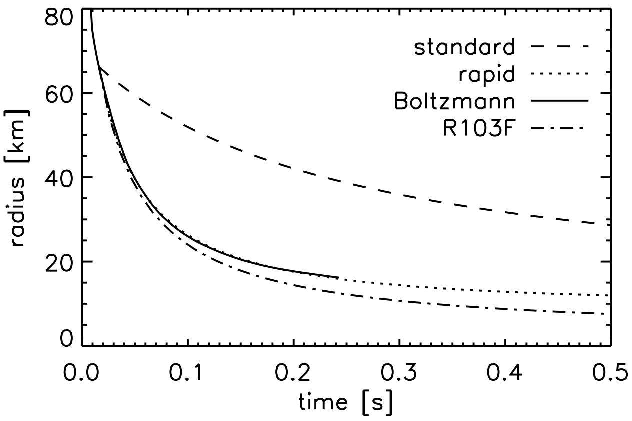

Figure 2.1: Evolution after core bounce of the radius corresponding to a mass coordinate of $1.1 M_\odot$ from a supernova simulation with Boltzmann neutrino transport (Buras et al. 2003), compared to the motion of the inner boundary radius as defined by Eq. (2.23) for the "standard" and "rapid" boundary contraction cases, as well as the somewhat faster contraction used for the rotating 3D Model R103F (see Chapter 5).

are assumed to be constant for a time interval t_L (typically 1 s), and to decay subsequently with a power-law:

$$L_{e,\nu_e}(R_{\mathrm{ib}},t) = L_\nu^{\mathrm{tot},0}\,K_{\nu_e}\,h(t), \tag{2.24}$$

$$L_{e,\bar\nu_e}(R_{\mathrm{ib}},t) = L_\nu^{\mathrm{tot},0}\,K_{\bar\nu_e}\,h(t), \tag{2.25}$$

$$L_{e,\nu_x}(R_{\mathrm{ib}},t) = L_\nu^{\mathrm{tot},0}\,K_{\nu_x}\,h(t), \tag{2.26}$$

where

$$h(t) = \begin{cases} 1.0 & \text{if } t \le t_L, \\ (t_L/t)^{3/2} & \text{if } t > t_L, \end{cases} \tag{2.27}$$

and $\nu_x \equiv \nu_\mu, \bar\nu_\mu, \nu_\tau, \bar\nu_\tau$. The constants K_{ν_i} denote the fractional contributions of the individual luminosities to the total neutrino luminosity. They fulfil the requirement

$$K_{\nu_e} + K_{\bar\nu_e} + 4\,K_{\nu_x} = 1. \tag{2.28}$$

The functional form used in Eq. (2.27) can be motivated by the Boltzmann transport calculations of Buras et al. (2003). These show that after a transient phase of $\sim$ 50 ms, which is short compared to the explosion time scales of our simulations, the sum of all luminosities is almost constant or varies only very weakly, at least over the next $\sim$ 250 ms, for which data from the Boltzmann transport simulations are available (see Fig. 2.2).

According to Eqs. (2.24–2.27) we need to prescribe the time scale t_L and the total initial luminosity $L_\nu^{\mathrm{tot},0}$. However, instead of choosing these two quantities as basic parameters of our models, we prefer to prescribe t_L and the gravitational binding energy $\Delta E_{\nu,\mathrm{core}}^\infty$ that is released by the neutron star core asymptotically (i.e. for $t \to \infty$) via neutrino emission. Introducing the energy that the core looses up to time t

$$\Delta E_{\nu,\mathrm{core}}^{\mathrm{tot}}(t) = \int_0^t L_\nu^{\mathrm{tot},0}\,h(t')\,\mathrm{d}t', \tag{2.29}$$

the following relations hold for the asymptotic energy loss

$$\Delta E_{\nu,\mathrm{core}}^\infty = \int_0^\infty L_\nu^{\mathrm{tot},0}\,h(t)\,\mathrm{d}t = 3\,\Delta E_{\nu,\mathrm{core}}^{\mathrm{tot}}(t_L) = 3\,L_\nu^{\mathrm{tot},0}\,t_L, \tag{2.30}$$

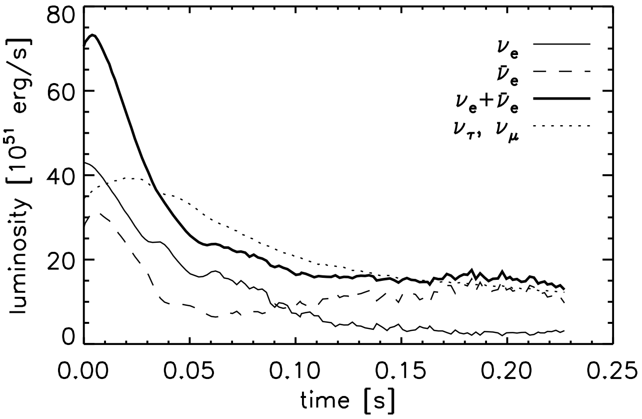

Figure 2.2: Evolution after core bounce of the neutrino luminosities at a Lagrangian mass shell of $1.1\,M_\odot$ from a supernova simulation with Boltzmann neutrino transport (Buras et al. 2003). After an initial phase of 50 ms duration, the sum of the ν_e and $\bar\nu_\mathrm{e}$ luminosities, as well as the ν_μ/ν_τ luminosities vary only slowly.

i.e. our ansatz of Eq. (2.27) implies that 1/3 of $\Delta E^\infty_{\nu,\mathrm{core}}$ is radiated away within the chosen time interval t_L in neutrinos and antineutrinos of all flavours.

We also prescribe the mean energies of neutrinos entering the computational grid at the inner boundary. The corresponding values are chosen to be $\langle\epsilon_{\nu_\mathrm{e}}\rangle^\mathrm{ib} = 12\,\mathrm{MeV}$, $\langle\epsilon_{\bar\nu_\mathrm{e}}\rangle^\mathrm{ib} = 16\,\mathrm{MeV}$, and $\langle\epsilon_{\nu_x}\rangle^\mathrm{ib} = 20\,\mathrm{MeV}$, and kept constant during our simulations. Thereby also the number fluxes $L_{n,\nu_i} = L_{e,\nu_i}/\langle\epsilon_{\nu_i}\rangle$ at $r = R_\mathrm{ib}$ are defined.

The total lepton number lost by the neutron star core until time t, normalised to the total baryon number $N_\mathrm{b,\,core}$ of the core, is given by

$$\Delta Y_\mathrm{e,core}(t) = N^{-1}_\mathrm{b,\,core}\int_0^t \left(L_{n,\nu_\mathrm{e}}(R_\mathrm{ib},t') - L_{n,\bar\nu_\mathrm{e}}(R_\mathrm{ib},t')\right)\mathrm{d}t'. \tag{2.31}$$

For $t = t_\mathrm{L}$ this yields

$$\Delta Y_\mathrm{e,core}(t_L) = \frac{L_\nu^\mathrm{tot,0}\,t_\mathrm{L}}{N_\mathrm{b,\,core}}\left(\frac{K_{\nu_\mathrm{e}}}{\langle\epsilon_{\nu_\mathrm{e}}\rangle^\mathrm{ib}} - \frac{K_{\bar\nu_\mathrm{e}}}{\langle\epsilon_{\bar\nu_\mathrm{e}}\rangle^\mathrm{ib}}\right). \tag{2.32}$$

We assume that the lepton number loss during time interval t_L is proportional to the energy loss during this time. Therefore we choose $K_{\nu_i} = \mathrm{const}$, because $\langle\epsilon_{\nu_i}\rangle^\mathrm{ib} = \mathrm{const}$, and set $K_{\nu_\mathrm{e}} = 0.2$, $K_{\bar\nu_\mathrm{e}} = 0.215$ for the calculations in this work. K_{ν_x} follows from Eq. (2.28).

2.4.3 Moving the inner boundary to a different mass shell

The rapid boundary contraction we assume for some of our models leads to a fast increase of the speed of sound and the optical depth at the inner boundary, which can cause numerical problems in the neutrino transport routine and small time steps due to the CFL condition. To avoid these issues, we shift the inner boundary to higher radii (i.e. to a different mass shell) each time the optical depth for electron neutrinos becomes higher than a certain value, typically $\tau_\mathrm{max} = 200$. We place the new inner boundary at a radius $R_\mathrm{ib}{}'$ where the optical depth is about 100. Note that this procedure is not necessary for models with the slower "standard" boundary contraction.

When the optical depth at the inner boundary has become too high at a time t, we shift the boundary from the original radius R_{ib} to ${R_{\mathrm{ib}}}'$ and adjust the boundary parameters and the point mass are in the following way ($\delta t \to 0^+$):

$$\begin{aligned}
L_{\mathrm{ib}}^{\nu_{\mathrm{e}}}(t+\delta t) &= L_{\nu_{\mathrm{e}}}({R_{\mathrm{ib}}}', t-\delta t) \\
L_{\mathrm{ib}}^{\bar{\nu}_{\mathrm{e}}}(t+\delta t) &= L_{\bar{\nu}_{\mathrm{e}}}({R_{\mathrm{ib}}}', t-\delta t) \\
L_{\mathrm{ib}}^{\nu_x}(t+\delta t) &= L_{\nu_x}({R_{\mathrm{ib}}}', t-\delta t) \\
{R_{\mathrm{ib}}}^i(t+\delta t) &= {R_{\mathrm{ib}}}^i(t-\delta t) \times ({R_{\mathrm{ib}}}'/R_{\mathrm{ib}}) \\
{R_{\mathrm{ib}}}^f(t+\delta t) &= {R_{\mathrm{ib}}}^f(t-\delta t) \times ({R_{\mathrm{ib}}}'/R_{\mathrm{ib}}) \\
M_{\mathrm{ib}}(t+\delta t) &= M({R_{\mathrm{ib}}}', t-\delta t) \qquad (2.33)
\end{aligned}$$

This means that the luminosity produced in the region $[R_{\mathrm{ib}}, {R_{\mathrm{ib}}}']$ that is “cut off” the numerical grid is added to the new boundary luminosity, and that the mass $M({R_{\mathrm{ib}}}') - M(R_{\mathrm{ib}})$ in this region is added to the point mass M_{ib} representing the inner part of the neutron star. Therefore the luminosity and gravitational acceleration above ${R_{\mathrm{ib}}}'$ do not change, and global quantities, e.g. the heating rate in the gain layer, do not show jumps or kinks at the time we shift the boundary. However, in the subsequent evolution small differences can be observed, compared to a corresponding run performed without this boundary shifting. This is due to the fact, that the velocity we assume for the new inner boundary at ${R_{\mathrm{ib}}}'$ may not agree with the velocity of the mass shell $M({R_{\mathrm{ib}}}')$ in a run where we leave the boundary at the original mass coordinate (the same applies for the luminosity). Yet, several 10 ms after shifting the boundary, we see only very small differences.

3

Explosion anisotropy in two dimensions

In this chapter we will investigate the anisotropy of core collapse supernova explosions and the associated acceleration of neutron stars by means of two-dimensional simulations. We start by discussing the considered progenitor stars and defining physical quantities which characterise the different runs of our large set of simulations in Sect. 3.1. Moreover, we describe the post-processing procedures that we applied to the numerical calculations to compute these characteristic quantities. In Sect. 3.2 we present results for two exemplary neutrino-hydrodynamic calculations. In Section 3.3 we explore the dependence of our simulations on the properties of the stellar progenitors and on the assumed core neutrino fluxes, and establish correlations between explosion parameters and neutron star kicks. Section 3.4 is devoted to the effects of rotation. In Sect. 3.5 we return to the neutron star recoils and investigate their robustness with respect to the approximations and assumptions that we have employed. Furthermore, we investigate the long-time evolution of the recoil velocities for a few models beyond the time interval of one second after core bounce, for which we have evolved most of our models. Estimating the terminal values of the NS velocities by a calibrated extrapolation procedure, we will finally speculate about the possible implications of our results for the velocity distribution of neutron stars in Sect. 3.6.

3.1 Preliminaries

3.1.1 Initial models and initial perturbations

Our calculations are started at $\sim 15-20\,\mathrm{ms}$ after core bounce from detailed post-collapse models. We make use of four such models which are based on three different progenitors. The first was calculated by Bruenn (1993) with a general relativistic, one-dimensional (1D), Lagrangian hydrodynamics code coupled to neutrino transport by multi-group, flux-limited diffusion (see his Model WPE15 LS 180). It employs the $15\,M_\odot$ progenitor of Woosley et al. (1988). Simulations based on this model will henceforth be called the “B-series”.

Our second 1D post-collapse model, provided by M. Rampp (priv. comm.), uses a $15\,M_\odot$ progenitor star of Limongi et al. (2000) and was computed with the PROMETHEUS PPM hydrodynamics

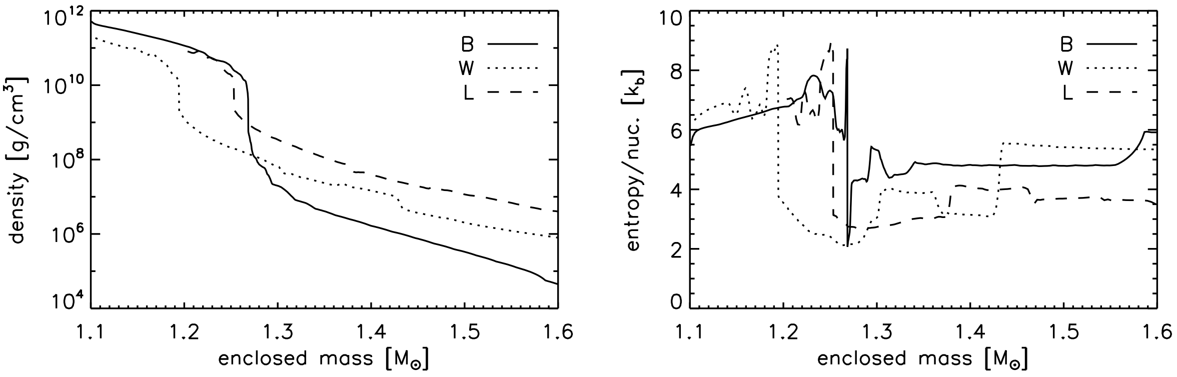

Figure 3.1: Density and entropy as functions of the enclosed mass for the B, L and W initial models a few milliseconds after core bounce (see the main text for details). The differences in the density profiles have a strong influence on the mass accretion rates. The relatively low densities in the B model lead to a small accretion rate and a fast onset of the explosion. The opposite is true for the L model, which shows the highest densities (see Sect. 3.3). The small steps in the density profiles correspond to interfaces separating shells of different composition. These interfaces are better visible in the entropy profiles. The pronounced "discontinuity" at $\rho = 10^{10}\,\mathrm{g/cm^3}$ is the supernova shock.

code coupled to the VERTEX multi-group variable Eddington factor/Boltzmann neutrino transport solver (Rampp & Janka 2002). Our "L-series" of simulations makes use of that model.

We also consider two post-bounce models that were computed for the s15s7b2 progenitor of Woosley & Weaver (1995) with PROMETHEUS/VERTEX by Buras et al. (2003, 2006a) (see their Models s15/1D and s15r). The first of these models is from a one-dimensional simulation and gives rise to the "W-series" of runs, while the second is a rotating, two-dimensional (axisymmetric) model, which we use for our "R-series" of calculations. Density and entropy profiles of all 1D initial models plotted as a function of the enclosed mass are displayed in Fig. 3.1.

To obtain the rotating model, Buras et al. (2003, 2006a) imposed the angular velocity profile shown in Fig. 3.2 on the s15s7b2 progenitor and followed the evolution of this model through core bounce, assuming equatorial symmetry and using a computational wedge extending over $0 \leq \theta \leq \pi/2$. The initial angular frequency was assumed to be constant in the Fe and Si core and to decrease as $r^{-3/2}$ outside a radius of 1750 km (corresponding to a mass coordinate of $1.425\,M_\odot$, which is the inner edge of the oxygen-rich silicon layer in the progenitor). Outside the iron core the rotation profile followed (on average) the profile of the rotating $15\,M_\odot$ progenitor of Heger et al. (2000). Inside the iron core an angular frequency of $\Omega = 0.5\,\mathrm{rad/s}$ was chosen, which is lower than in the stellar evolution calculations for non-magnetised stars of Heger et al. (2000), but somewhat higher than in the calculations of Heger et al. (2004), which include the effects of magnetic torques. This choice ensured that the ratio of the centrifugal to the gravitational force was below 7×10^{-3} everywhere in the pre-collapse core. The ratio of the rotational energy to the gravitational binding energy of the pre-collapse star was only $T/W \approx 10^{-3}$, which resulted in negligible effects of rotation on the evolution until core bounce.

The level of numerical noise in our hydrodynamics code is so low that a one-dimensional, isotropic initial configuration remains isotropic, even in the presence of a convectively unstable stratification. Therefore we need to explicitly add random perturbations in order to start the convective activity. The portable, high-quality random number generator RANLUX due to James (1994, 1996) and Lüscher (1994) is employed. We apply the perturbation to the velocity field and typically use an amplitude of 0.1%. To break the equatorial symmetry of the rotating 2D model of Buras et al. (2003, 2006a), we have to add perturbations with an amplitude of several per

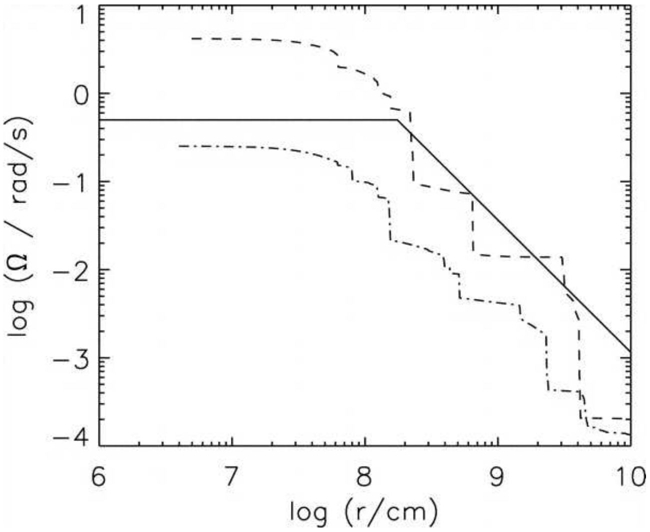

Figure 3.2: Angular velocity profiles for the rotating $15 M_\odot$ pre-supernova model (dashed curve) of Heger et al. (2000), for the magnetised, rotating $15 M_\odot$ pre-supernova model (dash-dotted curve) of Heger et al. (2004), and for the rotating model s15r of Buras et al. (2003) prior to core collapse (solid curve).

cent, since in this model the initial perturbations have already grown to such a level by the time we map the model to our full 180° grid (see Sect. 2.3).

3.1.2 Overview of the simulations

Tables 3.1–3.3 give an overview of the parameters and characterising quantities (that will be defined in Sect. 3.1.3) for all simulations performed with our "standard boundary contraction". The naming convention we have chosen for our models is the following: The first letter denotes the initial model (i.e. the progenitor/post-bounce data), followed by a two-digit code which corresponds to the chosen value for the total neutrino energy loss of the neutron star core, $\Delta E^{\infty}_{\nu,\mathrm{core}}$ (see Eq. 2.30), in units of $\frac{1}{100}\,M_\odot c^2$. Thus B18, for example, refers to a simulation based on the Woosley et al. (1988)/Bruenn (1993) initial data with an assumed release of gravitational binding energy of the core of $\Delta E^{\infty}_{\nu,\mathrm{core}} = 0.18\,M_\odot c^2$. In Tables 3.1–3.3 we give also a value for the energy lost by the core in the first second,

$$\Delta E^{\mathrm{tot}}_{\nu,\mathrm{core}}(t) = \int_0^t L^{\mathrm{tot}}_{\nu}(R_{\mathrm{ib}}, t')\,\mathrm{d}t', \tag{3.1}$$

with $t = 1\,\mathrm{s}$. The second fundamental model parameter, the luminosity time scale t_L (see Sect. 2.4.2), is not taken into account in the model names, because it has the same value for all models of a series. The chosen value in each case is given in the captions of Tables 3.1–3.3.

Simulations performed on a larger grid (with an outer boundary radius of 10^{10} cm and 500 radial zones) are indicated by the letter "g" appended to the model name, e.g. B18-g, simulations which account for the recoil motion of the neutron star contain the letter "m" in the model name, and model series started from different random seed perturbations are denoted by numbers appended to the model names. Hence Model B18-1 differs from Model B18 (and from Models B18-2, B18-3 etc.) only in the random perturbations imposed on the initial velocity distribution (with the perturbation amplitude being the same in all cases).

The model parameters should be chosen (or should come out) such that basic constraints for the loss of energy and lepton number from the forming neutron star core are fulfilled. For example the lepton number loss during time t_L is in all cases of order 0.1–0.2, and the total (asymptotic) energy loss

$$\Delta E^{\infty}_{\text{core}} = 3 \times \Delta E^{\text{tot}}_{\nu,\text{core}}(t_L) \tag{3.2}$$

does not exceed the gravitational energy

$$E \approx 3 \times 10^{53} \left(\frac{M_{\text{ns}}}{M_{\odot}}\right)^{2} \left(\frac{R_{\text{ns}}}{10\,\text{km}}\right)^{-1} \ \text{ergs}, \tag{3.3}$$

which can be released during the birth of a neutron star. The energy ΔE_{500} radiated in ν_{e} and $\bar{\nu}_{\text{e}}$ is roughly consistent with the expected contribution of these neutrinos to the energy loss during the time interval t_L, i.e. $\Delta E_{500} \approx \frac{1}{3} \times \frac{1}{3}\,E$.

3.1.3 Definitions and approximations for post-processing the simulations

We evaluate our about 80 hydrodynamic models for interesting characteristic quantities by post-processing the data of the simulations. To keep the evaluation as straightforward as possible we sometimes employ approximations which we will define below.

A characterising value for the neutrino luminosities imposed at the inner boundary is

$$L_{\text{ib}}(t) \equiv L_{e,\nu_{\text{e}}}(R_{\text{ib}}, t) + L_{e,\bar{\nu}_{\text{e}}}(R_{\text{ib}}, t), \tag{3.4}$$

neglecting the contribution from heavy-lepton neutrinos, whose interactions in the computational domain are less important than those of ν_{e} and $\bar{\nu}_{\text{e}}$, and who, in particular, do not contribute to the neutrino heating behind the shock at a significant level. We also consider the sum of the ν_{e} and $\bar{\nu}_{\text{e}}$ luminosities at a radius of 500 km,

$$L_{500}(t) = L_{e,\nu_{\text{e}}}(r = 500\ \text{km}, t) + L_{e,\bar{\nu}_{\text{e}}}(r = 500\ \text{km}, t), \tag{3.5}$$

and define the time average of this quantity in the time interval $[0, t_{\text{exp}}]$ as

$$\langle L_{500} \rangle = {t_{\text{exp}}}^{-1} \int_0^{t_{\text{exp}}} L_{500}(t)\ \text{d}t. \tag{3.6}$$

The value of $\langle L_{500} \rangle$ represents approximatively the $(\nu_{\text{e}} + \bar{\nu}_{\text{e}})$ luminosity that is responsible for the energy deposition behind the supernova shock until the explosion sets in at a post-bounce time $t = t_{\text{exp}}$. Therefore the difference between $\langle L_{500} \rangle$ and L_{ib} can be considered as a rough measure for the radial change of the neutrino luminosities in contrast to their constancy in case of the light-bulb scheme used by Janka & Müller (1996).

We will also consider the total energy in ν_{e} and $\bar{\nu}_{\text{e}}$ neutrinos that streams through a sphere with a radius of 500 km in the time interval $[0, t]$,

$$\Delta E_{500}(t) = \int_0^{t} (L_{e,\nu_{\text{e}}} + L_{e,\bar{\nu}_{\text{e}}})(r = 500\,\text{km}, t')\,\text{d}t'. \tag{3.7}$$

The explosion energy, E_{exp}, of a model is defined as the sum of the total energy of all zones of the grid where this energy is positive, i.e.

$$E_{\text{exp}} = \sum_{e_{\text{tot},i}>0} e_{\text{tot},i}\,\Delta m_i, \tag{3.8}$$

Table 3.1: Simulations based on the Woosley et al. (1988)/Bruenn (1993) post-bounce model. The luminosity time scale t_L is 1 s. Unless noted otherwise the inertial mass of the neutron star is assumed to be infinite for these and the simulations listed in the following tables, i.e. the neutron star takes up momentum but cannot move on the grid. For the definitions of the listed quantities, see Sect. 3.1.3. All time-dependent quantities are given at a time $t = 1\,\mathrm{s}$, when we terminated the simulations. Energies are given in units of $1\,\mathrm{B} = 1\,\mathrm{bethe} = 10^{51}\,\mathrm{erg}$.

Model	L_ib [B/s]	$\Delta E_{\nu,\mathrm{core}}^\mathrm{tot}$ [B]	$\Delta Y_\mathrm{e,core}$	$\langle L_{500} \rangle$ [B/s]	ΔE_{500} [B]	E_exp [B]	t_exp [s]	M_ns [$M_\odot$]	v_z^ns [km/s]	$v_z^{\mathrm{ns},\nu}$ [km/s]	a_z^ns [km/s^2]	α_gas	d_shock
B10	24.7	59.6	0.09	57.1	45.9	0.19	0.294	1.426	-164.1	44.4	-180.2	0.24	0.67
B11	27.2	65.5	0.10	58.8	46.3	0.27	0.280	1.401	-23.6	0.7	-248.9	0.03	0.97
B12	29.7	71.5	0.11	60.6	48.7	0.37	0.220	1.399	-389.5	45.0	-372.4	0.32	0.06
B12-1	29.7	71.5	0.11	60.5	47.5	0.33	0.228	1.377	72.8	-4.7	47.9	0.07	0.22
B12-2	29.7	71.5	0.11	60.9	48.5	0.39	0.212	1.391	85.8	9.7	345.7	0.07	0.82
B12-3	29.7	71.5	0.11	60.9	46.5	0.38	0.207	1.369	242.0	2.0	464.3	0.18	0.97
B12-4	29.7	71.5	0.11	61.1	47.7	0.35	0.216	1.385	-115.1	20.4	-154.2	0.10	0.51
B12-5	29.7	71.5	0.11	61.0	47.8	0.33	0.211	1.387	-206.9	11.6	-483.1	0.19	0.52
B13	32.2	77.5	0.12	62.4	49.6	0.45	0.188	1.378	-355.3	32.0	-408.0	0.25	0.36
B14	34.6	83.4	0.13	63.6	49.6	0.51	0.198	1.345	-128.0	-11.2	-66.7	0.07	0.40
B15	37.1	89.4	0.14	65.3	50.3	0.65	0.162	1.318	36.1	-1.0	36.0	0.02	0.27
B16	39.6	95.3	0.15	66.3	51.8	0.81	0.160	1.305	-214.6	-2.6	-334.4	0.08	0.57
B17	42.1	101.3	0.15	67.6	53.3	0.95	0.146	1.289	-25.5	14.8	-102.6	0.01	0.05
B17-1	42.1	101.3	0.15	67.8	53.4	0.92	0.160	1.290	-354.0	5.6	-202.2	0.12	0.31
B18	44.5	107.3	0.16	68.3	54.8	1.16	0.152	1.275	515.3	5.2	290.5	0.15	0.42
B18-1	44.5	107.3	0.16	68.4	54.7	1.12	0.154	1.274	-126.5	-0.8	-49.1	0.04	0.20
B18-2	44.5	107.3	0.16	68.9	54.7	1.14	0.152	1.268	82.5	-5.2	16.5	0.02	0.07
B18-3	44.5	107.3	0.16	68.8	57.1	1.15	0.142	1.305	798.8	-41.2	552.1	0.24	-0.06
B18-4	44.5	107.3	0.16	68.2	54.6	1.14	0.150	1.272	-171.6	4.0	65.7	0.05	0.46
B18-5	44.5	107.3	0.16	68.5	55.2	1.09	0.164	1.280	-121.8	-0.9	15.4	0.04	-0.02
B18-6	44.5	107.3	0.16	68.7	55.4	1.11	0.160	1.283	502.1	-20.6	220.0	0.15	-0.06
B18-g1	44.5	107.3	0.16	68.7	54.5	1.12	0.142	1.269	-60.3	3.9	-55.4	0.02	0.06
B18-g2	44.5	107.3	0.16	68.7	54.8	1.12	0.138	1.273	267.9	-8.1	126.7	0.08	0.28
B18-g3	44.5	107.3	0.16	68.5	54.9	1.10	0.150	1.274	-7.4	-3.5	0.9	0.00	0.02
B18-g4	44.5	107.3	0.16	68.7	54.5	1.16	0.132	1.270	-416.8	1.7	-150.9	0.11	0.37
B19-g1	47.0	113.2	0.17	69.6	55.9	1.31	0.148	1.253	-273.8	0.3	-96.7	0.07	0.41
B19-g2	47.0	113.2	0.17	69.5	56.0	1.33	0.148	1.255	188.5	6.4	48.8	0.05	0.15
B19-g3	47.0	113.2	0.17	70.0	56.6	1.26	0.132	1.263	366.6	1.1	183.7	0.10	0.13
B19-g4	47.0	113.2	0.17	70.0	56.8	1.33	0.130	1.267	477.1	-18.3	195.6	0.12	-0.02
B20	49.5	119.2	0.18	71.0	57.3	1.49	0.128	1.238	133.2	5.6	52.6	0.03	0.40
B21	51.9	125.1	0.19	72.1	58.5	1.72	0.122	1.222	30.6	-0.9	-20.2	0.01	0.24

Table 3.2: Simulations based on the Limongi et al. (2000)/Rampp progenitor and the Woosley & Weaver (1995)/Buras et al. (2003) post-bounce model (non-rotating and rotating cases). The luminosity time scale t_L is 0.7 s for the Limongi et al. (2000)/Rampp simulations and $t_L = 1$ s for the Woosley & Weaver (1995)/Buras et al. (2003) models. For more details, see the caption of Table 3.1.

Model	$L_{\rm ib}$ [B/s]	$\Delta E^{\rm tot}_{\nu,\rm core}$ [B]	$\Delta Y_{\rm e,core}$	$\langle L_{500}\rangle$ [B/s]	ΔE_{500} [B]	$E_{\rm exp}$ [B]	$t_{\rm exp}$ [s]	$M_{\rm ns}$ [$M_\odot$]	$v_z^{\rm ns}$ [km/s]	$v_z^{\rm ns,\nu}$ [km/s]	$a_z^{\rm ns}$ [km/s^2]	$\alpha_{\rm gas}$	$d_{\rm shock}$
L12	42.4	94.6	0.13	90.7	70.7	0.51	0.321	1.677	278.5	-12.9	334.3	0.24	0.11
L13	45.9	102.5	0.14	91.7	69.2	0.68	0.268	1.620	-92.6	-5.9	-333.6	0.05	0.77
L14	49.5	110.4	0.15	94.6	72.8	0.81	0.280	1.628	482.1	-22.0	297.1	0.26	0.31
L15	53.0	118.3	0.17	96.2	75.2	1.02	0.266	1.617	-239.5	-3.9	-378.5	0.10	0.63
L16	56.5	126.2	0.18	97.8	76.3	1.07	0.256	1.586	-437.9	12.8	-715.2	0.17	0.47
L17	60.1	134.0	0.19	100.3	77.4	1.19	0.256	1.558	-24.7	5.5	-47.6	0.01	0.37
W10	24.7	59.6	0.09	64.3	55.4	0.21	0.420	1.568	-129.8	42.1	-443.1	0.15	0.81
W12	29.7	71.5	0.11	69.0	53.9	0.31	0.322	1.501	-97.7	-9.7	-132.5	0.10	0.61
W12-1	29.7	71.5	0.11	68.0	59.5	0.32	0.374	1.563	-363.8	81.2	-377.0	0.32	0.13
W14	34.6	83.4	0.13	72.9	56.6	0.46	0.250	1.473	-62.0	-1.5	66.1	0.04	0.37
W16	39.6	95.3	0.15	76.0	58.5	0.67	0.244	1.430	287.2	-5.5	464.2	0.14	0.68
W18	44.5	107.3	0.16	79.3	61.5	0.89	0.226	1.401	-283.6	4.2	-290.1	0.11	0.44
W20	49.5	119.2	0.18	82.0	63.5	1.36	0.216	1.354	-377.3	0.6	-277.0	0.10	0.39
R10	24.7	59.6	0.09	59.9	48.8	0.25	0.418	1.521	-15.4	-14.3	-118.7	0.02	-0.02
R12	29.7	71.5	0.11	64.6	49.9	0.50	0.316	1.461	-235.8	17.5	-203.4	0.16	0.15
R14	34.6	83.4	0.13	69.2	52.4	0.69	0.264	1.420	88.4	14.6	86.9	0.04	0.15
R16	39.6	95.3	0.14	71.9	56.0	0.98	0.256	1.396	321.2	-8.9	210.1	0.11	0.06
R18	44.5	107.3	0.16	75.8	58.3	1.24	0.232	1.349	-4.8	-3.7	-26.7	0.00	-0.07
R18-g	44.5	107.3	0.16	75.8	58.5	1.23	0.226	1.352	-113.9	2.1	-188.1	0.03	0.07
R20	49.5	119.2	0.18	78.8	60.9	1.64	0.214	1.309	280.1	0.8	123.9	0.06	0.14

Table 3.3: Simulations based on the Woosley et al. (1988)/Bruenn (1993) post-bounce model. The luminosity time scale t_L is 1 s. For more details, see the caption of Table 3.1. Different from the models listed in all other tables, the recoil motion of the neutron star was accounted for in the simulations listed here (as described in Sect. 2.3).

Model	L_{ib} [B/s]	$\Delta E^{\mathrm{tot}}_{\nu,\mathrm{core}}$ [B]	$\Delta Y_{\mathrm{e,core}}$	$\langle L_{500}\rangle$ [B/s]	ΔE_{500} [B]	E_{exp} [B]	t_{exp} [s]	M_{ns} [$M_\odot$]	v^{ns}_z [km/s]	$v^{\mathrm{ns},\nu}_z$ [km/s]	a^{ns}_z [km/s^2]	α_{gas}	d_{shock}
B12-m1	29.7	71.5	0.11	60.9	47.4	0.36	0.226	1.384	-56.8	-1.7	-208.2	0.06	0.48
B12-m2	29.7	71.5	0.11	60.9	47.7	0.31	0.222	1.385	-100.0	19.1	-63.5	0.10	0.72
B12-m3	29.7	71.5	0.11	61.2	47.8	0.38	0.210	1.388	272.6	-16.5	91.9	0.23	0.35
B12-m4	29.7	71.5	0.11	60.9	47.0	0.35	0.209	1.378	-104.3	-7.4	-197.2	0.09	0.43
B12-m5	29.7	71.5	0.11	60.8	47.9	0.35	0.219	1.389	365.6	-10.1	219.1	0.32	0.47
B12-m6	29.7	71.5	0.11	60.7	48.4	0.36	0.229	1.395	-334.1	42.4	-462.9	0.30	0.26
B18-m1	44.5	107.3	0.16	68.9	54.9	1.12	0.136	1.274	43.3	-4.8	-108.8	0.02	0.12
B18-m2	44.5	107.3	0.16	68.9	54.8	1.14	0.139	1.273	-86.8	-1.1	-31.1	0.03	0.20
B18-m3	44.5	107.3	0.16	68.8	55.3	1.12	0.131	1.281	76.4	-8.8	-11.4	0.03	0.39
B18-m4	44.5	107.3	0.16	68.5	54.9	1.14	0.150	1.274	-118.7	14.5	-156.4	0.05	0.13
B18-m5	44.5	107.3	0.16	68.3	54.7	1.12	0.166	1.273	-339.7	-4.5	-152.4	0.13	-0.06
B18-m6	44.5	107.3	0.16	68.6	55.4	1.12	0.166	1.283	-439.3	14.0	-194.5	0.17	0.04
B18-m7	44.5	107.3	0.16	68.8	54.7	1.12	0.138	1.272	109.2	8.6	2.1	0.04	0.38
B18-m8	44.5	107.3	0.16	69.3	54.5	1.13	0.134	1.269	455.0	-4.1	187.4	0.17	0.05

where i is the zone counter, Δm_i the mass contained in zone i, and the total specific energy e_{tot} is given by the sum of the specific gravitational, kinetic, and internal energies,

$$e_{\mathrm{tot}} = e_{\mathrm{grav}} + \frac{1}{2}v^2 + e_{\mathrm{int}}. \tag{3.9}$$

For the sake of simplicity we use here the one-dimensional Newtonian expression

$$e_{\mathrm{grav}}(r) = -\frac{GM(r)}{r} \tag{3.10}$$

to evaluate the gravitational energy, neglecting the relatively small general relativistic corrections, which have been taken into account in the simulations.

Another quantity of interest is the explosion time scale, t_{exp}, which we define as the time after the start of the simulation when E_{exp} exceeds 10^{48} erg. It turns out that the exact choice of this threshold value does not matter very much. Other definitions of the explosion time scale (e.g., linked to the time when the expansion velocity of the shock exceeds a certain value) do also not lead to qualitatively different results.

The neutron star mass and the neutron star radius are considered to be associated with a certain value of the density, $\rho_{\mathrm{ns}} = 10^{11}\mathrm{g\ cm}^{-3}$. The neutron star radius, R_{ns}, is then simply defined as the radius where the lateral average of the density is equal to ρ_{ns}, and the baryonic mass of the neutron star, M_{ns}, is given by the sum of the central point mass and the mass integral over all grid zones with densities $\geq \rho_{\mathrm{ns}}$. Since M_{ns} will in general vary with time due to accretion and mass stripping in the neutrino-driven wind, we also monitor the rate of mass change, $\dot{M}_{\mathrm{ns}}$, using finite differences in time. The sign of $\dot{M}_{\mathrm{ns}}$ is positive/negative when net accretion/ablation of matter occurs.

In evaluating the neutron star recoil velocity, $\vec{v}_{\mathrm{ns}}$, we have to distinguish between simulations in which we consider the neutron star motion relative to the ejecta by changing the frame of reference after each time step (see Sect. 2.3), and simulations in which this motion is not accounted for. In the first case no post-processing is required, because the neutron star velocity is given at all times by the accumulated effects of the Galilei transformations applied until time t or time step n,

$$\vec{v}_{\mathrm{ns}}(t) = \sum_{m=1,\ldots,n} \Delta\vec{v}^{\,m}_{\mathrm{core}}. \tag{3.11}$$

In the second case, $\vec{v}_{\mathrm{ns}}$ is computed a posteriori, by making use of linear momentum conservation. The total momentum of the system, i.e. the sum of the neutron star momentum $\vec{P}_{\mathrm{ns}} = M_{\mathrm{ns}}\vec{v}_{\mathrm{ns}}$ and the momentum of the surrounding gas on the computational grid, $\vec{P}_{\mathrm{gas}}$, is initially zero (because all models that we consider are spherically symmetric or equatorially and axially symmetric just after collapse). Hence we have for all times

$$\vec{v}_{\mathrm{ns}}(t) = -\vec{P}_{\mathrm{gas}}(t)/M_{\mathrm{ns}}(t), \tag{3.12}$$

and $\vec{v}_{\mathrm{ns}}(t)$ can be determined by evaluating the neutron star mass and the momentum integral of the ejecta gas,

$$\vec{P}_{\mathrm{gas}}(t) = \int_{R_{\mathrm{ns}}<r<\infty} \rho\,\vec{v}\,\mathrm{d}V. \tag{3.13}$$

Here $\mathrm{d}V = r^2\sin\theta\ \mathrm{d}r\ \mathrm{d}\theta\ \mathrm{d}\phi$. Note that the volume integral in Eq. (3.13) is limited by the outer boundary of our Eulerian grid and that the momentum flux associated with anisotropic mass flow over the grid boundary would have to be taken into account.

Equation (3.12) may actually also be coined in terms of an anisotropy parameter of the ejecta, α_{gas} (see Janka & Müller 1994; Herant 1995). To accomplish this, we make use of the following scalar quantity

$$P_{\mathrm{ej}}(t) := \int_{R_{\mathrm{ns}}}^{R_{\mathrm{s}}(\theta)} \rho\,|\vec{v}|\;\mathrm{d}V, \tag{3.14}$$

which has the dimension of a momentum. Then we can write the anisotropy parameter as

$$\alpha_{\mathrm{gas}} := |\vec{P}_{\mathrm{gas}}| \;/\; P_{\mathrm{ej}}, \tag{3.15}$$

and the absolute value of the neutron star velocity as

$$|\vec{v}_{\mathrm{ns}}| = \alpha_{\mathrm{gas}}\, P_{\mathrm{ej}} \;/\; M_{\mathrm{ns}}. \tag{3.16}$$

The neutron star acceleration corresponding to the velocity change at a given time is calculated by finite differences:

$$\vec{a}_{\mathrm{ns}}^{(n)} = \frac{\vec{v}_{\mathrm{ns}}^{(n+1)} - \vec{v}_{\mathrm{ns}}^{(n-1)}}{t^{(n+1)} - t^{(n-1)}}. \tag{3.17}$$

In computing the recoil velocity according to Eqs. (3.12) and (3.16), we have so far neglected the fact that the neutron star may also be accelerated by anisotropic neutrino emission. While our core luminosities at the inner grid boundary are assumed to be *isotropic at all times* and no neutron star acceleration can result from these, direction-dependent variations of the thermodynamic variables in layers close to the neutron star surface develop during the simulations and ultimately lead to anisotropies of the neutrinospheric emission of neutrinos. In particular, density inhomogeneities and local hot-spots (in temperature) occur as a consequence of narrow accretion flows that transport gas from the postshock layers to the neutron star, where they are decelerated in shocks and radiate away energy in neutrinos. The anisotropy of this neutrino emission can give rise to a “neutrino rocket effect”, whose magnitude can be estimated by considering the integrated momentum of the escaping neutrinos.

For a transport scheme along radial rays like ours, the neutrino momentum density has only a radial component and can thus be written as (see also Appendix A)

$$p_\nu\,\vec{e}_r = \frac{n_\nu \epsilon_\nu}{c}\,\vec{e}_r = \frac{F_\nu}{c^2}\,\vec{e}_r, \tag{3.18}$$

where F_ν is the local neutrino energy flux and $\vec{e}_r$ the unit vector in the radial direction. The integrated neutrino momentum at time t is then given by

$$\begin{aligned}\vec{P}_\nu(t) &= \int_{R_{\mathrm{ib}}<r<\infty} p_\nu\,\vec{e}_r\,\mathrm{d}V \\ &= \int_{R_{\mathrm{ib}}<r<R_{\mathrm{ob}}} p_\nu\,\vec{e}_r\,\mathrm{d}V + \int_0^t \mathrm{d}t \oint_{r=R_{\mathrm{ob}}} p_\nu c\,\vec{e}_r\,\mathrm{d}S,\end{aligned} \tag{3.19}$$

with the surface element $\mathrm{d}S = r^2 \sin\theta\;\mathrm{d}\theta\;\mathrm{d}\phi$. Here the surface integral accounts for the fact that a significant amount of neutrino momentum may have left our grid through the outer boundary by the time t. The momentum of the neutron star, including now also the effect of anisotropic neutrino emission, is

$$\vec{P}_{\mathrm{ns}} = -\left(\vec{P}_{\mathrm{gas}} + \vec{P}_\nu\right), \tag{3.20}$$

so that the neutron star velocity, corrected for the recoil by anisotropic neutrino emission, can be written as

$$\vec{v}_{\mathrm{ns,corr}} = \vec{v}_{\mathrm{ns}} + \vec{v}_{\mathrm{ns},\nu} = -\vec{P}_{\mathrm{gas}}/M_{\mathrm{ns}} - \vec{P}_{\nu}/M_{\mathrm{ns}}. \tag{3.21}$$

We finally note that for symmetry reasons $\vec{P}_{\mathrm{gas}}$ and $\vec{P}_{\nu}$, and thus also $\vec{P}_{\mathrm{ns}}$ and $\vec{v}_{\mathrm{ns}}$, can have only a component parallel to the symmetry axis, i.e. along the z-axis, in 2D axisymmetric calculations. Equation (3.13), for instance, therefore reduces to

$$\begin{aligned} P_{z,\mathrm{gas}} &= 2\pi \int_{R_{\mathrm{ns}}}^{\infty} \mathrm{d}r \int_{0}^{\pi} \mathrm{d}\theta\, r^2 \sin\theta \; p_z(r,\theta) \\ &= 2\pi \int_{R_{\mathrm{ns}}}^{\infty} \mathrm{d}r \int_{0}^{\pi/2} \mathrm{d}\theta\, r^2 \sin\theta \; [\, p_z(r,\theta) + p_z(r,\pi-\theta)\,] \\ &= P^{\mathrm{N}}_{z,\mathrm{gas}} + P^{\mathrm{S}}_{z,\mathrm{gas}}. \end{aligned} \tag{3.22}$$

Here $p_z(r,\theta) = \rho\,(v_r \cos\theta - v_\theta \sin\theta)$ is the z-component of the momentum density of the gas, and $P^{\mathrm{N}}_{z,\mathrm{gas}}$ and $P^{\mathrm{S}}_{z,\mathrm{gas}}$ are introduced as the z-momenta of the gas in the northern and southern hemispheres, respectively.

To characterise the deviation of the shape of the supernova shock from a sphere we introduce a shock deformation parameter,

$$d_{\mathrm{shock}} := \frac{\max\left(R_{\mathrm{s}}(\theta)\cos\theta\right) - \min\left(R_{\mathrm{s}}(\theta)\cos(\theta)\right)}{2 \times \max\left(R_{\mathrm{s}}(\theta)\sin\theta\right)} - 1, \tag{3.23}$$

where $R_{\mathrm{s}}(\theta)$ is the local shock radius as a function of polar angle θ. The numerator and denominator in Eq. (3.23) are the maximum shock diameters in projection on the symmetry axis and perpendicular to it, respectively. A prolate deformation leads to a positive value of d_{shock}, an oblate deformation gives a negative value. Note that a linear shift of the shock surface in the direction of the z-axis does not change d_{shock}.

Note that in Tables 3.1–3.3 the time-dependent quantities $\Delta Y_{\mathrm{e,core}}$, $\Delta E^{\mathrm{tot}}_{\nu,\mathrm{core}}$, ΔE_{500}, E_{exp}, M_{ns}, v_z^{ns}, $v_z^{\mathrm{ns},\nu}$, a_z^{ns}, α_{gas} and d_{shock} are given at the time $t = 1\,\mathrm{s}$, at which we usually stop our simulations. We have to point out here that the listed neutron star recoils velocities, v_z^{ns}, are *not* the final ones, but that even at the end of our simulations the neutron star can still experience a large acceleration. We therefore also give the neutron star acceleration, $a_z^{\mathrm{ns}} = \mathrm{d}v_z^{\mathrm{ns}}/\mathrm{d}t$ (averaged over the last 100 ms and without neutrino effects), at the end of our simulations and will attempt to estimate final velocities of the neutron stars in Sect. 3.5.4.

3.2 Two representative models

3.2.1 The character of the flow

Giving an accurate qualitative description of the flow that establishes in our calculations is a difficult endeavour, as the evolution that we observe during the first $\sim 300-400\,\mathrm{ms}$ is wildly time-dependent and extremely non-linear. One may even characterise it as chaotic (see Sect. 3.2.5). The layer between the proto-neutron star and the supernova shock is Ledoux-unstable, because a negative entropy gradient is established due to neutrino heating within $\sim 50\,\mathrm{ms}$ after bounce. Small Rayleigh-Taylor mushrooms grow from the imposed random seed perturbations and start rising towards the shock. They merge quickly and grow to fewer but larger bubbles that deform the shock and push it outward (Fig. 3.3). Initially, this deformation of the shock is confined to

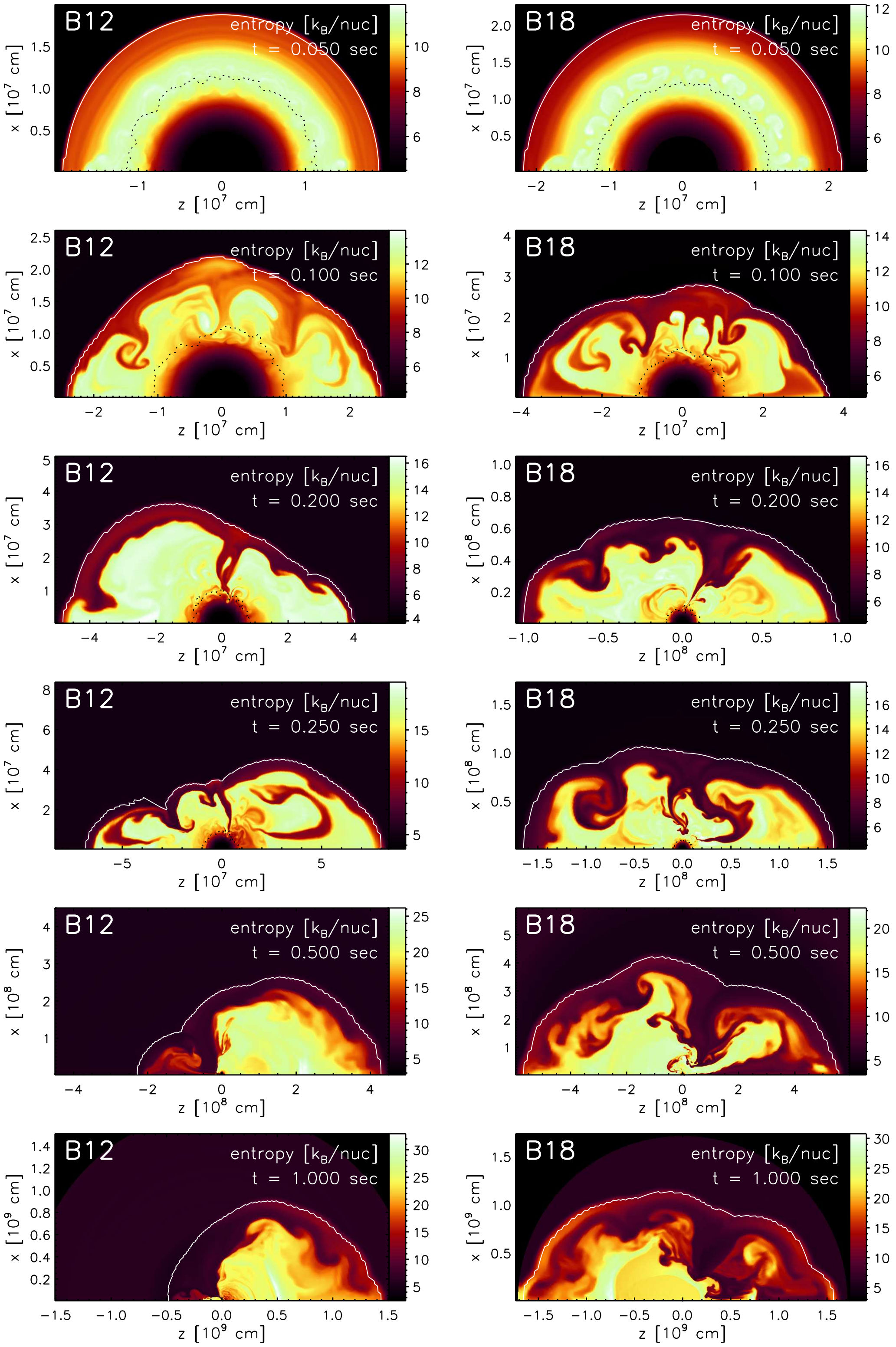

Figure 3.3: Entropy distributions in Model B12 (left column) and Model B18 (right column) for different times. The figures are plotted such that the polar axis is oriented horizontally with “south” ($\theta = \pi$) on the left and “north” ($\theta = 0$) on the right. Dotted black lines mark the gain radius and white lines the supernova shock. Note that the scales differ between the plots. Convective activity starts with small Rayleigh-Taylor structures ($t = 50\,\mathrm{ms}$) which then grow and merge to larger cells and global anisotropy. In contrast to Model B18, the low-energy model B12 develops pronounced bipolar oscillations (compare the plots for $t = 200\,\mathrm{ms}$ and $t = 250\,\mathrm{ms}$ between both cases). After the explosion has set in, the convective pattern “freezes out” and the expansion continues essentially self-similarly (see the plots for $t = 500\,\mathrm{ms}$ and $t = 1000\,\mathrm{ms}$).

latitudes close to the poles, where the growth of the bubbles is faster than near the equator (cf. Sect. 3.2.3), but soon the entire shock surface is affected.

Due to the violent convective motions of the rising high-entropy plumes the shock gets bumpy and deformed, and caustic-like kinks of the shock emerge where two such bubbles approach each other and collide. Downstream of the shock, decelerated and compressed matter forms a high-density (low-entropy) shell, which sits atop high-entropy material that boils vigorously as it is heated by neutrinos from below. The interface between these layers is Rayleigh-Taylor unstable (Herant 1995) and gives therefore rise to narrow, low-entropy downflows of matter, which penetrate from the postshock layer to the neutron star with supersonic velocities. When they reach surroundings with entropies lower than their own, the downflows are decelerated and their material spreads around the neutron star. The evolution of these downflows is highly dynamic. They form, merge with other accretion funnels, or are blown away by the rising buoyant matter on a time scale of 10–20 ms, while their number decreases with time. The most massive of these downflows originate from the kinks at the shock surface, where the deceleration of the infalling matter is weaker due to the (local) obliqueness of the shock. During this phase of violent "boiling" the shock develops a strong, time-dependent deformation and expands slowly outward. In Model B12, whose evolution is shown in the sequence of plots on the left side of Fig. 3.3, pronounced bipolar hemispheric oscillations become visible after about 150 ms. This model differs from Model B18 (on the right side of Fig. 3.3) by lower neutrino luminosities at the inner boundary and a correspondingly lower explosion energy and later onset of the explosion. Model B18 shows also violent convective activity, but no such bipolar oscillations.

Owing to the persistent deposition of energy by neutrinos in the region between gain radius and shock, and the increase of the efficiency of the heating by convection, Models B12 and B18 ultimately explode at $t_{\text{exp}} = 220\,\text{ms}$ and $t_{\text{exp}} = 152\,\text{ms}$, respectively, in contrast to one-dimensional counterparts of both models, which fail to explode. At these times the morphology is still evolving rapidly. About $100 - 200\,\text{ms}$ later, however, the overall flow has settled into a quasi-self-similar state and has become remarkably stable (as predicted by Herant 1995), in stark contrast to the preceding phase. The boiling motions have given rise to only two bubbles, which show a Kelvin-Helmholtz unstable shear layer at their outer boundaries, and are separated by a single accretion funnel. The bubbles may occupy roughly a hemisphere each as in Model B18, but they may also differ significantly in size, resulting in a global $l = 1$ mode anisotropy as in Model B12 (see Fig. 3.3).

For sufficiently high core luminosities, accretion of matter onto the neutron star is eventually superseded by the onset of a neutrino-driven wind (see also Burrows et al. 1995; Janka & Müller 1996). If the wind is strong enough, as in Model B18 where the mass-loss rate of the nascent neutron star by the wind is $\dot{M}_{\text{ns}} = -5.1 \times 10^{-2}\, M_\odot/\text{s}$, it blows away the accretion funnel and establishes a high-entropy shell or cavity of rapidly expanding low-density material around the neutron star, which is separated from the ejecta by a strong reverse shock. Otherwise accretion through the funnel continues until more than about 1 s after bounce, as in Model B12. In this case the accreted material reaches infall velocities of about 1/4 of the speed of light, while the accretion rate at $t = 1\,\text{s}$ has decreased to $\dot{M}_{\text{accr}} \approx 4 \times 10^{-2}\, M_\odot/\text{s}$. Since at the same time the neutron star mass changes at a rate of $\dot{M}_{\text{ns}} \approx 1.1 \times 10^{-2}\, M_\odot/\text{s}$, only a fraction of $\sim 25\%$ of the infalling matter is actually integrated into the neutron star. The remaining 75% are heated and reejected with high velocity, inflating the buoyant bubble of neutrino-heated gas. The resulting flow, which is characterised by a strong dipole mode, can be conveyed only incompletely with plots such as Fig. 3.3 and is much more impressively captured by movies that we have produced from our data and which are available as online material to Scheck et al. (2006).

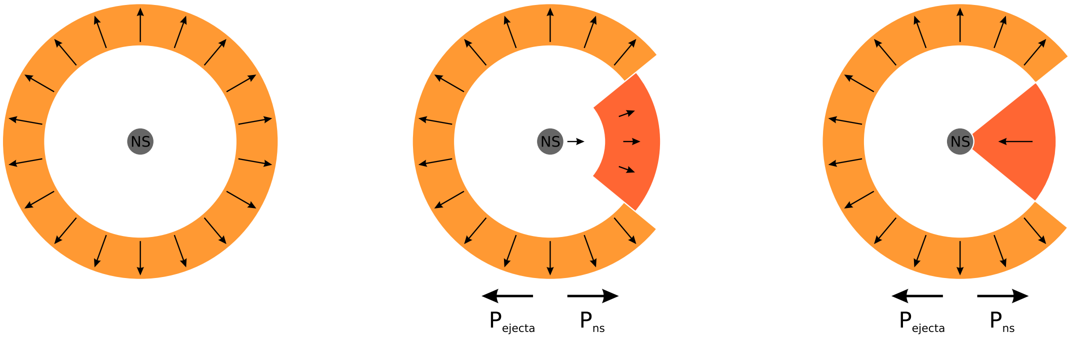

Figure 3.4: Graphical illustration of the momentum balance between neutron star and ejecta. The largest fraction of the ejecta mass is concentrated in a dense shell behind the shock (bright coloured ring). For a spherical explosion (left panel) the momenta of the neutron star and the ejecta are zero. If the expansion of one hemisphere lags behind the other, the gas has a net momentum in the direction of the faster expanding hemisphere. The neutron star is always accelerated in the opposite direction, i.e towards the slower moving gas (middle and right panels). This acceleration can be mediated by the gravitational attraction of the anisotropic ejecta (middle panel). In case accretion flows reach down to the neutron star surface (right panel), additional (hydrodynamic) forces may contribute, but the gravitational force, in general, remains dominant.

At the end of the simulations, Models B12 and B18 have attained explosion energies of 0.37×10^{51} erg and 1.16×10^{51} erg, respectively, which makes them representative of a low-energy and a rather high-energy (more standard) explosion.

3.2.2 Acceleration and recoil of the neutron star

We have shown in Sect. 3.1.3 that in a 2D axisymmetric calculation the neutron star recoil can only have a component parallel to the z-axis, and that for its calculation only the z-momenta of the gas in the northern and southern hemispheres need to be considered (see Eq. 3.22). If the momentum density of the ejecta, $p_z(r, \theta)$, is mirror symmetric with respect to the equatorial plane, i.e., if

$$p_z(r, \theta) = -p_z(r, \pi - \theta) \tag{3.24}$$

holds, the sum of the $z-$momenta of the two hemispheres vanishes

$$P_{z,\mathrm{gas}} = P^{\mathrm{N}}_{z,\mathrm{gas}} + P^{\mathrm{S}}_{z,\mathrm{gas}} = 0, \tag{3.25}$$

and thus also the neutron star remains at rest (cf. Eqs. 3.22 and 3.12). The latter situation is given e.g. for an $l = 2$ mode, i.e. for two polar bubbles of equal size separated by a single downflow which is located in the equatorial plane. However, in general the expansion of the ejecta will proceed differently in the two hemispheres, so that a net momentum $P_{z,\mathrm{gas}} \neq 0$ will result.

If a single downflow has formed, e.g., in the southern hemisphere, the expansion of the ejecta will be hampered there. On the other hand it will proceed unaffected in the northern hemisphere, and thus $|P^{\mathrm{N}}_{z,\mathrm{gas}}|$ will be larger than $|P^{\mathrm{S}}_{z,\mathrm{gas}}|$. Hence, $P_{z,\mathrm{gas}}$ will be dominated by $P^{\mathrm{N}}_{z,\mathrm{gas}}$ (which is positive since all of the gas in this hemisphere is moving outwards). According to Eq. (3.12), the neutron star must then be accelerated in the negative z-direction, i.e. towards the (southern) hemisphere which contains the downflow. This is the situation that ultimately establishes in Model B12 (compare Fig. 3.3 and Table 3.4), and which is also illustrated in the right panel of

Table 3.4: Integrated momenta of the ejecta in the northern ($\theta < \pi/2$) and southern hemispheres as well as their sum, $P_{z,\mathrm{gas}}$, and the resulting neutron star recoil velocity, v_z^{ns}, at $t = 1\,\mathrm{s}$.

Model	$P^{\mathrm{N}}_{z,\mathrm{gas}}$ $[\frac{\mathrm{g\,cm}}{\mathrm{s}}]$	$P^{\mathrm{S}}_{z,\mathrm{gas}}$ $[\frac{\mathrm{g\,cm}}{\mathrm{s}}]$	$P_{z,\mathrm{gas}}$ $[\frac{\mathrm{g\,cm}}{\mathrm{s}}]$	v_z^{ns} $[\frac{\mathrm{km}}{\mathrm{s}}]$
B12	1.26×10^{41}	-0.20×10^{41}	1.06×10^{41}	-389.3
B18	1.77×10^{41}	-3.07×10^{41}	-1.30×10^{41}	515.1

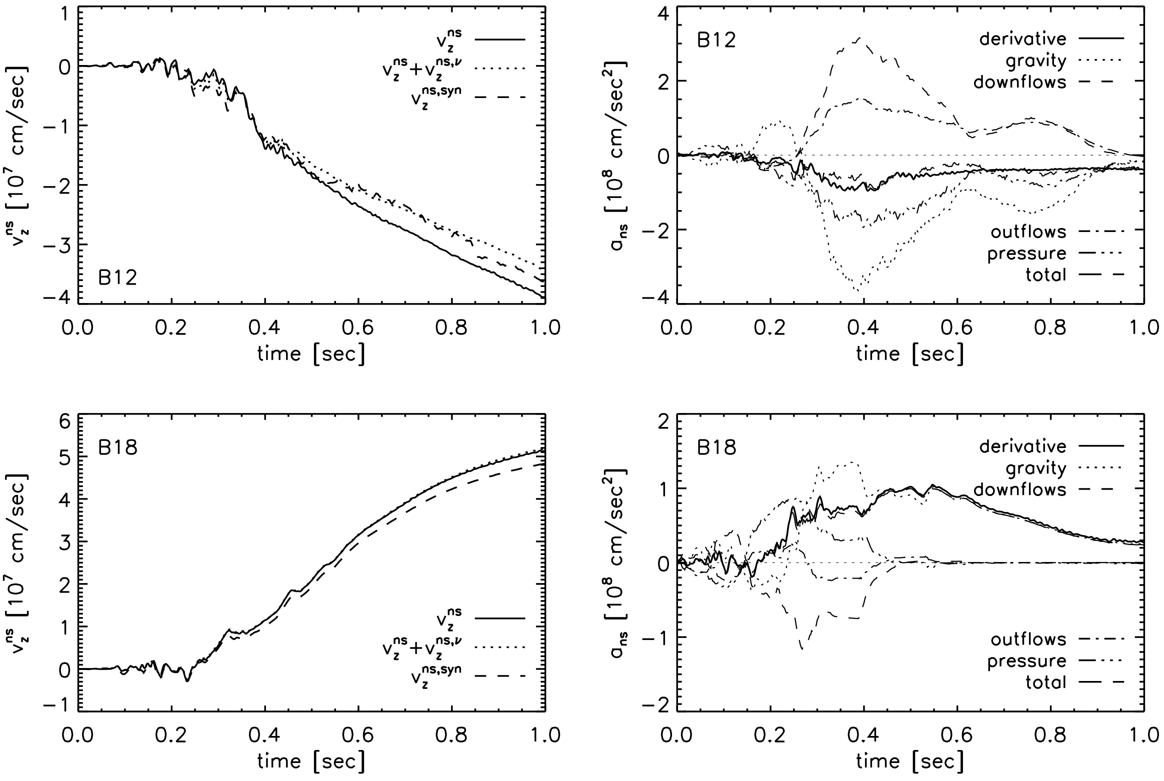

Figure 3.5: *Left:* Evolution of the neutron star velocities for Models B12 and B18. The solid curve is the neutron star recoil velocity derived from total momentum conservation of gas and neutron star (see Eq. 3.12). The dotted curve includes corrections due to anisotropic neutrino emission. The dashed curve is an estimate obtained by integrating Eq. (3.26) over time. *Right:* Evolution of the neutron star acceleration (solid curve), as computed from the (numerical) time derivative of the solid curve shown in the velocity plots on the left side. Also shown are the individual terms of Eq. (3.26), corresponding to momentum transfer due to downflows, outflows (e.g. in the neutrino-driven wind), anisotropic pressure distribution around the neutron star, and gravitational pull of the anisotropic ejecta. The sum of these terms (the long-dashed curve labelled "total") agrees well with the (solid) curve obtained independently from total momentum conservation applied to the hydrodynamics results.

Fig. 3.4. In this case the neutron star has attained a velocity of $v_z^{\mathrm{ns}} = -389\,\mathrm{km/s}$ one second after core bounce, and is still accelerated with $a_z^{\mathrm{ns}} = -372\,\mathrm{km/s}^2$ (Fig. 3.5).

Model B18 also develops a single downflow, which, however, is located in the northern hemisphere, rather close to the equator. Although this model is clearly less anisotropic than Model B12 (which is dominated by an $l = 1$ mode), the larger explosion energy and faster expansion result in a larger $|P_{z,\mathrm{gas}}|$ (Table 3.4). This leads to a larger neutron star kick of $v_z^{\mathrm{ns}} = 515\,\mathrm{km/s}$ at $t = 1\,\mathrm{s}$, while the acceleration at this time is $a_z^{\mathrm{ns}} = 290\,\mathrm{km/s}^2$ (Fig. 3.5). Note that these values are comparable to the mean pulsar birth velocities derived from observations (see Sect. 3.5.4), and that they are considerably higher than those found in earlier simulations (e.g. Janka & Müller 1994). This is mainly due to the low-order modes in our calculations, which result in a larger anisotropy, α_{gas}, compared to previous work.

The neutron star velocities shown in Fig. 3.5 (left panel), as well as their time-derivatives labelled with “derivative” and plotted with solid lines in the acceleration plots of Fig. 3.5 (right panel), are calculated from the simulation data with our standard post-processing approach by assuming total momentum conservation (see Sect. 3.1.3). The use of this approach requires a justification, because momentum conservation may be numerically violated due to deficiencies of the solver for the gravity potential. Moreover, it can be guaranteed analytically and rigorously only if the gravitational potential can be written as the solution of a Poisson equation. This is, of course, the case for Newtonian gravity. Yet, for the “general relativistic potential” of Rampp & Janka (2002) that we used in the simulations, an equivalent of the Poisson equation cannot be derived (Marek et al. 2006).

We do not expect that the small general relativistic corrections can seriously affect the results of our post-processing to an extent that unrealistically large values for the neutron star recoil velocities are obtained, especially because we find similarly large neutron star kicks in simulations with Newtonian gravity (see Sect. 3.5.3). Yet, to provide additional support that our standard post-processing method yields reliable results, we check it by calculating the neutron star acceleration as a sum of the different forces which contribute to the momentum transfer to the neutron star.

For this purpose we consider a sphere of radius $r_0 \approx 1.1 R_{\mathrm{ns}}$ that encloses the neutron star. The time-derivative of the neutron star momentum (and hence the neutron star acceleration at a certain time) can then be obtained by integrating the Euler equation over the volume of that sphere, resulting in

$$\dot{\vec{P}}_{\mathrm{ns}} \approx -\oint_{r=r_0} p\,\mathrm{d}\vec{S} - \oint_{r=r_0} \rho\vec{v}\,v_r\,\mathrm{d}S + \int_{r>r_0} G M_{\mathrm{ns}} \frac{\vec{r}}{r^3}\,\mathrm{d}m. \tag{3.26}$$

Here the individual terms account for the varying pressure p around the sphere, the flux of momentum through the surface of the sphere, and the gravitational acceleration due to the anisotropic matter distribution outside the sphere. For the gravitational term we assume that the matter distribution inside the sphere is spherically symmetric and that the gravitational potential is *Newtonian*.

The time evolution of the acceleration corresponding to these terms, calculated from the data of Models B12 and B18, is shown in the right panels of Fig. 3.5. Here the second term has been split into two components associated with momentum flux into (“downflows”) and out of the sphere (“outflows”). Also displayed is the sum of all terms (labelled by “total”). Integration over time of the latter quantity yields the dashed velocity curve for $v_z^{\mathrm{ns,syn}}$ in the left panels of Fig. 3.5. This should be compared to the solid curve (v_z^{ns}) which was computed with our standard post-processing approach of the gas momentum (and which includes the effects due to general relativistic corrections). It is evident that there are only small differences between both

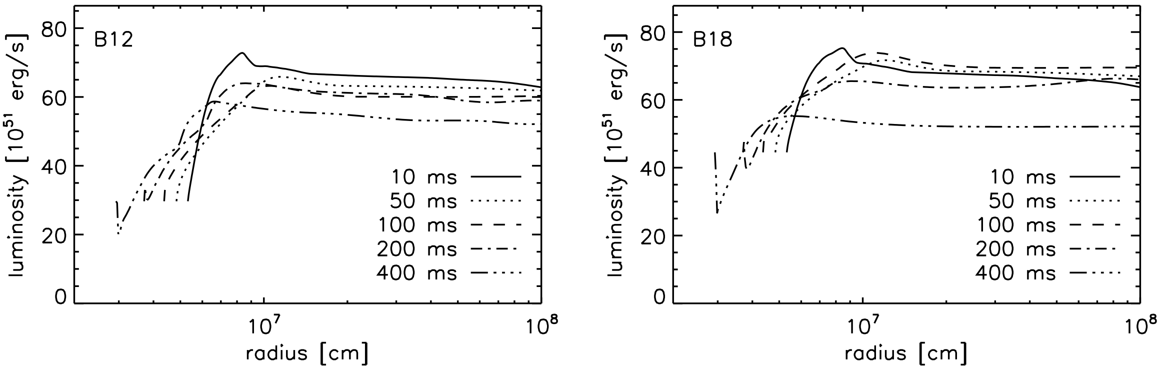

Figure 3.6: Radial profiles of the sum of the ν_e and $\bar{\nu}_e$ luminosities for Models B12 and B18 at different times after the start of the simulations.

results, which are significantly smaller than 10%. This demonstrates that the use of relativistic corrections to the gravitational potential is not the cause of our high neutron star velocities.

An interesting implication of Fig. 3.5 is the fact that the largest contribution to the acceleration is, in general, due to the gravitational term. In certain evolutionary phases also the other terms may contribute significantly. Yet, the total acceleration points nearly always in the same direction as the gravitational pull. Momentum transfer by pressure and gas flow (the first and the second term in Eq. 3.26) are only important as long as the inhomogeneous ejecta have sonic contact with the neutron star and thus can exert hydrodynamic forces on the central object. This is the situation found in Model B18 for times before $t \approx 0.5\,\mathrm{s}$. After that time the supersonic neutrino-driven wind, which is very strong in this energetic model (due to the high neutrino luminosities) has blown away the accretion downflows from the neutron star. Ongoing acceleration is then exclusively caused by the gravitational pull of the anisotropic ejecta and decreases slowly as the nearly spherically symmetric wind clears the surroundings of the neutron star. Hydrodynamic forces therefore do not contribute at later times in Model B18. On the other hand, they are important at all times in Model B12. The acceleration due to the momentum flux associated with the narrow downflows that reach the neutron star is usually the second most important term, and is directed opposite to the gravitational acceleration. Anisotropies in the pressure distribution and wind outflow contribute on a smaller level.

Finally, we show in Fig. 3.5 (left) with dotted lines the neutron star velocities corrected for the effects of anisotropic neutrino emission (see Sect. 3.1.3). These effects turn out to be small. For Model B12 the neutron star kick is thus reduced by about 10%, which is unusually large. For most of our models (including Model B18) the corrections due to anisotropic neutrino emission are smaller than 5% (see Sect. 3.5.1).

3.2.3 Possible origin of the low-order modes

In all simulations discussed in this chapter, it is Ledoux convection which breaks the initial spherical symmetry. However, as we have discussed in Sect. 1.2.2, it is not clear if convection alone can explain globally anisotropic explosions like those that develop in our simulations. Other instabilities like the "advective-acoustic cycle" (Galletti & Foglizzo 2005) or the "standing accretion shock instability" (Blondin et al. 2003) may be responsible for the excitation of low modes. It is possible that such instabilities are present, but not clearly visible due to the convective overturn. In fact, the bipolar oscillation (or "sloshing") of the shock in low-energy models, like B12, resembles the $l = 1$ mode instabilities as associated with the advective-acoustic s

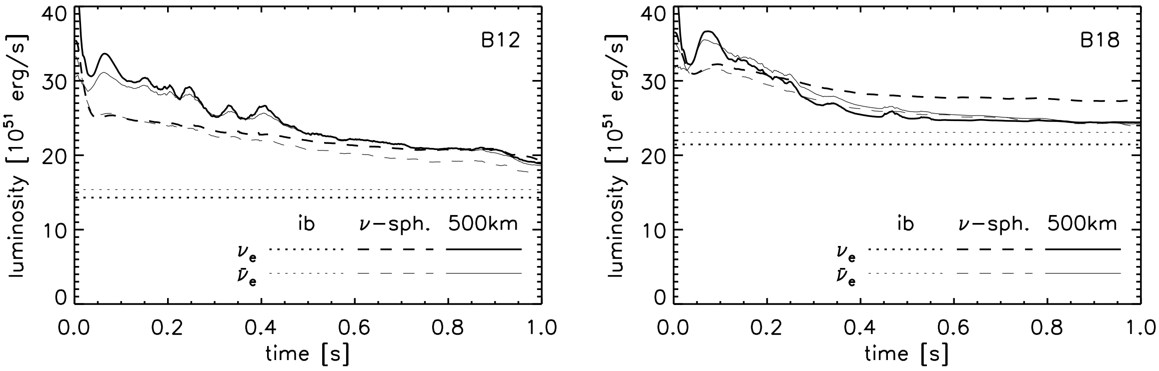

Figure 3.7: Luminosities of ν_e and $\bar{\nu}_e$ at the inner boundary, at the ν_e-sphere, and at a radius of 500 km. Note the different importance of the accretion contribution to the luminosity in the low-energy explosion (Model B12) compared to the high-energy explosion (Model B18) and the rapid decay of the accretion luminosity after the onset of the explosion in the latter model.

instability and the SASI much more than the non-oscillatory growth (at intermediate values of the mode index ℓ) that is expected for convection (Foglizzo et al. 2006b). We will postpone a more detailed discussion of the origin of global modes to Chapter 4.

It should be noted that for the simulations discussed in this chapter we have constrained ourselves to 2D axisymmetry, deferring the three-dimensional case to Chapter 5. It is well-known that the assumption of axisymmetry leads to smaller growth rates for equatorial, toroidal structures than for polar buoyant bubbles, and that both of these growth rates differ from those in a corresponding 3D calculation (see Kane et al. 2000). Furthermore, the use of reflecting boundary conditions in θ restricts the degrees of freedom of the flow. In addition, a coordinate singularity is present at the polar axis of a spherical grid. Therefore the question arises whether these shortcomings of axisymmetric calculations are causal for a preference of low-mode flows in two dimensions, whereas the true 3D situation might look different. This point was also raised by Blondin et al. (2003). The preliminary three-dimensional simulations that we have performed (Chapter 5) suggest that this is not the case. Low-order modes occur also in these simulations, and the evolution resembles qualitatively the two-dimensional case.

3.2.4 Comparison with previous works

In previous 2D simulations Janka & Müller (1996) and Kifonidis et al. (2003) did *not* obtain the global anisotropies and low-mode flows that we discuss in this work. Instead, these models developed only small scale anisotropies, except for one model in Janka & Müller (1996), which exploded with a rather low energy and revealed the tendency towards an $l = 1$ asymmetry in the late post-bounce flow.

The fact that these earlier 2D simulations, which were performed with a neutrino light-bulb description, were not dominated by low-order modes, poses the question to which extent the development of such global asphericity in the flow is sensitive to the treatment of the neutrino transport. Figure 3.6 shows that our new neutrino transport description (which is presented in detail in Appendix A) yields radial profiles for the sum of the ν_e and $\bar{\nu}_e$ luminosities which deviate markedly from the radius-independent luminosities used in a light-bulb approach: The luminosities are significantly modified compared to the values imposed at the inner boundary. After some adjustment to the local thermodynamic conditions, which takes place in a few radial

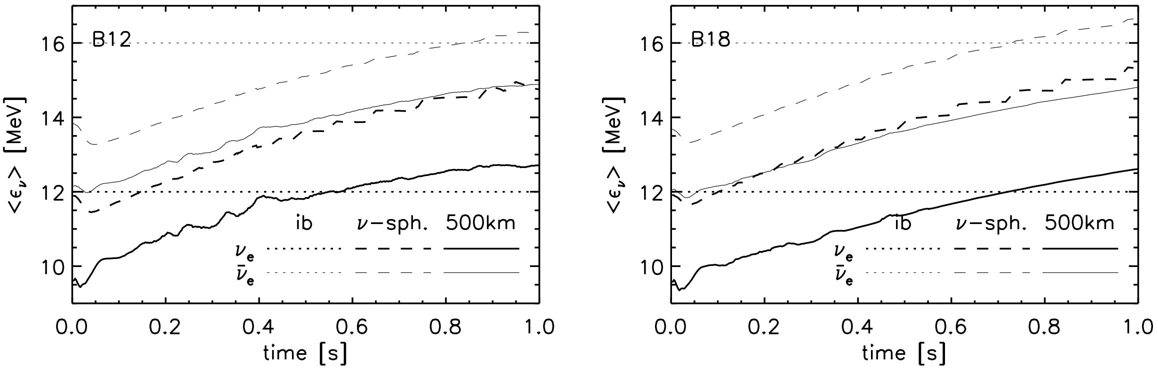

Figure 3.8: Evolution of the mean ν_e and $\bar\nu_\mathrm{e}$ energies at the inner boundary (ib), at the ν_e-sphere, and at a radius of 500 km. Note that due to the contraction and compressional heating of the nascent neutron star the average energies of the radiated neutrinos continue to rise until the end of our simulated evolution.

zones next to the inner boundary, the luminosities rise steeply in the cooling region below the gain radius, and decline slightly in the heating region farther out. The rise is caused by the creation of neutrinos when gravitational energy is released during the accretion and the contraction of the neutron star, while the slight decline results from the absorption of the ν_e and $\bar\nu_\mathrm{e}$ in the heating region.

The "accretion" luminosity that is produced on the grid is usually of the same order as the luminosity emerging from the core. In low-energy models, like B12, the accretion component exceeds the core component early on, while in high-energy models the core component is dominant at all times (see the neutrino "lightcurves" for Models B12 and B18 shown in Fig. 3.7).

Yet, we point out here that all these (previously not modelled) effects are *not* the reason why the development of $l = 1, 2$ modes is seen here, whereas it was not visible in the calculations of Janka & Müller (1996) and Kifonidis et al. (2003). Highly anisotropic explosions can also be obtained with the light-bulb assumption (see Janka et al. 2003; Janka et al. 2004 for an example). In other words, the details of the functional form of $L(r)$, which are visible in Fig. 3.6, are *not* decisive for the growth of the $l = 1, 2$ modes. What is crucial, however, is that the explosions in the current models start *slowly*. This was not the case in all but one of the simulations of Janka & Müller (1996) and Kifonidis et al. (2003), where the neutrino luminosities were assumed to decay exponentially instead of varying slowly. The exponential, "burst-like" decline of the neutrino light bulb implied fairly high initial luminosities – which were required in case of the exponential decay for getting "typical" supernova explosion energies – and thus strong neutrino heating occurred at early times after bounce. This led to rapid explosions, which in turn did not leave enough time for the convective cells and bubbles to merge before the expansion became so fast that it continued in a quasi self-similar way. Since the convective bubbles are initially small, their early "freezing out" in the rapidly expanding flow had the effect that small structures (i.e. high-order modes) prevailed until very late times. The rapid explosions also caused a quick end of the accretion of the proto-neutron star, and therefore the neutron stars remained small. In contrast, the present transport description gives neutrino luminosities between the neutrino spheres and a radius of 500 km that vary much less steeply than exponentially with time (see Fig. 3.7). This leads to explosion time scales that are sufficiently long to allow for the formation of low-order convective modes.

A comparison with hydrodynamic supernova models which solve the Boltzmann equation for neutrino transport (e.g. Liebendörfer et al. 2001; Liebendörfer et al. 2005; Rampp & Janka

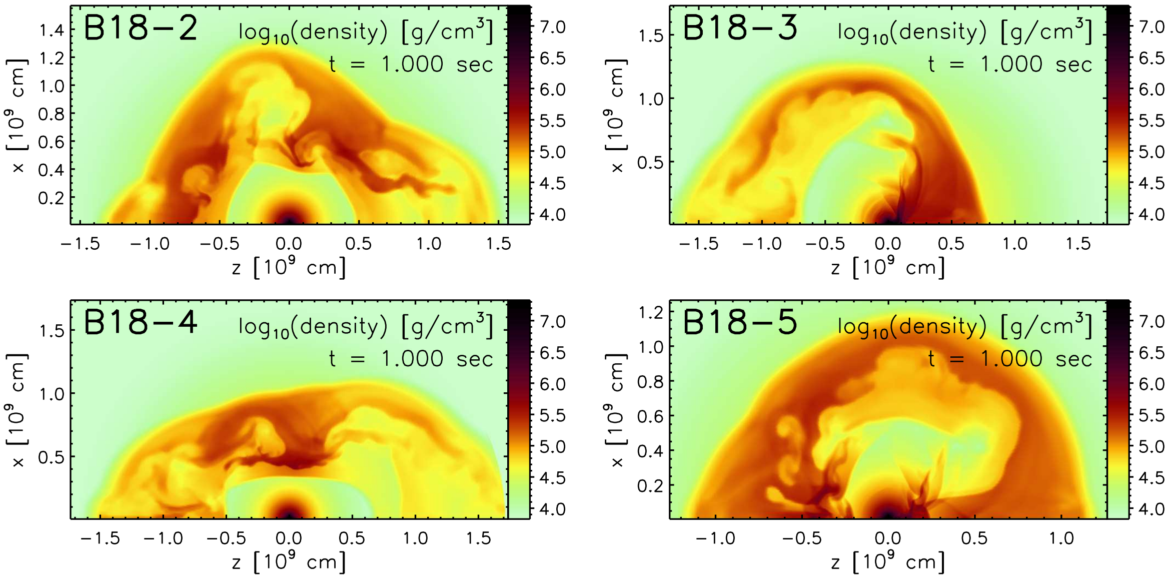

Figure 3.9: Density distributions one second after core bounce for four simulations with the same initial and boundary conditions as Model B18, but different patterns of the random seed perturbations imposed on the velocity field of the initial model. The amplitudes of the perturbations (10^{-3}) are the same in all cases. The morphology of the explosion depends in a chaotic way on the initial perturbations.

2000; Buras et al. 2003, 2006a,b; Thompson et al. 2003) shows that the approximative transport description of this work reproduces qualitatively well the temporal behaviour of the ν_e and $\bar{\nu}_\mathrm{e}$ emission (luminosities, Fig. 3.7, and mean energies, Fig. 3.8) after core bounce found with the more accurate spectral transport solvers. Also the size of the neutrino luminosities and mean neutrino energies is in reasonably good agreement with the Boltzmann results. A more detailed comparison beyond the qualitative level, however, is not possible and in fact does not make much sense, because the approximations employed in the transport description of this work are manifold, e.g., the spectra are assumed to have Fermi-Dirac shape, the effective neutrino flux velocity is parametrised, and the relativistic effects and $\mathcal{O}(v/c)$ corrections in the transport are neglected. Therefore important differences in the neutrino-matter coupling must be expected. For these reasons one should not demand a quantitative reproduction of the behaviour of hydrodynamic models with Boltzmann transport when the luminosities at the inner boundary are adopted from the Boltzmann results at the corresponding Lagrangian mass coordinate.

Nevertheless, our transport scheme can account qualitatively well for the evolution of core and accretion components of the neutrino luminosities, for the radial and temporal evolution of the luminosities and mean energies of the radiated neutrinos, and for the relative sizes of the ν_e and $\bar{\nu}_\mathrm{e}$ emission. We therefore think that our current transport treatment is a reasonably good method for performing parametric explosion studies with the aim to better understand the role of hydrodynamic instabilities during the shock-revival phase of neutrino-driven supernova explosions. This confidence is supported by comparisons of our models to Models s11.2 and s15r of Buras et al. (2003), and to the (flux-limited diffusion) 2D simulations of Burrows et al. (1995), who found similar shock "pulsations" and the same boiling of neutrino-heated matter that we see in our models. However, both groups used computational wedges of only 90° latitudinal width with periodic boundaries in θ-direction. In thus constrained simulations global $l = 1, 2$ modes cannot occur.

We believe that the use of small computational wedges was one of the major drawbacks of previous calculations (e.g. Herant et al. 1992; Burrows et al. 1995; Buras et al. 2003). It is likely that the occurrence of low-mode instabilities would have been observed if these simulations had been carried out with a full 180° grid for a sufficiently long period of post-bounce evolution. Indeed Buras et al. (2006b) have recently recalculated their Model s11.2 on a 180° grid, and obtained a pronounced $l = 2$ mode with significant $l = 1$ contribution. Moreover, this model exploded whereas its 90° counterpart failed. Apparently, low-order convective modes can help or even trigger the supernova, if the neutrino luminosities are close to the threshold required for an explosion. This is in agreement with the results of our calculations and lends support to the idea that low-order convective modes, the explosion itself, and large neutron star kicks can go hand in hand. The 2D simulations of Fryer (1999) and Fryer & Heger (2000) as well as 3D simulations of Fryer & Warren (2002, 2004) are not in conflict with our findings, because their transport treatment leads to very rapid and powerful explosions in which case we usually also observe that the growth of $l = 1, 2$ mode instabilities is suppressed.

3.2.5 Sensitivity to the seed perturbations

The highly nonlinear character of the evolution that we see within the first $\sim 300\,\mathrm{ms}$ suggests that the convective mode that will finally establish in a simulation, might be sensitive to the seed perturbation for triggering convection. To test this we repeat the calculations of some models with varied random seeds for the initial velocity perturbations. Figure 3.9 displays density plots at $t = 1\,\mathrm{s}$ for the B18-series of models thus obtained. These differ from the original Model B18 (Fig. 3.3, right column) only in that they are computed with different seed values for the random number generator. The *amplitude* of the perturbations is kept the same (the effects of different perturbation amplitudes will be discussed in the Chapter 4; but see also Sect. 3.3). The outcome supports our conjecture: A sensitive dependence of the late-time shock morphology and anisotropy of the explosion on the initial seed is visible. In fact this sensitivity is so extreme that the system may be described as exhibiting symmetry breaking in a chaotic manner. Even the same model computed on different machines (with supposedly IEEE compliant 64-bit arithmetics) may actually end up with a different morphology.

We emphasise here that integral quantities like the explosion energy, E_{exp}, the explosion time scale, t_{exp}, or the mean shock radius are only weakly affected by varying the random seed perturbations in the described way (see Tables 3.1–3.3 and Fig. 3.9). In contrast, quantities like the neutron star recoil velocity, v_z^{ns}, and the anisotropy parameter, α_{gas}, which depend on the morphology of the ejecta, are affected dramatically. Given the extreme sensitivity on the initial perturbations, such quantities must be regarded as stochastic. Meaningful conclusions concerning their average values, the shape and width of their distribution functions, etc., can thus only be drawn on the basis of a large number of simulations. The large scatter of neutron star recoil velocities for Models B18-2 to B18-5 (see Table 3.1) illustrates this clearly. While the neutron star in Model B18-2 moves with only $\sim 80\,\mathrm{km/s}$, it is accelerated to $800\,\mathrm{km/s}$ in Model B18-3. This latter model is actually the most extreme one that we have found in our ~ 80 simulations. It features an $l = 1$ mode with a long-lasting downflow (Fig. 3.9), which, despite the relatively high core luminosity of this model, is still connected to the neutron star at times as late as $t = 1\,\mathrm{s}$ after bounce. We also see that neither bipolar oscillations nor the dominance of an $l = 1$ mode are excluded when the explosion energy is relatively large.

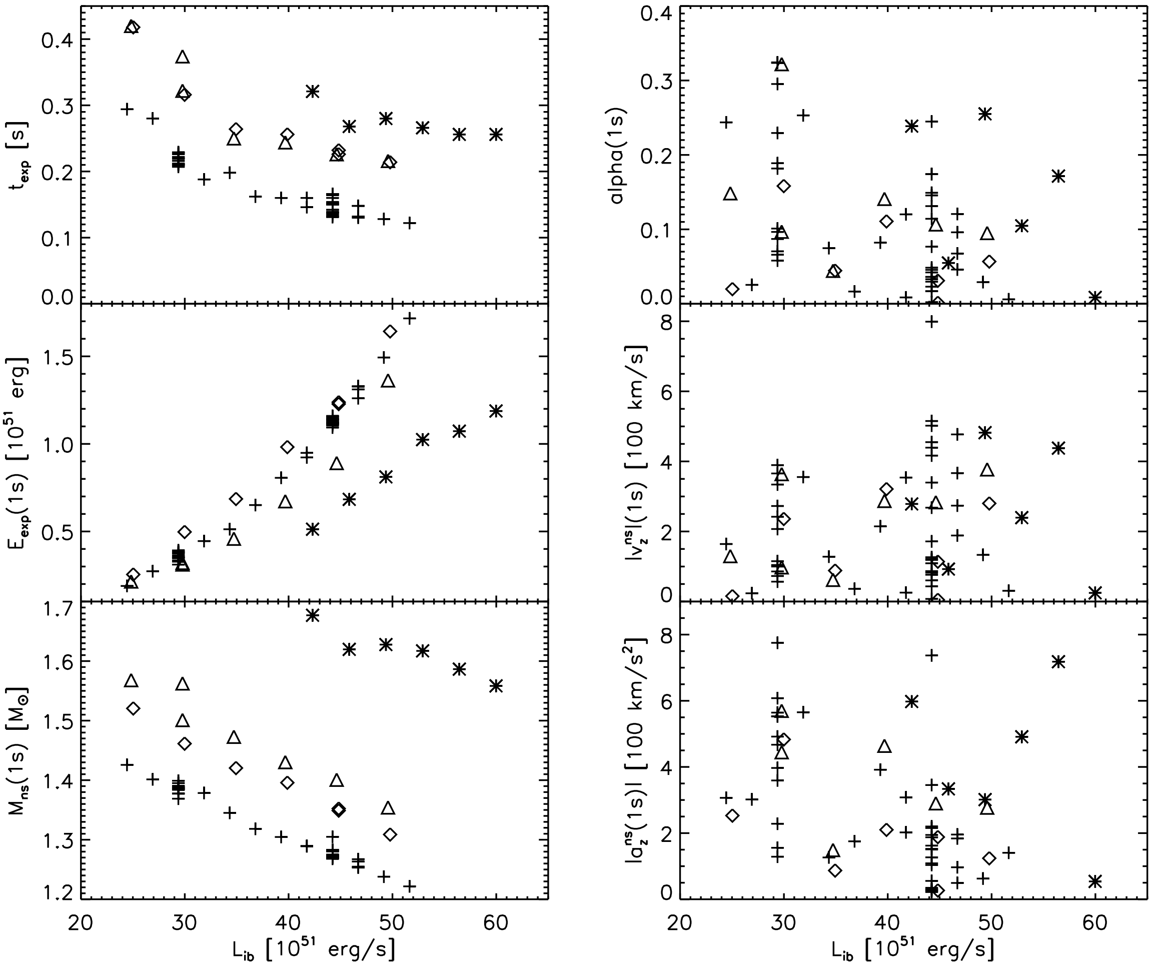

Figure 3.10: Dependence of some global quantities on the inner boundary luminosity. The quantities in the left column (explosion time scale, explosion energy, and neutron star mass) depend only on the progenitor and the boundary conditions. The quantities in the right column (anisotropy, neutron star velocity, and acceleration) are strongly influenced by the initial perturbations. All time-dependent quantities are shown at $t = 1s$. Crosses stand for the B-series of models, stars mark results for the L-series, triangles denote the W-series, and diamonds refer to the R-series of models (see Sect. 3.1.1 for the differences between these models).

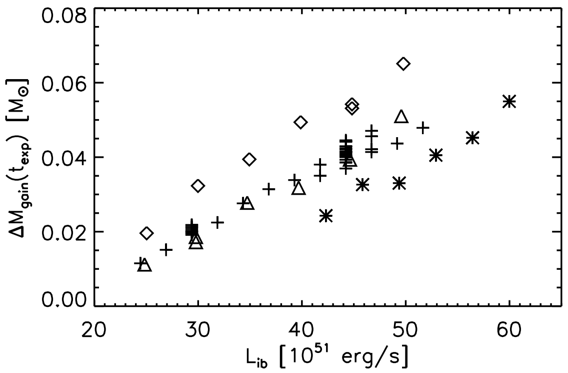

Figure 3.11: Mass of the gain layer at the onset of the explosion ($t_{\rm exp}$) as a function of the boundary luminosity for the set of models displayed in Fig. 3.10. For every initial model there exists an approximately linear relation between $\Delta M_{\rm gain}$ and $L_{\rm ib}$.

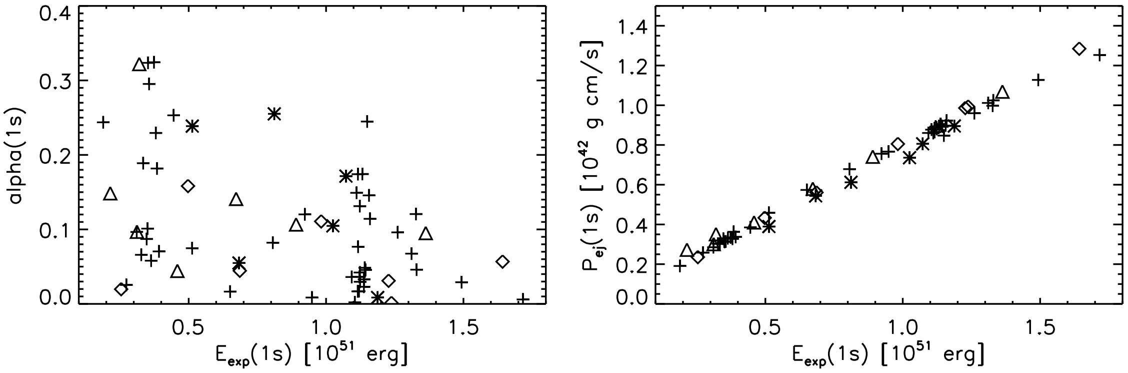

Figure 3.12: Anisotropy parameter $\alpha_{\rm gas}$ (upper panel) and (scalar) quasi-momentum of the ejecta, $P_{\rm ej}$, (lower panel, see Eq. 3.14) for a time of 1 second after core bounce as a function of the explosion energy. The different symbols have the same meaning as in Fig. 3.10.

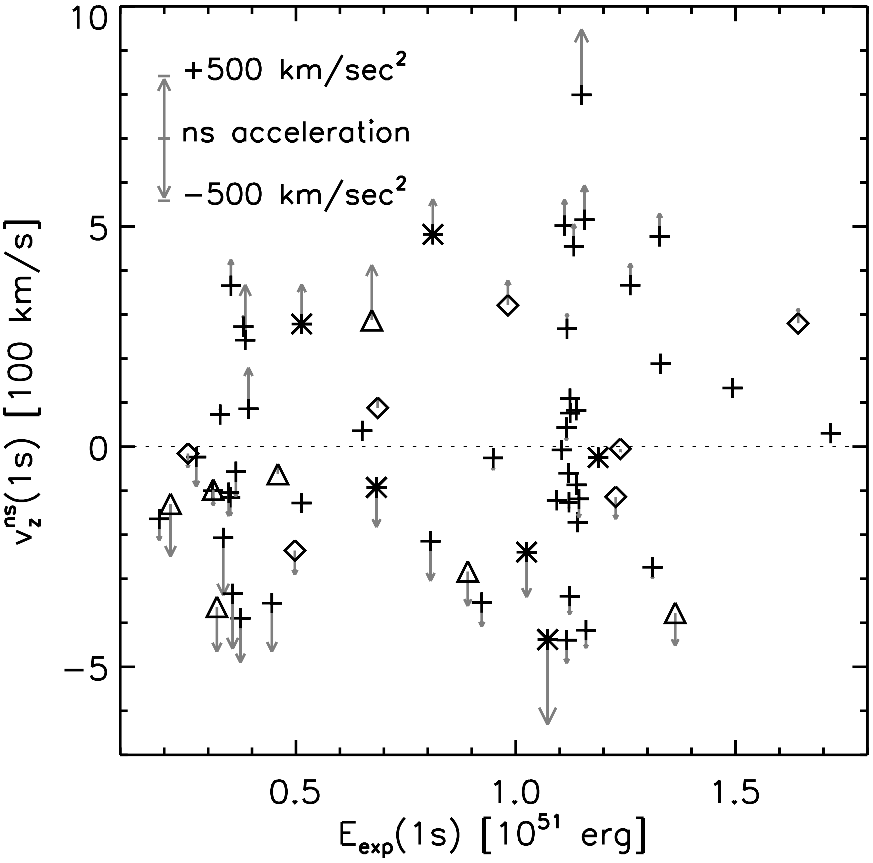

Figure 3.13: Neutron star velocities $v_z^{\rm ns}$ and accelerations $a_z^{\rm ns}$ as functions of the explosion energy for all models of Tables 3.1–3.3. The plot displays the situation at $t = 1\,$s and shows that the accelerations (indicated by the arrows) are still high at this time. The different symbols have the same meaning as in Fig. 3.10.

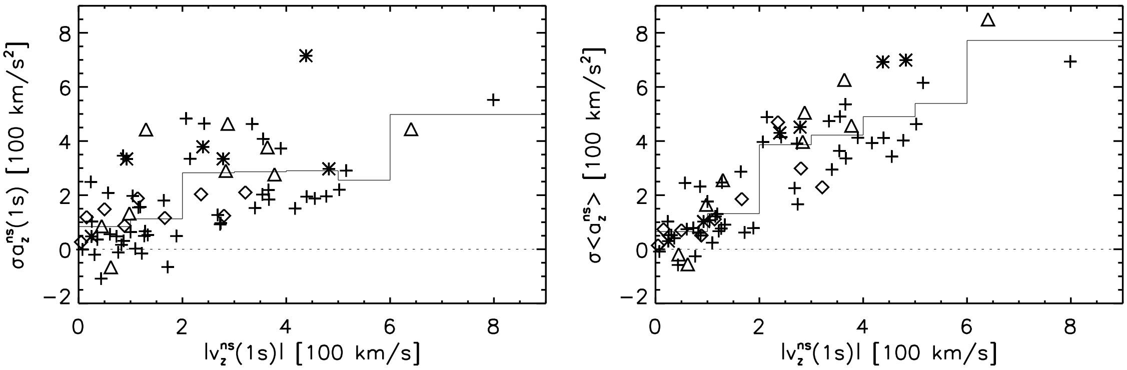

Figure 3.14: *Top:* Neutron star acceleration as a function of the neutron star velocity after one second. *Bottom:* Acceleration computed as time-averaged value over the last half of a second of the simulations versus neutron star velocity. The acceleration is multiplied by a factor $\sigma = \mathrm{sign}(v_z^{\mathrm{ns}})$, i.e. $\sigma\langle a_z^{\mathrm{ns}}\rangle < 0$ corresponds to a deceleration of the neutron star. The different symbols have the same meaning as in Fig. 3.10. Typically, low values of the acceleration ($\sigma\langle a_z^{\mathrm{ns}}\rangle \lesssim 250\,\mathrm{km/s^2}$) are associated with low velocities ($|v_z^{\mathrm{ns}}| < 200\,\mathrm{km/s}$), while much higher values of $\sigma\langle a_z^{\mathrm{ns}}\rangle$ are reached for higher velocities $|v_z^{\mathrm{ns}}|$. This suggests two components of the distribution, one with low velocities and lower average acceleration values and one with both values being higher. The thin solid line indicates the mean values of $\sigma\langle a_z^{\mathrm{ns}}\rangle$, binned in velocity intervals of 100 km/s.

3.3 Dependence on the initial model and the core luminosity

In this section we discuss the variation of the quantities introduced in Sect. 3.1.3 as functions of the initial model and a systematic variation of the imposed core neutrino luminosity L_{ib}. Tables 3.1–3.3 give an overview. To facilitate their interpretation, we also display the most important quantities for all models as a function of L_{ib} graphically in Fig. 3.10.

The results plotted in that figure show that the neutrino-driven mechanism as computed in our models is able to account for different key observational aspects of supernovae and neutron stars simultaneously, provided that sufficient time is available for low-order convective modes to form. Typical supernova explosion energies of about 10^{51} erg, typical baryonic neutron star masses around $1.4\,M_\odot$ (actually between 1.3 and $1.6\,M_\odot$ depending on the progenitor) *and* high neutron star recoils (with a maximum of 800 km/s in Model B18-3 after 1 s of post-bounce evolution, see Table 3.1), are obtained at the same time.

What is also apparent is that the quantities displayed in Fig. 3.10 can be grouped in two classes, those which show a clear correlation with the core luminosity, L_{ib}, and those which do not. Among the former are the explosion time scale, t_{exp}, the explosion energy, E_{exp}, and the neutron star mass, M_{ns}. For a given initial model these quantities show a systematic variation with the boundary luminosity with only little scatter. Among the latter quantities are the ones that depend on the morphology of the explosion, i.e. the anisotropy parameter, α_{gas}, the neutron star recoil velocity, v_z^{ns}, and the neutron star acceleration, a_{ns}. These show the essentially stochastic behaviour in dependence of the seed perturbations as discussed in Sect. 3.2.5.

A higher luminosity, L_{ib}, from the neutron star core causes the explosion to develop faster, to become more energetic, and to leave behind a neutron star with a smaller mass, because less material can be accreted onto the core when the explosion occurs faster. The monotonic correlation between L_{ib} and the explosion energy E_{exp} shows that our chosen approach to parameterise our simulations can also be interpreted as one in terms of explosion energy. In this sense L_{ib} and E_{exp} can be exchanged as governing parameters. Note, however, that the L_{ib}-E_{exp} relation differs between the initial models.

A similar behaviour is also visible in Fig. 3.11 for $\Delta M_{\rm gain}(t_{\rm exp})$, the mass contained in the gain layer at time $t_{\rm exp}$, as a function of $L_{\rm ib}$ for all models. In fact, it is actually $\Delta M_{\rm gain}(t_{\rm exp})$ which is responsible for the progenitor dependence of the $L_{\rm ib}$-$E_{\rm exp}$ relation visible in Fig. 3.10, mainly because the recombination of free nucleons to α particles and nuclei in the expanding and cooling ejecta from the gain layer yields a significant fraction of the final explosion energy. This energy contribution increases with more mass in the gain layer. The rest of the explosion energy is due to the power of the neutrino-driven wind of the proto-neutron star (see Appendix B). Since $\Delta M_{\rm gain}(t_{\rm exp})$ depends on the mass accretion rate through the shock, there is a dependence on the density profile of the progenitor star. The different initial models reveal significant differences in this respect. In particular, the Limongi et al. progenitor exhibits considerably higher densities at the edge of the iron core and in the silicon shell than the Woosley et al. models (Fig. 3.1), but this progenitor explodes later and thus at a time when the mass accretion rate has already decreased significantly.

It should be noted that rotation will also affect $\Delta M_{\rm gain}(t_{\rm exp})$ (see Sect. 3.4). The systematically larger mass of the gain layer (Fig. 3.11), and the up to $\sim 50\%$ higher explosion energies of the rotating models compared to the non-rotating models of the s15s7b2 progenitor (Fig. 3.10), though, are strongly affected by the larger initial perturbations that we have used in the rotating case (see Sects. 3.1.1 and 3.4).

A progenitor dependence is also visible in case of $t_{\rm exp}$ and $M_{\rm ns}$ as a function of $L_{\rm ib}$, as displayed in the left column of Fig. 3.10. The simulations that are based on the newer $15\,M_\odot$ progenitor model s15s7b2 of Woosley & Weaver (1995) give explosion time scales that are systematically higher by $\sim 30\%$, and final neutron star masses that are higher by $\sim 10\%$ than those of the older Woosley et al. (1988) core. On the other hand, the results belonging to the Limongi et al. (2000) progenitor again exhibit larger systematic deviations from those for the Woosley et al. stars. The higher mass accretion rate in simulations with the Limongi et al. progenitor delays the development of convective motions, and thus the onset of the explosion ($t_{\rm exp}$) compared to the other models. This prolongs the time that the revived bounce-shock needs to reach a certain radius. It also reduces the explosion energy, and leads to a larger neutron star mass, for a given value of the boundary luminosity $L_{\rm ib}$.

We focus now on the right column of Fig. 3.10. Recalling the highly nonlinear, chaotic hydrodynamic evolution in response to a variation of the initial perturbations as described in Sect. 3.2.5, one can understand that there is no clear correlation between $L_{\rm ib}$ and the quantities $\alpha_{\rm gas}$, $v_z^{\rm ns}$, and $a_z^{\rm ns}$, which depend on the explosion morphology. When, however, $\alpha_{\rm gas}$ is plotted as a function of the explosion energy (see Fig. 3.12), it becomes apparent that the area near the upper right corner in the $\alpha_{\rm gas}$–$E_{\rm exp}$ diagram, satisfying

$$\alpha_{\rm gas}\,/\,\alpha_0 \;+\; E_{\rm exp}\,/\,E_{\rm exp,0} \;>\; 1 \tag{3.27}$$

with $E_{\rm exp,0} \approx 2\times10^{51}$erg and $\alpha_0 \approx 0.3$, is almost void. This indicates that high-energy explosions with large anisotropies are disfavoured, which is plausible because there is not sufficient time available for high-order modes to merge. In order to assess the impact of this result on the neutron star recoil by virtue of Eq. (3.16), we need to consider also the scalar quantity $P_{\rm ej}$, which is defined in Eq. (3.14). Figure 3.12 shows that it is linearly increasing with the explosion energy. Since $|v_z^{\rm ns}| \propto \alpha_{\rm gas} P_{\rm ej}$, this increase of $P_{\rm ej}$ with $E_{\rm exp}$ will tend to compensate the smaller values of $\alpha_{\rm gas}$ for higher explosion energies. Therefore high neutron star velocities (up to 800 km/s at $t = 1\,$s) can result for a wide range of explosion energies (cf. Fig. 3.13). We expect, however, that for sufficiently large boundary luminosities the explosion time scale, and correspondingly $\alpha_{\rm gas}$, will become so small that the neutron star velocities will remain low for (very) large explosion energies.

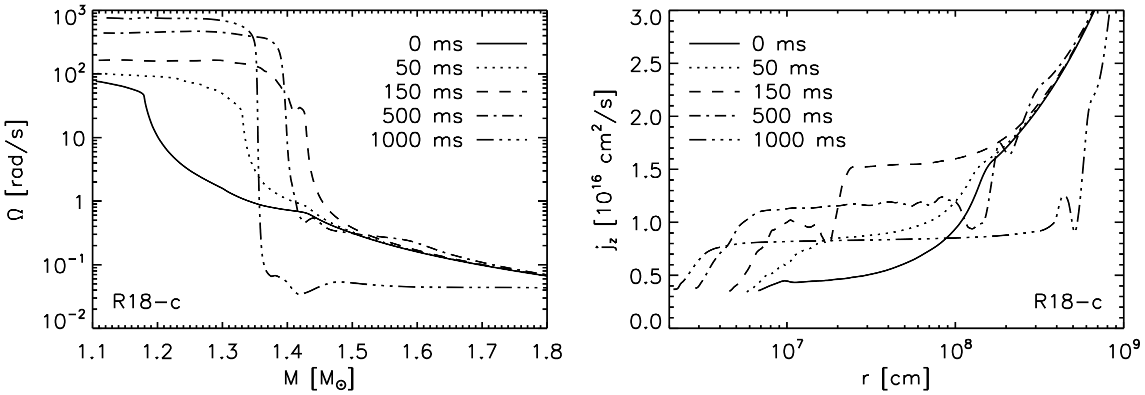

Figure 3.15: Angular frequency, Ω, as a function of the enclosed mass, and radial profiles of the specific angular momentum, j_z, for several times after the start of the simulation for Model R18-c. In both cases the *equatorial* profiles of the quantities are shown. The "mass coordinate" is defined by the masses enclosed by spheres with different radii.

Fig. 3.13 shows that also high acceleration rates (up to more than $700\,\mathrm{km/s^2}$) are obtained for the range of explosion energies covered by our simulations. In particular, the neutron stars that have already reached high velocities at $t = 1\,\mathrm{s}$ have typically higher accelerations, too. This becomes somewhat more apparent in the panels of Fig. 3.14, which display the acceleration at the end of our simulations (top) or averaged over the last half of a second, respectively, as a function of the neutron star recoil velocity. One may discriminate two populations, a low-velocity, low-acceleration component in the lower left corner of the figure and a second component extending to much higher accelerations and velocities. The latter contains simulations with a strong contribution of the $l = 1$ mode, whereas the former is made up of models in which $l = 2$ or higher modes are dominant. Since in many of the simulations the accelerations are still high at $t = 1\,\mathrm{s}$, one can expect that their neutron star recoil velocities will significantly increase at still later times. We will discuss this in Sect. 3.5.4.

3.4 The effects of rotation

We have shown that the magnitude of the neutron star recoil depends sensitively on the convective mode. Here we will consider the influence of rotation, which can have an effect on the pattern of convection (see e.g., Tassoul 1978). In order to investigate how rotation changes the morphology, the energetics of the explosion, and the neutron star recoil velocities, we have computed the R-series of our models. These models start from a post-bounce configuration with a perturbation amplitude of several percent (cf. Sect. 3.1.1), which is more than an order of magnitude larger than the standard perturbations that we employed in our non-rotating models. Such a large increase of the perturbation amplitude leads to noticeable changes in the explosion time scale and energy. A clean discussion of rotationally induced effects therefore requires recomputing some of the non-rotating models with a higher amplitude of the initial random perturbations. We do this in case of Models W12-c and W18-c (see Table 3.5), in which the same initial perturbations are applied as in Models R12-c and R18-c, whose results are listed in Table 3.5, too.

Table 3.5: Rotating and non-rotating models with the same initial perturbations. For more details, see the caption of Table 3.1.

Model	L_{ib}	E_{exp}	t_{exp}	M_{ns}	v_z^{ns}	$v_z^{\text{ns},\nu}$	a_z^{ns}	α_{gas}	d_{shock}
	[B/s]	[B]	[B]	[s]	[$M_\odot$]	[km/s]	[km/s]	[km/s^2]	
W12-c	29.7	0.40	0.301	1.535	44.4	54.0	85.4	0.03	0.63
W18-c	44.5	1.06	0.215	1.392	640.4	-8.5	444.4	0.21	0.08
R12-c	29.7	0.43	0.329	1.480	49.9	31.3	148.1	0.04	-0.03
R18-c	44.5	1.26	0.236	1.345	166.1	-3.5	116.2	0.04	0.05

3.4.1 Evolution of the rotation rate

The initial rotation profile that we employ was already discussed in Sect. 3.1.1. Our choice of this angular velocity profile on the one hand maximises rotational effects in view of the most recent evolution calculations for magnetised rotating massive stars, it yields rotation rates that are more than a factor of two higher in the iron core, and on average a factor of ten higher in the silicon shell than in the calculations of Heger et al. (2004). On the other hand, it avoids sub-millisecond rotation of the newly formed neutron star, which would result for even higher pre-collapse rotation rates. Figure 3.15 shows that due to angular momentum conservation the contracting proto-neutron star spins up to a maximum angular velocity of about $8 \times 10^2\,\text{rad/s}$ until one second after core bounce for the assumed contraction. This corresponds to a rotation period of several milliseconds.

3.4.2 Morphology

Figure 3.16 compares Model R18-c with its non-rotating counterpart W18-c. It is evident that during the first 75 ms after the start of the calculations both models evolve quite similarly. Convection sets in between 100 and 150 km, and bubbles of high-entropy matter start rising above the gain radius. The number, wavelength, and location of the convective structures show hardly any differences between both models. This may appear somewhat surprising because the criteria for convective stability differ between the rotating and non-rotating cases. In the former case the flow is stable to convection only if the Høiland condition,

$$\begin{aligned} \mathcal{C}_{\text{H}} &:= \mathcal{C}_{\text{S}} + \mathcal{C}_{\text{L}} \\ &= \frac{1}{x^3}\frac{\mathrm{d}{j_z}^2}{\mathrm{d}x} + \frac{1}{\rho}\vec{a}\cdot\left\{\left(\frac{\partial\rho}{\partial S}\right)_{P,Y_e}\vec{\nabla}S + \left(\frac{\partial\rho}{\partial Y_e}\right)_{P,S}\vec{\nabla}Y_e\right\} > 0, \end{aligned} \tag{3.28}$$

is fulfilled (Tassoul 1978). Here $\vec{a}$ is the total (gravitational and centrifugal) acceleration, and j_z is the specific angular momentum ($j_z = x \cdot v_\phi$, where $x = r\sin\theta$ is the distance from the axis of rotation). In the non-rotating case the condition of Eq. (3.28) reduces to the familiar Ledoux criterion for stability, $\mathcal{C}_{\text{L}} > 0$, whereas for negligible entropy- and Y_{e}-gradients Eq. (3.28) becomes the Solberg-condition $\mathcal{C}_{\text{S}} > 0$.

Note that since we assume axisymmetry, there are no forces (other than fictitious ones) acting in ϕ direction, and hence no source terms for j_z are present. The specific angular momentum of a fluid element therefore remains constant, and j_z is simply carried along with the flow. In three dimensions j_z is not conserved and this leads to *significant* differences (see Chapter 5) compared to the flow that develops in 2D and which we will discuss in the following.

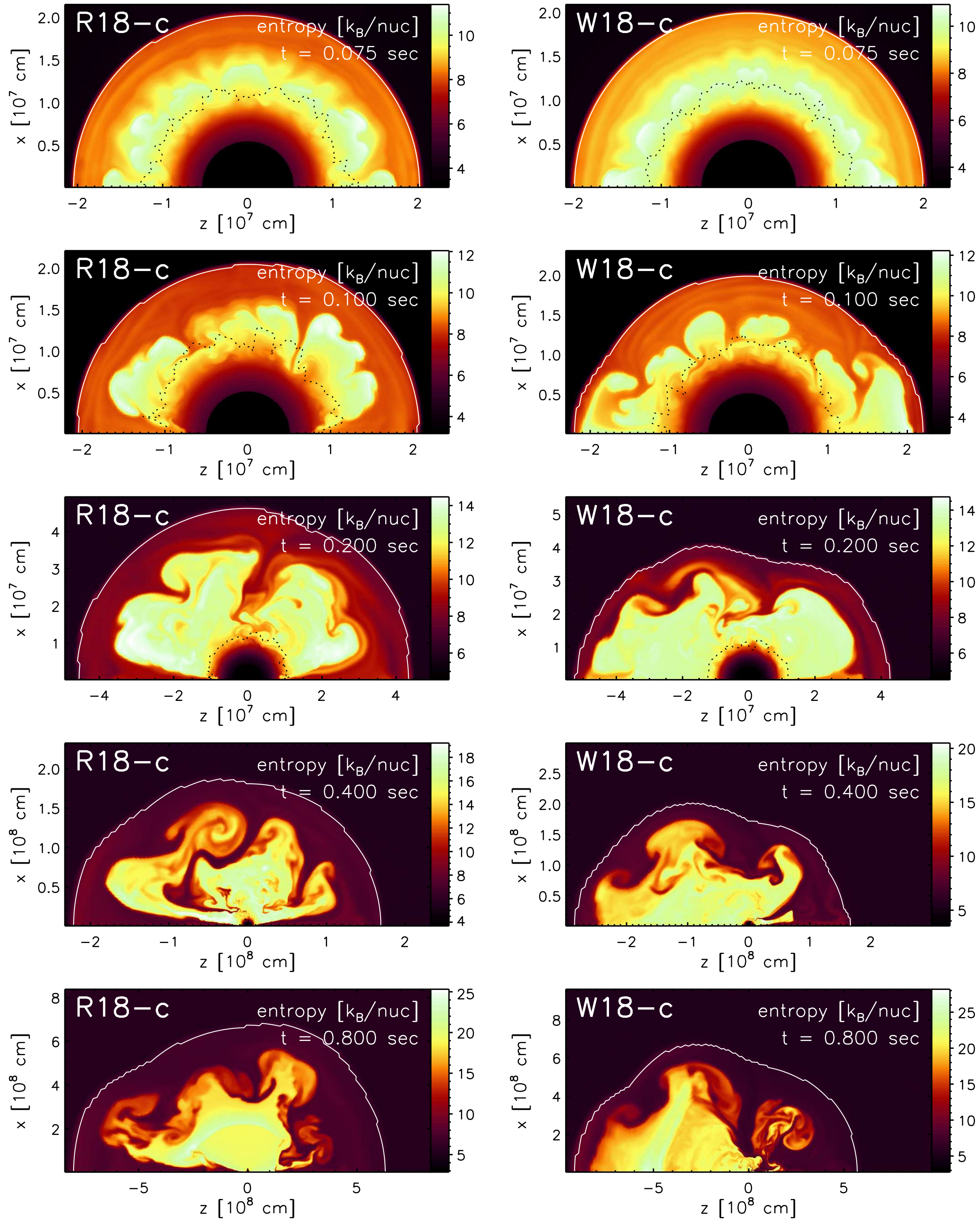

Figure 3.16: Entropy distributions of the rotating Model R18-c (left) and of the non-rotating Model W18-c at 75 ms, 100 ms, 200 ms, 400 ms, and 800 ms after the start of the simulations. Dotted black lines mark the gain radius and white lines the supernova shock. Note the two polar downflows in the rotating model, which form soon after convection has set in, and are visible for $t \geq 100\,\mathrm{ms}$. At $t = 800\,\mathrm{ms}$ they have been blown away from the vicinity of the neutron star by the neutrino-driven wind. The rotation axis is oriented horizontally in the left panels.

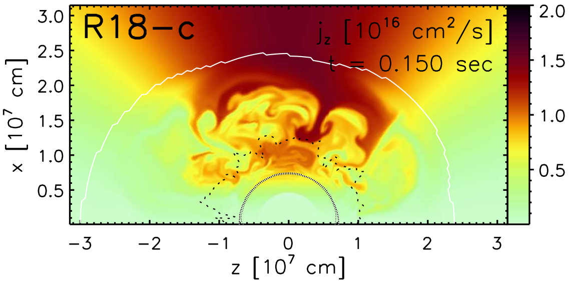

Figure 3.17: Distribution of the specific angular momentum j_z of the rotating model R18-c at $t = 150\,\text{ms}$. Matter with larger and larger specific angular momentum has fallen through the shock (outer solid line), which leads to an overall positive gradient $\text{d}{j_z}^2/\text{d}x$ in the gain layer. However, due to convection, which is suppressed only near the poles, the j_z stratification and its gradient are locally perturbed. The rotation axis is oriented horizontally.

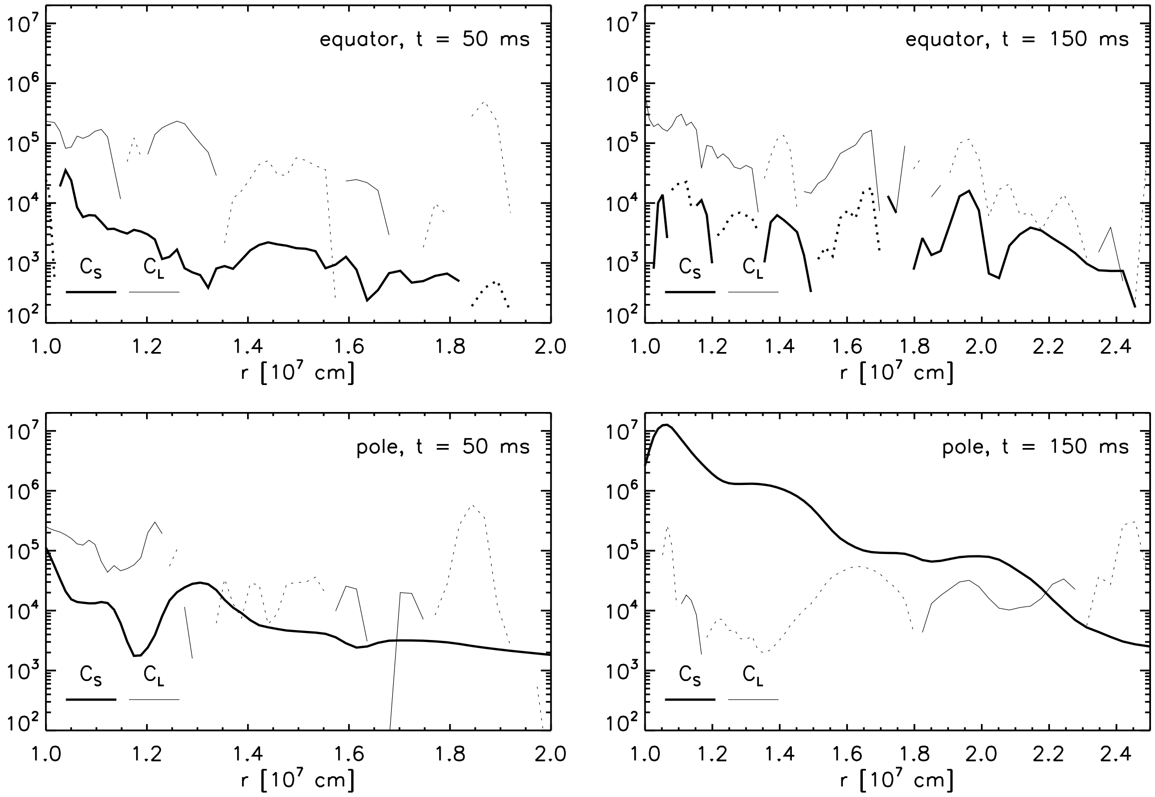

Figure 3.18: Radial profiles of the Solberg-term, $\mathcal{C}_\text{S}$, and of the Ledoux-term, $\mathcal{C}_\text{L}$, (see Eq. 3.28) for $\theta = 5°$ ("pole") and $\theta = 90°$ ("equator") in Model R18-c. We show these quantities for $t = 50\,\text{ms}$ (left column) and $t = 150\,\text{ms}$ (right column). For regions in which $\mathcal{C}_\text{S}$ or $\mathcal{C}_\text{L}$ are negative, the absolute values are plotted as dotted lines. At $t = 50\,\text{ms}$ $|\mathcal{C}_\text{L}| > |\mathcal{C}_\text{S}|$ and unstable regions ($\mathcal{C}_\text{L} + \mathcal{C}_\text{S} < 0$) are present for both latitudes. At a time of 150 ms the gradient $\text{d}{j_z}^2/\text{d}x$ has become sufficiently large to make $\mathcal{C}_\text{S} > |\mathcal{C}_\text{L}|$ at the pole, and thus to stabilise the flow, whereas in the equatorial region $|\mathcal{C}_\text{S}|$ is still small.

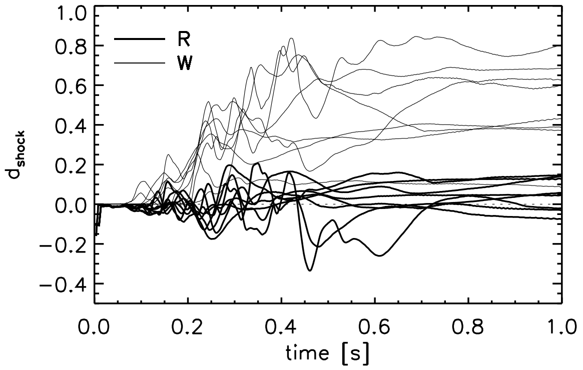

Figure 3.19: Evolution of the shock deformation parameter d_{shock} (see Eq. 3.23) for the rotating (R-series) and the non-rotating models (W-series). Positive and negative values of d_{shock} characterise oblate and prolate deformation of the shock, respectively.

Both Models show a very similar evolution during the first 75 ms because the Solberg-term, $\mathcal{C}_{\mathrm{S}}$, is negligible in this phase. The total angular momentum and the derivative of j_z in the postshock region are initially rather small (see Fig. 3.15). However, the influence of the Solberg term increases with time because there is a positive gradient of j_z upstream of the shock, and matter with increasingly large specific angular momentum is advected into the postshock region. Therefore the positive derivative of this quantity with x grows within the postshock flow (Figs. 3.15 and 3.17).

For $t > 75$ ms this causes the Solberg term to become sufficiently large so that it affects the pattern of convection. The latter exhibits differences now compared to the non-rotating case. All the rotating models develop downflows at both poles, whereas there is no preference for the formation of polar downflows in the non-rotating models (see Fig. 3.16). These polar downflows remain stable until they are blown away from the vicinity of the neutron star by the neutrino-driven wind (Fig. 3.16). The stabilisation is caused by the positive x-derivative of j_z^2 in the Solberg term, which is amplified by the factor $1/x^3$ near the axis of rotation. Given a positive derivative of j_z^2, a matter element pushed towards the axis feels a larger centrifugal acceleration $a_c = j_z^2/x^3$ than the surrounding matter, and therefore moves back to its original position. Analogously, a fluid element pushed away from the axis feels a restoring force as well. Thus, perturbations perpendicular to the axis are suppressed and perturbations of a gas configuration in rotational equilibrium can only grow parallel to the axis of rotation.

For $t > 75$ ms this stabilising effect of the positive angular momentum derivative becomes sufficiently large to suppress convection near the axis of rotation, i.e. to make $\mathcal{C}_{\mathrm{H}} = \mathcal{C}_{\mathrm{S}} + \mathcal{C}_{\mathrm{L}} > 0$ there. In the rest of the postshock flow the Solberg term is negligible (because of its dependence on x^{-3}) compared to the Ledoux term (i.e. $|\mathcal{C}_{\mathrm{S}}| \ll |\mathcal{C}_{\mathrm{L}}|$) and convection is not affected much. Radial profiles of $\mathcal{C}_{\mathrm{S}}$ and $\mathcal{C}_{\mathrm{L}}$ illustrating this situation are shown in Fig. 3.18.

The fact that only polar downflows and no polar outflows form can also be easily explained. Material inside a polar downflow always consists of the lowest j_z-gas which is advected through the shock (see Fig. 3.17). This guarantees a stable situation because the angular momentum derivative with x remains positive. In contrast, a polar outflow, i.e. a rising polar bubble, would contain postshock matter that would be rather well mixed, because a convective plume encompasses matter from a larger range of latitudes. Therefore such a polar bubble would not consist of gas with a lower j_z than the infalling material near the poles that surrounds such a bubble. This situation would therefore be unstable due to the absence of a positive derivative $\mathrm{d}{j_z}^2/\mathrm{d}x$.

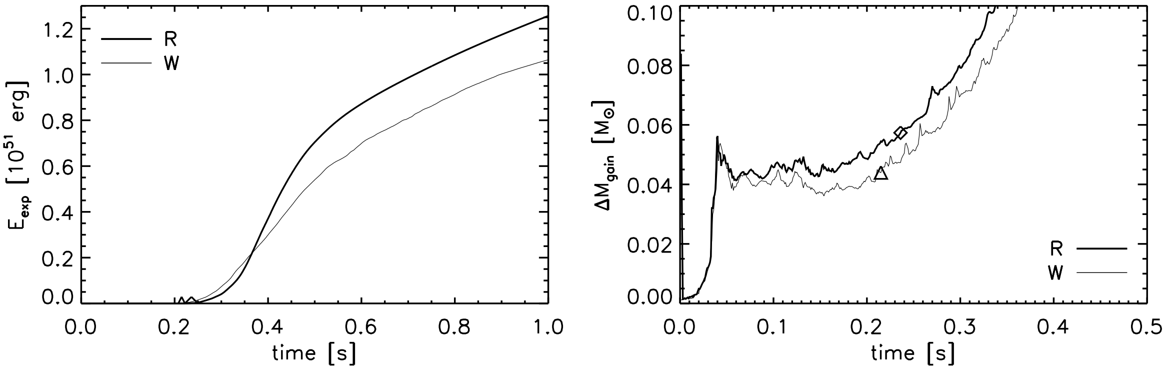

Figure 3.20: Evolution of the explosion energy and of the mass in the gain layer for Models R18-c and W18-c. The symbols mark the onset of the explosion at $t = t_{\mathrm{exp}}$. The rotating model attains an explosion energy which is higher by 0.2×10^{51} erg than in the non-rotating model due to a mass in the gain layer that is larger by $0.013\,M_\odot$.

Besides the differences in the pattern of convection another morphological difference becomes evident: The rotating models remain more spherical, whereas the non-rotating models in general develop a clear prolate deformation (Fig. 3.19). This is partly due to the polar downflows, which damp the shock expansion near the poles. A second reason is the centrifugal acceleration of the matter between neutron star and shock. Owing to the accumulation of angular momentum behind the shock, the initially weak centrifugal forces increase, and their radial components reach up to 20% of the gravitational acceleration. Consequently the shock is pushed out farther in the equatorial region than in the non-rotating models. This has interesting consequences for the explosion energy.

3.4.3 Energetics

In both rotating Models R12-c and R18-c the explosion energies are higher and the neutron star masses are correspondingly lower than in the non-rotating counterparts of these models (Table 3.5). In case of models R18-c and W18-c the energy difference amounts to $\sim$ 20% (i.e. 0.2×10^{51} erg) and must be caused by rotational effects. This difference builds up when the expanding and cooling neutrino-heated matter in the gain layer recombines from free nucleons to alpha particles (and partly to nuclei) and remains approximately constant in the subsequent phase, in which the explosion energy increases further due to the neutrino-driven wind (see Fig. 3.20 and Appendix B). It is caused by the larger equatorial shock radius in the rotating model R18-c and the thus wider gain layer, which increases the recombining mass by $0.013\,M_\odot$ compared to the non-rotating case.

3.4.4 Neutron star recoil

What are the implications of the morphological differences between rotating and non-rotating models for the neutron star kicks? In the non-rotating case we found that the highest recoil was obtained for Model B18-3, in which a pronounced $l = 1$ mode with a single polar downflow is present. In the rotating case such a flow pattern cannot establish, since we always obtain downflows at both poles. However, significant asymmetries can still develop, since one of the polar accretion funnels may be much stronger than the other, or a third downflow may be dominating the mass distribution. High neutron star recoils are thus not precluded, although

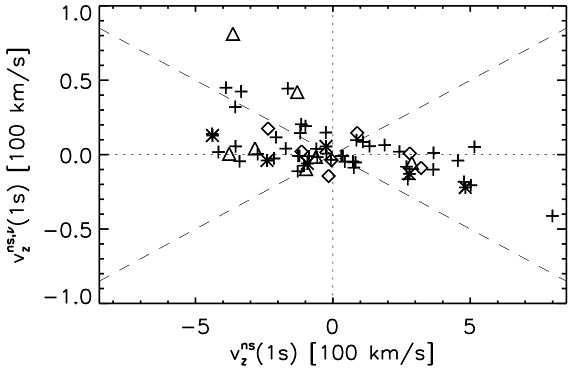

Figure 3.21: Estimated velocity correction due to anisotropic neutrino emission, $v_z^{\mathrm{ns},\nu}$, as a function of the neutron star velocity v_z^{ns} caused by the anisotropies in the gas ejecta. The dashed lines correspond to a ratio $|v_z^{\mathrm{ns},\nu}/v_z^{\mathrm{ns}}|$ of 10%.

we expect the mean and the maximum kicks to be somewhat smaller than in the non-rotating case.

The results of our rather few simulations, which comprise only nine rotating models (see Tables 3.2 and 3.5), are in agreement with this expectation: The largest neutron star recoil velocity obtained in the R-series of models is 321 km/s, whereas it is 640 km/s in case of the W-series (see Model W18-c in Table 3.5). The average kick velocities for the R- and W-type models are 151 km/s, and 280 km/s, respectively. If one omits Model W18-c, the only W-type model with a "pure $l = 1$ mode", the average kick velocity of the non-rotating models decreases to only 228 km/s, i.e. it is 50% larger than that of the rotating models. This is a relatively moderate effect if one recalls that the initial angular velocity assumed in the progenitor core of our calculations is clearly extreme compared to the rotation rates obtained from the latest stellar evolution calculations (Heger et al. 2004). Furthermore, for a more rapid contraction — a parameter we have kept constant in this section — higher kick velocities can be expected (this will be discussed in Sect. 3.5.3) and a model with rapid contraction that will be presented in Sect. 5.3 reaches a velocity of more than 450 km/s already at $t = 0.7$ s.

3.5 Robustness and long-time evolution of the neutron star recoils

We have seen above that rotation, even when it is noticeably faster than in the most recent stellar evolution models, does not preclude neutron star kicks of several hundred km/s. However, we have made a number of approximations in our post-processing analysis and used assumptions in our simulations whose impact on the neutron star recoil still needs to be assessed. In addition, we have stopped most of our simulations at a time of one second after core bounce, when the neutron star acceleration was, in many cases, still high. Hence we need to comment also on the later evolution of the kicks. These issues are discussed in the following.

3.5.1 Anisotropic neutrino emission

The neutron star recoil velocities, v_z^{ns}, that are listed in Tables 3.1–3.3 are computed from Eq. (3.12), i.e. they do not include the effects of anisotropic neutrino emission. As we have shown in Sect. 3.1.3, anisotropic neutrino emission results in a correction, $v_z^{\mathrm{ns},\nu}$, of the neutron star velocity which is described by Eqs. (3.19) and (3.21). In Sect. 3.2 we have already seen

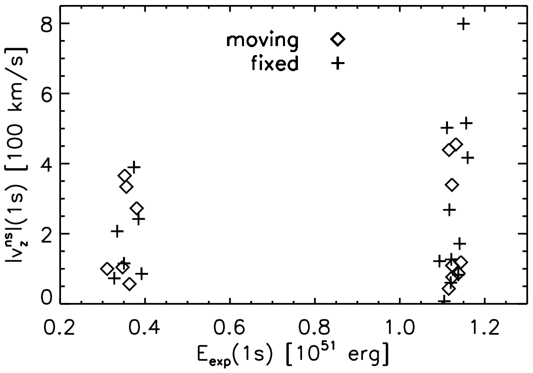

Figure 3.22: Neutron star velocity as a function of the explosion energy for simulations with "fixed" (i.e. infinite inertial mass) and "moving" (i.e. finite inertial mass) neutron stars. All models of the left/right group have the same boundary luminosity as Model B12/B18, respectively.

that this correction is small for Models B12 and B18. In Fig. 3.21 we now display $v_z^{\mathrm{ns},\nu}$ as a function of the neutron star velocity v_z^{ns} for all models of Tables 3.1–3.3. It is obvious that for most models $v_z^{\mathrm{ns},\nu}$ is only a small fraction of the velocity which the neutron star obtains due to anisotropies in the gas ejecta. Only in some cases is $|v_z^{\mathrm{ns},\nu}/v_z^{\mathrm{ns}}| > 10\%$, and in most of these cases the neutron stars have small recoil velocities. Note that the correction due to anisotropic neutrino emission in general reduces the kick. This can be understood from the fact that in most models a single prominent accretion funnel is present. The neutron star recoil caused by gas anisotropies is always directed towards this downflow, while the neutrino emission associated with the "hot-spot" created by the downflow on the neutron star surface results in a "neutrino-rocket engine" that kicks the neutron star in the opposite direction.

3.5.2 Inertial mass of the neutron star

In most of our simulations we make the simplifying assumption that the inertial mass of the neutron star is infinite, i.e. the consequences of the neutron star motion are ignored during the hydrodynamic simulation. This assumption is dropped in one set of models which is listed in Table 3.3. In these simulations the feedback effect of the neutron star motion is taken into account by changing the frame of reference in every time step, thus allowing the ejecta to move relative to the neutron star instead of following the neutron star motion through the ambient gas (see Sects. 2.3 and 3.1.3 and Appendix C).

In Fig. 3.22 results obtained from this approach are compared with corresponding simulations in which the neutron star is assumed to have infinite inertial mass. The neutron star velocities are displayed versus explosion energies for a bunch of low-energy and a number of high-energy models computed with the boundary parameters of Models B12 and B18, respectively. Each group contains simulations with and without "neutron star motion" (labelled as "moving" and "fixed", respectively, in Fig. 3.22). The distribution of data points is very similar for both sets of simulations in both the high- and low-energy groups. A single model with $v_z^{\mathrm{ns}} \approx 800\,\mathrm{km/s}$ sticks out, but represents the rather rare cases where neutron star velocities higher than about 500 km/s are reached after one second. Usually a larger set of computations is needed to get statistically significant results for these extreme velocities.

Table 3.6: Important parameters of models W12-c and W12F-c.

Model	L_{ib} [B/s]	E_{exp} [B]	t_{exp} [s]	M_{ns} [$M_\odot$]	v_z^{ns} [km/s]	$v_z^{\text{ns},\nu}$ [km/s]	a_z^{ns} [km/s^2]	α_{gas}	d_{shock}
W12-c	29.7	0.40	0.301	1.535	44.4	54.0	85.4	0.03	0.63
W12F-c	29.7	0.94	0.118	1.411	611.7	-1.9	580.6	0.21	0.31

3.5.3 Neutron star contraction and gravitational potential

For practical reasons, all simulations listed in Tables 3.1–3.3 and Table 3.5 were performed with our “standard” prescription for the contraction of the neutron star core (see Sect. 2.4.1), although the “rapid contraction case” also discussed in Sect. 2.4.1 might be more realistic. To study the corresponding differences, we take the “high-perturbation”, non-rotating Model W12-c (see Sect. 3.4 and Table 3.5) as a reference case and perform an additional simulation, Model W12F-c, in which we replace the slowly contracting inner boundary of Model W12-c with the prescription for a rapidly contracting proto-neutron star. Table 3.6 compares some quantities characterising the two models.

Model W12F-c explodes earlier and attains a higher explosion energy than Model W12-c. This can be explained by the facts that for a smaller inner boundary radius more gravitational energy is released, and that for a shorter contraction time scale this release occurs earlier (see also Appendix B). With $v_z^{\text{ns}}(1\,\text{s}) = 611\,\text{km/s}$ the neutron star recoil velocity of Model W12F-c is very high. Large kicks are also found in a set of simulations performed with rapid boundary contraction in combination with

1. smaller initial random velocity perturbations of 0.1% (Model W12F in Fig. 3.23),
2. a Newtonian gravitational potential and a constant central point mass chosen such that the same initial gravitational acceleration is obtained at a mass coordinate of 1.1 $M_\odot$ as in the models of Buras et al. (2003), see Models W12F-n0, W12F-n1 and W12F-n2 in Fig. 3.23,
3. a Newtonian gravitational potential and a varying central point mass, which is increased with time to reproduce the evolution of the gravitational acceleration at a mass coordinate of 1.1 $M_\odot$ in the models of Buras et al. (2003), see Models W12F-nv, W12F-nv1 and W12F-nv2 in Fig. 3.23.

All of these models have in common that they explode more quickly than models with the standard boundary contraction. Yet, for all of these variations we obtain at least one simulation with a neutron star recoil velocity of more than 400 km/s at $t = 1\,\text{s}$ (see Fig. 3.23). This demonstrates that a faster neutron star contraction does not preclude high neutron star kicks and in particular it shows that it is *not the absolute value of the time scale* for the onset of the explosion which matters. What matters is the time delay until the start of rapid expansion *relative* to the growth time scale of low-mode anisotropies by hydrodynamic instabilities like convection, the acoustic-vortex cycle or the SASI mechanism. With the faster shrinking of the neutron star not only the explosion time scale decreases, but also other important conditions change, e.g. the neutrino luminosities and ν-heating become larger, the advection time scale in the postshock layer shorter and the sound speed between shock and neutron star higher. These changes affect the growth of instabilities strongly, which will be discussed in detail in Chapter 4.

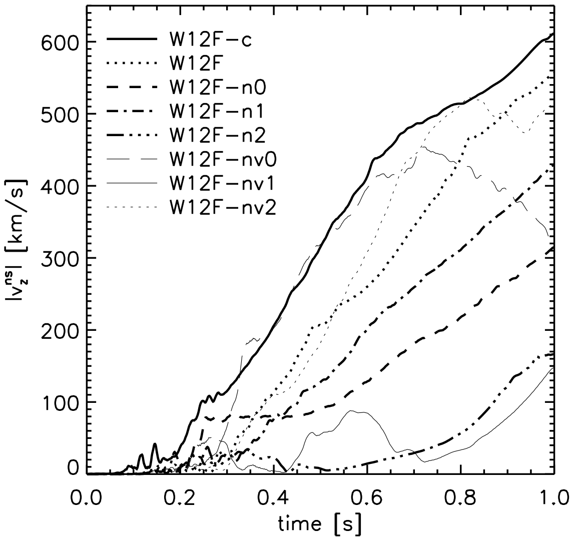

Figure 3.23: Neutron star velocities (absolute values) as functions of time for Models W12F-c, W12F and several other models with fast neutron star contraction. In six out of eight models the neutron star moves faster than 300 km/s at $t = 1$ s.

In fact, there are indications that a faster contraction of the nascent neutron star favours higher values for the average recoil velocity. In our largest sample of models sharing the same (slowly contracting) boundary condition, i.e. the 18 B18-like models listed in Tables 3.1 and 3.3, only three simulations develop neutron star recoil velocities of more than 500 km/s, and only seven produce neutron stars with more than 300 km/s at 1 second. In contrast, in just eight simulations with rapid boundary contraction we obtain six models with neutron star velocities of more than 300 km/s and three models with neutron stars moving faster than 500 km/s (Fig. 3.23). Better statistics would require more simulations, which should also be based on the same initial model[1] and should make use of the same gravitational potential.

We performed some of the simulations discussed above with Newtonian gravity to demonstrate that the choice of the effective relativistic potential in our models was not essential for our results. We recall that only when we use the Newtonian gravitational potential, momentum is strictly conserved in our simulations (also when the point mass is increased with time). The results therefore show that large neutron star recoil velocities are *not* linked to any violation of total momentum conservation associated with the use of the effective relativistic potential (see the discussion in Sect. 3.2.2).

3.5.4 Long-time evolution of the neutron star kicks

In order to investigate how the neutron star recoil velocities evolve beyond a time of one second after core bounce, we perform six exemplary long-time simulations. For these we add 150 radial zones to our grid and place the outer grid boundary at a larger radius of 10^{10} cm, which allows us to simulate the first 3–4 s of the post-bounce evolution. In three of the simulations an infinite inertial neutron star mass is assumed, while in the other models the hydrodynamic feedback of the neutron star motion is taken into account. Four of the six models are just continued from models which we have computed up to a time of one second with our standard grid. We map the corresponding data onto the larger grid at $t = 750\,\mathrm{ms}$ and extend the initial model profile from the old to the larger outer boundary of the new grid.

---

[1] The comparison between B and W models is viable, however, because both progenitor models are quite similar.

The evolution of the neutron star velocities for all of the long-time simulations is displayed in Fig. 3.24. The neutron star of Model B18-3, which we already discussed as an extreme case in Sect. 3.2.5, is accelerated to more than 1200 km/s within 3.7 s. This demonstrates that the acceleration mechanism at work in our calculations has the potential to explain even the highest observed pulsar velocities (see e.g. Chatterjee et al. 2005). The fact that Model B18-3 is the only one in our sample that produces a neutron star with more than 1000 km/s does not appear problematic to us. It may be a matter of low-number statistics and might also change when more extreme conditions are realized in models, e.g. by a faster contraction of the neutron star than assumed in our standard set of models. In this respect the sample of simulations plotted in Fig. 3.23 looks promising. In quite a number of those the neutron stars have large velocities at one second and also still high accelerations (see, e.g., Model W12F-c in Table 3.6).

After 3–4 s the neutrino-driven wind has blown away all downflows from the neutron star vicinity and has generated a nearly spherically symmetric wind bubble around it. Therefore the neutron star acceleration diminishes and the recoil velocities approach their terminal values. The latter can be estimated by extrapolating the velocities at $t = 1\,\mathrm{s}$, applying an average acceleration value $\langle a_z^{\mathrm{ns}} \rangle$, as computed for the time interval between $t = 0.5\,\mathrm{s}$ and 1 s, over a time period $\Delta t_{\mathrm{extrapol}}$, according to

$$v_{\mathrm{ns}}^{\infty} = v_z^{\mathrm{ns}}(t = 1\,\mathrm{s}) + \Delta t_{\mathrm{extrapol}} \times \langle a_z^{\mathrm{ns}} \rangle. \tag{3.29}$$

The average acceleration $\langle a_z^{\mathrm{ns}} \rangle$ is introduced as a time-average which is less sensitive to short-time variations of the neutron star acceleration and thus allows for a more robust extrapolation of the velocities. The factor $\Delta t_{\mathrm{extrapol}} = 0.35\,\mathrm{s}$ is “calibrated” by optimising the estimates in case of the models of Fig. 3.24. The agreement of extrapolated and computed terminal velocities is typically of the order of 10%. In the following section we use Eq. (3.29) to estimate the final neutron star velocities for all models listed in Tables 3.1–3.3. The basic findings of our analysis do not depend on whether we use a_z^{ns} (the acceleration values at the end of our simulations) or $\langle a_z^{\mathrm{ns}} \rangle$ (the mean values in the last 0.5 s) for extrapolating the velocities beyond the simulated period of one second of evolution.

3.6 Implications for the neutron star velocity distribution

In Sect. 3.3 we mentioned that Fig. 3.14, showing the neutron star velocities and accelerations at $t = 1\,\mathrm{s}$, suggests the existence of two groups of models. One group consists of cases with low velocities and on average low acceleration, and the other group cases with high velocities and significantly higher average acceleration. The latter models are typically characterised by a strong $l = 1$ mode in the flow pattern at the end of our simulations.

Provided the acceleration shows a trend of increasing more steeply than linearly with the neutron star velocity, one can expect a growth of the separation of both populations when the acceleration continues over a longer period of time. Thus a bimodal velocity distribution will emerge, caused by the larger acceleration associated with the presence of a dominant $l = 1$ mode in the models of the high-velocity group. To test this possibility, we extrapolate the neutron star motions of all of our 70 models listed in Tables 3.1–3.3 from one second to the expected final conditions by applying Eq. (3.29). Figure 3.25 displays both the velocity distribution at the end of the simulated evolution (at $t = 1\,\mathrm{s}$; left panel) and the terminal distribution (right panel).

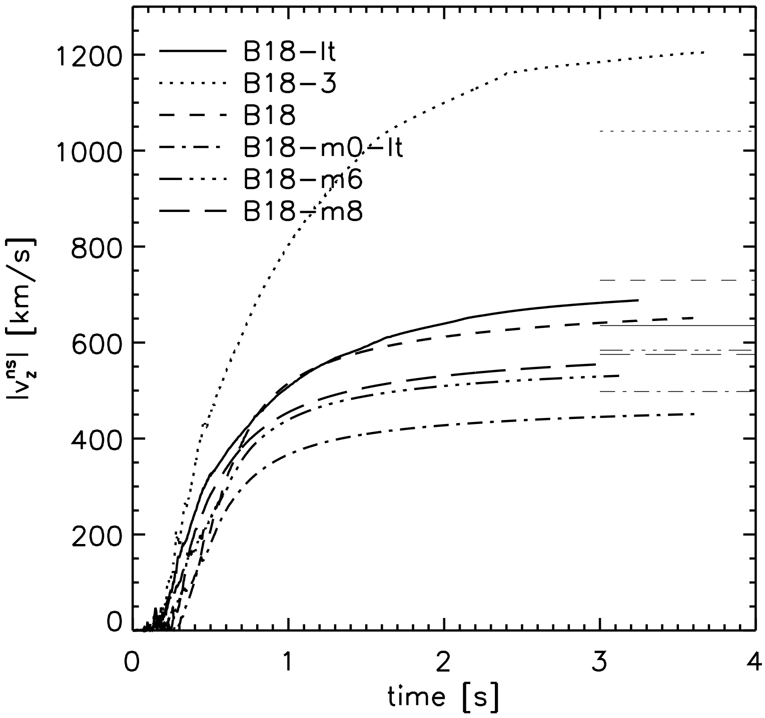

Figure 3.24: Evolution of the neutron star velocities in six long-time simulations with the same boundary conditions as Model B18. After four seconds the acceleration has become very weak in all models and no significant further increase of the velocities is expected. For each model a thin horizontal line marks the extrapolated velocity value $v_{\rm ns}^{\infty}$ according to Eq. (3.29), which is a rough estimate of the final neutron star velocity.

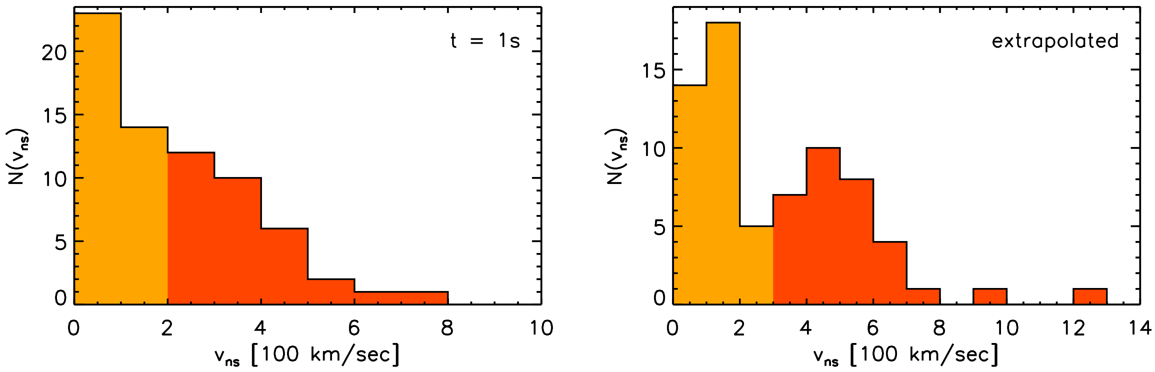

Figure 3.25: Histograms of the neutron star velocity distribution for the 70 models of Tables 3.1–3.3. The left panel shows the velocity distribution at $t = 1\,$s (solid black line). The darker shaded area corresponds to the fraction of models whose neutron stars are moving with more than 200 km/s one second after bounce. The same models are displayed with dark shading also in the right panel, which shows the final velocity distribution as obtained by extrapolation with Eq. (3.29).

A comparison of the panels in Fig. 3.25 shows that most neutron stars of the high-velocity and high-acceleration group (which is indicated by the darker shading) accelerate to significantly higher velocities on time scales longer than one second. In contrast, only very few stars of the low-velocity group reach velocities in excess of 200 km/s. As a consequence, a minimum develops in the extrapolated distribution around 300 km/s, separating clearly the two components in velocity space.

We interpret this result as an interesting demonstration that the kick mechanism discussed here is able to produce a bimodal distribution of neutron star velocities simply due to the presence or absence of a dominant $l = 1$ mode in the spatial distribution of the supernova ejecta. Invoking two different processes for neutron star acceleration is not required. It is, however, unclear whether this may provide an explanation of a possible bimodality in the observed velocity distribution of pulsars. The existence of such a bimodality is not only ambiguous, some authors finding hints (e.g. Cordes & Chernoff 1998; Fryer et al. 1998; Arzoumanian et al. 2002; Brisken et al. 2003), while others favour a one-component Maxwellian distribution (e.g. Lyne & Lorimer 1994; Hansen & Phinney 1997; Hobbs et al. 2005; Zou et al. 2005). Also the parameters for the two-component fits differ significantly between the publications.

Though our result is inspiring as well as tantalising, we refrain from making a direct connection with observations. Such attempts are hampered by the limitations of our analysis, which does not only assume the extrapolation of Eq. (3.29) to be valid for all cases. Our analysis is also affected by our finding that the magnitude of the neutron star kicks seems to depend on the neutron star contraction (see Sect. 3.5.3) that is mimicked in our simulations by a moving inner boundary of the computational grid. Moreover, our analysis is constrained to a set of $15\,M_\odot$ stars[2], while linking theory with observations would require modelling explosions for a representative distribution of supernova progenitors, making reasonable assumptions about the progenitor dependence of the explosion energy and including the effects from binary breakup. A large set of calculations would have to account for the stochastic nature of the discussed neutron star acceleration mechanism, thus establishing the distribution of kick velocities as a function of the progenitor properties. One might have the concern that in the combined data of all of these runs the minimum visible in the velocity distribution of Fig. 3.25 is filled up. Finally, quantitatively meaningful calculations of neutron star kicks will ultimately have to be obtained by three-dimensional modelling.

---

[2] The employed progenitor models, however, exhibit large differences in core sizes and core density profiles, which actually may be considered as reflecting the variations over a broader range progenitor masses.

4

The origin of the global anisotropy

The simulations that we have presented in the last chapter developed pronounced global modes and neutron stars moving with high recoil velocities. These promising results seem to be in agreement with observations concerning the anisotropy of core collapse supernova and the measured neutron star kick velocities. What is still missing, however, is a better understanding of the origin of the global anisotropy.

As we mentioned already in Chapter 1, it is unlikely that convection alone can explain that low modes dominate our models. Non-radial, non-convective instabilities like the "advective-acoustic cycle" (Galletti & Foglizzo 2005; Foglizzo et al. 2006a) may play an important role and have already been observed in simulations: Blondin & Mezzacappa (2006) and Ohnishi et al. (2006) demonstrated that there is a non-radial instability in the flow below a standing accretion shock, even if neutrinos (which could have a damping influence) are taken into account. Yet, because of strong simplifications, theses simulations are not able to assess the importance of the instability for supernova explosions. In these simulations boundary and initial conditions were taken from a stationary solution, which means that the growth rate of the hydrodynamic instability (that depends solely on the properties of the flow) is constant and determined by the initial conditions (as long as non-linear effects can be neglected). In real supernovae, however, the flow changes continuously, because the shock adapts to the varying mass accretion rate, the neutrino heating below the shock changes, and the proto-neutron star contracts. Therefore the growth rate also varies, and a priori it is not clear, whether it will be sufficiently high for a sufficiently long time to allow a growth of the instability into the non-linear phase on a time scale comparable to the explosion time scale (which is, of course, a priori also unknown).

Our aim is therefore to go one step further in the direction of realism and abandon the assumption of stationarity. Yet, as we are using the same numerical setup as for the simulations of Chapter 3, our simulations must still be regarded as simplified compared to state-of-the-art supernova simulations with a detailed description of the neutrino transport (Rampp & Janka 2002; Liebendörfer et al. 2001; Liebendörfer et al. 2005; Thompson et al. 2003; Buras et al. 2003, 2006a,b). This approximative, parametric approach appears to be justified, because we do not aim at demonstrating the viability of the neutrino-driven mechanism, but just want to study the evolution of instabilities in a plausible scenario. In particular we will address the following questions:

- Is a non-radial instability of the accretion shock able to develop in a “real” supernova core on time scales comparable to the explosion time scale? How is this influenced by neutrino effects?
- Can this instability be identified as an amplifying advective-acoustic cycle, a growing standing pressure wave (Blondin & Mezzacappa 2006) or something else?
- What determines the growth rate? Is it possible that the instability grows faster than convection and which influence will this have on the subsequent evolution?
- What is the relationship between convection and the instability in the non-linear phase?
- What is the influence of the instability on the explosion energetics and the neutron star recoil?

We proceed by summarising the most important properties of convection in the gain layer and the advective-acoustic cycle in Sect. 4.1. In Sect. 4.2, we present eight two-dimensional simulations that address the questions listed above. Then we discuss these results in detail, the linear phase in Sect. 4.3 and the non-linear phase in Sect. 4.4.

4.1 Hydrodynamic instabilities

4.1.1 Linear and non-linear convective growth of perturbations

In a hydrostatic atmosphere, regions with negative entropy gradients are convectively unstable for all wavelengths. Short wavelength perturbations grow fastest, with a local growth rate equal to the Brunt-Väisäla frequency

$$\omega_{\mathrm{buoy}} \equiv \sqrt{-a_{\mathrm{grav}}\,\mathcal{C}\,/\,\rho}. \tag{4.1}$$

Here a_{grav} is the local gravitational acceleration, ρ is the density and

$$\mathcal{C} \equiv \left(\frac{\partial\rho}{\partial S}\right)_{P,Y_l} \cdot \frac{\mathrm{d}S}{\mathrm{d}r}. \tag{4.2}$$

Note that $\mathcal{C} < 0$ is the instability condition for Schwarzschild convection.

Foglizzo et al. (2006b) noticed that in the stalled shock phase, the convective growth time scale $\omega_{\mathrm{buoy}}^{-1}$ in the unstable layer below the shock is of the same order as the time scale for advection from the shock to the gain radius,

$$\tau_{\mathrm{adv}}^{\mathrm{g}} \equiv \int_{R_{\mathrm{g}}}^{R_{\mathrm{s}}} \frac{\mathrm{d}r}{|v_r(r)|}, \tag{4.3}$$

where R_{g} is the gain radius, R_{s} the shock radius and v_r the radial velocity. Advection is stabilising because it gives perturbations only a finite time to grow, before they are advected into the stable layer below the gain radius. Considering only local instability (see below), the amplitude δ of a small-wavelength perturbation may grow during the advection from the shock to the gain radius, at best by a factor $\exp(\chi)$,

$$\delta_{\mathrm{gain}} = \delta_{\mathrm{shock}}\, \exp(\chi), \tag{4.4}$$

where the quantity

$$\chi \equiv \int_{R_\mathrm{g}}^{R_\mathrm{s}} \omega_\mathrm{buoy}(r) \, \frac{\mathrm{d}r}{|v_r(r)|} = \tau_\mathrm{adv}^\mathrm{g} / \tau_\mathrm{conv} \tag{4.5}$$

can be interpreted as the ratio between the advection time scale and the average local growth time scale the perturbation experiences, $\tau_\mathrm{conv} \equiv \langle \omega_\mathrm{buoy}^{-1} \rangle$ (the latter quantity is implicitly defined by Eq. 4.5). Thus it would appear that in order to reach a given perturbation amplitude at the gain radius, a certain seed perturbation amplitude of the matter crossing the shock would be necessary.

However, in their linear stability analysis of the stationary flow below the shock, Foglizzo et al. (2006b) found that a *global* instability can occur in the gain layer and grow from *arbitrarily* small seed perturbation amplitudes, if sufficient time is available. According to Foglizzo et al. (2006b) this instability occurs for a limited range $[l_\mathrm{min}, l_\mathrm{max}]$ of modes, when χ exceeds a critical value χ_0,

$$\chi > \chi_0 \quad \text{where} \quad \chi_0 \approx 3. \tag{4.6}$$

For $\chi < \chi_0$ the flow remains linearly stable, even though a negative entropy gradient is present.

The analysis of Foglizzo et al. (2006b) applies only for the linear phase of the instability, i.e. for small perturbation amplitudes. However, it is possible that the situation has to be regarded non-linear right from the beginning, i.e. that already the seed perturbations grow to large amplitudes during the advection to the gain radius. In this context "large" can be defined by considering the buoyant acceleration of the perturbations.

For a small bubble, in which the density ρ is lower than the one of the surrounding medium, ρ_surr, the convective growth during the advection to the gain radius may lead to an increase of the relative density deviation $\delta \equiv |\rho - \rho_\mathrm{surr}|/\rho_\mathrm{surr}$ (which can be considered as the perturbation amplitude) as given by Eq. (4.4). The bubble experiences a buoyant acceleration $|a_\mathrm{grav}|\,\delta$ towards the shock, which is proportional to the local gravitational acceleration a_grav. The time integral of the buoyant acceleration becomes comparable to the advection velocity, when the perturbation amplitude reaches a critical value

$$\delta_\mathrm{crit} \equiv \frac{\langle |v_r| \rangle_\mathrm{gain}}{\langle a_\mathrm{grav} \rangle_\mathrm{gain} \, \tau_\mathrm{adv}^\mathrm{g}} \approx \frac{\langle |v_r| \rangle_\mathrm{gain}^2}{R_\mathrm{s} \, \langle a_\mathrm{grav} \rangle_\mathrm{gain}} \, \frac{R_\mathrm{s}}{R_\mathrm{g} - R_\mathrm{s}} \approx \mathcal{O}(1\%), \tag{4.7}$$

where $\langle |v_r| \rangle_\mathrm{gain}$ and $\langle a_\mathrm{grav} \rangle_\mathrm{gain}$ are the average values of the radial velocity and the gravitational acceleration in the gain layer, respectively. For $\delta_\mathrm{gain} > \delta_\mathrm{crit}$ a small-scale perturbation is able to rise against the accretion flow. If the full flow is perturbed, the buoyant motions on small scales affect the situation globally and could allow for the onset of a convective overturn also on larger scales. Note that in contrast to the linear growth of the instability this process does not require $\chi > \chi_0$, but it does require sufficiently large seed perturbations,

$$\delta_\mathrm{shock} > \delta_\mathrm{crit} \, / \, \exp(\chi). \tag{4.8}$$

A sufficient condition for the suppression of convection is therefore that neither Eq. (4.6) nor Eq. (4.8) are fulfilled.

4.1.2 The advective-acoustic cycle

A second hydrodynamic instability has recently been recognised to be of potential importance in the stalled shock phase. The so-called "advective-acoustic cycle" (in short AAC) was first

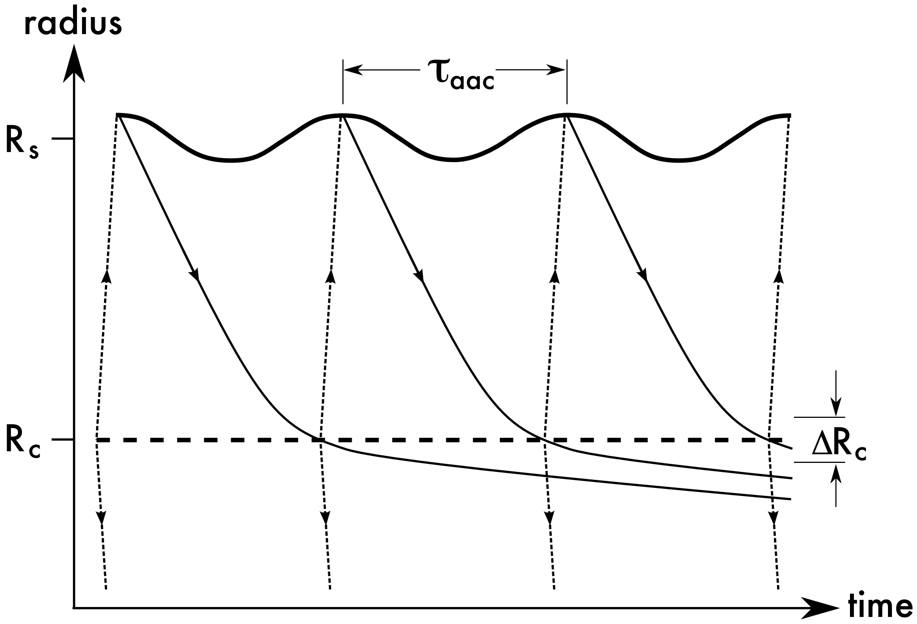

Figure 4.1: Schematic view of the advective-acoustic cycle between the shock at R_s (thick solid line) and the coupling radius, R_c (thick dashed line), in the linear regime. Flow lines carrying vorticity perturbations downwards are drawn as solid lines, and the pressure feedback corresponds to dotted lines with arrows. In the gray shaded area around R_c the flow is decelerated strongly.

discussed by Foglizzo & Tagger (2000) in the context of accretion onto black holes, and later studied for supernovae by Galletti & Foglizzo (2005) and Foglizzo et al. (2006a), who performed a linear stability analysis. The explanation for these oscillations is based on the linear coupling between advected and acoustic perturbations, due to flow gradients.

Although this linear coupling occurs continuously throughout the accretion flow from the shock to the neutron star surface, some regions may contribute more than others to produce a pressure feedback towards the shock and establish a global feedback loop. The analysis of the linear phase of the instability in Sect. 4.3 reveals the importance of a small region at a radius R_c above the neutron star surface, where the flow is strongly decelerated. The feedback loop can be described schematically as follows (see Fig. 4.1): small perturbations of the supernova shock cause entropy and vorticity fluctuations, which are advected downwards. When the flow is decelerated and compressed above the neutron star surface, the advected perturbations trigger a pressure feedback, which hits the shock, causing new vorticity and entropy perturbations. Instability corresponds to the amplification of perturbations by a factor $|Q_\mathrm{aac}| > 1$ through each cycle.

The duration $\tau_\mathrm{aac}^\mathrm{f}$ of each cycle is a fundamental time scale: it corresponds to the the time needed for the advection of vortical perturbations from the shock to the coupling radius R_c, where the pressure feedback is generated, plus the time required by the pressure feedback to travel from this region back to the shock.

The exponential growth resulting from the AAC can be described by a complex eigenfrequency ω satisfying the following equation:

$$\exp(-i\omega\tau_\mathrm{aac}^\mathrm{f}) = Q_\mathrm{aac}, \tag{4.9}$$

where the real part ω_r is the oscillation frequency and the imaginary part ω_i is the growth rate of the AAC. Note that Eq. (4.9) is a simplified form of Eq. (49) of Foglizzo (2002): for the sake of simplicity, it neglects the marginal influence of the purely acoustic cycle of pressure waves trapped between the shock and the accretor.

According to Eq. (4.9), the oscillation period $\tau_{\rm osc} \equiv 2\pi/\omega_r$ of the AAC depends both on the duration $\tau^{\rm f}_{\rm aac}$ of the cycle and on the phase φ of $Q_{\rm aac}$:

$$\omega_r \tau^{\rm f}_{\rm aac} + \varphi = 2k\pi, \tag{4.10}$$

where k is an integer. The fundamental mode of the AAC is thus identical to the duration $\tau^{\rm f}_{\rm aac}$ of the cycle only in the particular case when $Q_{\rm aac}$ is real and positive. However, according to Foglizzo et al. (2006a) $|\varphi|$ is small and therefore $\tau_{\rm osc} \approx \tau^{\rm f}_{\rm aac}$ is a reasonable approximation for the fundamental oscillation period, which we will use in the following.

The amplitude of perturbations in the AAC increases like $\exp(\omega_i\, t)$, with a growth rate ω_i deduced from Eq. (4.9):

$$\omega_i \equiv \frac{\log(|Q_{\rm aac}|)}{\tau^{\rm f}_{\rm aac}}. \tag{4.11}$$

Comparing equations (4.5) and (4.11) it is interesting to note that while the growth of entropy-driven convection is suppressed for small advection time scales, the latter actually leads to higher growth rates for the AAC (neglecting the logarithmic dependence on $Q_{\rm aac}$). Thus the AAC may operate under conditions which are not favourable for convection and vice versa.

4.2 Simulations

In the following we will present a sequence of eight two-dimensional simulations, which are characterised by an increasing degree of realism, concerning the physics we take into account and the boundary conditions we employ. The most simplified case, Model W00FA, does not include neutrinos and serves mainly to demonstrate the effects of a shrinking inner boundary (as opposed to the fixed inner boundary used e.g. in Blondin & Mezzacappa (2006)) and, in comparison with the other models, the influence of neutrino cooling and heating. For five further simulations including neutrino transport, Models W00F, W00, W00S, W05S and W05V we choose boundary conditions such that convection is suppressed, which allows us to identify and study other instabilities like the AAC more easily. For Models W12F and W12F-c, finally, we adopt boundary conditions motivated by state-of-the-art Boltzmann simulations, which leads to typical explosion energies of about 10^{51} erg. Table 4.1 lists some important parameters and results for the models presented below.

4.2.1 A model without neutrinos

Model W00FA is a purely hydrodynamic simulation without neutrinos. This description applies also for the simulations of Blondin et al. (2003), who use an inner boundary at a fixed radius with outflow boundary conditions to allow for a stationary unperturbed flow. In our simulations, however, the inner boundary is an impenetrable Lagrangian mass shell which contracts, mimicking the shrinking of a cooling proto-neutron star. Furthermore unlike in Blondin et al. (2003) also the accretion rate varies, as stellar matter of different composition falls through the shock. Thus the postshock flow is generically non-stationary.

Due to the stalling shock and the neutrino heating up to 16 ms after bounce (i.e. before the start of our simulation) a convectively unstable negative entropy gradient is present in the

Table 4.1: Some important quantities for the models discussed in this section: Boundary luminosity L_{ib}, final inner boundary radius $R^{\mathrm{f}}_{\mathrm{ib}}$, contraction time scale t_{ib}, amplitude of initial perturbations δ_{i}, time at which the average lateral velocity in the gain layer exceeds 10^9 cm/s, t_{nl}, mass in the gain layer ΔM_{gain} at the explosion time t_{exp}, explosion energy E_{exp}, neutron star mass M_{ns} and neutron star velocity v_{ns}. The latter three quantities are given at $t = 1$ s, for model W00F at $t = 750$ ms. Model W00FA does not include neutrinos and does not produce a well-defined neutron star, and only the models W00F, W12F and W12F-c explode. Therefore the related quantities are not specified. The luminosity decay time scale t_L (see Sect. 2.4.2) is set to one second for all models containing neutrinos. We use the unit 1 B = 10^{51} erg and give all times relative to the start of the simulation, i.e. $t = 0\,s$ means 16 ms after core bounce.

Name	L_{ib} [B/s]	$R^{\mathrm{f}}_{\mathrm{ib}}$ [km]	t_{ib} [s]	δ_{i}	t_{nl} [s]	t_{exp} [s]	ΔM_{gain} [$M_\odot$]	E_{exp} [B]	M_{ns} [$M_\odot$]	v_{ns} [km/s]
W00FA	–	8.0	0.5	$10^{-3}\,v_r$	–	–	–	–	–	–
W00F	0.2	8.0	0.5	$10^{-3}\,v_r$	0.154	0.194	0.004	0.37	1.50	200
W00	0.2	15.0	1.0	$10^{-3}\,v_r$	0.346	–	–	–	1.63	-3
W00S	0.2	15.0	4.0	$10^{-3}\,v_r$	–	–	–	–	–	–
W05S	7.4	15.0	4.0	10^6cm/s	–	–	–	–	–	–
W05V	7.4	15.0	10.0	3×10^7cm/s	–	–	–	–	–	–
W12F	29.7	10.5	0.25	$10^{-3}\,v_r$	0.144	0.164	0.010	0.87	1.44	-558
W12F-c	29.7	10.5	0.25	$\mathcal{O}(10^{-2})\,v_r$	0.090	0.117	0.015	0.94	1.41	612

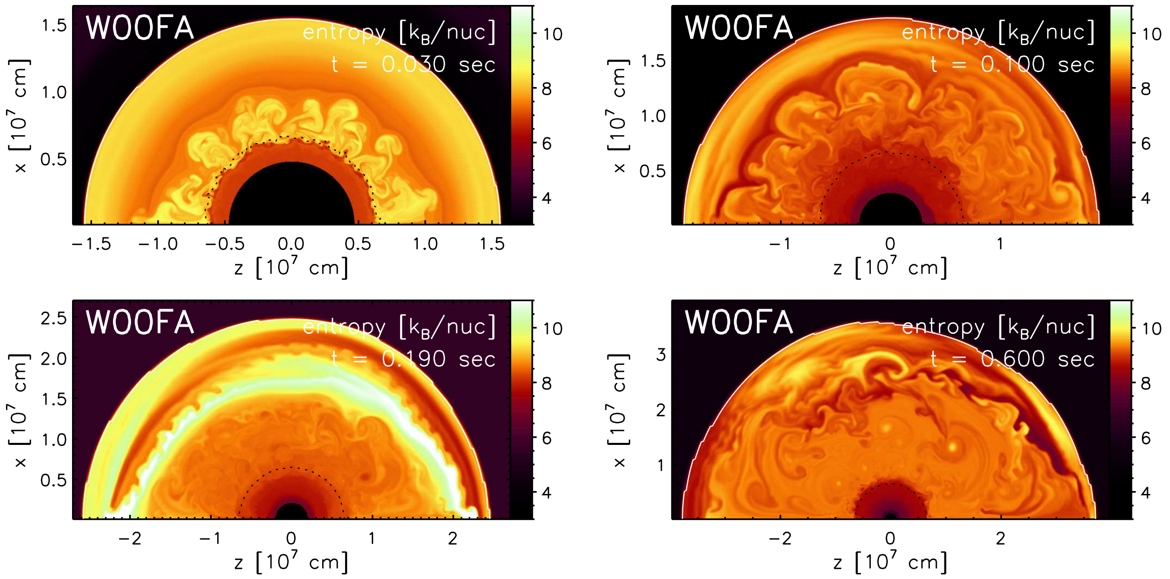

Figure 4.2: Entropy distribution of model W00FA 30 ms and 190 ms after the start of the simulation. The initial entropy profile and the postshock entropy gradients caused by the varying preshock conditions give rise to weak convection. A weak $l = 1$ oscillation develops.

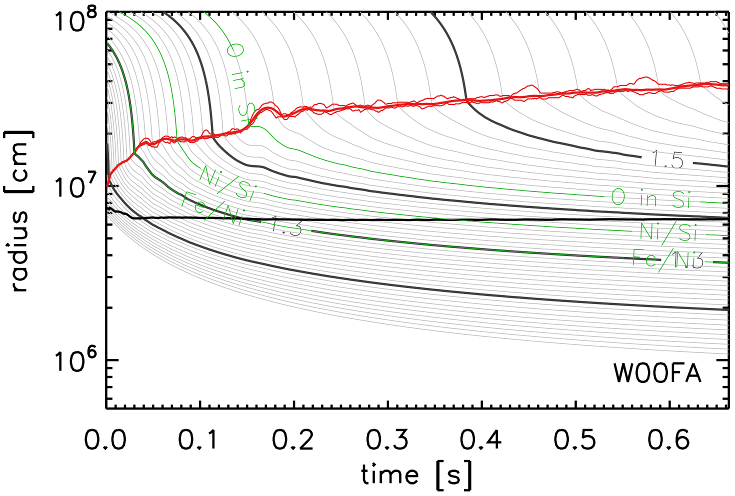

Figure 4.3: Mass shell trajectories for model W00FA. The spacing of the thin lines is $0.1\,M_\odot$. Green lines mark the mass shells at which the composition of the progenitor changes. The red lines are the minimum, average and maximum shock radius, the black line marks the radius, at which the average density is $10^{11}\,\mathrm{g/cm^3}$. The difference between minimum and maximum shock radius are caused by bipolar shock oscillations (see Fig. 4.2).

initial model, around $r \approx 70\,\mathrm{km}$. Soon after the start of the simulation buoyant bubbles form in this region and rise towards the shock (Fig. 4.2). Convection is present throughout the whole simulation, because on the one hand the postshock entropy varies and therefore unstable entropy gradients are newly created all the time and, on the other hand, cooling processes that could dampen the convective motions are absent. However, without neutrino heating the convective overturn does not become as strong and dynamic as in the simulations of Chapter 3 including neutrino transport. The varying postshock entropies are caused by the varying preshock state and the radial motion of the shock (which adapts to changes in the accretion rate), as well as by bipolar shock oscillations (see Sect. 4.4.1). The latter are rather weak (the amplitude does not exceed 15%) and occur semi-periodically on time scales of 20–50 ms (Fig. 4.3).

These multi-dimensional effects do not seem to be important for the model, though, as the evolution of the shock position is almost identical to the one of a one-dimensional simulation with the same parameters. Although the inner boundary is contracting the shock expands slowly but continuously (Fig. 4.3). A temporarily faster expansion occurs at $t \approx 150\,\mathrm{ms}$, when a progenitor composition interface falls through the shock, abruptly lowering the mass accretion rate. After 660 ms we stop the simulation. At this time the shock has reached a radius of 400 km.

Although the shock is expanding slowly, this can by no means be interpreted as an explosion – without neutrino-heating the total energy of the matter below the shock remains negative. The reason for the shock expansion is rather that matter piles up in the postshock region, slowly pushing the shock further out and forming an extended atmosphere around the neutron star. The matter cannot loose entropy (which would require neutrino cooling) and thus is not able to settle down onto the neutron star quickly. Therefore the flow that develops in Model W00FA is quite different from the ones found in detailed supernova simulations or the stationary flows that have been assumed for the simulations of Blondin et al. (2003). The advection velocity remains much lower and the shock radius becomes larger.

On the one hand this demonstrates that once a "realistic" boundary condition (mimicking an shrinking neutron star) is used, also neutrino transport has to be included. On the other hand,

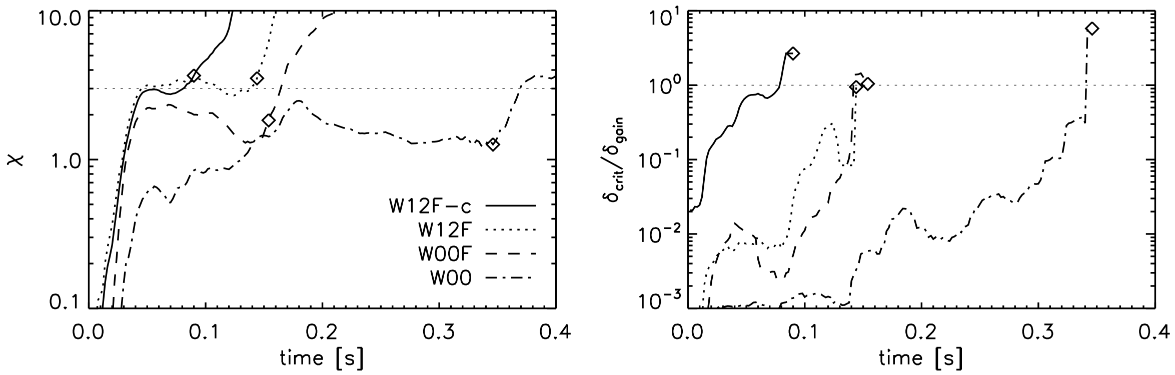

Figure 4.4: Evolution of the quantity χ (left panel, see Eq. 4.5) and the ratio $\delta_{\text{gain}}/\delta_{\text{crit}}$ (right panel, see Eqns. 4.4, 4.7) for Models W12F-c, W12F, W00F and W00. For each model a diamond symbol marks the time t_{nl}, at which the average lateral velocity in the gain layer exceeds 10^9 cm/s. For later times χ and δ_{crit} cannot be measured reliably any more. $\chi \lesssim \chi_0 \approx 3$ for $t < t_{\text{nl}}$ in all models. Only Model W12F-c comes close to $\delta_{\text{gain}}/\delta_{\text{crit}} = 1$ *before* $t = t_{\text{nl}}$, i.e. only in this model convection is able to set in.

it shows that neutrinos are actually required to create the conditions needed for an effective advective-acoustic cycle, for which small advection times from the shock to the neutron star are necessary (see Sec. 4.1.2). Including the effects of neutrino emission, like in the models described below, leads after some time to quasi-stationary flows (because neutrino radiating matter can settle onto the forming neutron star) that are more similar to the ones considered by Blondin et al. (2003) and Ohnishi et al. (2006). Yet, unlike in the latter two works, the quasi-stationary flow is not put in "by hand" (i.e., by prescribing boundary conditions taken from a stationary solution), but establishes during the simulation and varies with time, as it adapts to changes of the accretion rate and the neutron star contraction.

4.2.2 Models with suppressed convection

For the simulations discussed in this section we include neutrino effects. However, in an intermediate step we do not apply boundary conditions motivated by the results of Boltzmann simulations, but instead we choose boundary contraction prescriptions and core luminosities such that convection is suppressed. This will allow us to identify and study non-convective instabilities more easily. Suppressing convection is achieved by prescribing low or negligibly low core luminosities. In these cases essentially only the luminosity produced between the inner boundary and the gain radius is available to deposit energy in the gain layer. Thus the neutrino heating is reduced, which results in a weaker entropy gradient and consequently a larger buoyancy time scale. Therefore for low core luminosities the ratio of advection to buoyancy time scale, χ (see Eq. 4.5), remains below the critical value and convection is stabilised by advection (see Sect. 4.1.1). A second possibility to achieve $\chi < \chi_0$ would be to reduce the advection time scale, e.g. by prescribing a more rapid contraction of the inner boundary, which leads to small shock radii and high (negative) postshock velocities. In addition to the condition $\chi < \chi_0$ also the progenitor perturbations have to be small enough to avoid that convection starts in the non-linear way described in Sect. 4.1.1. Both conditions are fulfilled in our low core luminosity models (see Fig. 4.4).

We performed five simulations, in which convection is suppressed due to the low core luminosities, and which differ in the contraction prescription for the inner boundary. For Models W00 and W00F we use the "standard" and "rapid" contraction prescriptions (see Sect. 2.4.1), respectively.

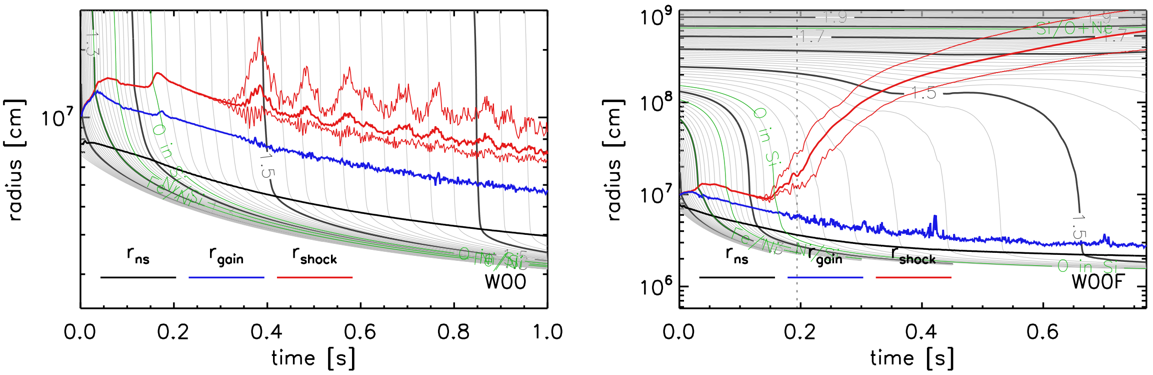

Figure 4.5: As Fig. 4.3, but for Models W00 (left panel) and W00F (right panel). Up to $t \approx 300\,\mathrm{ms}$ model W00 remains nearly spherical and evolves like a one-dimensional model with the same boundary conditions. However, an initially very weak $l = 1$ oscillation mode in the postshock flow grows in this phase and finally becomes non-linear, causing strong shock oscillations. Yet, this model does not explode – although the shock expands transiently in a semi-periodic way, the average shock radius decreases and all matter remains bound. In Model W00F an $l = 2$ mode develops and starts to affect the shock shape at $t \approx 100\,\mathrm{ms}$, much earlier than in model W00. The oscillations become non-linear, and at $t = 194\,\mathrm{ms}$ (marked with a dotted line) the model explodes.

In order to cover a wider range of advection time scales (which will turn out to be decisive for the identification of the low mode instability we observe in our simulations, see Sect. 4.3), we performed three simulations with slower boundary contraction, Models W00S, W05S and W05V (see Tab. 4.1). In the latter two models the boundary luminosity is set to a non-negligible (but still low) value, which leads to larger shock radii and even longer advection times. For Models W00F, W00 and W00S we apply our standard perturbations (0.1% random noise in the velocity). For Models W05S and W05V we use an $l = 1$ velocity perturbation, which allows us to suppress high mode noise and to measure the oscillation period of the low mode instability despite of the low growth rates in these models.

Figure 4.5 gives an overview of the evolution of Models W00 and W00F. In the first 200 ms the evolution of Model W00 is quite similar to models with larger boundary luminosity, like Model W12 from Chapter 3, except that there is no convective overturn. At $t \approx 150\,\mathrm{ms}$ the accretion rate declines steeply, when a composition interface (the one where oxygen appears inside the silicon shell) is falling through the shock. In models with "normal" boundary luminosity (see the W series in Chapter 3), this leads to a shock expansion, enhanced convection and, 50 to 150 ms later, to the onset of the explosion. In model W00, though, the shock expands only temporarily by about 20 km, and contracts continuously in the following 150 ms (Fig. 4.5).

Already several ten milliseconds after the start of the simulation a lateral velocity component (which changes direction with a period of about 30 ms) is observable in the flow between shock and neutron star surface. The amplitude of this $l = 1$ oscillation mode starts to increase continuously after $t \approx 100\,\mathrm{ms}$ and grows by a factor of about two per period. Only at $t \approx 250\,\mathrm{ms}$ the amplitude is sufficiently large to affect the shock shape. This is due to the finite resolution of the numerical grid — the shock cannot be pushed out by less than one radial zone and thus remains perfectly spherical for low oscillation amplitudes (lateral variation is already visible in the postshock flow, though).

In the subsequent evolution the shock radius is initially still slowly decreasing and the shock shape remains approximately spherical, but the shock surface shifts back and forth along the symmetry axis. The direction of the postshock flow changes periodically and alternatingly

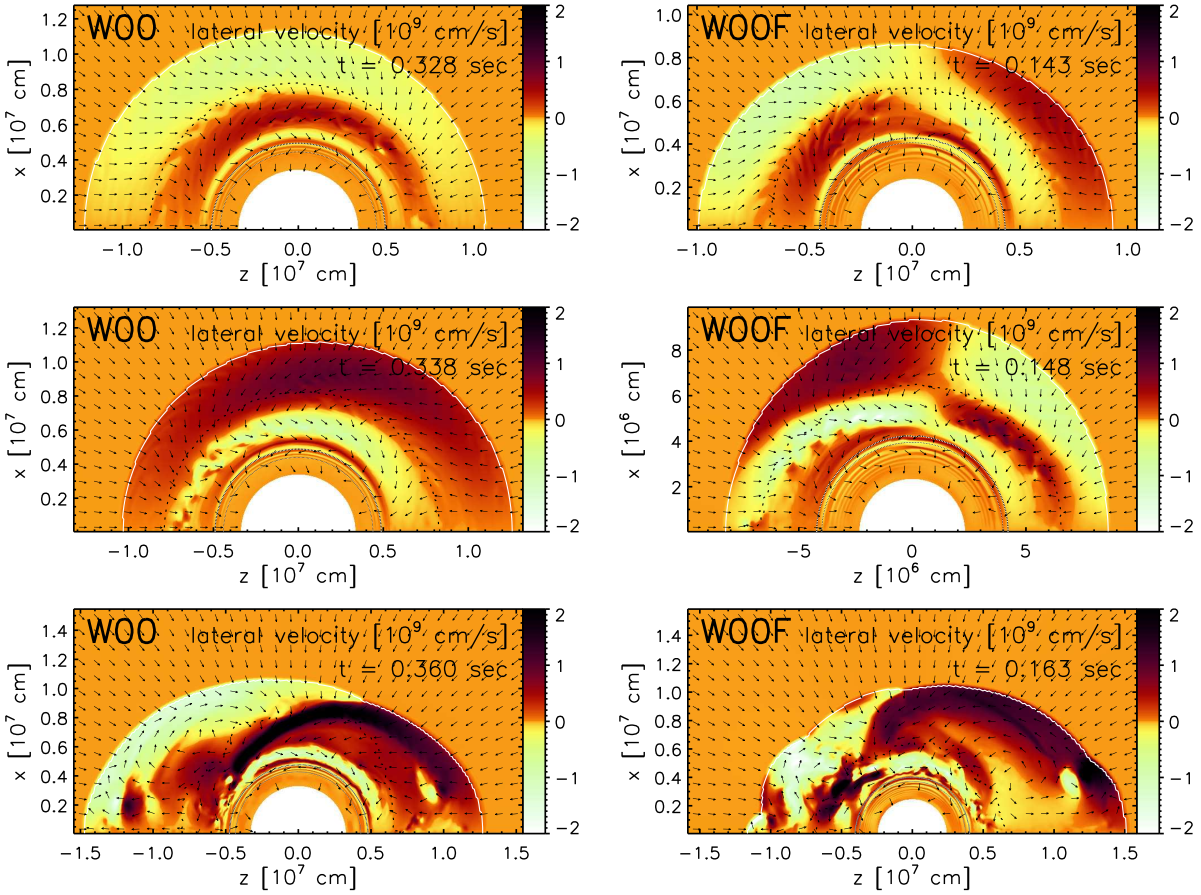

Figure 4.6: Lateral velocity distributions (with superimposed vectors indicating the direction of the flow) for Models W00 and W00F. The white lines mark the shock, the black, dotted lines the gain radius. For each model we show the situation for two times near $t = t_{\rm nl}$, in which the oscillations are in opposite phases (i.e. the times differ by half an oscillation period) and a third time, at which the oscillations have run out of phase (see Sect. 4.4.1). In Model W00 an $l = 1$ mode develops, i.e. the still nearly spherical shock shifts back and forth along the z-axis, whereas in Model W00F an $l = 2$ mode develops, i.e. the shock oscillates between a prolate and an oblate deformation. The postshock matter attains high lateral velocities, because the radial preshock flow hits the deformed or displaced shock at an oblique angle.

transports matter from the southern into the northern hemisphere and vice versa (Fig. 4.6). This behaviour is quite similar to the bipolar oscillations of the low-energy models discussed in Chapter 3. However, due to the missing convection the flow pattern and the shock shape are much simpler in Model W00.

At $t \approx 360$ ms the amplitude of the shock oscillations has become very large, the shock radii at the poles differs by up to 50 km, whereas the average shock radius is only about 100 km. In this phase the entropy behind the shock starts to vary strongly with time and angle (Fig. 4.7). Pronounced negative entropy gradients ($\mathrm{d}S/\mathrm{d}r = \mathcal{O}(1\,k_b/\mathrm{km})$) develop and convective instabilities start to grow at the interfaces between low- and high-entropy matter. The lateral postshock flow attains velocities of several 10^9 cm/s and supersonic downflows towards the neutron star form (see Sect. 4.4.1 for a discussion of these processes). Within a few oscillation cycles the whole postshock flow becomes very similar to the non-linear convective overturn present at the onset of the explosion in the low-energy models of Chapter 3.

However, in contrast to the latter, model W00 does not explode. At $t \approx 390$ ms the bipolar oscillations reach their maximum amplitude. In the further evolution they become weaker and on average the shock radius declines (Fig. 4.5). The slow decay of activity is interrupted by

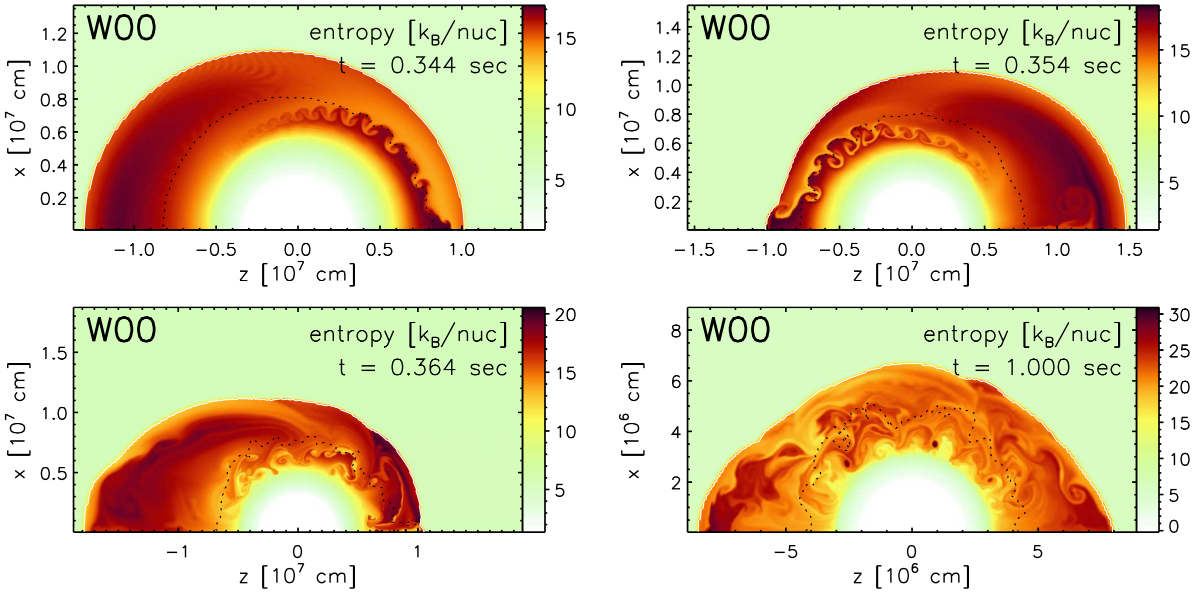

Figure 4.7: Evolution of the entropy distribution of Model W00 for several times at the begin of the non-linear phase (differing by half an oscillation period) and at $t = 1\,\mathrm{s}$. Within each oscillation cycle the postshock entropies vary strongly and steep, unstable entropy gradients develop in the postshock flow. Finally the Rayleigh-Taylor growth time scale becomes smaller than the oscillation period and perturbations are able to grow. In the subsequent evolution the low-mode oscillations saturate and the model does not develop an explosion.

several short phases of stronger shock expansion and bipolar oscillation, which occur semi-periodically every 50–100 ms. When we stop the simulation at $t = 1\,\mathrm{s}$ the shock is has retracted to a radius of only 70 km.

The slow-contracting Models W00S, W05S and W00V evolve qualitatively very similar to Model W00. However, with increasing contraction time scale the oscillation period becomes longer (up to 100 ms) and the growth rate of the low mode instability decreases. All of the models are dominated by an $l = 1$ mode and none of them is able to explode.

Also Model W00F with its rapidly contracting inner boundary evolves initially quite similar to Model W00. However, all time scales are smaller: The oscillation amplitude starts to grow already after 50 ms, the shock becomes non-spherical at $t \approx 100\,\mathrm{ms}$ and convection sets in at $t \approx 170\,\mathrm{ms}$. Furthermore, the $l = 2$ mode (i.e. oscillation between prolate and oblate states) is stronger than the $l = 1$ mode in this model (Fig. 4.6).

In contrast to the models with slower boundary contraction, the persistent neutrino heating in Model W00F is sufficiently strong to trigger an explosion at $t_{\mathrm{exp}} = 194\,\mathrm{ms}$. This difference is related to the fact that due to the faster contraction gravitational energy is released at a higher rate in Model W00F and therefore also the neutrino luminosity is higher (see Sec. 4.4.2 for a further discussion). The anisotropic morphology caused by the low-mode oscillations "freezes out" when the shock accelerates outward. A single accretion funnel forms in the northern hemisphere and the shock develops a prolate deformation. Thus the explosion proceeds very similar to what we found for models with "normal" boundary luminosities (see Chapter 3). As the boundary luminosity is negligible the energy of the explosions does not become very high (extrapolated 0.5×10^{51} erg after 1 s), but the neutron star is moving relatively fast ($v_{\mathrm{ns}} \approx 350\,\mathrm{km/s}$ for $t = 1\,\mathrm{s}$).

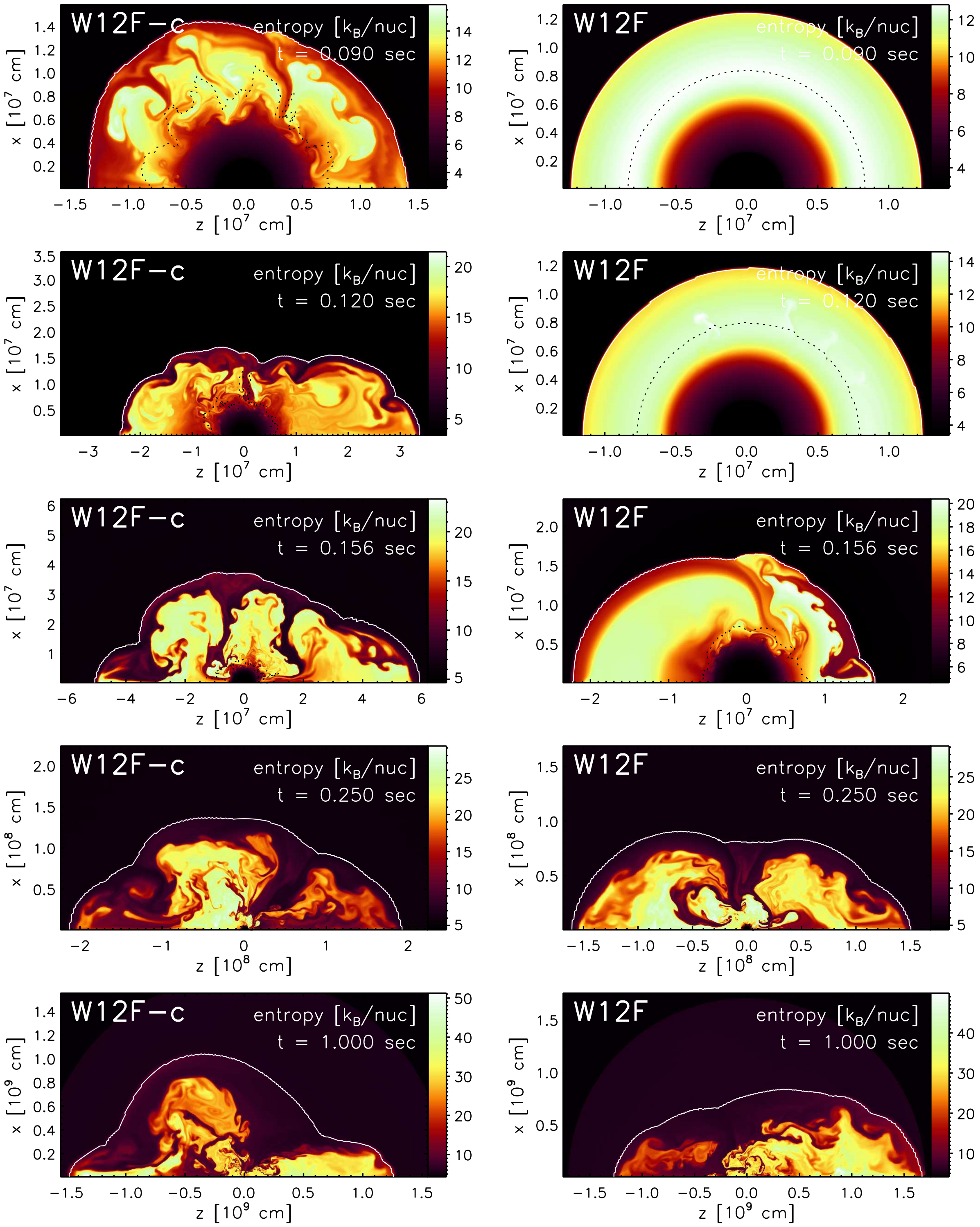

Figure 4.8: Entropy distribution at several times for Models W12F-c (left column) and W12F (right column). Model W12F-c becomes anisotropic quite early on due to the onset of convection, whereas in Model W12F convection is initially suppressed and low-mode oscillations become apparent after about 100 ms. After these oscillations have grown to large amplitudes and triggered convection also in Model W12F, the two models explode qualitatively very similar, whereas the positions of the downflows and the associated shock deformations differ.

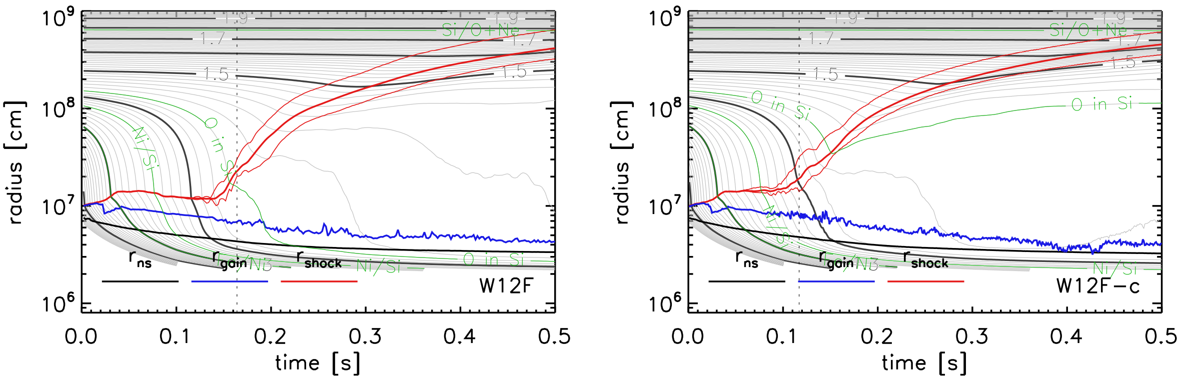

Figure 4.9: *Left panel:* As Fig. 4.3, but for model W12F. After an initial phase, in which the model remains nearly spherical symmetric, the AAC becomes strong enough to deform the shock and to trigger convection. This model explodes at $t \approx 160\,\mathrm{ms}$ (marked by the dotted line), when the oxygen-enriched silicon shell is falling through the shock. *Right panel:* As Fig. 4.3, but for model W12F-c. The convective overturn starts to deform the shock at $t = 60\,\mathrm{ms}$, and this model explodes already at $t = 120\,\mathrm{ms}$, even before the oxygen-enriched silicon layer (denoted with “O in Si”) has fallen through the shock.

4.2.3 Models with typical explosion energies

Is the non-radial instability present in Models W00 and W00F also able to develop in simulations with more realistic boundary conditions? To answer this question we performed two simulations, Models W12F-c and W12F, with boundary luminosities that allow for typical explosion energies of about 10^{51} erg. The contraction of the inner boundary is chosen to match the motion of the corresponding mass shell in a Boltzmann simulation of the same progenitor (Buras et al. 2003).

For the boundary luminosity and the contraction prescription used in the two models the parameter χ (see Sec. 4.1.1) is below the critical value of about 3 (Fig. 4.4). Therefore the progenitor perturbation amplitude decides, if convection is able to set in (in the non-linear way discussed in Sec. 4.1.1) or not. As the properties of these progenitor perturbations are not well-known, it appears interesting to compare two cases, one with a strongly perturbed initial model allowing for convection, and one with a rather weakly perturbed initial model, in which convection is suppressed. Thus for model W12F-c we use the same perturbations as for models W12-c and W18-c from Chapter 3, with radially varying amplitudes of up to several percent. These perturbation have been taken from a 2D core collapse Boltzmann simulation, Model s15r of Buras et al. (2003). For model W12F we apply our standard 0.1% velocity perturbations. An overview of the evolution of the two models is given in Figures 4.8 and 4.9, where we show the entropy distributions at several times and mass shell trajectories.

In the strongly perturbed Model W12F-c first convective bubbles form at $t \approx 60\,\mathrm{ms}$ and at $t \approx 90\,\mathrm{ms}$ the full gain layer has become convective (see Fig. 4.8). From this time on the total energy in the gain layer rises continuously and already at $t_{\mathrm{exp}} = 117\,\mathrm{ms}$ the first zones acquire positive total energy and the model explodes. The weakly perturbed Model W12F behaves quite differently in the first 200 ms. There is no indication of convection and for the first 100 ms the shock radius evolves as in a one-dimensional model with the same parameters. However, as in Model W00 a weak $l = 1$ oscillation mode is present in the postshock flow already at early times ($t \approx 30\,\mathrm{ms}$) and grows exponentially to large amplitudes. At about $t_{\mathrm{nl}} \approx 150\,\mathrm{ms}$ pronounced convectively unstable entropy gradients are generated below the oscillating shock and within two cycle periods a situation develops that strongly resembles model W12F-c at the onset of the explosion. Also Model W12F explodes soon afterwards, at $t = 164\,\mathrm{ms}$.

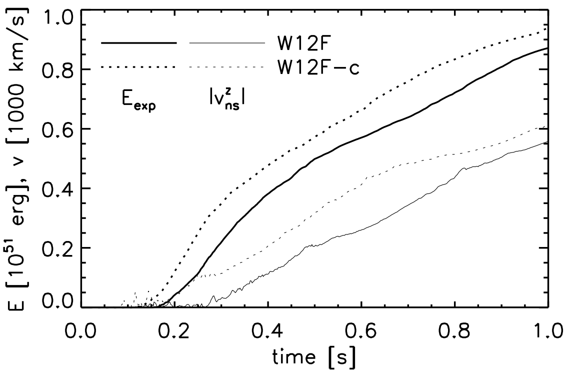

Figure 4.10: Evolution of the explosion energy (thick) and the neutron star velocity (thin) for Models W12F (solid) and W12F-c (dotted).

Although the pre-explosion evolutions and the explosion time scales are rather different for the two models, they behave quite similar after the explosion has set in. The convective structures merge and downflows form at the interface between rising, neutrino-heated matter and the matter with relatively low entropy directly below the shock. The number of downflows decreases with time and from $t \approx 200\,\mathrm{ms}$ on a single downflow dominates the morphology. Its position differs in the two models, as does the shape of the shock, but the explosion energy and even the neutron star velocities agree quite well for $t > 0.3\,\mathrm{s}$ (Fig. 4.10).

4.3 Interpretation of the linear phase

In the following we will discuss the non-radial instability growing in our simulations in detail. The determination and comparison of characteristic time scales and radii in the linear phase will allow us to identify the instability mechanism at work.

4.3.1 Measuring oscillation period and cycle efficiency

For a more quantitative analysis of the low-mode oscillations in our models we use a spherical harmonics expansion of the quantity A defined as

$$A(t,r,\theta) \equiv \frac{1}{\sin\theta}\,\frac{\partial}{\partial\theta}\left(v_\theta(t,r,\theta)\,\sin\theta\right). \tag{4.12}$$

rA is the divergence of the lateral velocity. At the gain radius,

$$A(t,R_\mathrm{g}(t),\theta) = \sum_{l=0}^{\infty} a_l(t)\,Y_{l,0}(\theta,0). \tag{4.13}$$

Here $Y_{l,m}(\theta,\phi)$ are the spherical harmonics and due to the assumption of axisymmetry only $m = 0$ has to be considered.

For $l > 0$, the spherical harmonics coefficients a_l of this quantity are proportional to the ones of the shock displacement (see Foglizzo et al. 2006b, Appendix F), so $A(t,R_\mathrm{g},\theta)$ contains basically the same information as $R_\mathrm{s}(t,\theta)$. We prefer to use $A(t,R_\mathrm{g}(t),\theta)$ rather than the shock displacement $\delta R = R_\mathrm{s}(\theta) - \langle R_\mathrm{s}\rangle_\theta$ (used in Blondin et al. 2003 and Ohnishi et al. 2006) because A is much less affected by noise ($A(t) = 0$ for a non-stationary spherical flow, whereas $R_\mathrm{s}(t)$ is

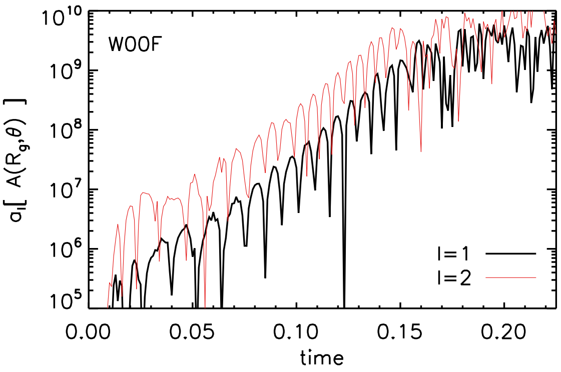

Figure 4.11: Evolution of the lowest spherical harmonics coefficients of the quantity $A(r, t, \theta)$ (Eq. 4.12) at the gain radius of Model W00F.

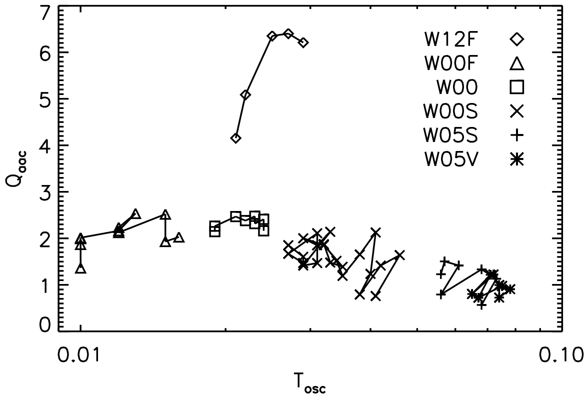

Figure 4.12: Cycle efficiency, $|Q_{\mathrm{aac}}|$, as a function of the oscillation period, τ_{osc}, for Models W00F, W00, W00S, W05S, W05V and W12F.

varying) and allows to measure the oscillation period and growth rate already much earlier than it is possible for R_{s}. As an example the coefficients for Model W00F are shown in Fig. 4.11.

For a given mode l the oscillation period $\tau_{\mathrm{osc},l}$ can be determined by detecting the minima of $|a_l(t)|$, which occur at times $t = t^n_{\mathrm{min},l}$. This detection works reliably only for a sufficiently high amplitude (i.e. it fails in the first 10–20 ms) and is not feasible any more, when convective instabilities involving a broad range of frequencies arise in the non-linear phase. During one cycle of mode l the corresponding coefficient $a_l(t)$ becomes zero two times, so the cycle period can be measured as

$$\tau_{\mathrm{osc},l}(t^n_{\mathrm{min},l}) = t^{n+1}_{\mathrm{min},l} - t^{n-1}_{\mathrm{min},l}. \tag{4.14}$$

The evolution of the period of the $l = 1$ modes, $\tau_{\mathrm{osc},1}$, obtained using Eq. 4.14 is displayed in Fig. 4.13 for three of the models. The periods range between ~ 15 ms and ~ 80 ms. The largest values are found for Model W05V, in which the advection time scale and the sound crossing time scale are rather long because the shock radius is quite large and the post shock velocities are low.

In order to measure the cycle efficiency, Q_{aac}, we use again the coefficients a_l defined in Eq. 4.13. We detect the positions of the maxima of $|a_l(t)|$, which occur at times $t = t^n_{\mathrm{max},l}$. If the oscillations of mode l are dominated by the kth harmonic (i.e. $\tau_{\mathrm{osc}} = \tau^{\mathrm{f}}_{\mathrm{aac}}/k$, where $\tau^{\mathrm{f}}_{\mathrm{aac}}$ is the period of the fundamental mode), $|a_l(t)|$ has $2k$ maxima during one fundamental cycle period $\tau^{\mathrm{f}}_{\mathrm{aac}}$, so the amplification per *fundamental* cycle can be measured as

$$Q_{\mathrm{aac},l}(t^n_{\mathrm{max},l}) = \left(\frac{a_l(t^{n+1}_{\mathrm{max},l})}{a_l(t^{n-1}_{\mathrm{max},l})} \right)^k . \tag{4.15}$$

This method fails, if several of the harmonics are excited with similar strength. However, these phases can be identified and in general one of the harmonics dominates (in most cases the fundamental mode, $k = 1$). The efficiencies measured using Eq. (4.15) are shown in Fig. 4.12. For the models with low boundary luminosity and contraction time scales up to 1 s, we find values between 2 and 3, whereas for the slowly contracting models the efficiency can even fall below 1. For Model W12F, the only simulation with a higher core luminosity, the efficiency reaches exceptionally high values of more than 6.

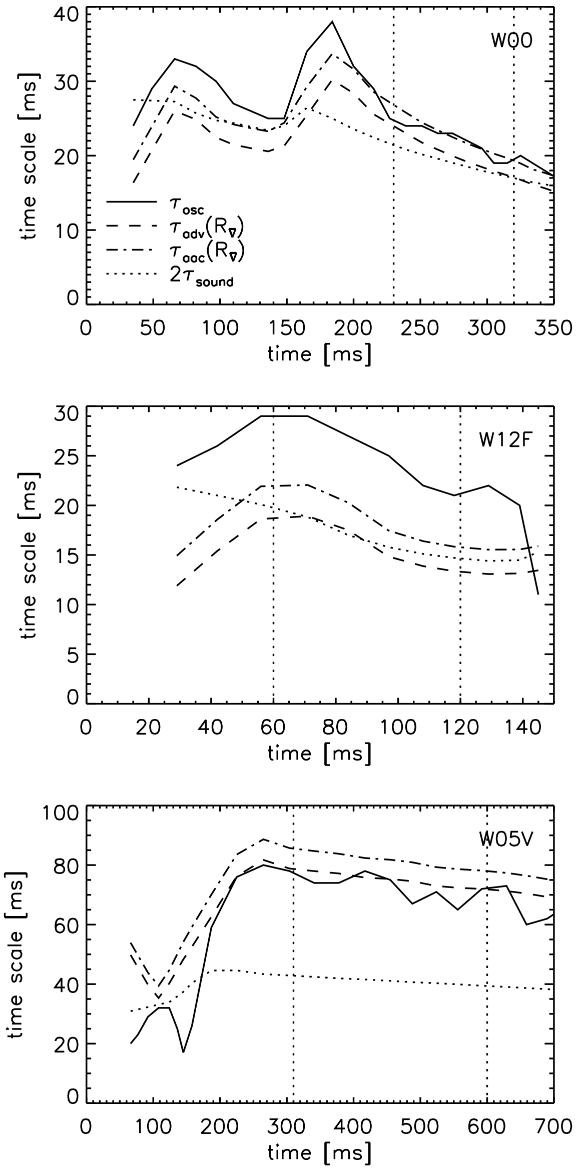

Figure 4.13: Evolution of the oscillation period, τ_{osc}, the advection time from the shock to the radius of the strongest deceleration, $\tau_{\mathrm{adv}}^{\nabla}$, and two times the sound travel time through the shock cavity, τ_{sound}, for Models W00, W12F and W05V. The vertical dotted lines enclose the time spans used in Figs. 4.17 and 4.12. While in Model W00 all time scales are similar ($\tau_{\mathrm{osc}} \approx \tau_{\mathrm{adv}}^{\nabla} \approx 2 \times \tau_{\mathrm{sound}}$), both $\tau_{\mathrm{adv}}^{\nabla}$ and $2 \times \tau_{\mathrm{sound}}$ are smaller than the oscillation period in Model W12F. In Model W05V only the advection time agrees with the oscillation period, whereas $2 \times \tau_{\mathrm{sound}}$ is significantly (about a factor 1/2) smaller.

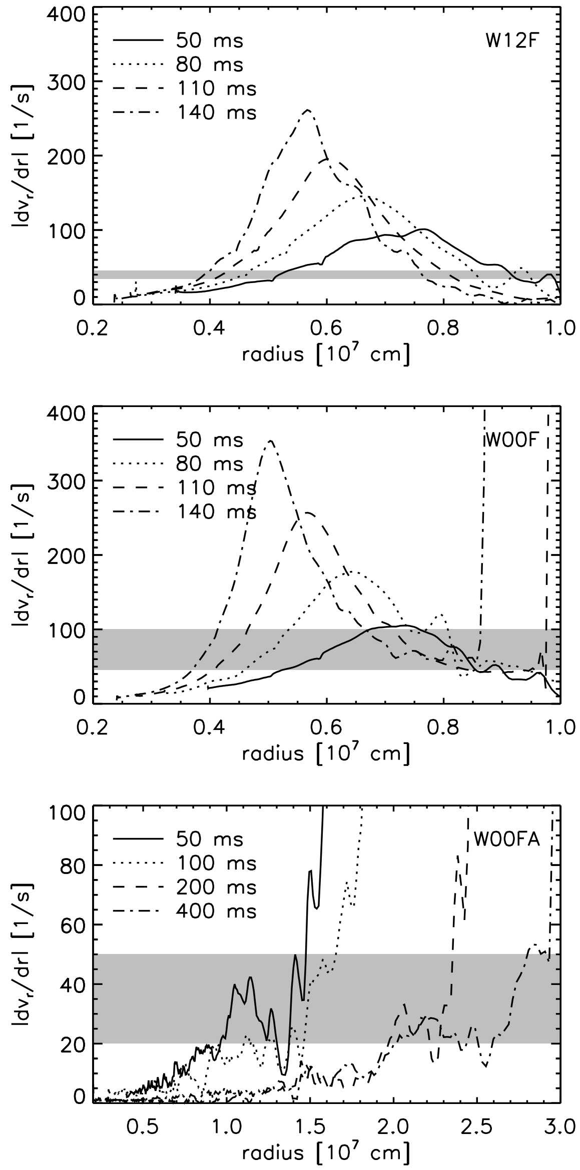

Figure 4.14: Radial profiles of the radial derivative of the radial velocity for Models W12F, W00F and W00FA at several times. The gray shaded area indicates the range of values $1/\tau_{\mathrm{osc}}$ takes on during these times. In the models including neutrinos a pronounced “deceleration peak” forms (with a maximum value significantly higher than $1/\tau_{\mathrm{osc}}$), whereas in Model W00FA the latter is absent.

4.3.2 Identification of the instability mechanism

So far we have discussed the temporal behaviour of the flow at one certain radius, R_g. The radial structure of the oscillations becomes evident in Figs. 4.15 and 4.16, where we show spherical harmonics coefficients of the lowest modes as a function of time and radius for Models W00, W00F and W12F. Figure 4.16, which displays the coefficients for the pressure, reveals the presence of coherent pressure modes (i.e. "acoustic perturbations"), which oscillate with the same period as the "advected perturbations" made visible using the quantity A (see Eq. 4.12) in Fig. 4.15. The advected perturbations are created at the shock, advected downwards and decelerated above the neutron star surface.

The pattern of the pressure perturbations reveals the presence of a particular radius, R_ϕ, where the phase is shifted. The dashed-dotted line in Figs. 4.15 and 4.16 is defined as the radius R_∇ where the velocity gradient of the unperturbed flow is strongest (i.e. at the maximum of $|\partial v/\partial r|$, which can be clearly localised in the linear phase and lies somewhat above the neutron star surface). This particular radius appears to be closely connected to the structure of pressure perturbations — in all the flows studied, these two radii coincide:

$$R_\nabla \approx R_\phi. \tag{4.16}$$

This striking coincidence may be a consequence of a particularly efficient coupling between advected and acoustic perturbations at this radius. In order to test this hypothesis, we have compared the wavelength $2\pi v/\omega_r$ of advected perturbations at this radius to the length scale $(\mathrm{d}\log v/\mathrm{d}r)^{-1}$ of this deceleration zone. An efficient coupling is expected if the flow velocity varies on a short distance compared to the wavelength of advected perturbations:

$$\left|\frac{\mathrm{d}\log v}{\mathrm{d}r}\right|^{-1} < \frac{2\pi v}{\omega_r} \quad \leftrightarrow \quad \tau_\mathrm{osc} > \left|\frac{\mathrm{d}v}{\mathrm{d}r}\right|^{-1} \tag{4.17}$$

If our interpretation of the phase shift is correct, condition (4.17) should be fulfilled at R_ϕ and the value $|\mathrm{d}v/\mathrm{d}r|$ at other radii should be significantly lower (otherwise efficient coupling and an associated phase shift would be expected for a wide range of radii). This is the case, as illustrated in Fig. 4.14. Further support comes from the observation that the deceleration peak is absent Model W00FA, in which the instability is very weak. Moreover, for the other models condition (4.17) is not or only marginally fulfilled in the first few oscillation periods, which is consistent with the fact that the growth rate is initially low. This leads us to interpret $R_\nabla \approx R_\phi$ as a radius of effective coupling:

$$R_\mathrm{c} \equiv R_\nabla \approx R_\phi \tag{4.18}$$

It should be mentioned that the "deceleration peaks" present in our simulations with approximate neutrino transport are also found in Boltzmann simulations and seem to be a generic feature of the post-shock flow.

Now that the main features of the AAC (downwards advected perturbations, acoustic perturbations and a coupling region) have been identified, it remains to be shown that the oscillation period observed in our simulations matches the predictions. For this purpose, we compare the oscillation period τ_osc with the time scale $\tau^\mathrm{f}_\mathrm{aac}$ of the cycle, approximated by the advection time $\tau_\mathrm{adv}(R_\nabla)$ from the shock to R_∇ in Fig. 4.13. In all models except W12F (that we will discuss later), this advection time is very close to the oscillation period. Fig. 4.13 also indicates the value $2 \times \tau_\mathrm{sound}$ of the sound travel time through the full diameter of the cavity. This time scale is the longest time scale which may be associated to a purely acoustic mode in the cavity, as advocated by Blondin & Mezzacappa (2006). According to Fig. 4.13, this time scale can

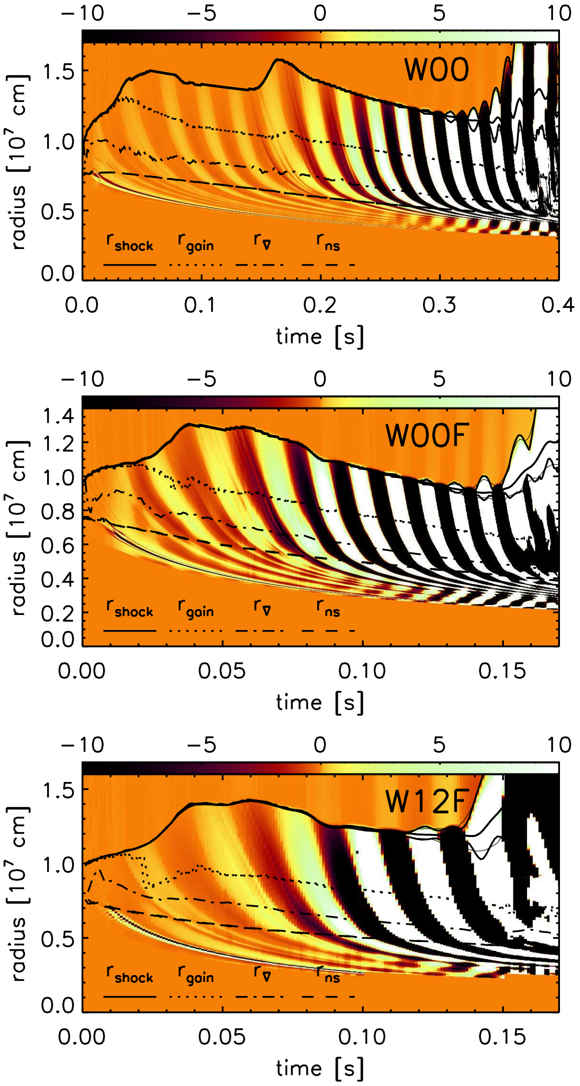

Figure 4.15: Spherical harmonics coefficients of the quantity A (corresponding to the dominating oscillation mode) as a function of radius and time for Models W00, W00F and W12F. The solid lines are the minimum, average and maximum shock radius, the dotted line is the gain radius, the dashed line is the neutron star surface and the dash-dotted line marks the location of the strongest velocity gradient. Already several ten milliseconds after bounce a zebra-like pattern becomes visible, which is caused by the advection of matter with lateral velocity from the shock towards the neutron star.

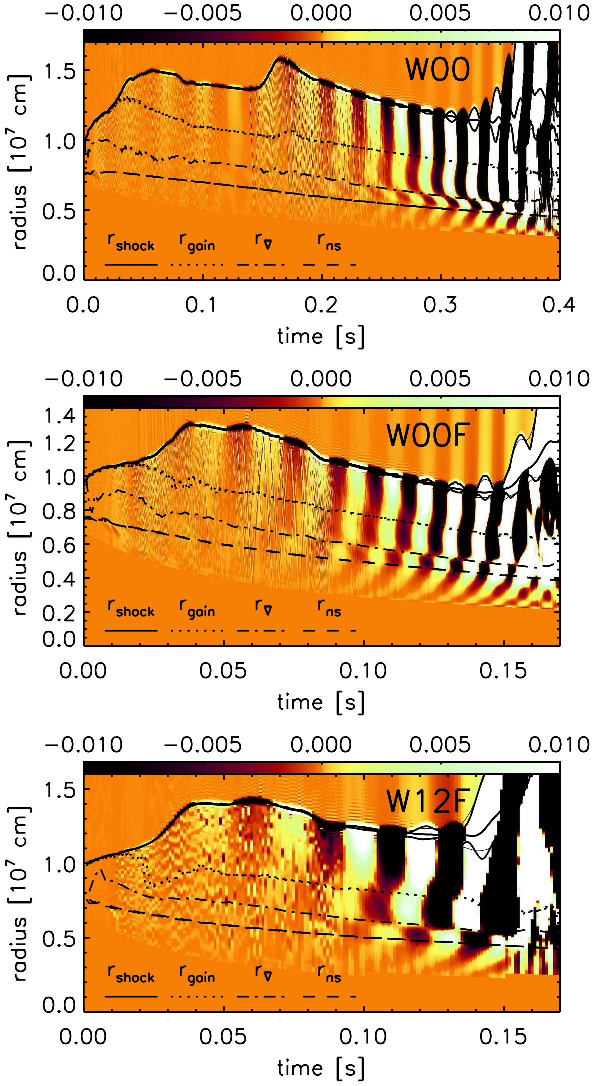

Figure 4.16: Spherical harmonics coefficients of the pressure (corresponding to the dominating oscillation mode and divided by the $l = 0$ coefficient) as a function of radius and time for Models W00, W00F and W12F. The lines have the same meaning as in Fig. 4.15. A low mode oscillation develops in the postshock flow. A pronounced phase shift is visible at a radius $R_\Phi(t)$ which agrees well with the position of the strongest velocity gradient, $R_\nabla(t)$. The "noise" (short-wavelength sound waves) visible in the early phases is caused by the shock propagation and not related to the advective-acoustic instability.

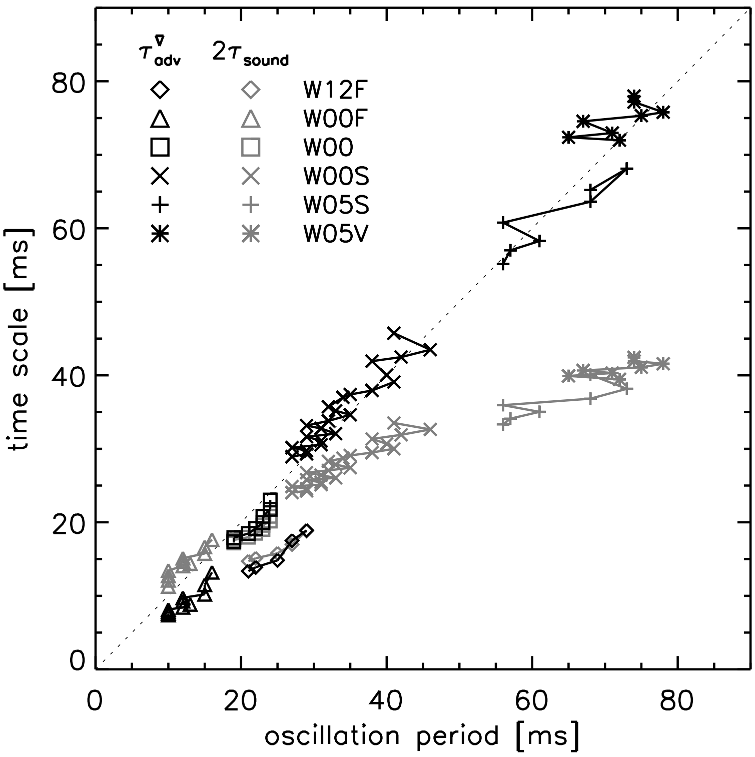

Figure 4.17: Advection time $\tau_{\rm adv}^{\nabla}$ (from the shock to the radius of maximum deceleration, R_{∇}) and two times the sound crossing time for the shock cavity, $2 \times \tau_{\rm sound}$, as a function of the oscillation period, $\tau_{\rm osc}$, for Models W00F, W00, W00S, W05S, W05V and W12F. For this plot only data from phases is used, in which the oscillations are clearly detectable and in which the flow is quasi-stationary (see Fig. 4.13). In particular from the models with slow neutron star contraction it becomes clear that the oscillation period scales with $\tau_{\rm adv}^{\nabla}$ rather than $\tau_{\rm sound}$. Model W12F is a special case (see text).

be comparable to $\tau_{\rm osc}$ as in Models W00, but is a factor two shorter in Model W05V. A more systematic comparison between the oscillation, acoustic, and advective time scales is shown in Fig. 4.17 for each of the eight models. This figure is a clear proof that the oscillations are not the consequence of a purely acoustic process, and that advection plays an important role. This leads us to the conclusion that the instability mechanism at work in our simulations is indeed the advective-acoustic cycle.

Figures 4.13 and 4.17 show that Model W12F, the only one in these figures with significant boundary luminosity, is a special case — the oscillation period is longer than expected. There is some delay, i.e. a phase shift, in each oscillation cycle of this model. This phase shift is actually visible on the pressure profile in the bottom plot of Fig. 4.16, and is localised in the vicinity of the gain radius. This exception might thus be due to the particular intensity of neutrino heating in Model W12F, which favours the Rayleigh-Taylor growth of perturbations in the gain region and may be responsible for an additional advective-acoustic coupling at the gain radius. The presence of an additional source of amplification in Model W12F is further supported by its exceptionally high amplification factor $Q_{\rm aac}$ (Fig. 4.12). This possible cooperation of the AAC and convection should be investigated further.

4.4 Interpretation of the non-linear phase

In the following we will focus on the non-linear phase, in which the AAC cannot be regarded as a small perturbation any more. In particular we will discuss the relation between the AAC and convection and the influence of these instabilities on the onset of the explosion and the explosion energy.

4.4.1 AAC triggers convection

Within a few oscillation cycles after $t = t_{\mathrm{nl}}$ (see Tab. 4.1) a flow has established in our simulations with low core luminosities that shows not only low-mode oscillations, but also small-scale structures and features typical for the non-linear convective overturn of the models of Chapter 3, like rising plumes of neutrino-heated matter and supersonic downflows of low-entropy matter. There are two effects that contribute to this change of the flow character, which are related to the motion and the deformation of the shock, respectively.

Firstly, due to the shock motion the flow becomes Rayleigh-Taylor unstable. This is because the shock attains local velocities of $\mathcal{O}(10^9 \mathrm{cm/s})$, a significant fraction of the preshock velocity. As the postshock entropy depends on the the preshock velocity *in the frame of the shock*, the fast shock oscillations result in strongly varying postshock entropies. Expanding parts of the shock leave high entropies behind, whereas contracting parts lead to lower postshock entropies. For a fixed angle the alternating shock expansion and contraction results in layers with high and low entropies on top of each other, which are compressed and advected towards the neutron star. With increasing shock oscillation amplitude the convectively unstable entropy gradients between these layers become finally sufficiently steep to bring the corresponding Rayleigh-Taylor growth time scales down to about 1 ms, much shorter than the advection time scale. Therefore perturbations are able to grow quickly at the interfaces and form vortices and mushroom-like structures (see Fig. 4.7).

Secondly, also the displacement (by the $l = 1$ mode) and deformation (by $l \geq 2$ modes) of the shock at large cycle amplitudes plays an important role. The radial preshock flow hits the deformed or displaced shock at an oblique angle. As the velocity component parallel to the shock is conserved, the matter crossing the shock attains a lateral velocity component (whose direction changes with the cycle period, see Fig. 4.6). As long as the cycle amplitude is low, these lateral velocities are small and the flow remains approximately radial. For a strong shock deformation, however, the flow becomes predominantly non-radial, as the lateral postshock velocity reaches a significant fraction of the preshock velocity (up to several 10^9 cm/s, i.e. the lateral flow becomes supersonic). For an $l = 1$ mode, the highest negative lateral velocities are obtained, when the shock has attained the maximum shift in negative z-direction (see Fig. 4.6, upper left panel). A shell of matter with high negative lateral velocity formed in this phase is advected towards the neutron star, and half an oscillation period later the highest positive lateral velocities are generated below the shock, when the latter is shifted into positive z-direction (see Fig. 4.6, middle left panel). With increasing oscillation amplitude the shock radius – and consequently also the advection time scale and the cycle period – vary finally so strongly during one cycle that the northern and southern hemispheres run “out of phase”, so that the local shock radii at the north ($\theta = 0°$) and the south pole ($\theta = 180°$) reach their maximum values not any more by turns, but at almost the same time. In this case streams of matter with high positive and high negative lateral velocities are produced simultaneously near the north and south pole, respectively. These streams collide and one of them is deflected upwards, producing a “kink” in the shock surface, while the other one is diverted downwards, forming a supersonic downflow akin to the ones we observe in the simulations of Chapter 3 (see Fig. 4.6, lower left panel and 4.8, middle right panel). By these two processes a large-amplitude AAC is able to trigger a non-linear convective overturn even in models in which the convective growth is suppressed according to Eqs. (4.6) and (4.7).

4.4.2 Explosion vs. non-explosion

Why is Model W00F able to explode whereas Model W00 and the models with even slower boundary contraction do not develop an explosion? The two parameters that differ between W00F and W00 are the final inner boundary radius, R_{ib}, and the contraction time scale, t_{ib}. A lower value of R_{ib} implies that the matter sinks deeper into the gravitational potential and thus more potential energy is released. The lower value of t_{ib} requires that this release of energy occurs earlier. Most of this potential energy is radiated away in the form of neutrinos. Consequently the luminosity in the gain layer is much higher for Model W00F at early times (Fig. 4.18).

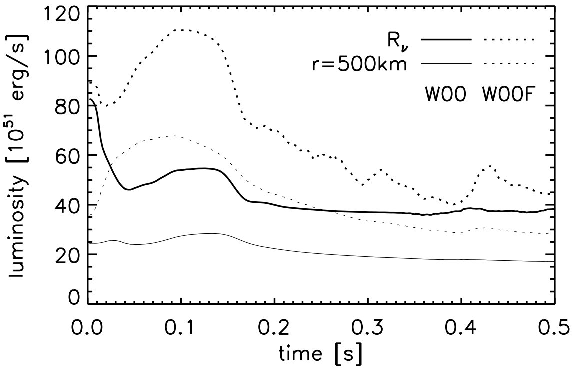

Figure 4.18: Evolution of the sum of the angle-averaged ν_{e} and $\bar{\nu}_{\mathrm{e}}$ luminosities at the neutrino sphere and at $r = 500\,\mathrm{km}$ for models W00 and W00F. The highest luminosities are found for early times ($t < 0.2\,\mathrm{s}$), when the accretion rate is still large. For model W00F the luminosities are higher, because the neutron star contracts faster, releasing more gravitational energy.

Yet, these high luminosities alone are not enough to start an explosion. This is demonstrated by a one-dimensional simulation with the same parameters as Model W00F, which fails to explode. However, in the two-dimensional case convection leads to an improved efficiency of the neutrino energy deposition in the gain layer. On the one hand this is because owing to the convective overturn the advection time scale is becoming larger, which increases the time during which a fluid element is exposed to the neutrino fluxes and enlarges the gain layer mass. On the other hand the neutrino-heated matter rises quickly to regions with lower temperature, which reduces energy loss by neutrino reemission. The former effect is working also if a high-amplitude AAC is present, because in this case the average shock radius increases, which results in a larger advection time and a higher gain layer mass.

In model W00F we observe such a rise of the advection time scale starting at $t \approx 150\,\mathrm{ms}$, when the postshock flow is already predominantly non-radial, but the non-linear convective overturn has not yet been triggered (Fig. 4.19). Like for convection the increasing $\tau_{\mathrm{adv}}^{\mathrm{g}}$ leads to a “boost” of the heating rate, which becomes even more pronounced once the non-linear convective overturn has established ($t \gtrsim 170\,\mathrm{ms}$). The total energy distribution in the gain layer peaks initially sharply at $-11\,\mathrm{MeV/nucleon}$, but the distribution becomes broader under the influence of the large-amplitude AAC and the convective overturn (Fig. 4.20). Due to the strong neutrino heating the mean value of the total energy increases and finally the first zones acquire positive total energy

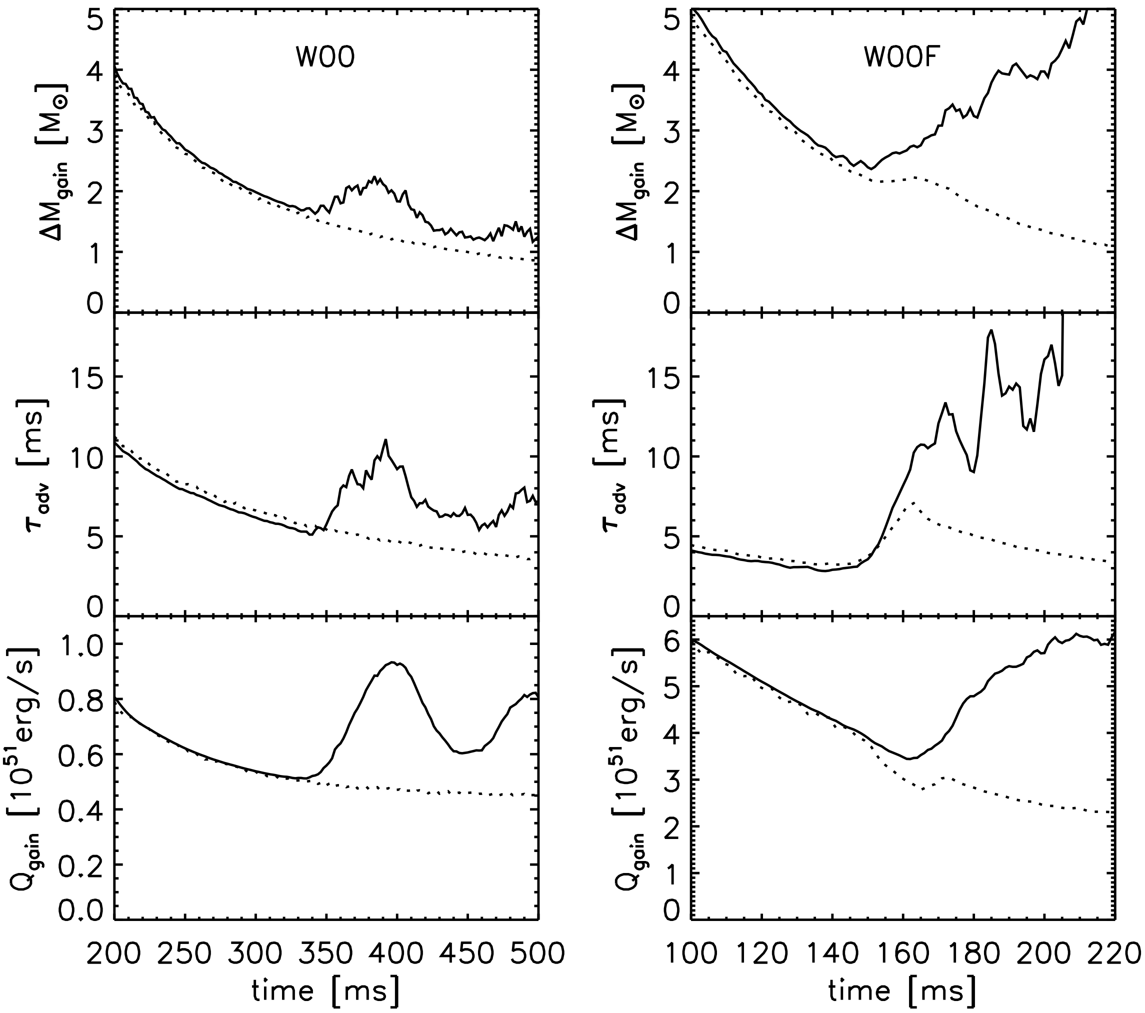

Figure 4.19: Evolution of the mass in the gain layer, the advection time scale and the heating rate in the gain layer for models W00 and W00F (solid lines). The dotted lines are from one-dimensional simulations with the same parameters. When the AAC becomes non-linear ($t \approx 350$ ms for W00, $t \approx 150$ ms for W00F) and triggers convection (about 30 ms later) the advection time scale and the mass in the gain layer increase. Thereby the heating rate is strongly enhanced, compared to the one-dimensional case. For model W00F this enhanced heating is sufficiently strong to make the gain layer unbound and produce an explosion. The advection time scale increases also in the one-dimensional version of model W00F, because a progenitor shell interface is falling through the shock at this time. However, this one-dimensional model does not explode, since without the multidimensional effects the heating does not become sufficiently strong. For model W00 the luminosity is so low that even the increase of the heating rate by almost a factor of two does not lead to an explosion.

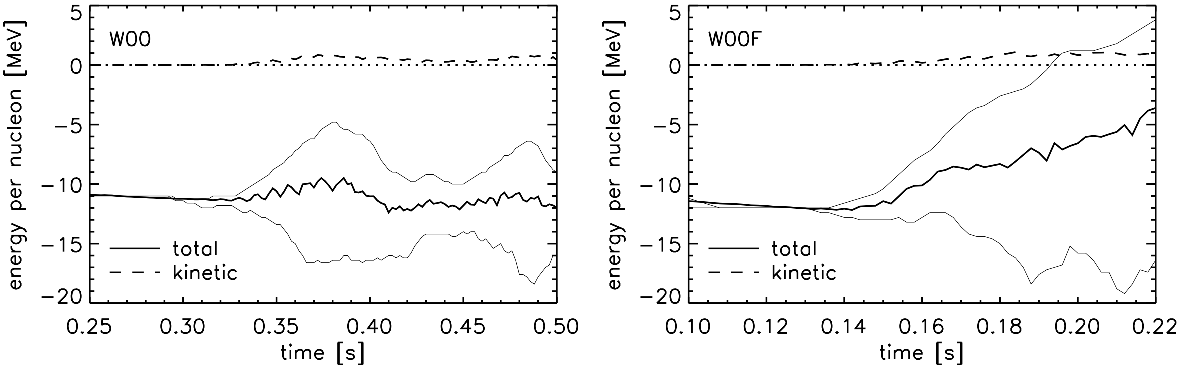

Figure 4.20: Evolution of the average total (thick solid line) and kinetic (dashed line) energy per baryon in the gain layer for models W00 and W00F. The thin solid lines enclose the energy range, in which 90% of the gain layer matter is contained.

and the explosion sets in. Also in model W00 we see an enhanced neutrino heating (up to two times higher than in the corresponding one-dimensional simulation) from $t \approx 350\,\mathrm{ms}$ on, caused by a combination of the non-linear AAC and convection (Fig. 4.19). However, due to the low accretion rate at this late time the absolute value of the luminosity and consequently also the heating rate are much lower than in model W00F. The total energy in the gain layer increases only temporarily by about 1 MeV, but falls back soon and decreases further (Fig. 4.20). The broadening of the energy distribution does not become sufficiently efficient to make any matter unbound. For both models the kinetic energy in the gain layer remains relatively small (about 1 MeV/nucleon, see Fig. 4.20).

The failed explosion of Model W00 is in contrast to the simulations of Blondin et al. (2003), in which the lateral kinetic energy below the shock increases continuously and the energy is redistributed efficiently so that some of the matter finally attains positive total energy (which is interpreted as an explosion). The likely cause for this discrepancy is the neutrino cooling present in our simulations, which acts as an energy sink and seems to dampen the AAC at high amplitudes. Thus in our simulations the redistribution of the energy by the cycle is not sufficient to allow for explosions.

This means that sufficiently strong neutrino heating is required and that also in the presence of the AAC there is a threshold luminosity, which has to be exceeded to allow for an explosion. This conclusion is in accordance with the fact that also Ohnishi et al. (2006) (who include neutrino cooling and heating) find an explosion only in one high-luminosity case, but not for lower luminosities. In fact the increase of the heating efficiency by the AAC and convection seems to be more important than the limited direct effect of the AAC on the explosion (by energy redistribution). Thus both convection and the AAC can be seen as “catalysts”, which facilitate an explosion, rather than sources of explosion energy. The failure of one-dimensional explosion models with detailed transport descriptions shows, however, that these multidimensional effects are important and required for successful neutrino-driven explosions. While the non-radial flow associated to the AAC may be helpful to reach the onset of an explosion, it is not important for the total energetics in the subsequent phase in our models. The lateral kinetic energy is limited to several 10^{49} erg in all of our simulations – two orders of magnitude smaller than typical explosion energies.

To allow for explosions, convection or the AAC have to become non-linear sufficiently early, in a phase in which the neutrino luminosities are still high enough. Whether this is the case or not, depends on the growth rate, which is determined by the properties of the postshock flow, which in turn depend in a complex way on the neutron star contraction, the core neutrino flux and the progenitor structure. Furthermore, also the amplitude of the progenitor perturbations from which instabilities start to grow can be important, as we will discuss in the next section.

4.4.3 The AAC as an alternative to convection

Detailed transport simulations (Buras et al. 2006a) suggest that the ratio of growth to advection time scale, χ, is below the critical value (see Eq. 4.8) and therefore convection can grow only in the non-linear way discussed in Sect. 4.1.1. This means that the progenitor perturbation amplitude is required to exceed a certain threshold value, estimated to be $\delta_c / \exp(\chi)$, where δ_c is typically one to several percent (see Eq. 4.8). It is unclear, though, which perturbation amplitude should be adopted, as stellar evolution calculations are still performed in one dimension and multidimensional simulations of the pre-collapse phase are just becoming practicable. According to Goldreich et al. (1996) and Bazan & Arnett (1998) shell nuclear burning leaves behind density perturbations with a radius-dependent amplitude of up to several percent. However, in the subsequent evolution the amplitudes are modified, e.g. during the collapse they are dampened in the subsonic region and grow by at most one order of magnitude in the supersonic region (Lai & Goldreich 2000). Thus the perturbation amplitude distribution after core bounce is still not well-known and one cannot exclude the possibility that the perturbations do not reach the critical amplitude, such that convection is suppressed.

Model W12F and W12F-c represent two cases in which $\chi \lesssim \chi_0$ due to sufficiently fast contraction of the inner boundary and in which the perturbation amplitudes remain below the threshold value and become higher than the threshold value, respectively (Fig. 4.4). Therefore the initial sources of anisotropy are the AAC in Model W12F and convection in Model W12F-c. Without the presence of the AAC model W12F would not become anisotropic and would fail to explode — a one-dimensional simulation with the same parameters as Model W12F does not develop and explosion. This demonstrates that the AAC could allow for explosions in cases, in which convection is not able to develop. In contrast to convection the AAC is neither hampered by low values of χ nor does it stop to work when the initial perturbations are below a certain amplitude.

Could one distinguish, whether the initial source of anisotropy in an observed supernova explosion is the AAC or convection? Considering Models W12F and W12F-c, this may be hard to achieve. Although the early evolution of the two models is rather different and the explosion time scales differ by 50 ms, they behave quite similar at late times. Although the morphologies of the two models are different, they do not differ qualitatively. Such differences are also found if only the initial seed perturbations are changed (see Sect. 3.2.5). Furthermore, important global parameters of the models are very similar: One second after core bounce both models reach explosion energies of about $0.9\,10^{51}$ erg, neutron star masses of $1.4\,M_\odot$ and neutron star velocities in excess of 500 km/s. They explosion energies are not affected strongly by the different explosion times, because the bulk of the explosion energy is built up after the onset of the explosion in the wind phase, which is very similar for both models (see Appendix B).

The high neutron star velocity of Model W12F demonstrates that the cycle alone is sufficient to excite low modes and that convection is not required. This is in accordance with the analysis of Foglizzo et al. (2006b), who found that the lowest modes become convectively unstable only for values of χ significantly higher than 3. Although the latter result is valid only in the linear regime, it supports the suspicion that the excitation of low modes in all of our simulations — also the ones in which convection is not suppressed — is mainly due to the AAC.

5

Three-dimensional effects

One-dimensional simulations are based on the physical assumption that anisotropies are negligible. Two-dimensional axisymmetric simulations, on the other hand, assume that anisotropies are confined to the latitudinal direction only, and that the flow does not vary in the longitudinal direction. All of these simplifying assumptions are artificial. The assumption of axisymmetry allows one to perform simulations, which are computationally much cheaper than three-dimensional calculations, while allowing for some important effects that are missing in one-dimensional simulations, as e.g. convection. Yet, 2D simulations can only be regarded as an intermediate step that can and should be taken as long as three-dimensional simulations are computationally still too expensive. Parameter studies like those discussed in the previous chapter require dozens of models and are still infeasible with a three-dimensional treatment. However, with the increase of computational capacity in the last years it has become possible to perform single three-dimensional simulations with an approximate treatment of the neutrino transport. First results of this kind have been reported by Fryer & Warren (2004) (but were not dominated by low modes).

In this chapter we present the first three-dimensional models based on a high-resolution shock-capturing finite-volume method (see Sect. 2.1). These simulations are still limited in several aspects. On the one hand, the physics we include is the same as in our two-dimensional simulations: We use an approximate neutrino transport scheme which considers transport in the radial direction only, and we do not simulate the inner core of the neutron star, whose influence is taken into account by prescribing appropriate boundary conditions. On the other hand the models are restricted due to numerical grid we use: The simulations had to be run on a rather coarse grid and in most cases do not contain the full (4π) solid angle. The probably strongest limitation, however, arises from the fact that only few models could be calculated. This means, that we cannot be sure that all features found in these simulations are generic and that questions requiring statistics (e.g., "What is the average kick velocity in 3D?") cannot yet be conclusively answered.

Despite of these limitations the simulations provide some insight in the differences between two- and three-dimensional supernova simulations that will prove useful on the way to the long-term goal of conducting a large number of three-dimensional simulations with high grid resolution using a detailed neutrino transport description.

5.1 Model parameters

5.1.1 Initial models and boundary conditions

Owing to the restricted computational resources, only three three-dimensional simulations could be performed. We chose to simulate two three-dimensional versions of model B12 from Paper I, because most of the two-dimensional variations of this model show clearly a single downflow in advanced stages of the evolution. Using such a model seemed therefore promising to investigate whether low-order modes establish also in three dimensions. Thus we performed two B12-like simulations, although they have the disadvantage that they attain only a somewhat low explosion energy ($E_{\mathrm{exp}} \approx 0.3 \cdot 10^{51}$ erg), compared to the typical supernova energy of 10^{51} erg.

The aim of the third simulation is to explore the influence of rotation on the explosion in three dimensions. It is based on the rotating inital model that we have already used for the 2D simulations in Chapter 3. The angular velocities in this initial model are somewhat higher than those expected for typical supernova progenitors (see Sect. 3.4), so that the effects of rotation are overestimated. The boundary contraction used for this model is slightly faster than the "rapid contraction" defined in Sect. 2.4.1. This requires that we apply also in this case the procedure to move the inner boundary to a different mass shell (see Sect. 2.4.3), each time the optical depth becomes too high for our transport scheme. The (extrapolated) explosion energy after one second for this model is about $1.5 \cdot 10^{51}$ erg.

5.1.2 Numerical grid

During our 3D simulations we encountered numerical problems in the polar regions. Independent of the resolution numerical noise started to affect these regions after some time. Several test showed that the noise was not created at the boundary, but inside the grid. The problem is probably related to the deformation of the grid zones near the poles and could not be fixed in a simple way. However, we have found two workarounds for this issue: It is possible to omit the "noisy" parts of the grid by setting $\theta_0 \approx 20°$ (see Sect. 2.3 for the definitions of grid related quantities) and thereby excluding two cones around the poles from the computational domain. The second possibility is to reduce the time step to $0.3 \cdot \tau_{\mathrm{CFL}}$ instead of the usual value $0.7 \cdot \tau_{\mathrm{CFL}}$ (where τ_{CFL} is the timestep obtained from the Courant-Friedrichs-Levy condition). For both methods the noise is dampened to a lower level than the perturbations we add to the initial model. Excluding cones around the poles has the additional advantage that a strong timestep restriction due to the very thin (in ϕ-direction) zones at the pole can be avoided.

For the non-rotating simulations we use the first method, i.e. we set θ_0 to a value greater than zero. The first B12-like simulation, Model B123-a, is rather limited in terms of the angular resolution (3°) and the covered solid angle ($\theta_0 = 22.5°$, i.e. $\Omega_{tot} \approx 3.7\pi$), but extends up to $t = 1\,\mathrm{s}$. For the second simulation, Model B123-b, we increased the angular resolution to 2° and extended the numerical grid to include almost the full sphere ($\theta_0 = 5°$, i.e. $\Omega_{tot} \approx 3.99\pi$). In this simulation we followed the evolution only up to $t = 0.5\,\mathrm{s}$. Even for this shorter duration the simulation required 85000 CPU hours – more than three months of continuous computation on a 32 processor IBM p690. For the rotating simulation, Model R103F, we included the full solid angle ($\theta_0 = 0$) and had therefore to reduce the CFL factor to 0.3. At an angular resolution of 4° we simulated about 400 ms post-bounce evolution.

5.1.3 Additional 2D simulations

To allow for a comparison of two- and three-dimensional simulations (see Section 5.2.2) we also calculated several sets of accompanying two-dimensional models. This was necessary to disentangle the origins of the differences between the models. These differences are not only caused by the different dimensionality, but can also depend on the angular resolution and the size of the numerical grid. A further problem is the chaotic dependence of the morphology on the initial perturbations. All of the interesting global quantities that we want to compare depend more or less strongly on the morphology. For a clean comparison it is therefore advisable to use averages of these quantities obtained from several sets of two-dimensional models, which differ only in the random numbers used for the initial perturbations.

Adopting this strategy we performed six sets of B12-like 2D simulations, four sets including the full solid angle ($\theta_0 = 0°$, i.e. $\theta_{tot} = 180°$) and angular resolutions of $\Delta\theta = 3°$, $2°$, $1°$ and $0.5°$, as well as two sets with a reduced azimuthal range, $\theta_0 = 22.5°$ ($\theta_{tot} = 135°$, $\Delta\theta = 3°$) and $\theta_0 = 5°$ ($\theta_{tot} = 170°$, $\Delta\theta = 2°$). The numerical grids of the latter two sets are, except for the longitudinal part, equal to the grid of the two B12-like three-dimensional models. For the models with $\Delta\theta = 0.5°$ the radial grid consists of 800 zones, whereas for all other models 400 radial zones have been used. Each set contains at least five models. The set with the 'standard resolution' of 400×180 zones contains twelve models. As a naming convention for the model sets we use "$\theta_{tot}[°]$ - $\Delta\theta[°]$".

We did not produce a comparably extensive set of 2D models for comparison with the rotating 3D Model R103F, but we performed at least six rotating 2D Models with the same boundary conditions, three with the same radial and angular (in θ-direction) resolution as the 3D model and three with $\Delta\theta = 0.5°$ and twice the radial resolution as the 3D model.

5.2 Non-rotating models

The most important quantities of all non-rotating 2D and 3D models discussed in this section are listed in Tab. 5.2. To allow for a reasonable comparison of models containing the full solid angle ($\Omega_{tot} = 4\pi$) and models covering only a part of the latter, we normalise all quantities, which are proportional to the grid size, e.g. $E_{\mathrm{exp}} \rightarrow E_{\mathrm{exp}} \cdot 4\pi/\Omega_0$. Before we compare two- and three-dimensional morphology and anisotropy in detail, we will first discuss the influence of the grid resolution and grid size on the evolution of global quantities.

5.2.1 Evolution of global quantities

Simulations should be run at a resolution for which they can be regarded to be numerically converged, i.e. the results should not change if the resolution is increased further. In one spatial dimension convergence can be tested easily by performing a few simulations with different resolutions, which are not very time-consuming. Using the PPM method and spherical coordinates a radial resolution (radial zone width divided by zone radius) increasing from $\mathrm{d}r/r = 0.5\%$ at the inner boundary to about $\mathrm{d}r/r = 1\%$ for larger radii (which requires 400 radial zones) is sufficient to achieve convergence for the present problem. The higher resolution at the inner boundary is required for several reasons: The resolution decreases with time, as the inner boundary contracts and the zone width stays constant. Furthermore, the neutrino transport routine fails if the change of optical depth per zone becomes too large. And finally, within the first second after bounce a steep density gradient forms at the neutron star surface. To resolve this gradient with

Table 5.1: Several quantities characterising the non-rotating two- and three-dimensional models with the same boundary conditions as model B12. The gain region mass M_{gain} is given for $t = t_{\rm exp}$. Explosion energy $E_{\rm exp}$, neutron star mass $M_{\rm ns}$, radius $R_{\rm ns}$, velocity $|v_{\rm ns}|$ and acceleration $a_{\rm ns}$ as well as the anisotropy parameter $\alpha_{\rm gas}$ are given for $t = 1\,{\rm s}$ (and therefore not available for Model B123-b).

Model	θ_0 [°]	$\Delta\theta$ [°]	t_{sim} [s]	$t_{\rm exp}$ [s]	$\Delta M_{\rm gain}^{\rm exp}$ [$M_\odot$]	$E_{\rm exp}$ [B]	$M_{\rm ns}$ [$M_\odot$]	$R_{\rm ns}$ [km]	$\lvert v_z^{\rm ns}\rvert$ [km/s]	$a_z^{\rm ns}$ [km/s^2]	$\alpha_{\rm gas}$
B123-a	23	3	1.0	0.272	0.019	0.36	1.383	37.2	113.5	73.8	0.11
B123-b	5	2	0.55	0.273	0.019	–	–	–	–	–	–
B12-z45	23	3	1.0	0.371	0.017	0.24	1.417	37.2	45.8	-59.6	0.07
B12-z45-1	23	3	1.0	0.336	0.013	0.24	1.417	37.2	15.8	36.0	0.02
B12-z45-2	23	3	1.0	0.364	0.013	0.25	1.411	37.2	26.8	53.9	0.04
B12-z45-3	23	3	1.0	0.342	0.015	0.29	1.405	37.2	73.3	-98.9	0.09
B12-z45-4	23	3	1.0	0.384	0.014	0.27	1.416	37.2	120.4	227.5	0.16
B12-z60	0	3	1.0	0.347	0.015	0.26	1.410	37.2	153.9	-311.1	0.19
B12-z60-1	0	3	1.0	0.250	0.018	0.28	1.389	37.2	15.0	268.7	0.02
B12-z60-2	0	3	1.0	0.306	0.017	0.26	1.425	37.2	270.0	-297.2	0.31
B12-z60-3	0	3	1.0	0.256	0.019	0.31	1.393	37.2	247.4	-568.6	0.25
B12-z60-4	0	3	1.0	0.312	0.015	0.26	1.408	37.2	210.3	366.5	0.25
B12-z85	5	2	1.0	0.324	0.014	0.26	1.411	37.2	218.2	298.5	0.25
B12-z85-0	5	2	1.0	0.302	0.017	0.32	1.400	37.2	37.2	170.7	0.04
B12-z85-1	5	2	1.0	0.276	0.018	0.26	1.406	37.2	117.2	166.3	0.15
B12-z85-2	5	2	1.0	0.297	0.014	0.30	1.397	37.2	76.7	-103.7	0.08
B12-z85-3	5	2	1.0	0.289	0.016	0.26	1.410	37.2	8.1	-43.9	0.01
B12-z85-4	5	2	1.0	0.285	0.017	0.31	1.383	36.9	48.9	54.0	0.05
B12-z90-1	0	2	1.0	0.275	0.018	0.24	1.407	37.2	105.1	-68.9	0.13
B12-z90-2	0	2	1.0	0.252	0.017	0.30	1.395	37.2	130.6	273.3	0.13
B12-z90-3	0	2	1.0	0.282	0.017	0.30	1.408	37.2	160.7	346.0	0.17
B12-z90-4	0	2	1.0	0.241	0.018	0.31	1.397	37.2	260.0	391.9	0.26
B12-z90-b0g	0	2	1.0	0.248	0.020	0.36	1.398	37.2	245.1	-229.3	0.22
B12-z90-b1g	0	2	1.0	0.258	0.019	0.28	1.385	36.9	46.7	13.7	0.05
B12-z90-b2g	0	2	1.0	0.242	0.018	0.32	1.378	36.7	130.0	-199.3	0.12
B12-z90-0	0	2	1.0	0.266	0.019	0.32	1.398	37.2	301.0	258.9	0.29
B12	0	1	1.0	0.220	0.020	0.37	1.399	37.3	389.5	-372.4	0.32
B12-1	0	1	1.0	0.228	0.021	0.33	1.377	37.7	72.8	47.9	0.07
B12-2	0	1	1.0	0.212	0.020	0.39	1.391	38.1	85.8	345.7	0.07
B12-3	0	1	1.0	0.207	0.021	0.38	1.369	37.2	242.0	464.3	0.18
B12-4	0	1	1.0	0.216	0.019	0.35	1.385	37.2	115.1	-154.2	0.10
B12-5	0	1	1.0	0.211	0.022	0.33	1.387	37.2	206.9	-483.1	0.19
B12-m1	0	1	1.0	0.226	0.020	0.36	1.384	37.2	56.8	-208.2	0.06
B12-m2	0	1	1.0	0.222	0.019	0.31	1.385	37.2	100.0	-63.5	0.10
B12-m3	0	1	1.0	0.210	0.022	0.38	1.388	37.2	272.6	91.9	0.23
B12-m4	0	1	1.0	0.209	0.021	0.35	1.378	37.1	104.3	-197.2	0.09
B12-m5	0	1	1.0	0.219	0.020	0.35	1.389	37.2	365.6	219.1	0.32
B12-m6	0	1	1.0	0.229	0.020	0.36	1.395	37.2	334.1	-462.9	0.30
B12-z360	0	0.5	1.0	0.200	0.020	0.31	1.380	37.9	169.7	357.7	0.16
B12-z360-1	0	0.5	1.0	0.219	0.022	0.34	1.383	37.9	149.3	-84.4	0.13
B12-z360-2	0	0.5	1.0	0.218	0.020	0.34	1.403	38.2	256.5	341.6	0.23
B12-z360-3	0	0.5	1.0	0.219	0.019	0.40	1.395	38.1	300.6	-147.9	0.24

sufficient accuracy, one has to avoid that the logarithm of the density changes by more than 1/10 per zone (R. Buras, personal communication).

In fact, due to the chaotic dependence on the initial perturbations numerical convergence in its strict sense cannot be achieved for the present problem in two or three spatial dimensions. Even the slightest changes in the initial state, which are unavoidable when the resolution is increased, will yield different final shock morphologies. In this case the only possible check for convergence is a comparison of quantities like the explosion energy and the mean shock radius, which depend only weakly on the morphology of the explosion. To minimise the influence of the random morphology one can consider averages of these quantities averaged over a set of models that use the same numerical grid and different initial perturbations. Although the 33 two-dimensional models we performed for this purpose cannot provide excellent statistics, they demonstrate some important dependencies on resolution and angular grid size quite clearly.

From Figs. 5.1 and 5.2 two fundamental trends are obvious: Both a lower resolution and a reduced angular grid size lead to a delayed onset of the explosion, a slower shock expansion and lower explosion energies. The averaged quantities of the models sets with $\Delta\theta = 1^\circ$ and $\Delta\theta = 0.5^\circ$ show a very similar evolution, the differences are much smaller than the variation within the sets. For coarser resolutions and narrower angular grids the differences in the averaged quantities become similar to the scatter within the model sets. Going from $\Delta\theta = 2^\circ$ to $\Delta\theta = 3^\circ$ at $\theta_{tot} = 180^\circ$ has a similar effect as changing from $\theta_{tot} = 180^\circ$ to $\theta_{tot} = 170^\circ$ at $\Delta\theta = 2^\circ$. However, there are no significant differences between the shock radii in the first 50 ms, only the mean convective velocity

$$v_{\mathrm{conv}} = \sqrt{\frac{E^{\mathrm{gain}}_{\mathrm{kin,lat}}}{\Delta M_{\mathrm{gain}}}} \tag{5.1}$$

(where $E^{\mathrm{gain}}_{\mathrm{kin,lat}}$ and ΔM_{gain} are the lateral kinetic energy and the mass contained in the gain region, respectively) deviates slightly in this phase. For $t > 50\,\mathrm{ms}$, v_{conv} increases much faster in the better resolved models. Consequently the shock radius and the gain region mass become larger for these models and the efficiency of neutrino energy deposition is higher. Thus the better resolved models explode earlier and the gain region mass at the onset of the explosion, $\Delta M_{\mathrm{gain}}(t_{\mathrm{exp}})$, is larger. The variation within a model set of this quantity, which is about $0.01\,M_\odot$, is consistent with the scatter in the explosion energy at $t = 1\,\mathrm{s}$ of about $0.1 \cdot 10^{51}$ erg. Considering all models, the scatter is about $0.2 \cdot 10^{51}$ erg, i.e. the most energetic models have twice the explosion energy of the least energetic models. The neutron star mass is also affected by the varying explosion time scale. The explosion stops the efficient accretion of matter, the subsequent accretion of matter through one or a few remaining downflows is much slower. Thus the neutron star masses of the better resolved, early exploding models are smaller.

How do grid resolution and grid size lead to this delayed onset of the explosion? Initially the solution is nearly spherical symmetric, so angular resolution and grid size do not play a role and the models evolve nearly identically. The onset of small-scale (high-mode) convection does not change this significantly. The convective growth rate increases with decreasing wave length, and therefore the convection grows somewhat faster in the better resolved models. However, in the presence of high-mode convection the situation is still nearly spherical symmetric and the convection is not yet important for the total energetics. This changes when the convective growth becomes non-linear and quickly-growing convective bubbles start to influence the shock shape. At $t = 75\,\mathrm{ms}$ most of the models have developed 3 to 5 large bubbles separated by thin downflows. In the models including the full solid angle one or two of the bubbles near the symmetry axis grow significantly faster than the other bubbles and start to deform the shock earlier. The faster non-linear growth of bubbles near the axis is a consequence of the axisymmetry: At the axis

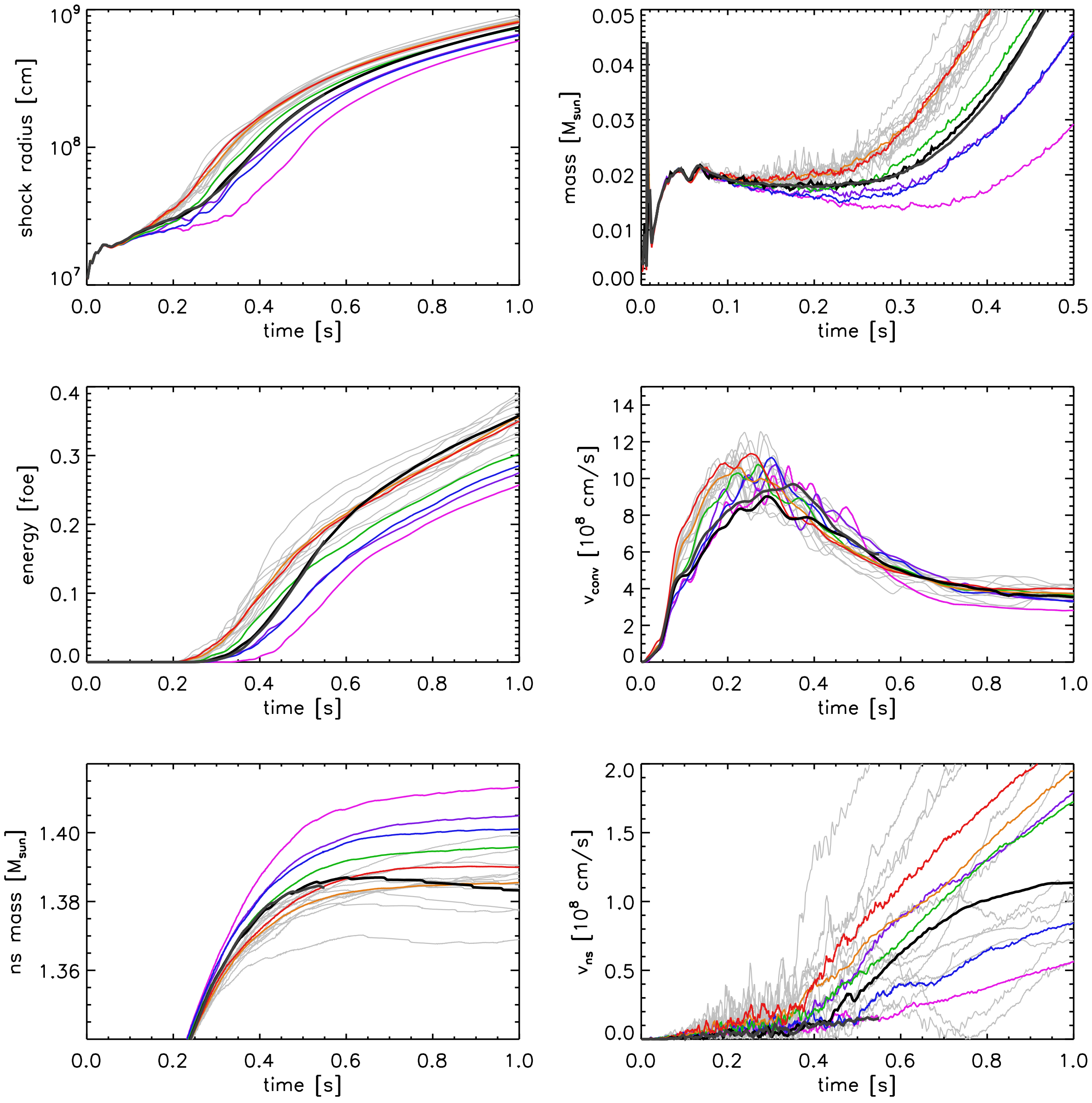

Figure 5.1: Evolution of the average shock radius, the gain region mass, the explosion energy, the convective velocity and the neutron star mass (from top to bottom row) for the models listed in table 5.2. The right column shows the evolution of the quantities for each individual model, whereas the in left column the average values for sets of models with the same resolution and grid size are displayed. The black and gray lines correspond to the three-dimensional models, the coloured lines correspond to the two-dimensional model sets (see upper left panel – the naming convention for the model sets is '$\theta_{tot}[°]$ - $\Delta\theta[°]$').

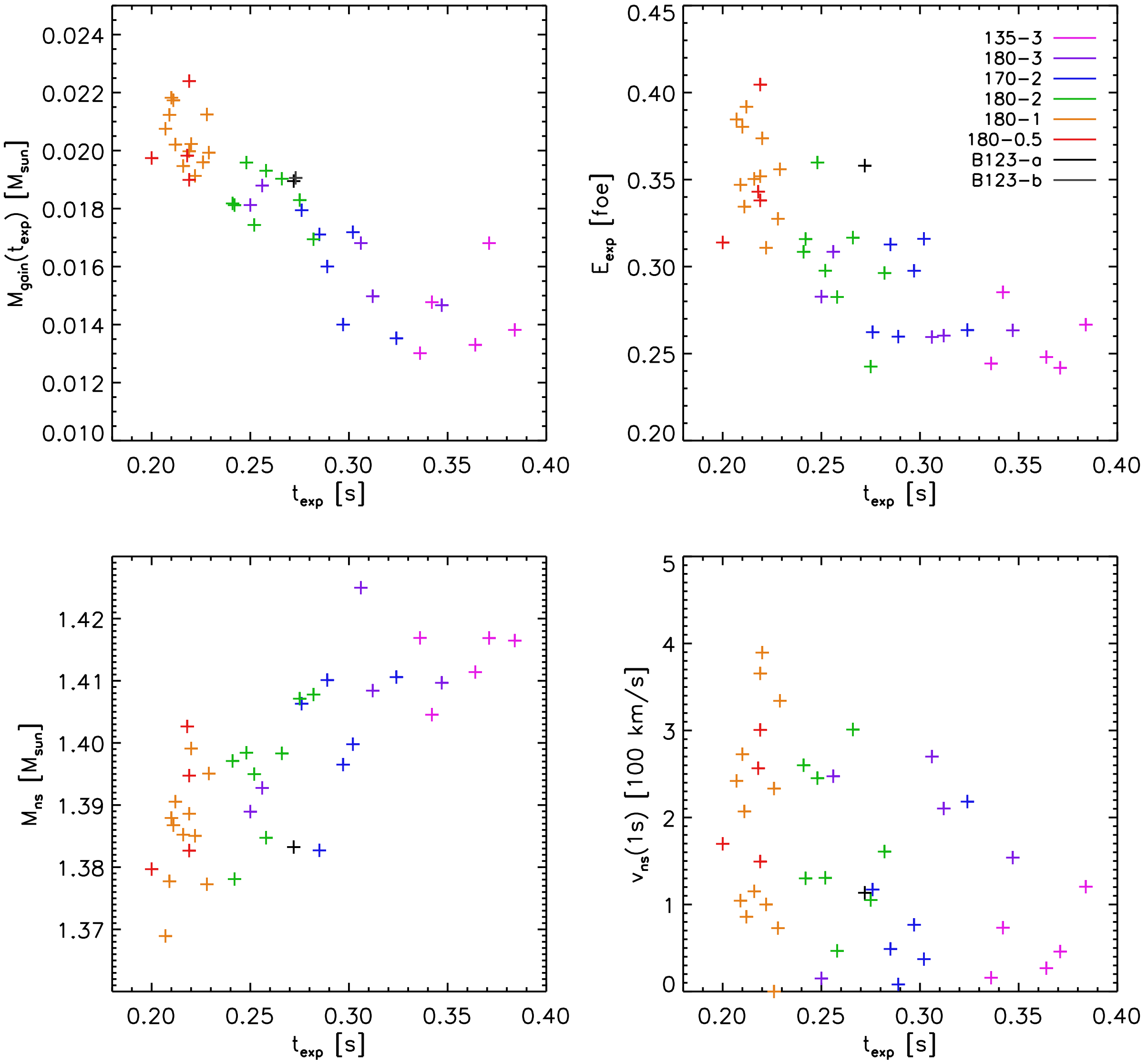

Figure 5.2: Correlations between several quantities and the explosion time scale $t_{\rm exp}$. The gain mass at the onset of the explosion and the explosion energy at $t = 1\,$s decline with an increasing explosion time scale, which depends clearly on the resolution and the grid size. The neutron star mass at $t = 1\,$s increases with $t_{\rm exp}$, because for $t > t_{\rm exp}$ the accretion is strongly suppressed. The average neutron star velocity seems to become lower with declining resolution (i.e. increasing $t_{\rm exp}$). However, there are to few low-resolution models to quantify the latter statement.

the two-dimensional bubbles have the same geometry as three-dimensional bubbles, whereas equatorial bubbles are ring-like. The different drag coefficients associated with these geometries lead to different non-linear growth rates (see Kane et al. 2000). If the polar regions are omitted ($\theta_0 > 0$), the faster-growing polar bubbles are suppressed and the excitation of convective modes as well as the deformation of the shock are delayed. This explains the difference between the model sets 180-2 / 170-2 and 180-3 / 135-3. Already $\theta_0 = 5°$ seems enough to suppress the faster polar growth, a larger θ_0 should not make a difference in this respect.

Like reducing the grid size, also reducing the resolution results in a delayed onset of the explosion. The very similar average evolution curves of total quantities for resolutions of 1° and 0.5° suggest that these models are nearly converged. What is causing the differences for coarser resolutions? As already mentioned, for the higher resolutions smaller wavelengths are resolved, for which the convective growth rates are higher. This explains the slightly faster increase of v_{conv} for the high-resolution models in the first 60 ms. However, the strongest differences arise only after this phase, when convection has become non-linear and low convective modes, i.e. large bubbles, dominate. The latter should be resolved quite accurately even on rather coarse grids. Yet there is feature that requires high resolution also in this phase: Due to the large pressure gradient in the vicinity of the neutron star the lowest parts of the downflows are compressed into very thin accretion funnels with a thickness of only a few degree. The matter which is accreted onto the neutron star and generates accretion luminosity – an important contribution to the total luminosity – must go through these funnels. It is therefore likely that these thin downflows must be resolved adequately to reach numerical convergence. Angular resolutions of 2° and 3° seem to be below the required minimum resolution.

For three-dimensional simulations it is not possible to find the resolution needed for numerical convergence by performing resolution studies. With the available CPU time only two simulations could be carried out, with angular resolutions that are not sufficient for convergence in two dimensions. In the first 400 ms the global quantities (Fig. 5.1) for model B123-b lie between those of the model sets 180-2 and 170-2. This is what one could expect, given that model B123-b also has an angular resolution of 2° and covers the same solid angle as the models of the 170-2 set. However, one would not expect that model B123-a with its lower resolution and covering a smaller solid angle, shows almost exactly the same behaviour and is not delayed, compared to model B123-b. This is clearly different from the two-dimensional case, where the delay between model sets 180-1 and 180-2 or 180-2 and 180-3 is obvious.

It is quite surprising that global quantities of the two models like the shock radius, the gain region mass and the explosion energy show almost exactly the same evolution. The differences between the global quantities of these two single models are as small as the differences between the averaged quantities for the models sets 180-0.5 and 180-1, which we regarded as nearly converged. If this coincidence is not accidental, it suggests that numerical convergence could be reached in three dimensions at a lower angular resolution than in two dimensions. The following discussion of the morphological differences between two- and three-dimensional models will yield a possible explanation.

5.2.2 Convective overturn

Considering the evolution of global quantities the three-dimensional are quite similar to the two-dimensional models. For all the global quantities shown in figure 5.1 one can find a two-dimensional model showing roughly the same behaviour as Models B123-a or B123-b. However, the flow developing in three dimensions shows some significant differences, compared to the two-dimensional case, which has been discussed in detail in Sect. 3.2.1.

Convection sets in at the same time in three as in two dimensions, and during the first 70 ms also the mean convective velocity evolves very similarly (Fig. 5.1). In the subsequent phase v_{conv} increases roughly as in the corresponding 2D model sets 170-2 and 135-3. The maximum of v_{conv} is reached at about 300 ms, shortly after the onset of the explosion. In the three-dimensional models it amounts to $v_{\mathrm{conv}} \approx 9 \cdot 10^8$ cm/s, whereas in two dimensions we find maximum average values of $v_{\mathrm{conv}} \approx 11 \cdot 10^8$ cm/s for the highest angular resolutions. These differences seem do not appear significant, considering that the variations of v_{conv} with time and within a model set are rather large.

However, obvious differences exists in the number of the buoyant bubbles: In three dimensions the convective instability is not restricted to the latitudinal direction any more, since a second angular direction is available. If the growth of convection from small to large scales proceeds similar in two and three dimensions, and we find N convective bubbles in a two-dimensional model at a certain time, we would expect to find of the order of N^2 bubbles at this time in a three-dimensional version of this model. Indeed we find that the ratio of $N : N^2$ for the number of bubbles in two- and three-dimensional models is roughly consistent with our simulations. E.g. at $t = 75$ ms about $15 \ldots 20$ bubbles with angular diameters of about $20 \ldots 30°$ are present in models B123-a and B123-b. At the same time we find typically 3–5 bubbles in the two-dimensional models. For later phases it is hard to verify this relation, because the convective structures become very complex and individual bubbles cannot be clearly distinguished.

A further difference in three dimensions concerns the morphology of the downflows between these bubbles. In two dimensions the downflows must extend over the full longitudinal range, due to the assumed axisymmetry, i.e. they are in general two-dimensional, sheet-like structures. In particular downflows near the equator can be considered as accretion disks and only downflows at the poles are funnel-like (or one-dimensional – in the sense we used two-dimensional for sheet). In three dimensions the sheet-like character of the downflows is retained – at least initially and for a certain radial range. Without the restriction of axisymmetry, a network of sheet-like downflows forms between the rising bubbles. This network can be seen nicely in Figs. 5.3 to 5.6 (in particular for $t = 60$ ms and $t = 80$ ms), which display the angular distributions of the maximum and minimum post-shock velocity. In these figures one can also observe that in the regions where several of the thin sheets intersect, somewhat thicker accretion funnels form, in which the flow becomes faster. As the velocity in the downflows is approximately the free-fall velocity, $\sqrt{2GM/r}$, the larger (negative) values indicate that these accretion funnels are able to reach down to lower radii than the sheet-like downflows, which initially occupy the same radial range as the rising bubbles. This means there is a transition from funnel-like downflow-structures at low radii to sheet-like structures further outward. During the merging of bubbles the accretion funnels become thicker and reach the neutron star surface, whereas the sheet-like downflow regions remain at larger radii (above 100 km). While the thickness of these sheet-like downflows is similar in two and three dimensions, there are significant differences at smaller radii. At $t = 75$ ms the angular diameter of the lower ends of the downflows in models B123-a and B123-b is about 10°–20°, similar to the polar downflows in two-dimensional simulations. In contrast to this, the downflows not located directly at the poles in two-dimensional simulations are only a few degrees thick near their lower ends.

The thinness of the downflows at low radii in two-dimensional simulations is a result of the axisymmetry. Due to the latter the downflows are forced to extend over the full longitudinal range, whereas in the latitudinal direction there is no such restriction. For lower radii this difference becomes more important: The matter streaming towards the neutron star is compressed, because the pressure in the matter surrounding the downflow increases strongly. In particular for $r < 200$ km the pressure gradient becomes very steep (when the composition of the surrounding medium changes from alpha particles to free nucleons) and the solid angle occupied

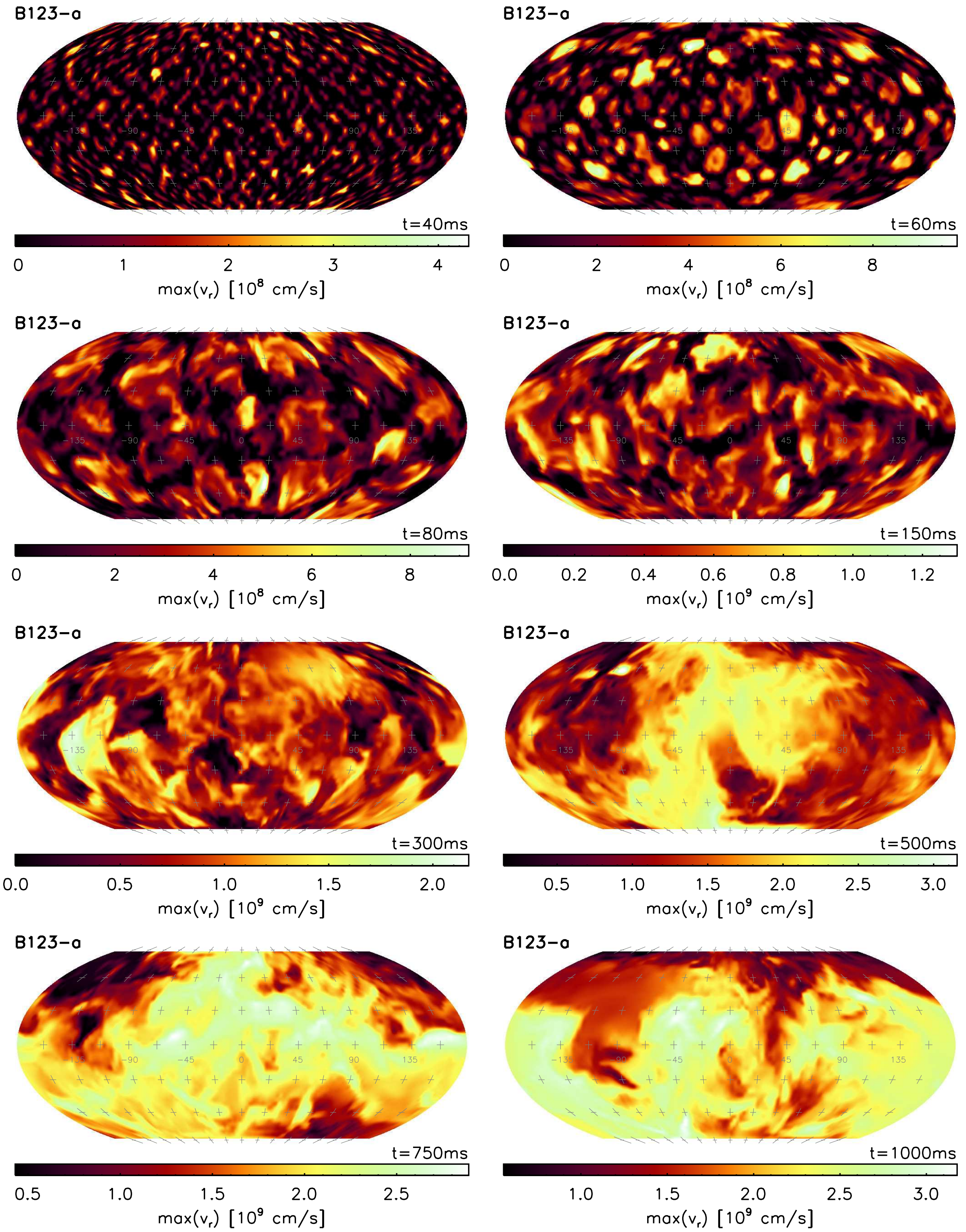

Figure 5.3: Maximum radial velocity $v_{max}(\theta,\phi) := \max\{v_r(r,\theta,\phi)\,|\,r \in [R_{\rm ib}, R_{\rm ob}]\}$ at several times for model B123-a. At $t = 40\,$ms numerous small, buoyant bubbles have formed and quickly merge to larger structures. At $t = 75\,$ms there are about 15...20 rising bubbles left with angular diameters of about 20...30°. In the subsequent evolution structures merge much slower and become more complex, so that individual bubbles cannot be distinguished any more. After $t \approx 400\,$ms a large area with high velocities develops around $\theta = 0°$, $\phi = 0°$, whereas in the opposite hemisphere the expansion of the ejecta is hampered by downflows. At $t = 1\,$s the situation is dominated by a single downflow wrapped around the northern cone ($\theta = 22.5°$).

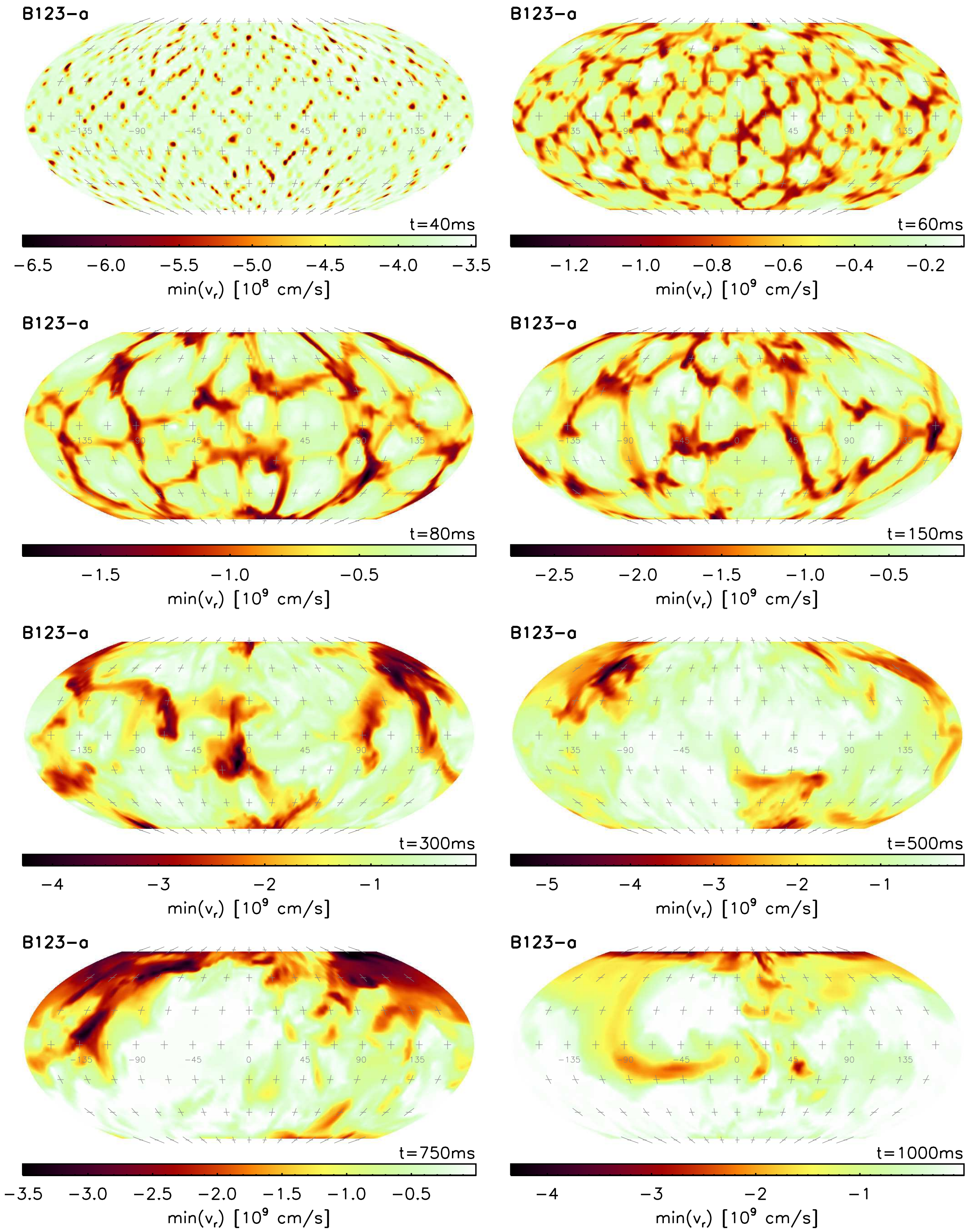

Figure 5.4: Minimum radial velocity $v_{min}(\theta,\phi) := \min\{v_r(r,\theta,\phi)\,|\,r \in [R_{\rm ib}, R_{\rm s}(\theta,\phi)]\}$ in the post-shock region at several times for model B123-a. As the velocity in the downflow regions is of order of the free-fall velocity $-\sqrt{2GM/r}$, the areas with the highest absolute value of the velocity are found at the lowest radii. The bright-coloured downflow regions between the rising bubbles are initially two-dimensional, wall-like structures. At the intersections of these walls one-dimensional accretion funnels develop, which obtain larger velocities and reach down deeper than the walls. The merging of convective structures leaves only a few of these accretion funnels, and a large downflow-free area forms. For $t > 0.5\,$s one large downflow at low latitudes dominates this model.

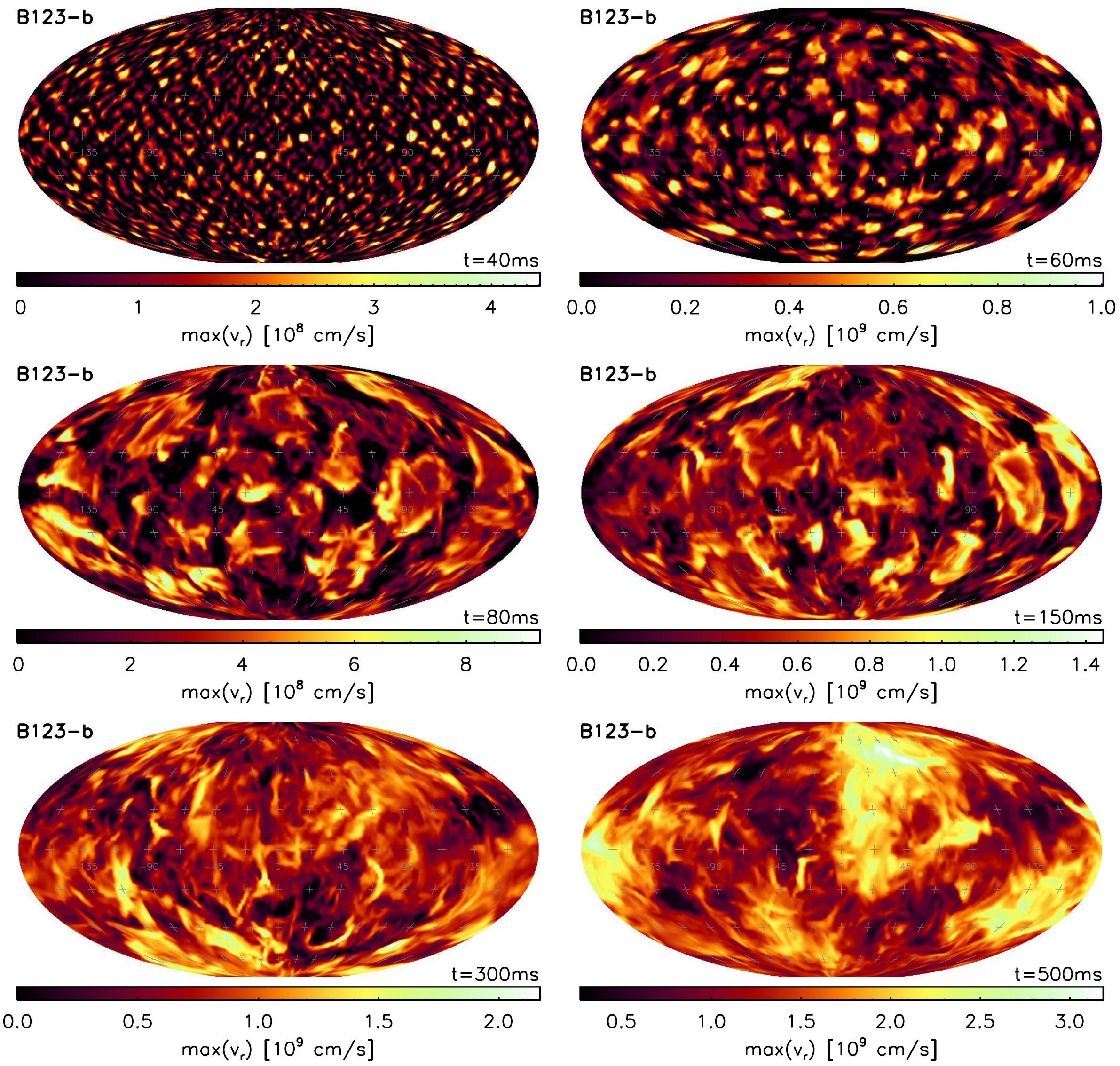

Figure 5.5: Like Fig. 5.3, but for model B123-b. In the first 300 ms there are no obvious differences compared to model B123-a, except that due to the higher resolution slightly more small-scale structures are visible in model B123-b. However, in the subsequent evolution the latter is not developing a large downflow-free area with high velocities as it is present in model B123-a.

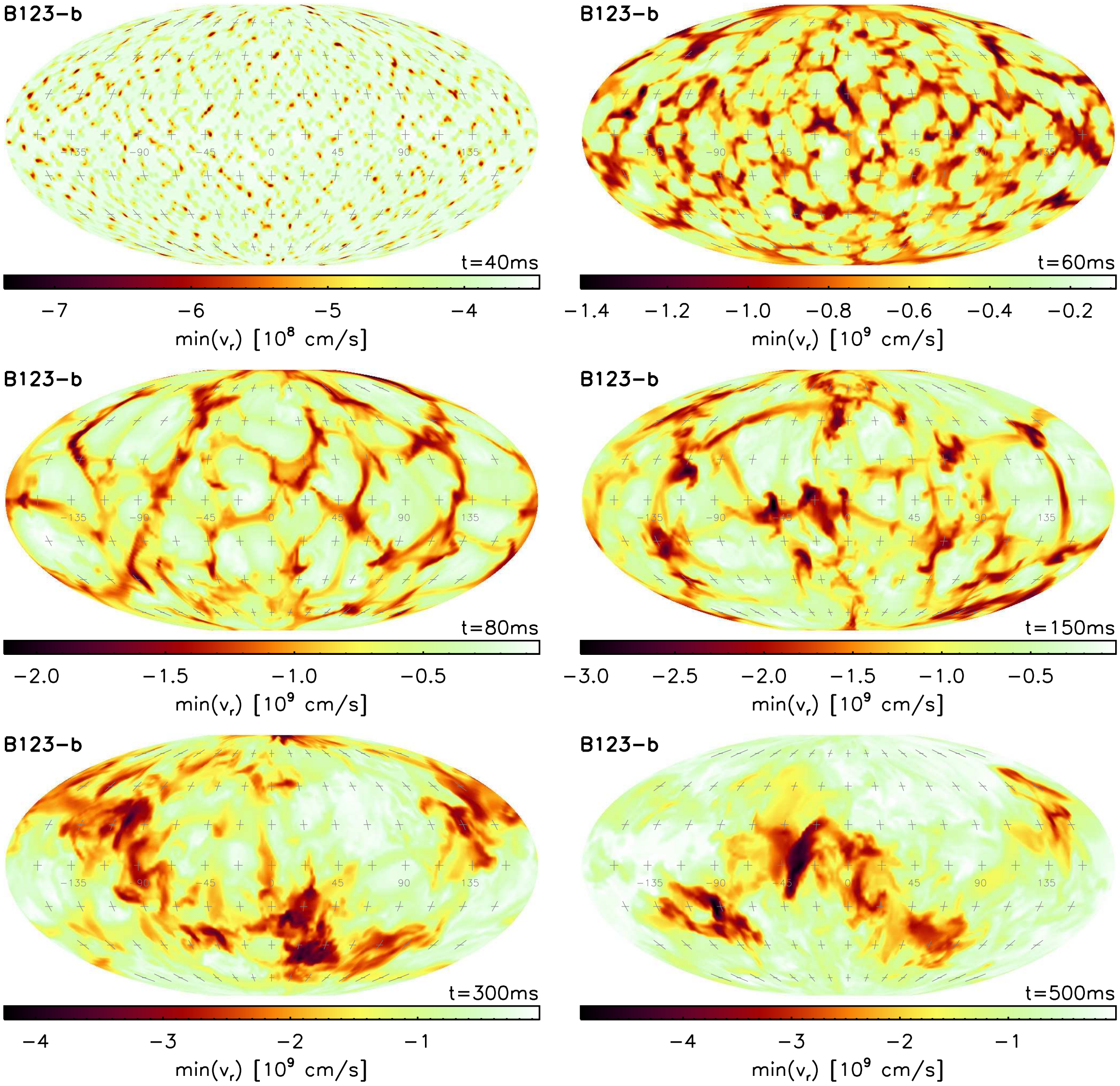

Figure 5.6: Like Fig. 5.4, but for model B123-b. At $t = 0.5\,\mathrm{s}$ there is one strong downflow at $\phi \approx -40°$, $\theta \approx 90°$ and two much weaker ones at $\phi \approx -90°$, $\theta \approx 110°$ and $\phi \approx 160°$, $\theta \approx 60°$. These three downflows occupy only a small solid angle at low radii ($r < 100\,\mathrm{km}$), but are connected to a large structure at higher radii, which extends over a significant fraction of the full numerical grid.

by the downflows is significantly reduced. This reduction can only occur in latitudinal direction and results in extremely thin downflows. If the downflows occupy the same solid angle in two and three dimensions (which is approximatively the case, see below), then the downflows in three-dimensional simulations will in general be thinner in longitudinal direction – they are not forced to extend over the full 2π – and therefore thicker in azimuthal direction.

To quantify this difference, one has also to consider that one downflow in a two-dimensional simulation will correspond to N downflows in a three-dimensional simulation, analogously to the number ratio $N : N^2$ of the buoyant bubbles. Assuming we find in a two-dimensional simulation at a certain radius a downflow with mass flux $\dot{M}$ and solid angle $\Delta\Omega$, then we should find in the corresponding three-dimensional calculation N downflows with mass fluxes $\dot{M}/N$ and solid angles $\Delta\Omega/N$. Near the equator the solid angles can be written as $\Delta\Omega \approx \Delta\theta_{2d} \cdot \pi$ and $\Delta\Omega/N \approx \Delta\theta_{3d} \cdot \Delta\phi_{3d}$, where $\Delta\theta$ is the azimuthal and $\Delta\phi$ the longitudinal thickness of the downflow. For the funnel-like downflows in three dimensions $\Delta\phi_{3d} \approx \Delta\theta_{3d}$, which yields

$$\Delta\theta_{3d} = \sqrt{2\pi\,\Delta\theta_{2D}/N} \tag{5.2}$$

For $t = 75\,\mathrm{ms}$ we find $N \approx 5$ and $\Delta\theta_{2d} \approx 3°$, and equation 5.2 yields $\Delta\theta_{3d} \approx 14°$. The thickness of the funnel-like downflows in the three-dimensional models (see figures 5.4 and 5.6) is in the same range as this prediction.

The thicker downflows in three-dimensional simulations may be the reason for the almost identical behaviour of the global quantities for models B123-a and B123-b (Fig. 5.1): In contrast to the thin downflows in two-dimensional models, the thicker downflows in three dimensions could be resolved accurately enough already with an angular resolution of 3°, so that an increase of the resolution to 2° will have little effect. However, to demonstrate that the three-dimensional models are really nearly numerically converged certainly more than two models are required, and it is not clear if this resolution is sufficient for later stages of the evolution. Even if the three-dimensional models are nearly converged, another interesting question remains to be answered: Why are these models delayed, compared to the two-dimensional models which we also regard as nearly converged? A possible explanation is the different convective growth rate for polar and non-polar bubbles in the two-dimensional simulations. It has already been discussed that two-dimensional models with fast-growing polar bubbles explode earlier than two-dimensional models, which do not contain the poles. This is, because the variation of the growth rate with the azimuthal angle leads to a faster excitation of low modes and an earlier shock deformation. While in three dimensions the non-linear growth rate should be comparable to the polar growth rate in two dimensions, the dependence on the azimuthal angle is missing – the growth rate near the poles should be the same as near the equator. Also the additional excitation of low modes is therefore missing in the three-dimensional models. However, like for the two-dimensional simulations this does not mean that the models cannot become highly anisotropic – there is plenty of time before the onset of the explosion to develop global modes.

5.2.3 Neutrino-driven outflows

Up to the onset of the explosion, the energetics of the two- and three-dimensional simulations are very similar. The lateral kinetic energy in the gain region $E^{\mathrm{gain}}_{\mathrm{kin,lat}}$ (and the associated convective velocity v_{conv}, see Figure 5.1) is slightly lower for the three-dimensional models, compared to the model 2D sets with 2° and 3° angular resolution. However, much more important for the total energetics is the potential recombination energy of the matter in the gain region. This energy, which is about $5\,\mathrm{MeV}$ per nucleon (see Section B) is converted to internal and kinetic energy after explosion has set in and yields about half of the total explosion energy after one second

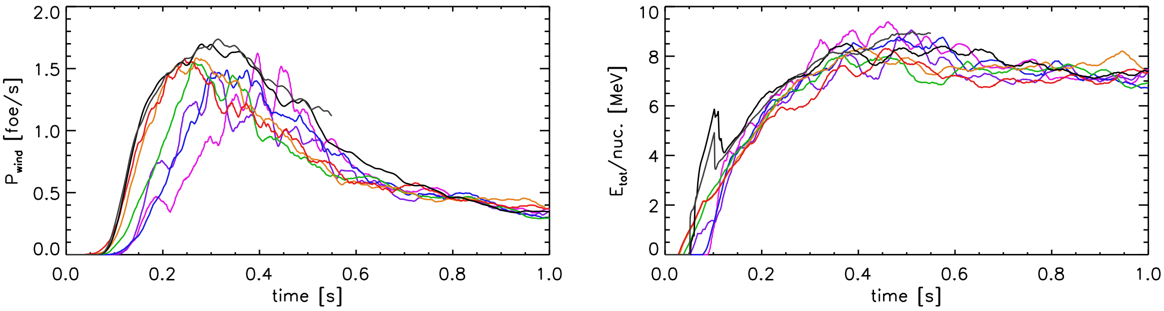

Figure 5.7: *Left panel:* Time evolution of the wind power, measured at 200 km. For $t \in [0.4\,\mathrm{s}, 0.6\,\mathrm{s}]$ the power is about $0.25 \cdot 10^{51}$ erg/s higher for the three-dimensional than for the two-dimensional models with high resolution. For $t > 0.6$ s this difference vanishes. *Right panel:* Evolution of the total energy (including recombination energy) per nucleon in the wind at 200 km. On average the energy is only slightly higher for the three-dimensional models in $[0.4\,\mathrm{s}, 0.6\,\mathrm{s}]$. This can not explain the difference in the wind powers, which must therefore be caused mainly by different mass fluxes in the wind.

(for the "standard" boundary contraction). The mass of the gain layer in the three-dimensional models is comparable to those of the 2D model sets 180-2 and 170-2 (Fig. 5.1). The contribution of the recombination energy to the total explosion energy should therefore be almost the same in two and three dimensions.

The other main contributor to the explosion energy is the neutrino driven wind. Between $t \approx 400$ ms and $t \approx 600$ ms the increase of explosion energy due to the wind is significantly larger in the three-dimensional models. Compared to the 2D models of set 170-2, which have a similar explosion time scale, the three-dimensional models gain about $0.05 \cdot 10^{51}$ erg more explosion energy in this period. This is due to the wind power, which is about $0.3 \cdot 10^{51}$ erg/s (i.e. about 30%) higher for these models for $0.4\,\mathrm{s} < t < 0.6\,\mathrm{s}$ (Fig. 5.7, left panel). As the total energy per nucleon in the wind is similar for the two- and the three-dimensional models (Fig. 5.7, right panel), a higher mass flux in the wind is required to explain the higher wind power of the three-dimensional models. Indeed the wind mass flux is about $0.02\,M_\odot$/s larger in the latter (Fig. 5.8, left panel). As furthermore the mass flux in the downflow is slightly weaker (Fig. 5.8, right panel) the accretion of mass onto the neutron star must proceed slower in three dimensions to explain the higher mass flux in the wind. In fact the neutron star mass in the three-dimensional models is increasing slower than in the two-dimensional models for $t > 0.4$ s. For $t > 0.7\,s$ the neutron star mass even declines in the three-dimensional models, whereas in two dimensions on average the neutron stars still gain mass (Fig. 5.1).

What is strengthening the wind mass flux in three dimensions, or what is hampering the wind in two dimensions? The solid angle occupied by the wind is similar in two and three dimensions, i.e. in three dimensions there is not more area available from which a wind could emanate (Fig. 5.9, left panel). However, in two dimensions there is an obstacle for the wind, which is much weaker in three dimensions: The turbulent layer above the neutron star surface that is formed by decelerated and deflected downflow matter. In two dimensions large vortices form at the "impact sites" of downflows and spread around the neutron star. At $t = 0.5$ s a significant fraction of the region between 30 km and 90 km is filled with these vortices, in which velocities of more than 10^9 cm/s are reached. The additional outward and inward going mass flux caused by the vortices is comparable to the mass fluxes in the downflow and in the wind (Fig. 5.9, right panel). In three dimensions the turbulent flow above the neutron star surface is much weaker and the large vortices are absent (Fig. 5.11).

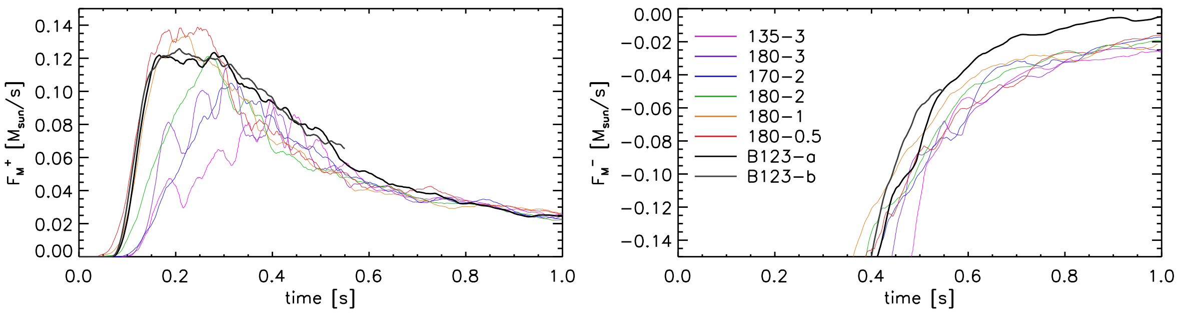

Figure 5.8: Time evolution of the positive (outward, left panel) and negative (inward, right panel) mass flux at 200 km. In $t \in [0.4\,\mathrm{s}, 0.6\,\mathrm{s}]$ the wind mass flux is about $0.02\,M_\odot$/s larger for the three-dimensional models than for the two-dimensional models with high resolution. In three dimensions the mass flux in the downflows is weaker by $0.01\ldots0.02\,M_\odot$/s for late times.

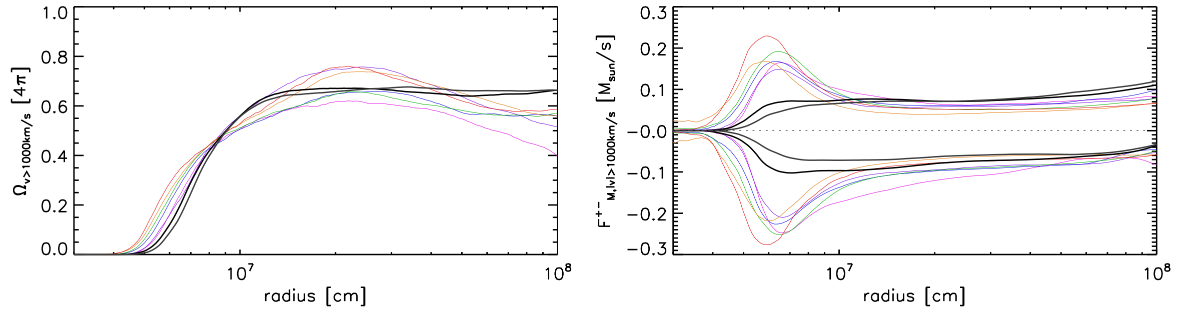

Figure 5.9: *Left panel:* Radial profile of the solid angle occupied by matter moving with $v_r > 10^8$ cm/s, time averaged over $[0.4\,\mathrm{s}, 0.6\,\mathrm{s}]$. *Right panel:* Radial profile of the positive (outward) and negative (inward) mass flux, time averaged over $[0.4\,\mathrm{s}, 0.6\,\mathrm{s}]$. The enhanced mass fluxes in the two-dimensional models for $r < 100$ km are caused by vortices above the neutron star surface, which are not present in three dimensions. For larger radii the inward mass flux is somewhat weaker and the outward mass flux somewhat stronger in the three-dimensional models.

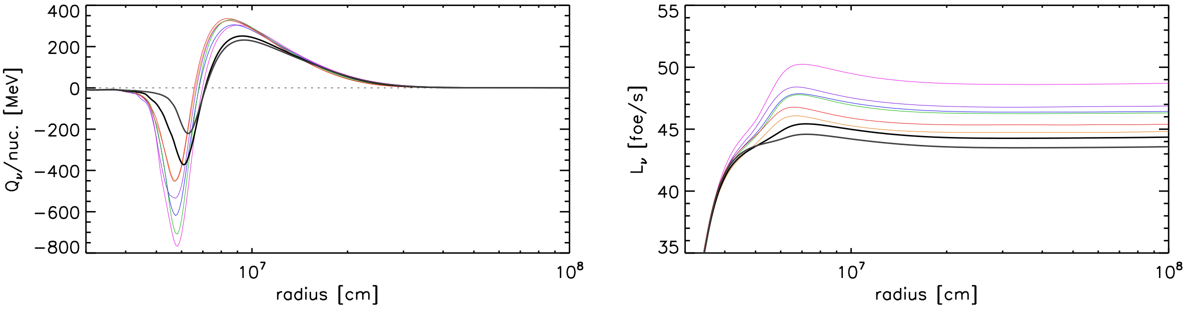

Figure 5.10: Radial profiles of the neutrino source term (per nucleon, left panel) and the neutrino luminosity (right panel), averaged over $[0.4\,\mathrm{s}, 0.6\,\mathrm{s}]$. The cooling is stronger for the two-dimensional models, which results in larger luminosities in the heating region, which starts at $r \approx 50$ km.

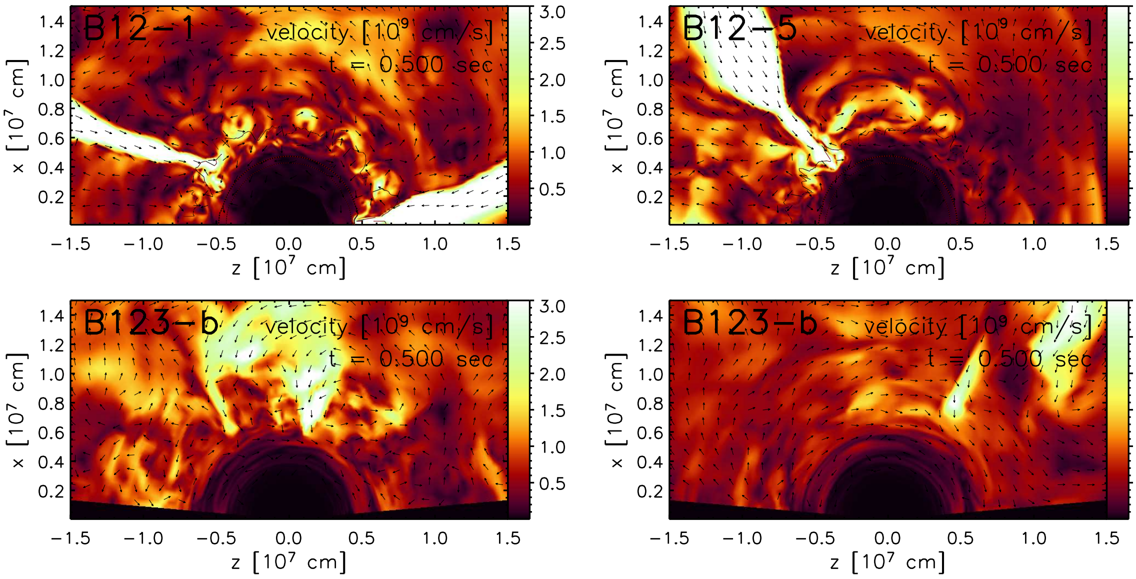

Figure 5.11: Velocity distributions at $t = 500\,\mathrm{ms}$ for the two-dimensional models B12-1 and B12-5 (upper row) and two $\phi = const$-slices from the three-dimensional model B123-b. The matter from the two downflows in model B12-1 forms a layer of vortices extending over the whole neutron star surface. In other models like B12-5 there are no clearly discernible vortices, but there is also a turbulent layer with large velocities covering a large fraction of the neutron star surface. In the three-dimensional simulations we find fast, turbulent flows only around the 'impact sites' of downflows (lower left panel), whereas in most regions above the neutron star surface the velocities remain low (lower right panel).

In two dimensions the vortices interfere with the formation of the wind: The gain radius, where neutrino heating becomes stronger than neutrino cooling, is located at 40–60 km – in the same region as the vortices. Thus a part of the matter that would in a spherical situation cross the gain radius and would become part of a neutrino-driven wind, becomes trapped in the vortices. In the outward moving parts of the vortices additional mass is transported into the region of strong neutrino heating, a process which by itself would be beneficial. However, after having gained internal energy in the heating region, this mass is brought back into the cooling region by the downward moving parts of the vortices and looses the internal energy by neutrino emission again. Thus the turbulent layer above the neutron star surface hampers the transfer of matter into the wind, thereby reducing the wind power. On average matter stays longer in the cooling region, which results in larger cooling rates per nucleon and therefore higher luminosities (Fig. 5.10) in the two-dimensional models, which also lead to somewhat higher heating rates outside of the gain radius. However, the wind power suffers more from the reduced mass flux than it gains from the slightly higher heating rate in the gain region. The differences in the wind power vanish after $t \approx 0.6\,\mathrm{s}$, when most of the downflows in the two-dimensional simulations are blown away, so that also the turbulent layers disappear.

For the models considered in this chapter the weakening influence of the turbulent layer on the wind power is not very important for the total energetics – it is a 10–15% effect. This could be different for a faster contraction of the inner boundary, where the neutrino-driven wind accounts for most of the explosion energy and downflows and wind coexist for a longer time. In this case the difference in the explosion energies of two- and three-dimensional models may become larger.

5.2.4 Global anisotropy and neutron star kicks

As in two dimensions, the convective overturn in the three-dimensional models is dominated by increasingly large structures and the number of bubbles and downflows decreases (Fig. 5.12). This leads to a global anisotropy of the mass and the momentum distributions, a strongly non-spherical shock and an acceleration of the neutron star. The degree of anisotropy is varying strongly from model to model for the two-dimensional simulations. This suggests that we cannot make definite statements about the anisotropy in three dimensions based on only two models. However, compared to the two-dimensional models there are some generic differences that we will discuss in the following.

Downflow structure

In most of the two-dimensional models only one downflow is left about 100 ms after the onset of the explosion. This is also the case in the three-dimensional simulations: Both models have developed a single, massive downflow at this time, which evolves only slowly afterwards. In model B123-a this dominating downflow is located at $\theta \approx 50°$, $\phi \approx -120°$ for $t = 500\,\mathrm{ms}$ and moves slowly towards the northern grid boundary ($\theta = 22.5°$). After $t \approx 800\,\mathrm{ms}$ the downflow starts to wrap around the grid boundary. A second, weaker downflow near the southern grid boundary is still reaching down to the neutron star at $t = 400\,\mathrm{ms}$, but is blown away slowly in the subsequent evolution (Fig. 5.4). In model B123-b the dominating downflow forms at $\phi \approx -30°$ near the equator and stays near this location until we stop the simulation at $t = 550\,\mathrm{ms}$ (Fig. 5.6). Additional, weaker downflows are also present in this model (e.g. at $t = 500\,\mathrm{ms}$ near $\theta = 120°$, $\phi = -90°$), which merge with the main downflow soon. Although both models show these transient additional downflows there is one downflow that clearly dominates for $r < 10^7\,\mathrm{km}$.

However, for larger radii the regions with negative radial velocity become more and more extended and include areas far away (in θ, ϕ) from the impact site of the dominating downflow. This upper part of the downflow originates from the network of sheet-like downflow regions that forms soon after the onset of convection. Due to the merging of convective structures only a few of these sheets are left after the onset of the explosion. They occupy a large solid angle and show a complex substructure. The neutrino driven wind emanating from the vicinity of the neutron star is stopped at the lower boundary of these dense downflow sheets in a reverse shock. In the low-density regions outside of the downflows the wind is able to expand and accelerate further, reaching velocities of several $10^9\mathrm{cm/s}$. These high-velocity areas correspond to the bright regions in Figures 5.3 and 5.5, whereas the darker areas coincide with the downflow regions. In Model B123-a at $t = 500\,\mathrm{ms}$ the downflows near the northern and the southern grid boundaries are connected with a broad region, in which the velocities stay rather low. However, around $\theta = 90°$, $\phi = 0°$ a large downflow-free area with lower density develops, in which velocities of more than $2 \cdot 10^9\mathrm{cm/s}$ are reached (Fig. 5.3). This area is present until the end of the simulation. In Model B123-b the downflow regions at larger radii are distributed more evenly than for Model B123-a and there are no large downflow-free areas. At $t = 500\,\mathrm{ms}$ there is a high-velocity region around $\theta = 40°$, $\phi = 40°$, but this area occupies only a small fraction of the full solid angle.

Although the details of the downflow structure of the three-dimensional models are different, they share a common property that is not present in the two-dimensional models: The upper part of the downflow is distributed over a large area, even though the lower end is strongly localised. This is illustrated in Figures 5.14 and 5.13, which show the radial velocity at several radii. At $r > 200\,\mathrm{km}$ areas with negative velocity can be found for almost every given longitude or every given latitude. In contrast to this, the angular position of the upper part of the downflow in two-dimensional simulations is more strongly correlated with the angular position of the lower end of

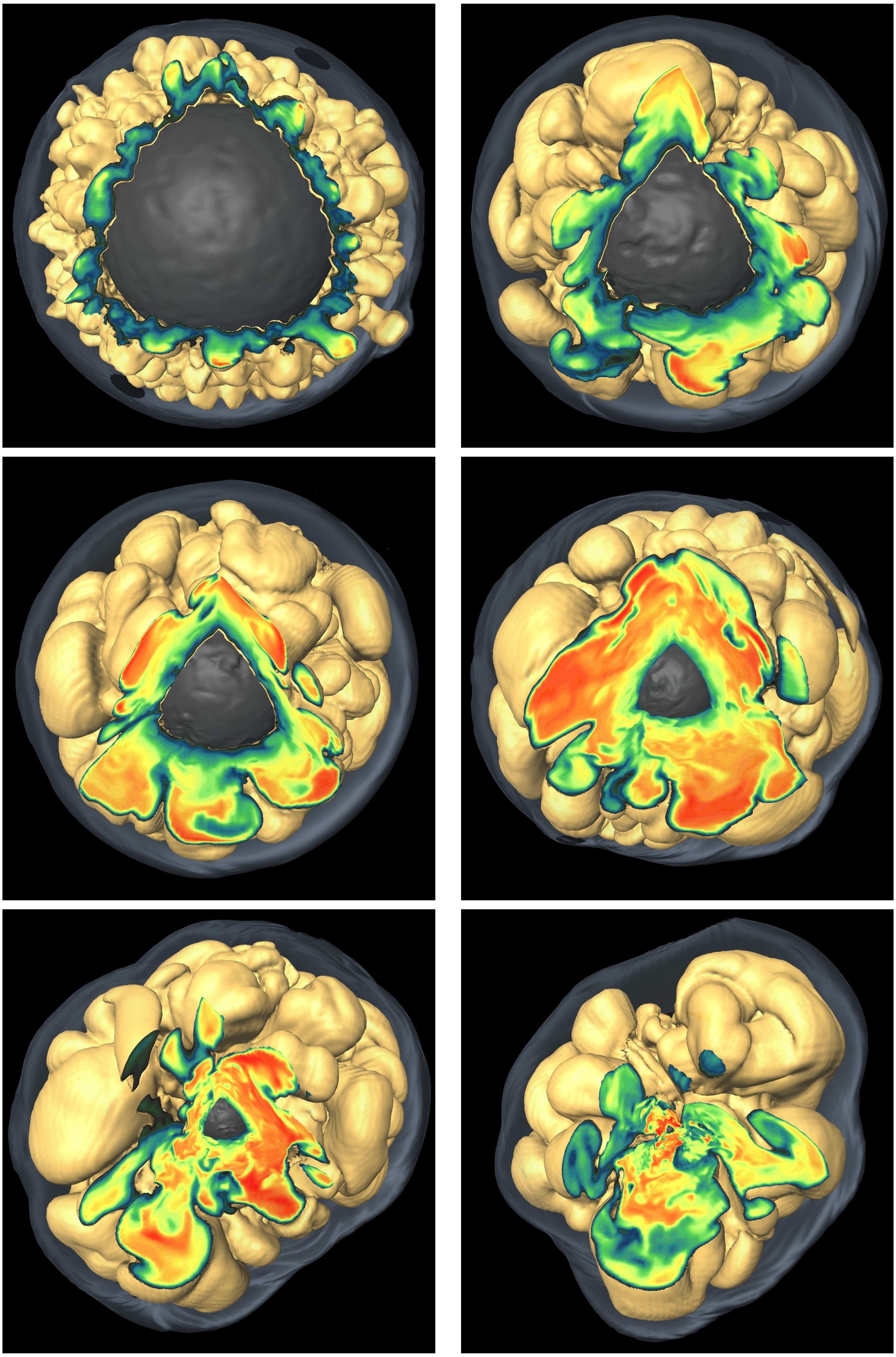

Figure 5.12: Snapshots of model B123-b showing the evolution from small-scale convection to global anisotropy. Displayed is the situation after 50, 75, 100, 200, 300 and 500 ms (from top left to bottom right panel). The outermost, bluish surface is the supernova shock, the solid bright surface is the interface between the rising high-entropy matter and the lower-entropy post-shock matter, and the dark gray shape is the neutron star surface. A octant is cut out to show the entropy distribution of the neutrino-heated matter – red means high, blue means low entropy.

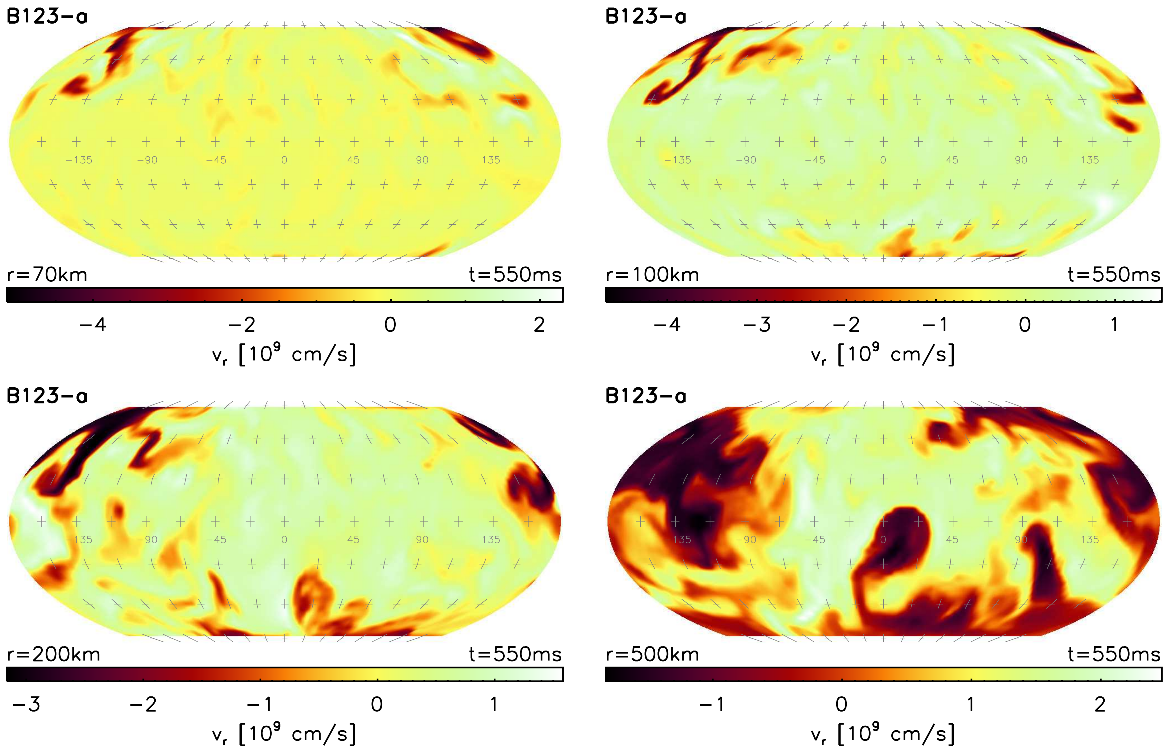

Figure 5.13: Like Figure 5.14, but for Model B123-a at $t = 550\,\mathrm{ms}$. Most of the infalling matter is located at $\phi \approx 180°$ and $\theta < 90°$. However, there is also infalling matter near $\theta \approx 150°$, which together results only in a weak acceleration of the neutron star in z-direction. On the other hand, the hemisphere $-90° < \phi < 90°$ contains for all radii much less of the dense, infalling matter than the other hemisphere. This leads to a considerable acceleration of the neutron star into the negative x-direction ($\phi = 180°$).

the downflow, e.g. cases where the upper part of the downflow extends far into the hemisphere not containing the lower end of the downflow are rare. From the two three-dimensional models one can not assess, if this is really a generic feature. However, there is an argument in favour of a more extended distribution of downflow regions: In three dimensions the downflow is no forced to extend from $\phi = 0°$ to $\phi = 360°$ any more. As the solid angle occupied by the downflow regions is similar in two and three dimensions, these regions will tend to be distributed over a broader area in azimuthal direction and over a narrower area in longitudinal direction.

Shock shape

Together with the mass and the momentum distribution also the shock surface develops a global anisotropy. The shape of the supernova shock is greatly affected by the neutrino-driven wind and the regions, which are occupied by downflows. Above these regions, and in particular above the main downflow, the shock expansion is slower, whereas in the downflow-free areas the neutrino-driven wind is able to push the shock further out. In two dimension this results in shock morphologies, which are in most cases rather simple: Most of the models develop a single downflow. If this downflow is located near one of the poles, there is a single bubble centred around the opposite pole. This results in a still nearly spherical shock surface, which however is shifted substantially along the symmetry axis. If the downflow is near the equator, there are two bubbles around the poles and the shock surface becomes prolate, with a shock minimum above the downflow. In three dimensions we find more complex shock morphologies: Both of our three-dimensional simulations show a clear global minimum of the shock radius, which is located

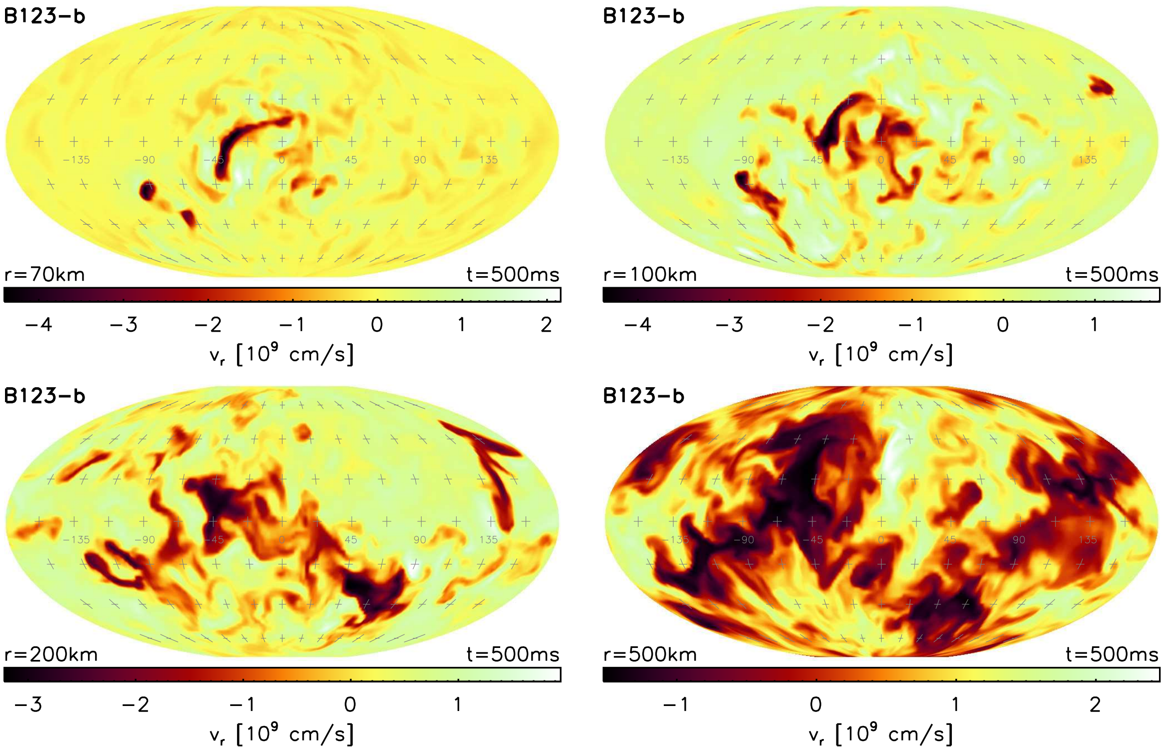

Figure 5.14: Radial velocity distribution of Model B123-b at $t = 500\,\mathrm{ms}$ on shells with radius 70, 100, 200 and 500 km. For $r = 70\,\mathrm{km}$ most of the matter with negative velocity is concentrated near $\phi = -30°$, $\theta = 90°$. This looks similar to the single downflow situation we see in many two-dimensional models. However, for larger radii the regions with negative velocity become more and more extended and include areas far away from $\phi = -30°$, $\theta = 90°$. For $r \geq 200\,\mathrm{km}$ one can find downflow areas for almost every given latitude or longitude. These areas are distributed over the sphere in a way that results only in a small total gravitational acceleration of the neutron star caused by the dense, infalling matter.

above the main downflow, and a global maximum located above the largest downflow-free area. However, there is no obvious relation between the positions these extrema (e.g. they are not located on opposite sides of the explosion). Furthermore, there are several other local maxima of the shock radius, which makes the shock shape quite complex (see Figures 5.15 and 5.16). The shock is deformed quite strongly already at the onset of the explosion. In the subsequent evolution the anisotropy increases slowly and the ratio of maximum to minimum shock radius reaches values of 1.5 (Models B123-b at $t = 550\,\mathrm{ms}$) to 1.8 (Models B123-a at $t = 1\,\mathrm{s}$). It should be noted that Kifonidis et al. (2006) showed for two-dimensional models that shock deformations of this magnitude are sufficient to trigger the growth of a strong Richtmyer-Meshkov instability at the He/H interface that results in a large-scale mixing of the ejecta, a feature that is required to explain observations of SN1987A.

Neutron star velocity

Due to the momentum transfer by downflows, the varying pressure around the neutron star and the gravitational pull of the anisotropic mass distribution, the neutron star is accelerated. This process has been discussed for the two-dimensional models in Section 3.2.2. It proceeds essentially in the same way also in three dimensions models. Before we will compare the resulting neutron star velocities, we have to discuss some complications for the determination of neutron star velocities in the three-dimensional case.

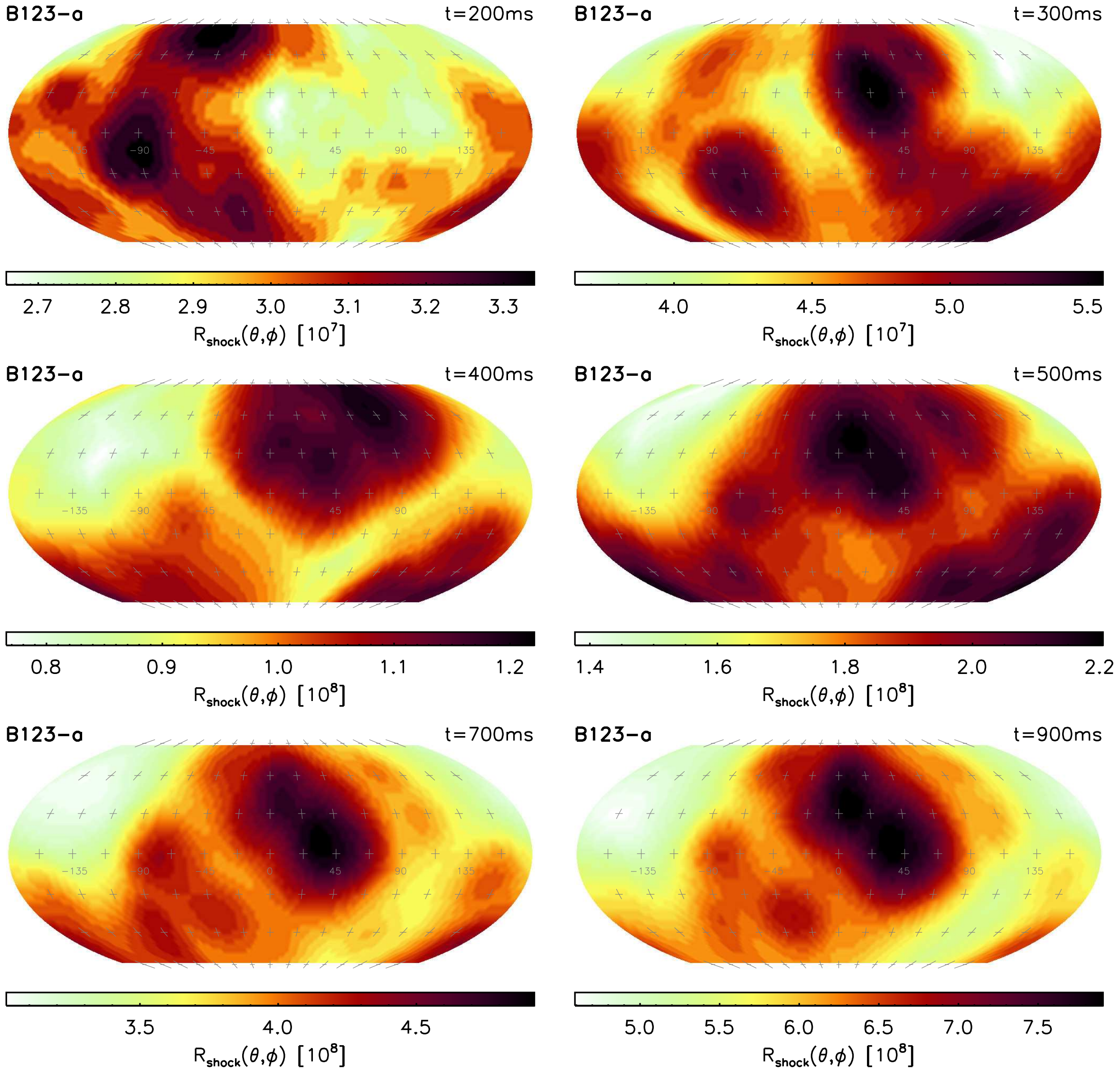

Figure 5.15: Angular distribution of the shock radius in units of the average shock radius $R_{\mathrm{s}}(\theta, \phi)/\langle R_{\mathrm{s}} \rangle$ of Model B123-a for several times. Initially the deviations of the shock surface from a sphere are only small, and the position and number of local extrema changes rapidly. After the onset of the explosion the anisotropy becomes stronger and the shape of the shock evolves only slowly. Over the dominating downflow near at low θ and $\phi \approx -160^\circ$ the shock radius is 30% smaller than the average value, whereas over the low-density region around $\theta \approx 60^\circ$ and $\phi \approx 30^\circ$ the shock is pushed out 30% further. Several other local shock maxima are still present at the end of the simulation.

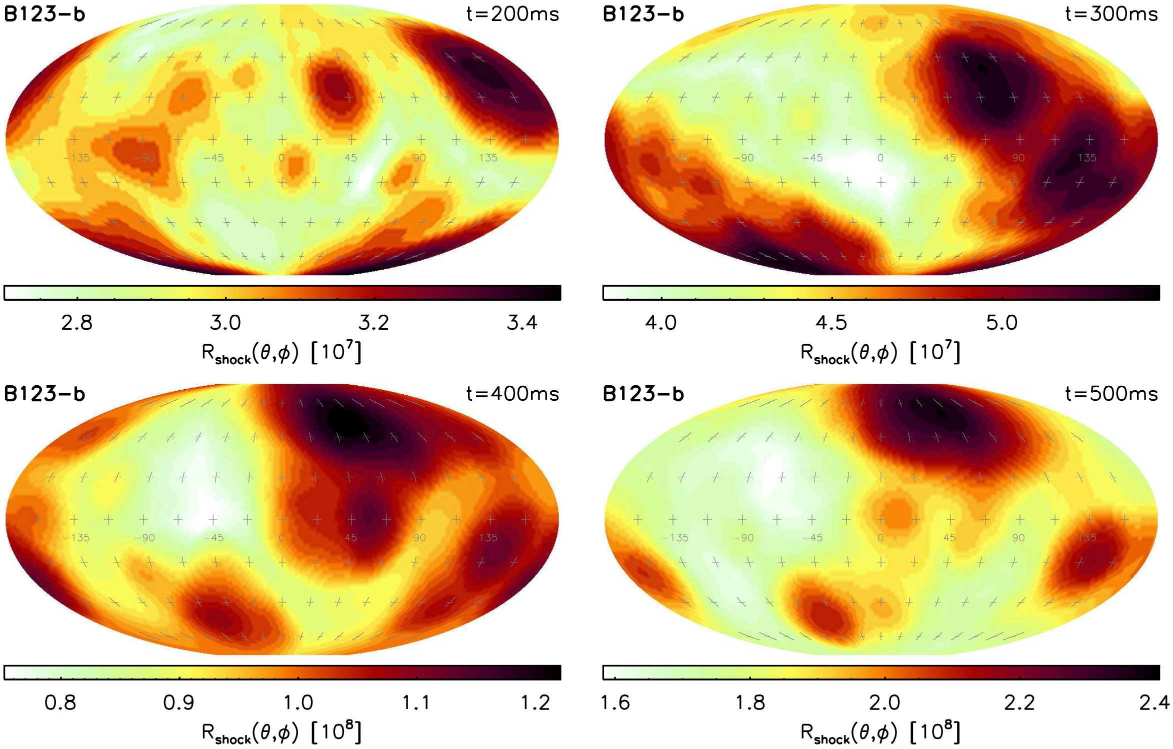

Figure 5.16: Like Fig. 5.15, but for Model B123-b. In this case the shock radius minimum (20% below the average value) develops above the main downflow near $\theta \approx 90°$ and $\phi \approx -90°$ and the shock is pushed out by almost 30% at low latitudes around $\phi \approx 60°$.

As in the two-dimensional simulations, we calculate the neutron star velocity by making use of total momentum conservation, i.e. the fact that the momentum of the neutron star should be equal to the (negative) momentum of the surrounding matter. While this works very well in two dimensions, it gives only approximate values for the setup we use in the three-dimensional simulations. As discussed in Section 2.3, the integrated momentum on the grid is not strictly conserved in this case, because momentum is created when matter is diverted by the reflecting boundaries at $\theta = \theta_{\text{min}}$ and $\theta = \theta_{\text{max}}$. However, we expect the momentum created at these boundaries to be small, compared to the integrated momentum on the grid: We replace only a small part of the total volume by the conical boundaries, so the explosion should be hardly restricted by these boundaries. And furthermore, after the onset of the explosion (when the major part of the momentum is built up) the flow is mostly radial, i.e. parallel to the boundaries, and will therefore barely generate momentum.

Apart from this boundary problem, our use of a one-dimensional gravitational potential for a three-dimensional calculation is also a possible source of artificially created momentum. In this approximation the gravitational mass distribution is assumed to be spherical symmetric, and hence it differs from the inertial mass distribution. This can lead to the same problems as discussed in Section 3.2.2. Yet, the largest component of the gravitational potential is caused by the point mass and the nearly spherical part of the neutron star between R_{ib} and R_{ns}. Therefore the gravitational potential should not deviate much from spherical symmetry. In the most anisotropic two-dimensional simulation from Table 5.2, Model B12, the angular variation of the gravitational potential is not more than about one percent. Thus it appears unlikely that the three-dimensional models are strongly affected by this problem.

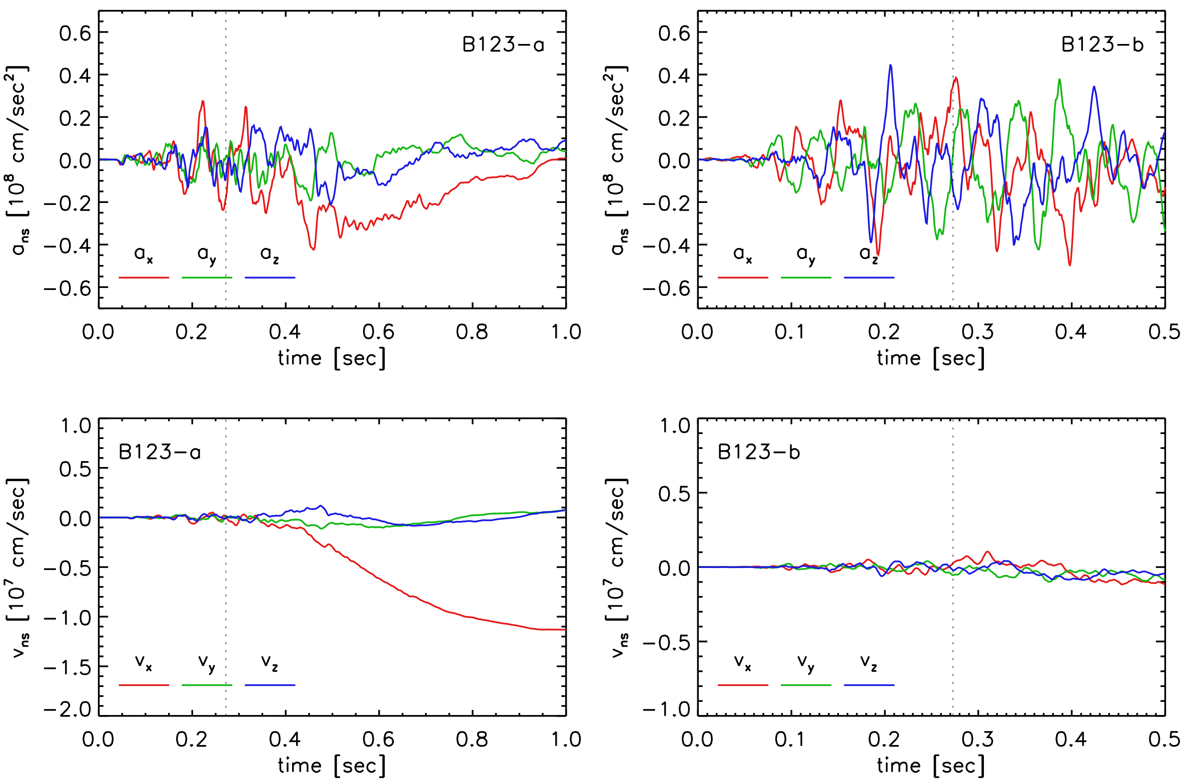

Figure 5.17: Neutron star acceleration (upper row) and velocity evolution (lower row) for the three-dimensional models. Prior to the explosion (indicated by the vertical dashed line) the absolute value and the direction of the acceleration vary strongly and do not lead to a significant neutron star velocity in both models. In the subsequent evolution the anisotropic, one-sided downflow distribution in model B123-a leads to considerable acceleration in negative x-direction. While B123-b becomes also anisotropic and is dominated by low modes, the downflow regions are distributed in a way that does not result in a strong acceleration (see Figure 5.14).

Of course a quantitative estimate of the artificially created momentum and its influence on the neutron star velocity would be preferable. Therefore we compute as in the two-dimensional case (see Sect. 3.1) in a post-processing step the acceleration of the neutron star using only the mass and momentum distribution on the numerical grid and assuming Newtonian gravity (see Eq. 3.26). The neutron star acceleration calculated this way is independent of all potential sources of artificial momentum mentioned above – neither the gravitational potential nor the boundaries enter the calculation. If the integration over this acceleration yields the same neutron star velocity as the one calculated from the total momentum, the generation of artificial momentum must be negligible.

Unfortunately, the data available for post-processing was too sparse in time to allow a precise calculation of the right side of Eq. (3.26). In particular the pressure was available only every 10 ms, which is not sufficient to perform a reasonable integration of this strongly varying quantity. However, for two-dimensional simulations the pressure term is small compared to the other terms in the phase, when the bulk of the total momentum is created ($t > 500\,\mathrm{ms}$). Thus it seems justified to omit the pressure term and compare the integral over the resulting acceleration, with the neutron star velocity computed from the total momentum. This comparison is shown for Model B123-a in Figure 5.18 (only for the x-direction, along which the strongest acceleration occurs). The similarity of the absolute values and the time dependence of the two curves show that the contribution of artificially created momentum to the neutron star velocity computed

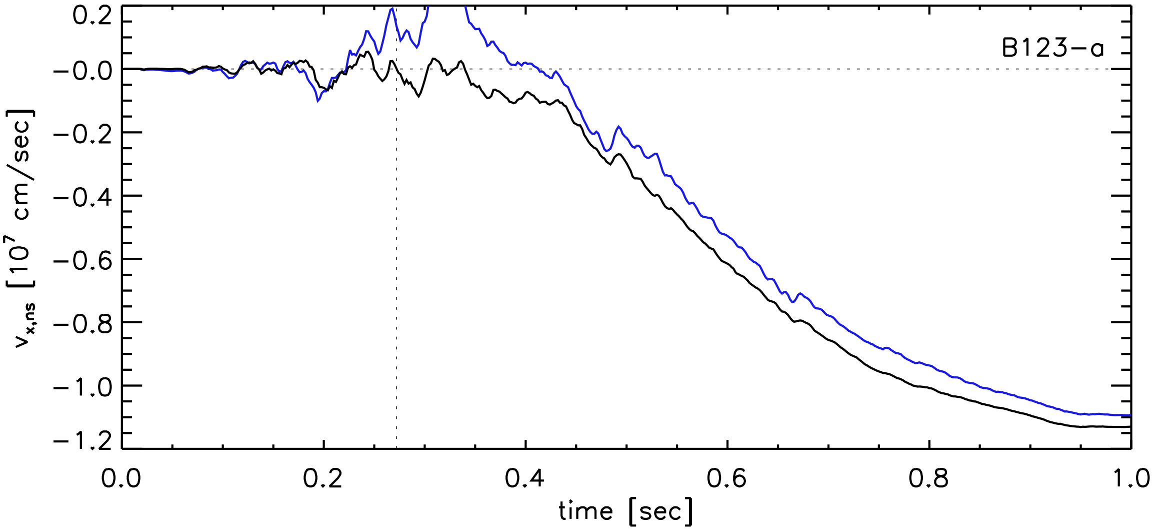

Figure 5.18: Time evolution of the x-component of the neutron star velocity for Model B123-a. The black curve is computed from the total momentum, the blue curve is the integral over the estimated neutron star acceleration. A fraction of the former may be caused by artificially created momentum, whereas the latter is computed directly from the mass and momentum distribution on the numerical grid and thus gives only the "physically" generated neutron star velocity. The similarity of the absolute values and the time dependence of the two curves show that the contribution of artificially created momentum to the neutron star velocity computed from the total momentum must be small. For $250\,\mathrm{ms} < t < 450\,\mathrm{ms}$ the agreement is not good, which is probably caused by the fact that we neglect anisotropic pressure effects in the calculation of the neutron star acceleration. However, most of the total momentum is produced only afterwards.

from the total momentum must be small. In the following we will therefore assume that the effects of artificially created momentum are negligible in our simulations.

In Fig. 5.17 we show the evolution of the neutron star acceleration and velocity for the three-dimensional models. The basic behaviour of Model B123-a is similar to most of the two-dimensional simulations: After the onset of convection the neutron star is accelerated strongly, but in rapidly changing directions, so that the total velocity fluctuates around zero. When the explosion has started the direction of the acceleration varies less strongly and finally remains roughly constant, while its absolute value is decreasing. After one second Model B123-a reaches a neutron star velocity of 113.5 km/s while the acceleration has become very small. For Model B123-b the amplitude of the acceleration is even somewhat higher than for Model B123-a, but its direction keeps on varying rapidly even after the explosion has set in and thus the neutron star has acquires a velocity of only 15.4 km/s until the end of the simulation at $t = 550\,\mathrm{ms}$.

Recalling that in two dimensions we have obtained neutron star velocities in excess of 1000 km/s these values may seem disappointingly small. However, for *most* of the two-dimensional models we do not find values of this magnitude either. Only four of the 39 two-dimensional models have neutron stars which are moving faster than 300 km/s. In fact the anisotropy parameter α_{gas} (which is directly connected to the neutron star velocity, see Eq. 3.16) for model B123-a evolves quite similar to the average α_{gas} of the 2D model sets 180-1 and 180-2, and becomes somewhat smaller only in the last 200 ms (Fig. 5.19). In this sense Model B123-a is of "average" anisotropy, compared to the two-dimensional models. The α_{gas} of Model B123-b, on the other hand, stays well below the two-dimensional average, but there are several 2D models with even weaker anisotropy.

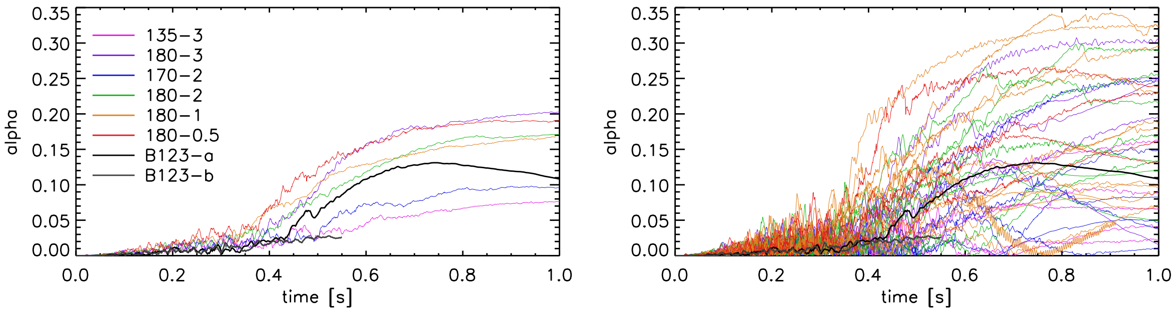

Figure 5.19: Evolution of the anisotropy parameter $\alpha_{\rm gas}$ for the models listed in table 5.2. The right panel shows the evolution of $\alpha_{\rm gas}$ for each individual model, whereas the in left panel the average $\alpha_{\rm gas}$ for sets of models with the same resolution and grid size are displayed. For $t < 750\,\rm ms$ the anisotropy parameter of Model B123-a evolves similar as the one of the 180-2 model set, but decreases afterwards and ends up at 11%. For Model B123-b $\alpha_{\rm gas}$ stays rather low – however this simulation was already stopped at $t = 550\,\rm ms$. From the right panel it is evident that the variation of $\alpha_{\rm gas}$ within each model group is large.

Very slow neutron stars are not unusual in two dimensions, owing to two reasons: Either there are two or more downflows dragging the neutron star in different directions, or a single downflow is located near the equator, which does not result in an acceleration due to the symmetry of the resulting matter distribution with respect to the equator. For models B123-a and B123-b both reasons do not apply: A single downflow dominates in both models, whose location should not influence the absolute value of the acceleration. Thus one could expect that the three-dimensional models would develop faster moving neutron stars. Why is this not the case? The reason is the mass distribution at intermediate radii ($r = 100\ldots1000\,\rm km$). The gravitational acceleration of the neutron star is mainly caused by the anisotropic mass distribution (dense downflow regions and less dense outflowing matter) within several 100 km. As already discussed above, the location of the downflow regions at intermediate radii is in three dimensions not as strongly correlated with the position of the lower end of the downflow as in two-dimensions. In two dimensions in general the gravitational acceleration of the neutron star due to the matter at these radii is even stronger and pointing roughly in the same direction as the gravitational acceleration caused by the matter within $r = 100\,\rm km$. In the three-dimensional models the downflow regions at intermediate radii are distributed over the whole sphere, which results in only a weak gravitational acceleration. In model B123-b the downflow regions are distributed so evenly (Fig. 5.14) that the neutron star is barely accelerated. Model B123-a develops a large downflow-free region (Fig. 5.13), which leads to a significant acceleration. Yet, the acceleration is not as strong as in typical two-dimensional models with a single, polar downflow (like Model B12).

It appears that the scatter of neutron star velocities for simulations started from different random seeds (see Sect. 3.2.5) is caused by different mechanisms in 2D and 3D: In 2D the number and position of downflows is decisive for the kick and depends chaotically on the initial conditions. In 3D the global anisotropy at intermediate radii is important for the kick, which probably also depends sensitively on the initial perturbations. Whatever the reason for the scatter is, of importance is that there is a scatter also in 3D, as the different outcomes of Models B123-a and B123-b show. This makes us optimistic that it is possible to produce faster neutron stars just by repeating the 3D simulations with different initial perturbations. On the other hand this means also, that many simulations are needed to clarify, whether there is any systematic difference in the magnitude of neutron star velocities between the two- and three-dimensional case.

Table 5.2: Several characterising quantities for the rotating 3D Model R103F and six two-dimensional models with the same boundary conditions. The gain layer mass M_{gain} is given for $t = t_{\mathrm{exp}}$. Explosion energy, E_{exp}, neutron star mass, M_{ns}, and radius, R_{ns}, as well as the anisotropy parameter α_{gas} are given for $t = 0.4\,\mathrm{s}$. The neutron star acceleration value, a_{ns}, was averaged over the time span $[0.2\,\mathrm{s}, 0.4\,\mathrm{s}]$. For the neutron star velocity, $|v_{\mathrm{ns}}|$, we give values at $t = 0.4\,\mathrm{s}$ and at the end of the simulation, $t = t_{\mathrm{sim}}$.

Model	θ_0 [°]	$\Delta\theta$ [°]	t_{sim} [s]	t_{exp} [s]	E_{exp} [B]	M_{ns} [$M_\odot$]	$\lvert v_{\mathrm{ns}}(0.4\,\mathrm{s})\rvert$ [km/s]	$\lvert v_{\mathrm{ns}}(t_{\mathrm{sim}})\rvert$ [km/s]	$\lvert a_{\mathrm{ns}}\rvert$ [km/s^2]	α_{gas}
R103F	0	4	0.4	0.136	0.60	1.402	75.6	75.6	288.0	0.05
R10F-l1	0	4	0.7	0.157	0.53	1.418	65.7	219.1	300.5	0.06
R10F-l2	0	4	0.7	0.157	0.59	1.416	146.6	264.5	724.1	0.13
R10F-l3	0	4	0.6	0.146	0.64	1.417	139.9	184.8	631.1	0.11
R10F-h1	0	0.5	0.8	0.134	0.68	1.402	79.9	107.2	339.9	0.06
R10F-h2	0	0.5	0.7	0.123	0.66	1.405	72.0	82.9	194.5	0.05
R10F-h3	0	0.5	0.7	0.125	0.67	1.399	228.7	457.6	980.7	0.17

5.3 A rotating model

For the three-dimensional rotating Model R103F we have not as many 2D models available for comparison as in case of the non-rotating models. Instead of discussing the evolution of global quantities in 2D and 3D, as well as the implications of different grid resolutions like for the non-rotating models (which should be similar), we will therefore focus on the most obvious difference between rotating 2D and 3D models and its influence on the explosions anisotropy and the neutron star acceleration: The downflows above the poles of the neutron star that we find in all of our rotating 2D models are absent in 3D. In fact, the strongest neutrino-heated *outflows* of matter are located above the poles in 3D. This fundamental difference becomes obvious in Fig. 5.20, where we compare the evolution of the entropy distribution in the $\phi = 0$–slice of the 3D model to a high-resolution 2D model. Two-dimensional models with lower angular resolution do not look qualitatively different, which shows that the absence of the downflows in 3D is not caused by insufficient resolution. The most important quantities for the rotating 2D and 3D simulations are listed in Tab. 5.3.

5.3.1 Missing polar downflows

In Chapter 3 we discussed the morphology of rotating two-dimensional models, for which we used the "standard" (slow) boundary contraction. An important finding was that two-dimensional rotating models develop downflows above both neutron star poles. These polar downflows remain stable for several 100 ms, until they are finally blown away by the neutrino-driven wind. The long-lasting downflows hamper the shock expansion near the poles and lead to a more spherical or even oblate shock shape, in contrast to the prolate shocks that non-rotating models develop. For the more rapid boundary contraction assumed for the two-dimensional models listed in Tab. 5.3, we find essentially the same behaviour: About 100 ms after core bounce, two polar downflows form and remain stable for 300–400 ms.

As discussed in Sect. 3.4, the reason for the stabilisation is the formation of a positive gradient $\mathrm{d}j_z^2/\mathrm{d}x$, where j_z is the specific angular momentum (which has only a component parallel to the symmetry axis in two-dimensional simulations) and x is the distance to the axis of rotation.

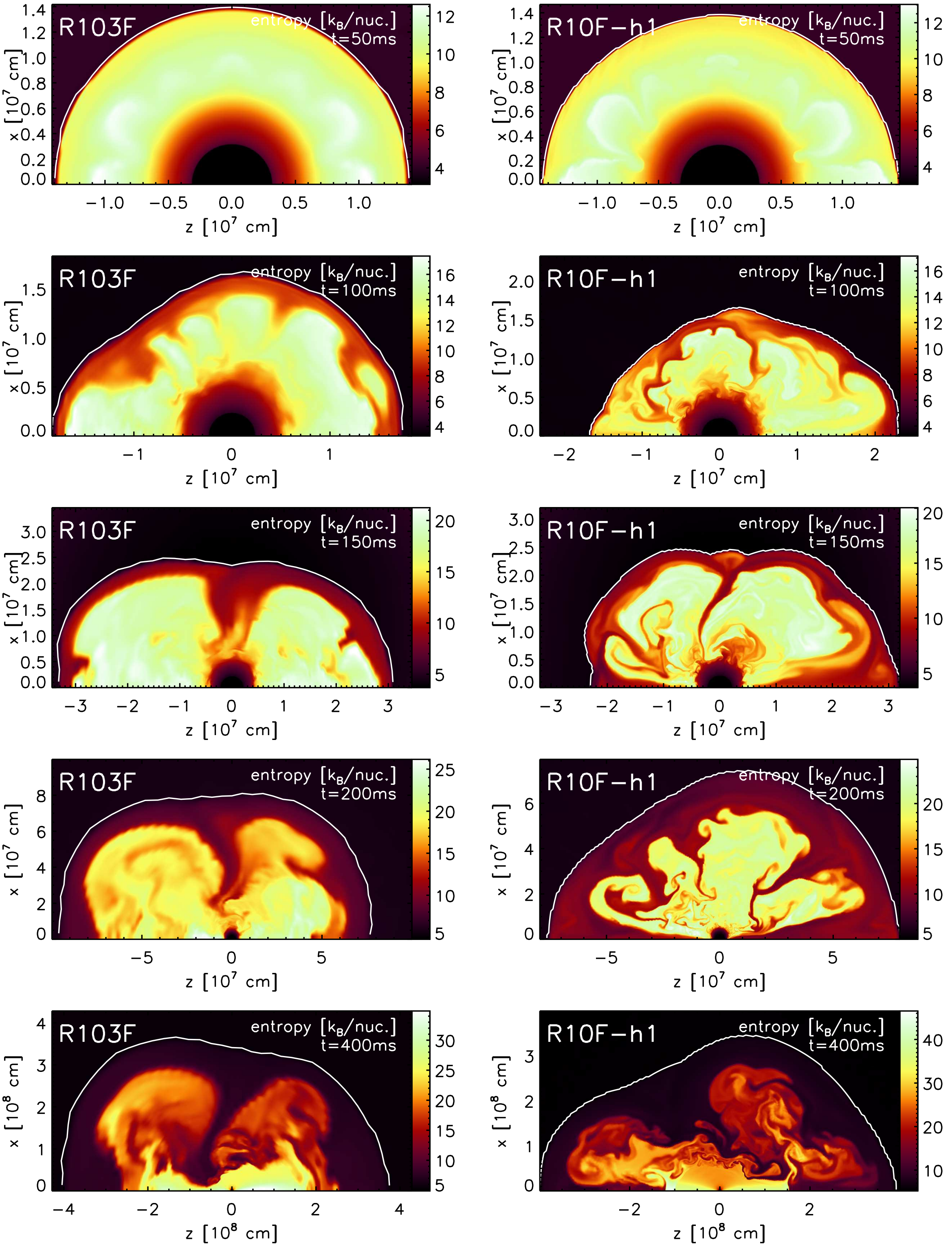

Figure 5.20: Entropy distribution in the $\phi = 0$ plane for the three-dimensional Model R103F and the two-dimensional high-resolution Model R10F-h1 for several times. Note the long-lasting polar downflows in the two-dimensional model, which are absent in three dimensions. At $t = 400\,\text{ms}$ these downflows have been blown away by the neutrino-driven wind also in the 2D model.

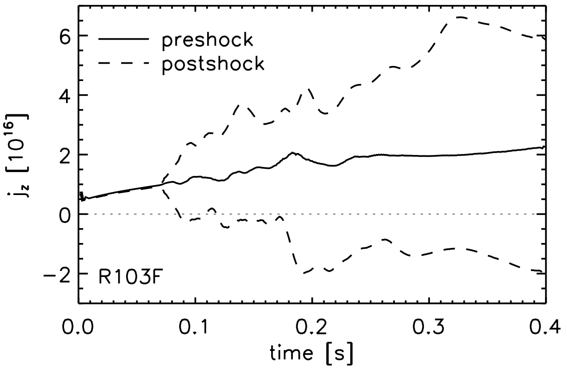

Figure 5.21: Specific angular momentum j_z at the equator above the shock ("preshock") and minimum and maximum values of j_z below the shock ("postshock"). The angular momentum of the matter crossing the oblique (non-spherical) shock is modified strongly – a part of the postshock matter rotates even retrograde.

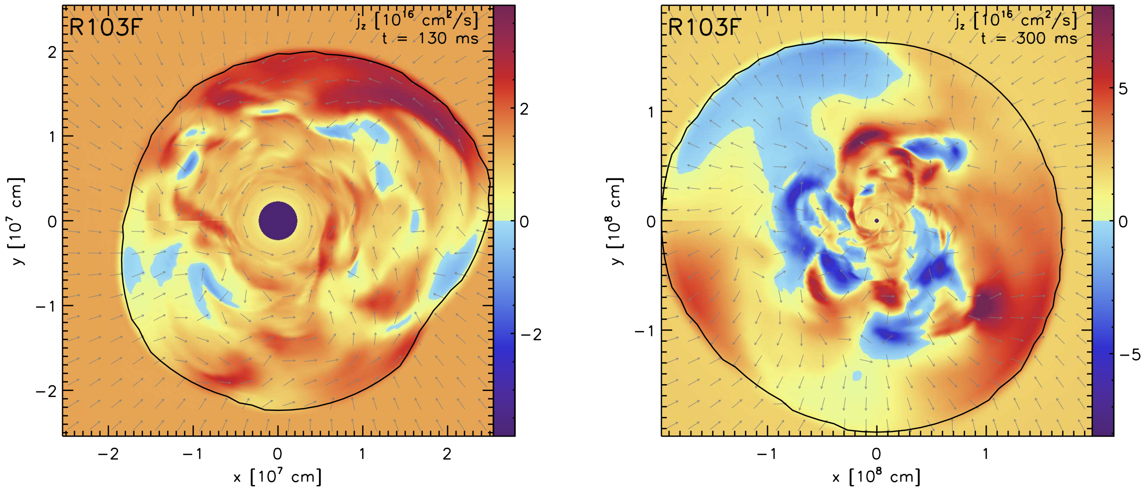

Figure 5.22: Specific angular momentum (z-component) in the equatorial plane of Model R103F for two times. The black line marks the shock, the arrows indicate the local direction of the flow. The obliqueness of the shock leads to a strong variation of the lateral postshock velocity. A part of the flow is even moving against the direction of the progenitor rotation and thus also negative values of the angular momentum are found.

In axisymmetry, the specific angular momentum of a fluid element remains constant and in particular is not modified when it crosses a shock. Owing to the "shellular" rotation (i.e. the angular velocity Ω is constant on $r = const$ shells) and the angular velocity profile ($\Omega \propto r^{-3/2}$ outside the iron core) assumed for the progenitor model we use (see Müller et al. 2004, for a detailed description), the specific angular momentum $j_z = r^2 \sin(\theta)\Omega(r)$ of the matter crossing the shock near the equator increases with time and is always higher than the one of the matter falling through the shock near the poles. Therefore polar low-j_z downflows, which are affected by comparably low centrifugal forces, are surrounded by matter with higher j_z that feels a stronger centrifugal force away from the axis. This situation is stable.

However, the stabilisation does not work any more in three dimensions: The specific angular momentum is not conserved, because now forces can act also in ϕ-direction. In particular, when a fluid element crosses the non-spherical supernova shock, its specific angular momentum can be strongly modified. At $t \approx 80\,\text{ms}$ the deformation of the shock has become sufficiently strong

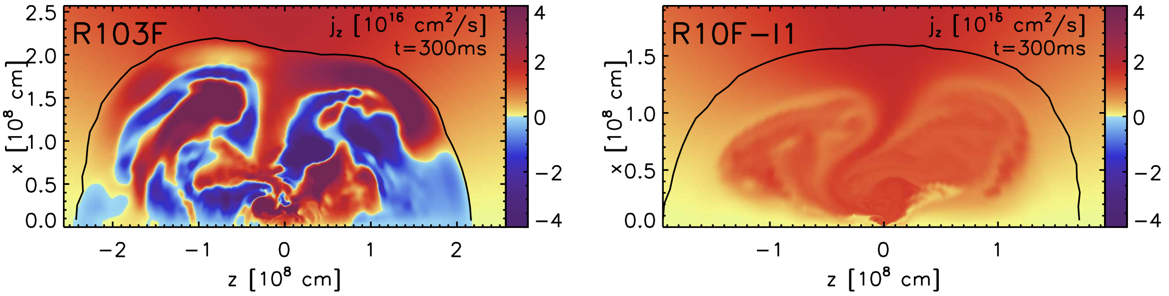

Figure 5.23: Distribution of the z-component of the specific angular momentum for the three-dimensional Model R103F and the two-dimensional Model R10F-l1 at $t = 300\,\mathrm{ms}$. In two dimensions j_z on average increases with distance to the axis of rotation. In the polar downflows j_z is lower than in the convection region. In three dimensions no such clear trends are visible.

to even change the sign of j_z for a part of the matter, which is therefore moving against the direction of rotation (Figs. 5.21, 5.22). Under such circumstances a stabilising j_z-gradient can not be maintained (Fig. 5.23).

5.3.2 Anisotropic, neutrino-driven outflows

The missing stabilisation explains why there are no long-lasting downflows at the poles in Model R103F. But why are there no polar downflows at all and the shock expands even faster in the polar regions? It is not completely clear whether this is a generic feature resulting from our progenitor model and the boundary conditions we apply, or just a morphology that develops by chance for the initial perturbations chosen for Model R103F. However, the fact that there are no downflows in the polar regions is quite striking and we see a possible explanation for this behaviour in the angular variation of the neutrino heating rate, which in turn results from the rotational deformation of the neutron star.

The neutron star accretes matter with increasingly high specific angular momentum and contracts at the same time. Therefore the neutron star spins up to rotation periods of several milliseconds and attains an oblate deformation due to the strong centrifugal forces. Once the accretion of mass and angular momentum has become negligible and the inner boundary contracts only slowly, the angular momentum of the neutron star does not increase further and the deformation, e.g. measured by the ratio of the equatorial to the polar neutrino sphere radius, $R_\nu^\mathrm{e}/R_\nu^\mathrm{p}$, remains constant (Fig. 5.24). This is the case at $t \approx 200\,\mathrm{ms}$, when the neutron star has acquired an angular momentum $L_\mathrm{ns} \approx 3.5 \times 10^{48} \mathrm{g\,cm^2/s}$ and $R_\nu^\mathrm{e}/R_\nu^\mathrm{p}$ is about 1.3. Similar values are found in a Boltzmann simulation of the same progenitor including the full neutron star (R. Buras, personal communication). Thus it appears that the deformation of the neutron star is not strongly influenced by excluding the innermost $1.1\,M_\odot$ from the simulation.

Due to the centrifugal forces, the shapes of surfaces of constant density and surfaces of constant temperature are different in the rotating neutron star (see, e.g., Tassoul 1978). In particular, the temperature at the neutrino-spheres (which can be approximated by density-isosurfaces) varies with the polar angle. At the poles the temperature at the neutrino-spheres is up to 20 percent higher than at the equator (Fig. 5.25, left panel). As the neutrinos are decoupling from the matter in the region around the neutrino-spheres, this variation of the matter temperature leads also to a variation in the mean neutrino energies, which are about 2–3 MeV higher at the poles than at the equator (Fig. 5.25, right panel). In contrast to this and in agreement with Boltzmann simulations (R. Buras, personal communication), the luminosities show only a weak

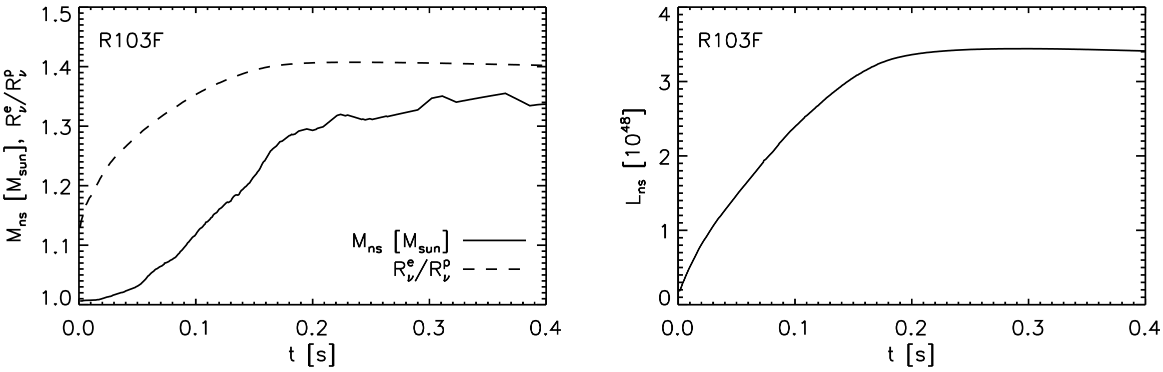

Figure 5.24: Evolution of the neutron star mass, $M_{\rm ns}$, and the ratio of the equatorial to the polar neutrino sphere radius, $R^{\rm e}_\nu/R^{\rm p}_\nu$ (left panel), as well as the angular momentum of the neutron star (right panel) for Model R103F. Once the neutron star does not gain mass and angular momentum any more and the contraction has become slow, the deformation of the neutrino sphere remains roughly constant.

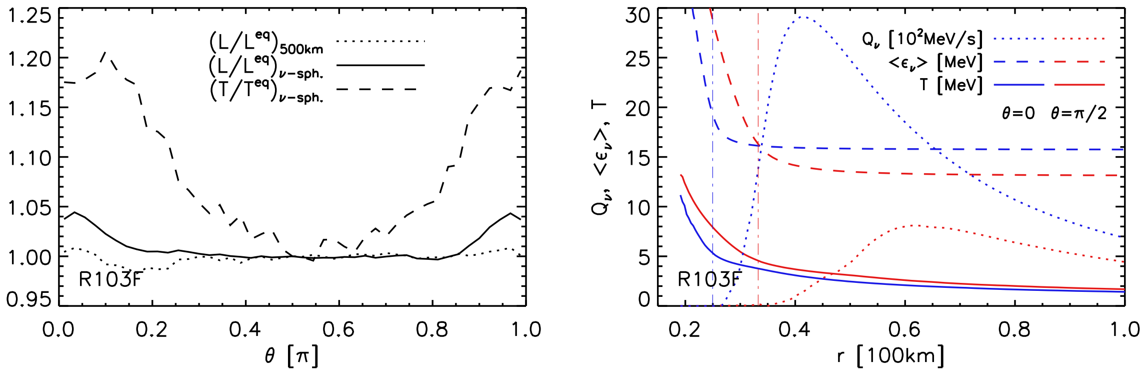

Figure 5.25: *Left panel:* Luminosity at the neutrino-sphere and at $r = 500\,$km and neutrino-sphere temperature as a function of the polar angle for Model R103F at $t = 300\,$ms. All quantities are normalised to the value at the equator. The luminosity is slightly higher at the poles, but at $r = 500\,$km this variation has almost vanished. The matter temperature at the neutrino-sphere, however, varies significantly and is about 20 percent higher at the poles than near the equator. *Right panel:* Radial profiles of the neutrino energy deposition rate Q_ν (per nucleon), the matter temperature T and the mean electron neutrino energy $\langle\epsilon_{\nu_{\rm e}}\rangle$ in Model R103F at the north pole and at the equator, respectively ($t = 300\,$ms). The vertical lines mark the positions of the electron neutrino sphere.

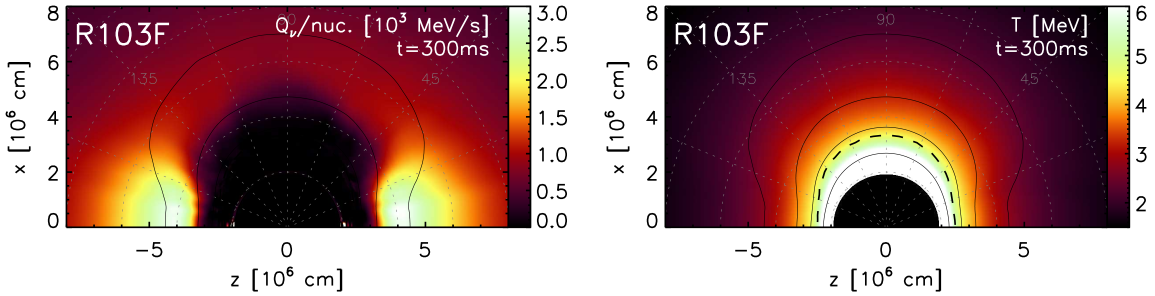

Figure 5.26: Neutrino energy deposition rate (per nucleon) (left) and matter temperature distribution (right) for Model R103F at $t = 300\,$ms. The solid black lines are density contours, the dashed line is the electron neutrino sphere.

angular dependence at the neutrino-spheres (less than 5 percent) which is not visible any more at a radius of 500 km (Fig. 5.25, left panel).

As the neutrino heating rate is proportional to $\langle \epsilon_\nu^2 \rangle$ (Janka 2001), the 20 percent higher neutrino energies at the poles can explain that, for large radii ($r > 100\,\mathrm{km}$), the heating rate is about 50 percent higher near the poles than at the equator (Fig. 5.25, right panel). For smaller radii, this asymmetry is even more extreme, because the steeper temperature gradient at the poles results in a smaller gain radius and thus a higher neutrino energy density $E_\nu \propto L_\nu / r^2$ at the radius of maximum heating (Fig. 5.26).

It seems likely that the enhanced heating at the poles disfavours downflows in this region and, on the contrary, leads to faster expansion of the ejecta there. The higher polar heating rates are also present in the two-dimensional models. However, for the latter the stabilisation of polar downflows due to the positive gradient of j_z^2 seems to be more important. Only after the polar downflows have been blown away by the neutrino-driven wind, the stronger polar heating becomes obvious in 2D. Such a situation is visible in the lowermost right panel of Fig. 5.20, which shows higher entropies above the poles of a 2D model, which are caused by stronger neutrino heating. Also two-dimensional Boltzmann simulations of the same progenitor show polar downflows and enhanced polar heating rates, which makes us optimistic that these results are not strongly affected by our simplified transport or by the use of an inner boundary.

5.3.3 Explosion anisotropy and downflow distribution

Once the neutron star has become significantly deformed by centrifugal forces, the higher neutrino heating rates above the neutron star poles prevent downflows from forming and lead to a faster expansion of the ejecta in these regions. For $t \gtrsim 150\,\mathrm{ms}$ the downflows are therefore mostly located near the equator – within 45° polar angle distance to the poles downflows occur seldom and only for short phases (Fig. 5.27). This leads to a slower shock expansion near the equatorial plane and consequently the shock develops a prolate deformation. The ratio of maximum to minimum shock radius reaches values of up to 1.6 (Fig. 5.29). This anisotropy of the explosion with the mainly equatorial accretion and the preferred polar expansion is visible in Fig. 5.28, where we show the situation at the end of the simulation.

The prolate deformation of the shock is in contrast to the nearly spherical shocks of the rotating 2D models discussed in Sect. 3.4. This is partly due to the polar downflows that hamper the shock expansion in 2D, but probably also due to the fact that for the rotating models of Chapter 3 the slower, “standard” boundary contraction was assumed, so that the centrifugal forces remained lower and the neutrino heating was less anisotropic than for the 2D models discussed in this section. The latter do indeed also develop a prolate deformation.

Before the fast expansion of the shock that sets in at about $t = 150\,\mathrm{ms}$, the downflows and the associated minima in the shock surface circle around the rotation axis with a rotation period that is of the order of 100 ms (Fig. 5.31). A mean value for the rotation period can be estimated as

$$\langle \tau_{\mathrm{rot}} \rangle \approx 2\pi \frac{\langle R_{\mathrm{s}} \rangle^2}{\langle j_z \rangle} , \tag{5.3}$$

using the average value of the specific angular momentum behind the shock, $\langle j_z \rangle$, and the average shock radius, $\langle R_{\mathrm{s}} \rangle$. When the shock accelerates after the onset of the explosion, $\langle j_z \rangle$ increases only slowly because in the initial model $j_z \propto \sqrt{r}$ (at the equator, see Sect. 3.1.1). Consequently the rotation period becomes large and the minima of the shock radius, to which the downflows

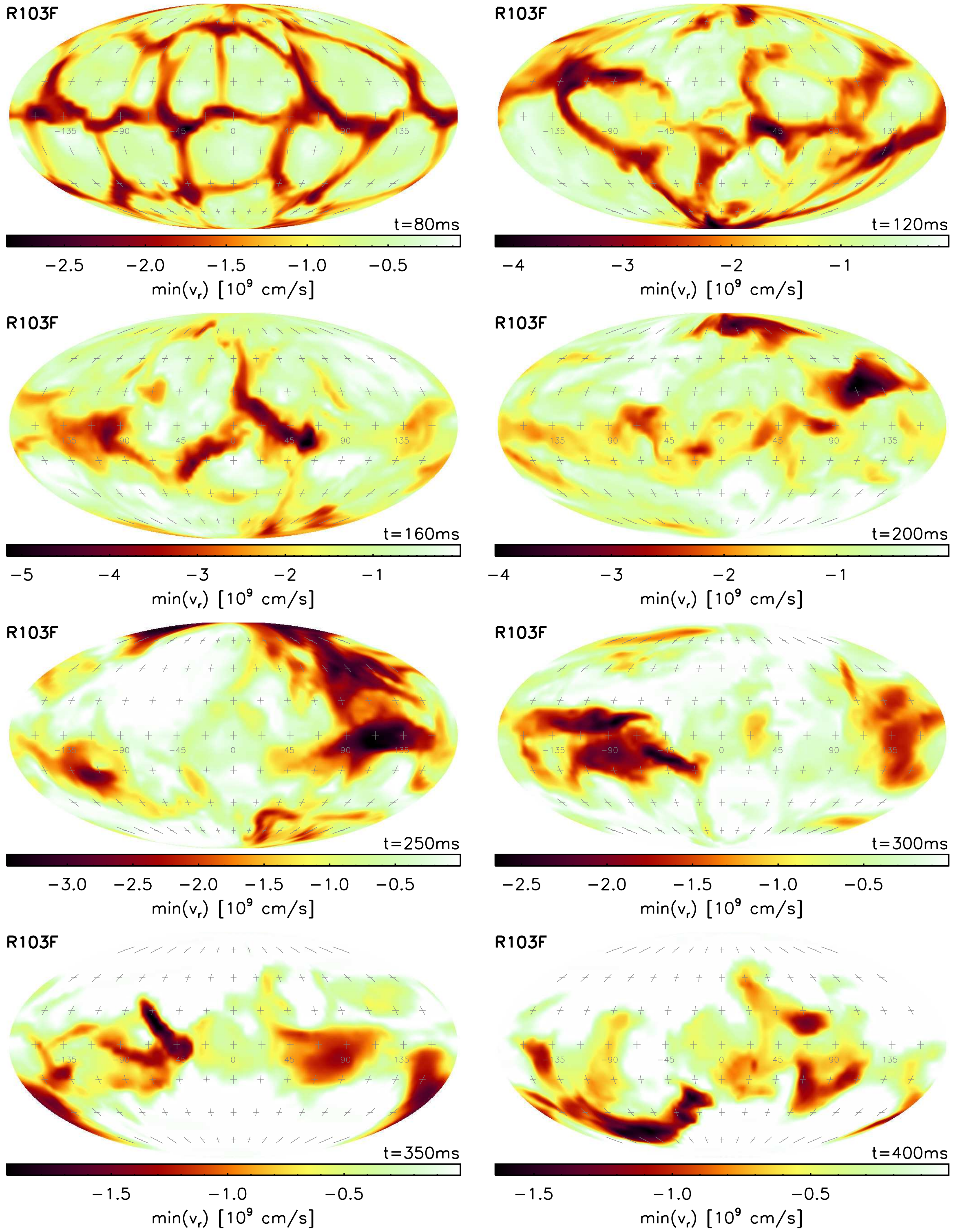

Figure 5.27: Like 5.4, but for Model R103F. Note that the downflows are located preferably near the equatorial plane.

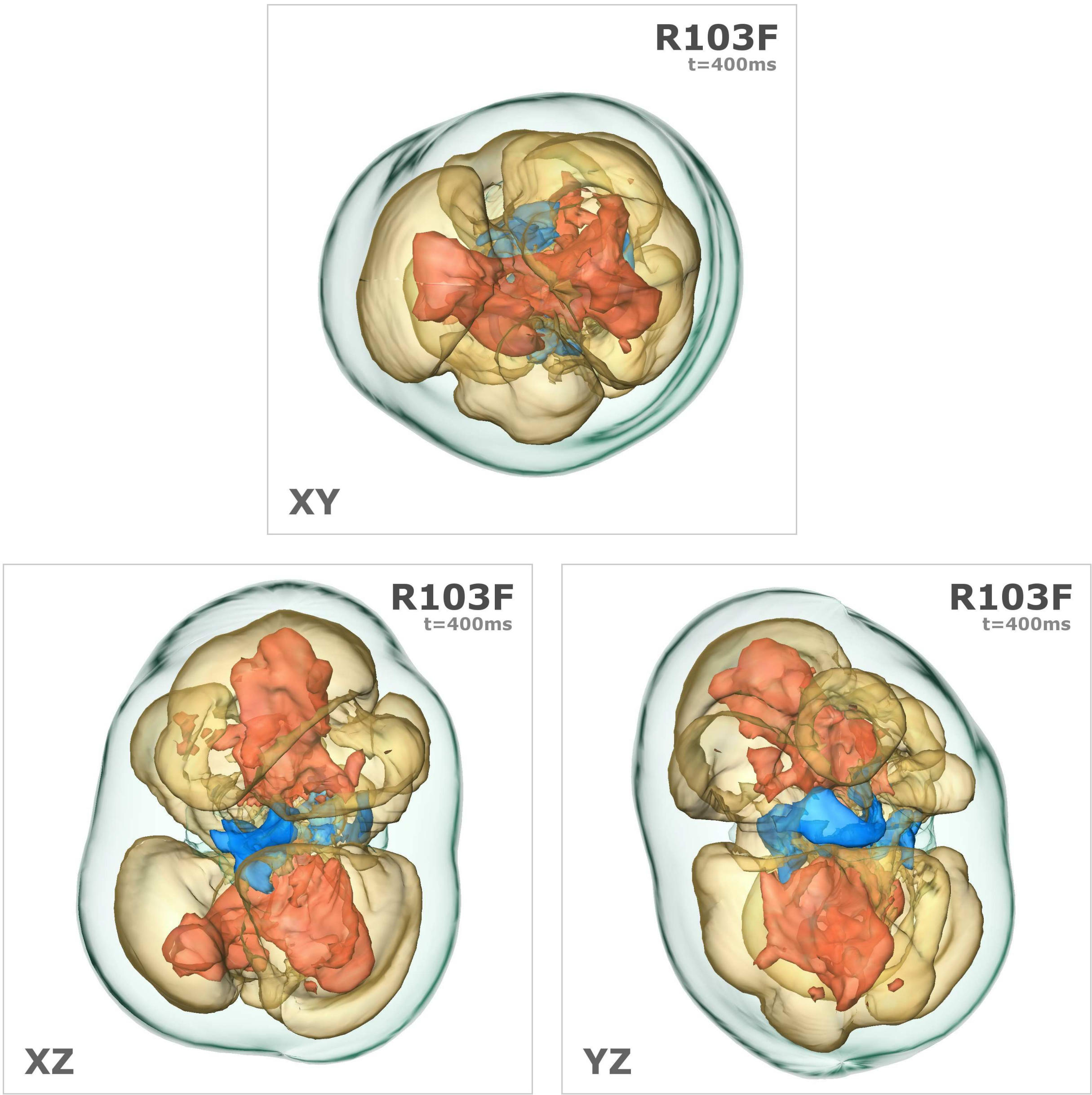

Figure 5.28: Several isosurfaces for Model R103F at $t = 400\,\mathrm{ms}$, looking onto the xy-plane (top panel), the xz-plane (middle panel) and the yz-plane (bottom panel). The outermost, bluish surface is the shock ($v_r = 0$), the yellow surface encloses the neutrino-heated rising matter, the red isosurface marks the fastest ejecta ($v_r > 10^9$ cm/s) and the blue one encloses downflow regions with $v_r < -3 \times 10^8$ cm/s.

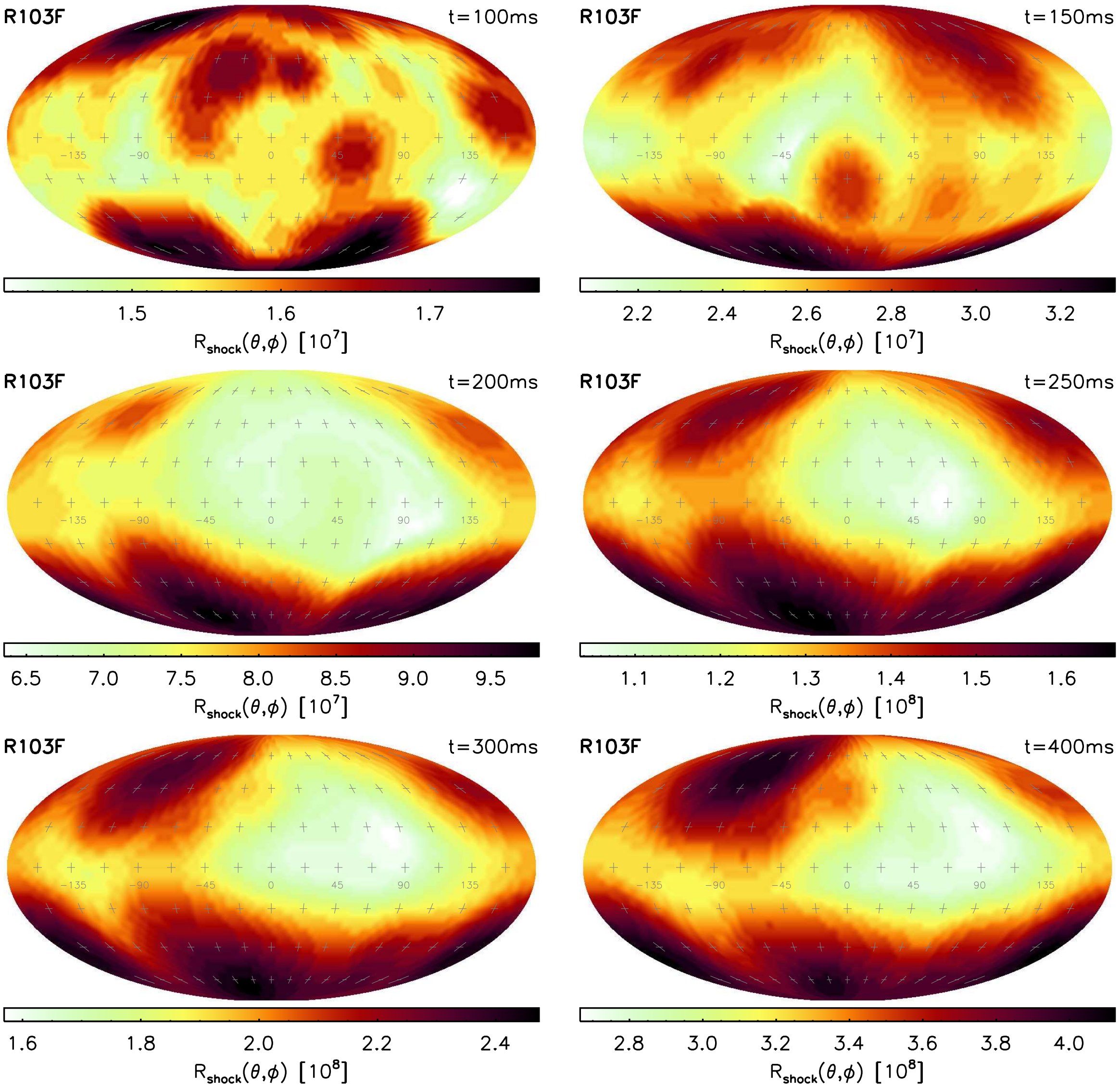

Figure 5.29: Shock radius of Model R103F for several times (in Mollweide equal area projection).

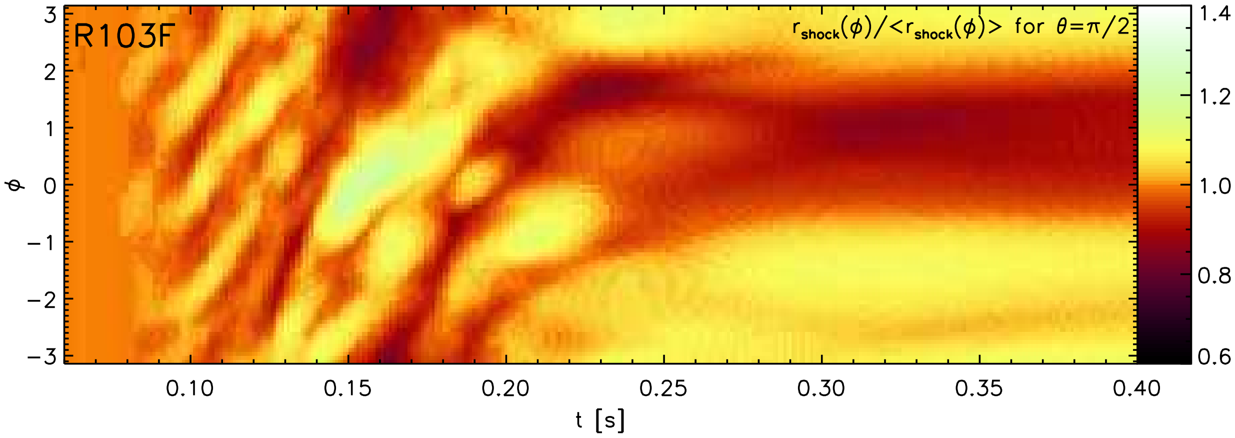

Figure 5.30: Equatorial shock radius (normalised to the average equatorial shock radius) as a function of longitude and time for Model R103F. The local extrema of $R(\phi, \theta = \pi/2)$ move on average with the angular velocity of the matter crossing the shock. For $t \gtrsim 150$ ms the corresponding rotation period becomes larger than one second and the shock radius extrema essentially remain at the same longitude.

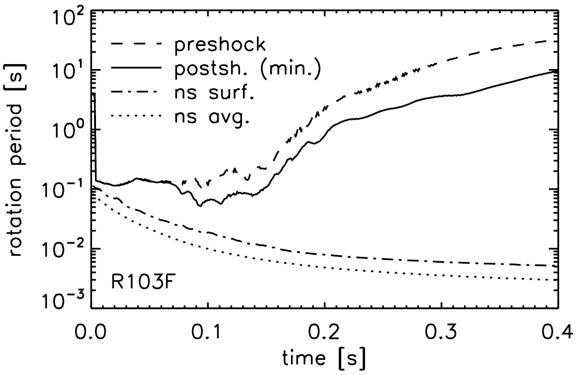

Figure 5.31: Evolution of the rotation period before and after the shock (minimal value), at the neutron star surface and the average rotation period of the neutron star. The postshock rotation period increases strongly, once the explosion has set in.

are “attached”, remain essentially at the same longitude (Fig. 5.31). At $t \approx 250$ ms there is only one such radius minimum left, which is located near the equator at $\phi = 45°$–$90°$ (Fig. 5.30).

5.3.4 Neutron star kick

In Fig. 5.32 (left panel) we show the evolution of the neutron star velocity components, v_i^{ns}, of Model R103F, as well as the absolute value. These quantities have been obtained making use of total momentum conservation in the same way as for the non-rotating models. A comparison of the measured acceleration components (i.e. the time derivatives of the v_i^{ns}) with the “predicted values” (according to Eq. 3.26) is shown in Fig. 5.33. Considering that again the time resolution of the pressure data was too sparse to compute the corresponding acceleration precisely, the measured and predicted values agree reasonably well and therefore it is unlikely that the measured neutron star velocity is significantly affected by errors resulting from the boundary conditions (see Sect. 2.3).

The neutron star is strongly accelerated quite early, starting at $t \approx 70$ ms, but only some time after the onset of the explosion the direction of acceleration evolves so slowly that a significant

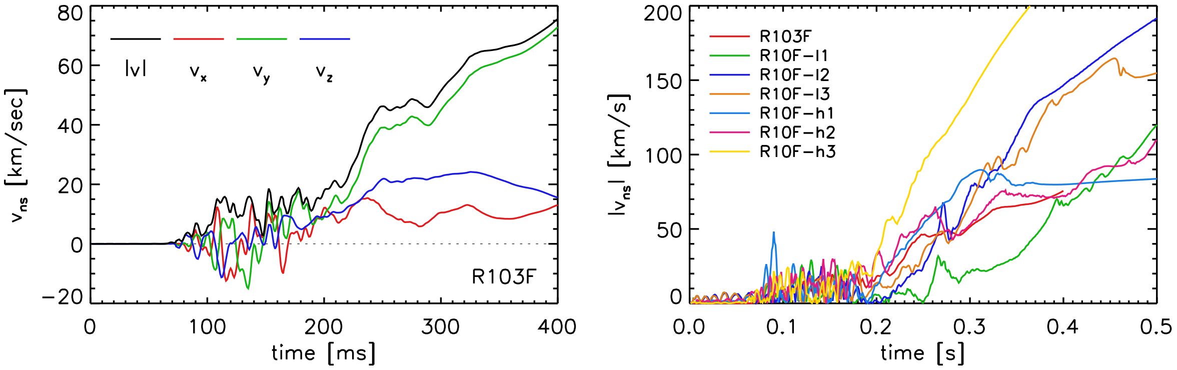

Figure 5.32: *Left panel:* Neutron star velocity components and absolute velocity for Model R103F. The acceleration in y-direction (i.e. in the equatorial plane) dominates. *Right panel:* Neutron star velocity evolution for all models discussed in this section. The three-dimensional model is accelerated similarly strong as the two-dimensional models.

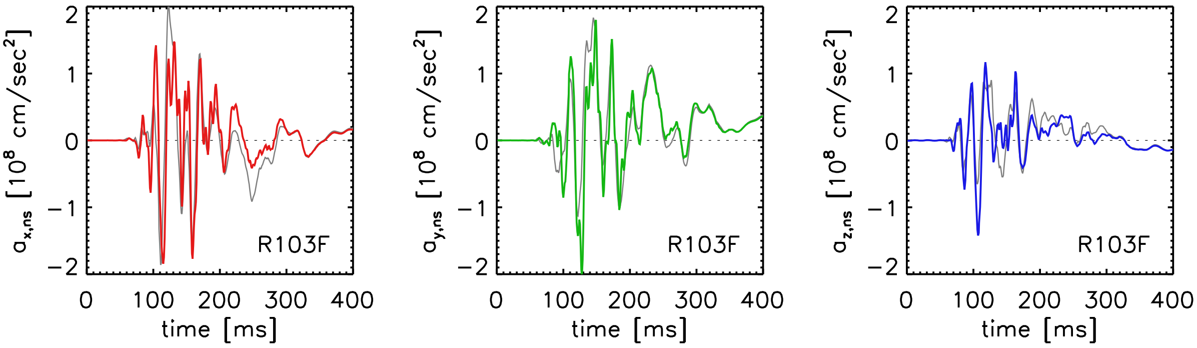

Figure 5.33: Neutron star acceleration components for Model R103F. The gray lines are estimates for the acceleration from post-processing.

neutron star velocity can be built up. Between $t = 200\,\text{ms}$ and $t = 400\,\text{ms}$ the average neutron star acceleration is about 290 km/s^2 and at the end of the simulation $v_{\text{ns}} \approx 75\,\text{km/s}$. These values are in the range of the 2D models, whose average velocity at $t = 0.4\,\text{s}$ is about 120 km/s. Three of the six 2D models have neutron star velocities smaller than 80 km/s at this time. If the scatter of neutron star velocities due to the chaotic dependence on initial perturbations (see Sect. 3.2.5) is similar in 2D and 3D (and we have so far no hints that it is very different) it should be possible to obtain final velocities of more than 500 km/s (which can be expected for Model R10F-h3, see Tab. 5.3) by repeating the 3D simulation sufficiently often using different random seeds.

Furthermore, although a rapid boundary contraction as used in Model R103F seems to increase the average neutron star kick significantly (see Sect. 3.5.3), rotation has the opposite effect. The rotating models of Chapter 3 attain neutron star velocities that are on average a factor of two lower than those of the non-rotating models. If this result holds true also in three dimensions, higher neutron star velocities can be expected for rotation rates lower, and probably more realistic, than those used for Model R103F.

While the absolute values for the acceleration are similar in two and three dimensions, the acceleration directions are different. In two dimensions the neutron star can move only along the symmetry axis, i.e. $\vec{v}_{\text{ns}}$ has only a z-component. This velocity component builds up due to the asymmetry of the mass distributions of the northern and the southern hemisphere. This effect is also present in Model R103F: The shock expansion in the southern hemisphere is somewhat faster and consequently the neutron star is attracted more strongly by the ejecta in the northern hemisphere, which leads to a positive z-component of the neutron star velocity. However, the largest component of $\vec{v}_{\rm ns}$ is $v_y^{\rm ns}$, i.e. the acceleration is roughly *perpendicular* to the axis of rotation, into positive y-direction.

This is because one downflow region near the equatorial plane is sufficiently massive to dominate the gravitational attraction of the neutron star in this plane. This downflow is connected to the pronounced minimum of the shock radius at $\phi = 45°–90°$ (Fig. 5.30). In the main acceleration phase ($t > 200\,\mathrm{ms}$) most of the time this downflow does not reach the neutron star surface but is dissolved already at $r \approx 100\,\mathrm{km}$ or even further out. In this case the lower end of the downflow, which has the strongest influence on the direction into which the neutron star is accelerated, is not far (in longitudinal direction) from the shock minimum. Therefore the neutron star will be mainly accelerated towards this minimum. However, there are two phases (around $t \approx 250\,\mathrm{ms}$ and $t \approx 340\,\mathrm{ms}$) in which the acceleration breaks down and the neutron star velocity does not increase further (see Fig. 5.32). At these times the lower end of the downflow comes closer to the neutron star and centrifugal forces (caused by the angular momentum of the accreting matter) force it to a different longitude than the shock minimum. Consequently the neutron star acceleration is not parallel to the velocity any more. These two situations are visible in Fig. 5.34.

5.3.5 Spin-kick alignment?

Does rotation lead to an alignment of the kick direction with the rotation axis (the so called "spin-kick alignment")? Recent studies of observational constraints on neutron star kicks for isolated pulsars and for neutron stars in binary systems come to the conclusion that this is the case, but only for a part of the neutron star population (Wang et al. 2006). The interpretation of observations is still ambiguous (Johnston et al. 2005), though. There are well-studied examples of pulsars with spin-kick alignment like the Crab pulsar, but on the other hand it has also been clearly shown, that the pulsar in Cas A is moving perpendicular to the symmetry axis of the remnant (which is interpreted as the rotation axis). The observational answer to this question is thus still somewhat unclear — both alignment and misalignment seem to be possible.

What can we predict for the hydrodynamic kick mechanism active in our models? This question cannot be conclusively answered on the basis of two-dimensional axisymmetric simulations, because in this case the neutron star kick is always along the rotation axis due to the assumed symmetry of the calculations. Therefore we are left with only one simulation, Model R013F. In this simulation the neutron star kick is approximately perpendicular to the axis of rotation. However, for a number of reasons this does not allow the conclusion that in general spin-kick misalignment is expected for our kick mechanism.

Firstly, a hemispherical asymmetry that leads to acceleration in spin-direction is present in Model R103F, but weaker than the acceleration perpendicular to the rotation axis. It is unclear, whether this is a generic feature, or if the component parallel to the spin could also dominate. Secondly, the perpendicular component could be overestimated by the fact, that most of the time the downflow does not reach the neutron star surface. It has to be tested, if this is caused by the low angular grid resolution we used. And finally, the progenitor rotation profile and the neutron star contraction adopted for Model R103F may both be too extreme. It is possible that for a weaker influence of centrifugal forces, the emission anisotropy is not strong enough to clear

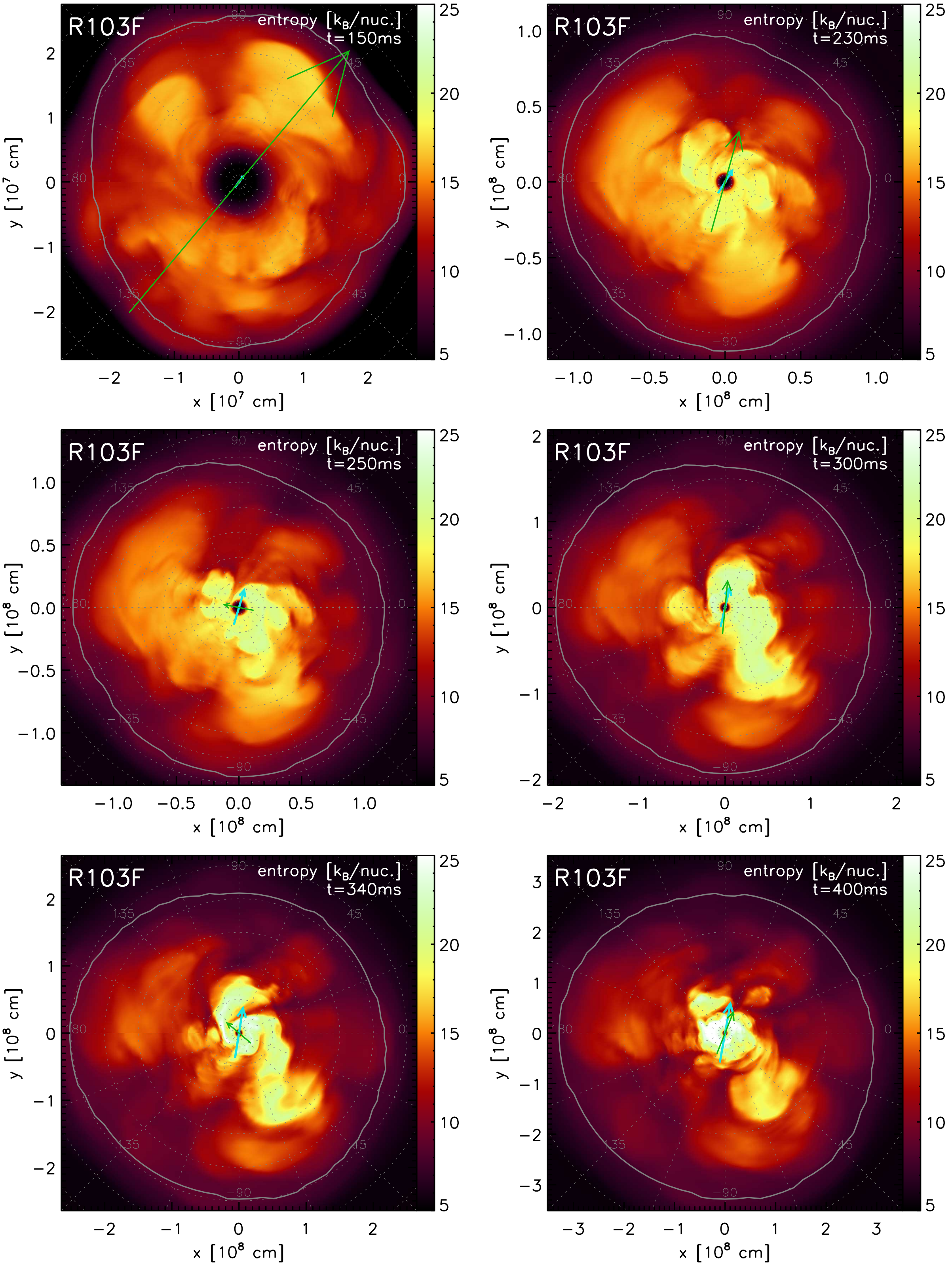

Figure 5.34: Entropy distribution around the equatorial plane (averaged over $\theta \in [-30°, 30°]$) of Model R103F for several times. The blue arrow indicates the velocity and the green arrow the acceleration vector of the neutron star. In general, the neutron star is accelerated towards the most massive downflow that originates from the minimum of the shock radius (gray line), which is most of the time at $\phi = 45°$–$90°$. Only when the downflow comes near to the neutron star surface (visible in the $t = 250$ ms and $t = 340$ ms panels) the direction of acceleration changes significantly.

the polar regions from downflows, but sufficient to define a preferred axis that guides growing instabilities. Also this could lead to spin-kick alignment.

In conclusion, at the moment we can only state that final answers, concerning the alignment of spin and kicks require more 3D models — to improve statistics and to cover a wider range of parameters.

6

Summary and conclusions

The aim of this work was to investigate the growth of hydrodynamic instabilities in the neutrino-heated postshock layer of core-collapse supernovae and the importance of such instabilities for the development of explosion anisotropies and the acceleration of neutron stars.

In core-collapse supernovae a shock wave is launched in the collapsed iron core of a massive star and stalls at a radius of 100–200 km. In the neutrino-driven explosion scenario the stalled shock is thought to be revived by the absorption of a small fraction of the neutrinos streaming out of the hot, nascent neutron star at the centre. This neutrino-heating of the postshock layer is stronger for smaller radii, which results in a radial entropy profile that is unstable to convection. Indeed it has been confirmed in several studies that convective overturn develops below the stalled supernova shock (Herant et al. 1994; Burrows et al. 1995; Janka & Müller 1996). However, it has also been proposed that the stalled shock wave itself may be subject to different, global instabilities. For instance, Houck & Chevalier (1992) predicted unstable oscillations of the shock for sufficiently large shock radii, and Thompson (2000) proposed that the shock may develop a global Rayleigh-Taylor mode.

We investigated the nature of such hydrodynamic instabilities and their influence on the stalled shock phase and the subsequent explosion by means of two- and three-dimensional hydrodynamic simulations. For these simulations we relied on the viability of the neutrino-driven explosion mechanism. Because the latter is still an open question (see Buras et al. 2006a,b), we triggered the explosions in our simulations by replacing the contracting core of the nascent neutron star by an inner boundary of the computational grid, where we assumed suitable neutrino luminosities from the neutron star core. A systematic variation in these core luminosities, which control the intensity of neutrino heating, allowed us to investigate the growth of hydrodynamic instabilities for different explosion time scales and energies.

We started the simulations shortly after the formation of the shock wave from spherical symmetric initial models. Low-amplitude small-scale perturbations which we imposed onto these initial models at the start of the simulations grew by hydrodynamic instabilities to high-amplitude, large-scale anisotropies. This nonlinear growth to large scales is an example for spontaneous, global symmetry breaking. Due to the stochastic nature of this process the final morphology of the explosion depend in a chaotic way on the initial perturbations.

Apart from features typical for a convective overturn (like rising Rayleigh-Taylor "mushrooms", narrow downdrafts and vortex structures) we found indications for an oscillatory instability of the shock wave in our simulations, which affected only the lowest modes. The nature of these dipole or quadrupole oscillations in our numerical models was more closely investigated in collaboration with a French group that studies the linearised problem in order to determine the stability properties of stationary accretion flows. Applying such complementary approaches proved to be very helpful for the understanding of the growth of perturbations taking place in the postshock layer and resulted in the discovery of a new instability mechanism different from convection (see Chapter 4). In this mechanism, the so-called "advective-acoustic cycle", perturbations caused by disturbances of the shock surface are advected downwards with the accretion flow, which is decelerated near the neutron star surface. The deceleration of perturbations triggers sound waves, which travel outward against the subsonic accretion flow and collide with the shock, thereby creating new shock disturbances. Such a process can lead to an amplifying feedback loop for perturbations. Similar phenomena are known from other fields, e.g., the "rumble instability" encountered in jet engines or the "impinging shear flow instability" that makes tea kettles whistle, but they had not been recognised before to be of relevance in the supernova core. A competing US group proposed an alternative, purely acoustic mechanism based on a standing pressure wave to explain the anisotropy of supernova explosion. By analysing the scaling behaviour of the oscillation periods in our simulations this hypothesis could be disproven.

Furthermore, the results of these simulations led us to the conclusion, that the "advective-acoustic cycle" is in fact the main mechanism creating anisotropy and that convection is not required to explain the dominance of low modes. In most of the 80 two-dimensional (i.e., assuming axisymmetry) models we computed for this study, the shock and the postshock flow developed a pronounced dipole or quadrupole anisotropy ($l = 1$ or $l = 2$ in terms of an expansion in spherical harmonics Y_l^m) before the onset of the explosion. In the subsequent evolution the expanding shock retained its non-spherical shape. The postshock flow was dominated by one or two downdrafts that allowed for further accretion of matter onto the neutron star, until they were blown away several 100 ms after the explosion by the neutrino-driven wind forming above the neutron star surface (see Chapter 3). Kifonidis et al. (2006) performed long-term simulations using the results of our simulations (which encompass the first second of post-bounce evolution) as initial models and found that the anisotropy present after one second is retained and triggers a large-scale mixing of the outer layers of the progenitor star some hours later.

In our highly anisotropic explosions the ejected mass attains a large net linear momentum. As the total momentum of the system must be conserved, this requires that the neutron star takes up the same amount of momentum in the opposite direction and is therefore accelerated to high velocities. The acceleration of the neutron star, which occurs on a time scale of several seconds, was found to be mediated mainly by gravitational forces that are caused by the anisotropic mass distribution of the ejecta. As long as accretion funnels reach down to the neutron star surface, also hydrodynamic forces (e.g. due to the transfer of momentum to the neutron star by the accreting matter) play a significant role. Near the lower ends of the accretion downdrafts the kinetic energy of the accreted matter is converted to internal energy in a strong shock and is partly radiated away in the form of neutrinos. In principle, this anisotropic neutrino emission could also lead to an acceleration of the neutron star, but it was found that this effect is weak and can be neglected in most of the models. The highest neutron star velocities are obtained for dipole (i.e. $l = 1$) dominated, almost "one-sided" explosions, in which the shock expansion in one hemisphere proceeds much faster than in the other. In one of these cases the neutron star reached a velocity of about 1200 km/s. In explosions dominated by $l = 2$ or higher modes, the acceleration is weaker.

The biggest shortcoming of the simulations discussed so far is their two-dimensionality, i.e. the fact, that the flow in our simulations was restricted by the assumption of axisymmetry. Due to the enormous computational cost of full three-dimensional simulations, it was not possible to perform parameter studies with a large number of models in 3D. However, we were able to run three 3D simulations (discussed in Chapter 5), which, however, are still limited in terms of grid resolution, grid size and the simulated time span. Nevertheless, these simulations provided first insights in three-dimensional effects. The most important conclusion we could draw from the outcome of these simulations is that the formation of low-mode anisotropies in our 2D models was not a result of the restriction of the flow by the assumption of axisymmetry. Also the 3D models develop dominant low-modes asymmetry.

However, several properties of the flow structure in 3D are fundamentally different from the 2D case. For instance, the downdrafts, in which matter is accreted onto the neutron star become extremely thin in 2D but are much wider in 3D. Furthermore, a turbulent layer above the neutron star that hampers the formation of the neutrino-driven wind in 2D models is much weaker in 3D. The most striking differences are found for rotating models: In 2D the regions above the poles of the neutron star are preferred locations for accretion funnels, whereas in 3D we find the strongest *outflows* of matter to occur in these regions, because the anisotropic heating by neutrinos emitted from the rotationally deformed neutron star is maximal there.

The values of the neutron star acceleration in the 3D models after the onset of the explosion turned out to be in the same range as in the 2D models. This makes us optimistic that very high neutron star velocities can also be reached in 3D, although at the time we had to stop the 3D runs the velocities are still rather low. It is probably only a matter of statistics to obtain a very high neutron star velocity also in a 3D model. Due to the stochastic dependence on the initial perturbations, a large number of 3D models will be needed to quantify the differences between 2D and 3D models and to determine the neutron star velocity distribution in three dimensions.

The kick velocity distribution of our two-dimensional models contains two populations: a high-velocity component (with an average kick velocity of $\sim 500\,\mathrm{km/s}$) in which the $l = 1$ dipole mode of the ejecta was dominant, and a low-velocity component (with an maximum kick velocity of $\sim 200\,\mathrm{km/s}$) in which mainly higher modes determined the morphology. Neutron star velocity distributions that have been deduced from observations might indeed show such a bimodality (Cordes & Chernoff 1998; Fryer et al. 1998; Arzoumanian et al. 2002; Brisken et al. 2003), but this issue is observationally still controversial (Hansen & Phinney 1997; Hobbs et al. 2005). Although the presence or absence of a pronounced dipole mode in the ejecta distribution would offer a natural and suggestive way to obtain a bimodality in the context of our hydrodynamic kick mechanism, we refrain from claiming that our result strongly supports the existence of such a bimodality in the observed distribution of pulsar velocities. A wider range of progenitor stars and 3D effects have to be included before such claims can be made. Furthermore, it has to be considered that in contrast to the kick velocities obtained from simulations, measured pulsar velocities may contain a contribution that results from the angular momentum conservation during the break-up of binary star systems in which one of the stars explodes as a supernova.

The proposed hydrodynamic kick mechanism, however, leads also to an unambiguous prediction: The measured neutron star velocity should be directed opposite to the momentum of the gaseous supernova ejecta. This is different from many theories that explain pulsar kicks by anisotropic neutrino emission from the nascent neutron star. In that case the direction of the acceleration can be independent of ejecta asymmetries. Recent observations show that the momenta of the ejecta and the pulsar in several supernova remnants seem to be compatible with the hydrodynamic kick mechanism (see, e.g. Winkler & Petre 2006). Future detailed studies of supernova remnants will show whether this is the case in general.

Another encouraging results provides further support for our studies: The long-time supernova simulations of Kifonidis et al. (2006), which were started from our models, show a large-scale overturn of the outer layers of the progenitor star, seeded and triggered by the core anisotropies found in our simulations, that can explain the velocity distribution of radioactive elements determined from spectra of Supernova 1987A. This was not possible when the simulations were started from less anisotropic early explosion models (Kifonidis et al. 2003).

The models presented in this work are the first to develop simultaneously neutron star masses, explosion energies, and neutron star velocities that lie in the ranges known from observations, without relying on special assumptions about the initial conditions (such as extreme perturbations and anisotropies present in the collapsing progenitor star, extreme rotation rates, or magnetic fields in the progenitor star). In view of these results, a consistent picture of the processes taking place after core bounce seems to emerge. The early anisotropy of supernova inferred from the polarised light emitted during the explosion, the large-scale mixing of radioactive elements into the hydrogen layer of the progenitor star (observed in the spectra of Supernova 1987A), the anisotropies of supernova remnants, and the extreme velocities of neutron stars can all be traced back to one common origin — delayed, neutrino-driven explosions, in which hydrodynamic instabilities grow to pronounced global modes.

Yet, more work has to be done to consolidate this picture. Apart from the obvious need to confirm the viability of the delayed, convectively supported explosion mechanism, more simulations of the kind presented in this work should be performed. Given the significant differences of the fluid dynamics in 2D and 2D discussed above, these simulations should be performed in three dimensions. In addition, it would be interesting to use more progenitor stars with different masses and different rotation rates and to run also long-term simulations. This will allow for new and more reliable predictions (e.g. concerning the distribution function of the kick velocities or a possible alignment of rotation axis and kick direction) that can be tested with future observations. Work is underway to extend this study and will hopefully yield further exciting results.

Bibliography

Arras, P. & Lai, D. 1999a, ApJ, 519, 745 11

Arras, P. & Lai, D. 1999b, Phys. Rev. D, 60, 043001 11

Arzoumanian, Z., Chernoff, D. F., & Cordes, J. M. 2002, ApJ, 568, 289 11, 61, 129

Baade, W. & Zwicky, F. 1934, Phys. Rev., 45, 138 6

Bazan, G. & Arnett, W. D. 1998, ApJ, 496, 316 86

Bethe, H. A. 1990, Physics Today, 43, 24 6

Bethe, H. A. & Wilson, J. R. 1985, ApJ, 295, 14 7

Blondin, J. M. & Mezzacappa, A. 2006, ApJ, 642, 401 10, 12, 63, 64, 67, 79

Blondin, J. M., Mezzacappa, A., & DeMarino, C. 2003, ApJ, 584, 971 10, 12, 40, 41, 67, 69, 70, 76, 85

Brisken, W. F., Fruchter, A. S., Goss, W. M., Herrnstein, R. M., & Thorsett, S. E. 2003, AJ, 126, 3090 11, 61, 129

Bruenn, S. W. 1985, ApJS, 58, 771 141

Bruenn, S. W. 1993, in Nuclear Physics in the Universe, ed. M. W. Guidry & M. R. Strayer (Bristol: IOP), 31 25, 27, 29, 31

Buras, R., Rampp, M., Janka, H.-T., & Kifonidis, K. 2003, Phys. Rev. Lett., 90, 241101 8, 21, 22, 23, 26, 27, 30, 43, 44, 57, 63, 75, 137

Buras, R., Rampp, M., Janka, H.-T., & Kifonidis, K. 2006a, A&A, 447, 1049 8, 26, 43, 63, 86, 127, 137, 147

Buras, R., Rampp, M., Janka, H.-T., & Kifonidis, K. 2006b, A&A, submitted, astro-ph/0512189 8, 9, 43, 44, 63, 127, 137

Burrows, A. & Hayes, J. 1996, Phys. Rev. Lett., 76, 352 11

Burrows, A., Hayes, J., & Fryxell, B. A. 1995, ApJ, 450, 830 8, 12, 36, 43, 44, 127

Burrows, A. & Thompson, T. A. 2004, in Stellar Collapse, ed. C. Fryer (Dordrecht: Kluwer Academic Publishers), 133 141

Chandrasekhar, S. 1961, Hydrodynamic and hydromagnetic stability (New York: Dover) 9

Chatterjee, S. & Cordes, J. M. 2002, ApJ, 575, 407 10

Chatterjee, S., Vlemmings, W. H. T., Brisken, W. F., et al. 2005, ApJ, 630, L61 10, 59

Colella, P. & Woodward, P. R. 1984, J. Comput. Phys., 54, 174 17

Colgan, S. W. J., Haas, M. R., Erickson, E. F., Lord, S. D., & Hollenbach, D. J. 1994, ApJ, 427, 874 8

Colgate, S. A. & White, R. H. 1966, ApJ, 143, 626 7

Cordes, J. M. & Chernoff, D. F. 1998, ApJ, 505, 315 11, 61, 129

Cordes, J. M., Romani, R. W., & Lundgren, S. C. 1993, Nature, 362, 133 10

Einfeldt, B. 1988, SIAM J. Num. Anal., 25, 294 17

Foglizzo, T. 2001, A&A, 368, 311 10

Foglizzo, T. 2002, A&A, 392, 353 10, 66

Foglizzo, T., Galletti, P., Scheck, L., & Janka, H.-T. 2006a, ApJ, submitted, astro-ph/0606640 10, 12, 63, 66, 67

Foglizzo, T., Scheck, L., & Janka, H.-T. 2006b, ApJ, submitted, astro-ph/0507636 10, 41, 64, 65, 76, 86

Foglizzo, T. & Tagger, M. 2000, A&A, 363, 174 10, 66

Freedman, D. Z., Schramm, D. N., & Tubbs, D. L. 1977, Ann. Rev. Nucl. Sci., 27, 167 141

Fryer, C., Burrows, A., & Benz, W. 1998, ApJ, 496, 333 11, 61, 129

Fryer, C. L. 1999, ApJ, 522, 413 44

Fryer, C. L. & Heger, A. 2000, ApJ, 541, 1033 44

Fryer, C. L. & Kusenko, A. 2006, ApJS, 163, 335 11

Fryer, C. L. & Warren, M. S. 2002, ApJ, 574, L65 44

Fryer, C. L. & Warren, M. S. 2004, ApJ, 601, 391 44, 87

Fuller, G. M., Kusenko, A., Mocioiu, I., & Pascoli, S. 2003, Phys. Rev. D, 68, 103002 11

Galletti, P. & Foglizzo, T. 2005, in Proc. of the SF2A meeting, 17-30 June 2005, Strasbourg, EDPS Conference Series in Astronomy & Astrophysics, ed. F. Casoli, T. Contini, H. M. Hameury, & L. Pagani, astro–ph/0509635 10, 40, 63, 66

Goldreich, P., Lai, D., & Sahrling, M. 1996, in Unsolved Problems in Astrophysics, ed. J. N. Bahcall & J. P. Ostriker (Princeton: Princeton Univ. Press) 86

Haas, M. R., Erickson, E. F., Lord, S. D., et al. 1990, ApJ, 360, 257 8

Hansen, B. M. S. & Phinney, E. S. 1997, MNRAS, 291, 569 10, 11, 61, 129

Heger, A., Langer, N., & Woosley, S. E. 2000, ApJ, 528, 368 26, 27

Heger, A., Woosley, S., Langer, N., & Spruit, H. C. 2004, in Proc. IAU Symp. No. 215, ed. A. Maeder & P. Eenens (San Francisco: Astronomical Society of the Pacific), 591, astro–ph/0301374 26, 27, 50, 55

Herant, M. 1995, Phys. Rep., 256, 117 11, 33, 36

Herant, M., Benz, W., & Colgate, S. 1992, ApJ, 395, 642 44

Herant, M., Benz, W., Hix, W. R., Fryer, C. L., & Colgate, S. A. 1994, ApJ, 435, 339 8, 12, 127

Hobbs, G., Lorimer, D. R., Lyne, A. G., & Kramer, M. 2005, MNRAS, 360, 974 11, 61, 129

Houck, J. C. & Chevalier, R. A. 1992, ApJ, 395, 592 127

Hwang, U., Laming, J. M., Badenes, C., et al. 2004, ApJ, 615, L117 8

James, F. 1994, Comput. Phys. Commun., 79, 111 26

James, F. 1996, Comput. Phys. Commun., 97, 357 26

Janka, H.-T. 1990, in Procs. of the 5th Workshop on Nuclear Astrophysics, held 30 January-4 February 1989 at Ringberg Castle, Tegernsee, FRG, ed. W. Hillebrandt & E. Müller (Garching: Max-Planck-Institut für Astrophysik), 130 138, 140

Janka, H.-T. 1991a, A&A, 244, 378 143, 144

Janka, H.-T. 1991b, Dissertation, Technische Universität München 138, 139, 140, 143, 145

Janka, H.-T. 2001, A&A, 368, 527 118

Janka, H.-T., Buras, R., Kifonidis, K., Plewa, T., & Rampp, M. 2003, in From Twilight to Highlight: The Physics of Supernovae, Proc. of the ESO/MPA/MPE Workshop, Garching, Germany, July 29–31, 2002, ed. W. Hillebrandt & B. Leibundgut (Berlin: Springer), 39, astro–ph/0212316 42

Janka, H.-T., Buras, R., Kifonidis, K., Plewa, T., & Rampp, M. 2004, in Stellar Collapse, ed. C. Fryer (Dordrecht: Kluwer Academic Publishers), 65, astro–ph/0212314 42

Janka, H.-T. & Hillebrandt, W. 1989, A&AS, 78, 375 139, 140

Janka, H.-T. & Müller, E. 1994, A&A, 290, 496 11, 33, 39

Janka, H.-T. & Müller, E. 1996, A&A, 306, 167 8, 12, 17, 18, 21, 28, 36, 41, 42, 127

Jennings, D. E., Boyle, R. J., Wiedemann, G. R., & Moseley, S. H. 1993, ApJ, 408, 277 8

Johnston, S., Hobbs, G., Vigeland, S., et al. 2005, MNRAS, 364, 1397 124

Kane, J., Arnett, W. D., Remington, B. A., et al. 2000, ApJ, 528, 989 41, 94

Keil, M. T., Raffelt, G. G., & Janka, H.-T. 2003, ApJ, 590, 971 139

Keil, W., Janka, H.-T., & Müller, E. 1996, ApJ, 473, L111 9

Kifonidis, K., Plewa, T., Janka, H.-T., & Müller, E. 2003, A&A, 408, 621 17, 18, 21, 41, 42, 130

Kifonidis, K., Plewa, T., Scheck, L., Janka, H.-T., & Müller, E. 2006, A&A, 453, 661 17, 107, 128, 129

Kitaura, F. S., Janka, H.-T., & Hillebrandt, W. 2006, A&A, 450, 345 8

Kuhlen, M., Woosley, W. E., & Glatzmaier, G. A. 2003, in ASP Conf. Ser. Vol. 293: 3D Stellar Evolution, ed. S. Turcotte, S. Keller, & R. Cavallo (San Francisco: Astron. Society of the Pacific), 147 9

Lai, D. 2001, in LNP Vol. 578: Physics of Neutron Star Interiors, ed. D. Blaschke, N. Glendenning, & A. Sedrakian (Berlin: Springer), 424 11

Lai, D., Chernoff, D. F., & Cordes, J. M. 2001, ApJ, 549, 1111 11

Lai, D. & Goldreich, P. 2000, ApJ, 535, 402 86

Lattimer, J. M. & Swesty, F. D. 1991, Nucl. Phys. A, 535, 331 21

Leonard, D. C., Filippenko, A. V., Ganeshalingam, M., et al. 2006, Nature, 440, 505 8

LeVeque, R. J. 1998, in Computational Methods for Astrophysical Fluid Flow, ed. O. Steiner & A. Gautschy (Berlin: Springer), 1 17

Liebendörfer, M., Mezzacappa, A., Thielemann, F., et al. 2001, Phys. Rev. D, 63, 103004 8, 42, 63

Liebendörfer, M., Rampp, M., Janka, H.-T., & Mezzacappa, A. 2005, ApJ, 620, 840 8, 42, 63

Limongi, M., Straniero, O., & Chieffi, A. 2000, ApJS, 129, 625 25, 30, 48

Lüscher, M. 1994, Comput. Phys. Commun., 79, 100 26

Lyne, A. G. & Lorimer, D. R. 1994, Nature, 369, 127 10, 61

Marek, A., Dimmelmeier, H., Janka, H.-T., Müller, E., & Buras, R. 2006, A&A, 445, 273 18, 39

Minerbo, G. N. 1978, J. Quant. Spectrosc. Radiat. Transfer, 20, 541 143

Minkowski, R. 1941, PASP, 53, 224 5

Müller, E. 1998, in Computational Methods for Astrophysical Fluid Flow, ed. O. Steiner & A. Gautschy (Berlin: Springer), 371 15

Müller, E., Rampp, M., Buras, R., Janka, H.-T., & Shoemaker, D. H. 2004, ApJ, 603, 221 115

Murphy, J. W., Burrows, A., & Heger, A. 2004, ApJ, 615, 460 11

Myra, E. S. & Burrows, A. 1990, ApJ, 364, 222 139

Ohnishi, N., Kotake, K., & Yamada, S. 2006, ApJ, 641, 1018 10, 12, 63, 70, 76, 85

Rampp, M. & Janka, H.-T. 2000, ApJ, 539, L33 8, 42

Rampp, M. & Janka, H.-T. 2002, A&A, 396, 361 18, 26, 39, 63, 147

Scheck, L., Kifonidis, K., Janka, H.-T., & Müller, E. 2006, A&A, in preparation 13, 36

Scheck, L., Plewa, T., Janka, H.-T., Kifonidis, K., & Müller, E. 2004, Phys. Rev. Lett., 92, 011103 13

Schinder, P. J., Schramm, D. N., Wiita, P. J., Margolis, S. H., & Tubbs, D. L. 1987, ApJ, 313, 531 143

Sehgal, I. 1974, Nucl. Phys. B, 70, 61 145

Socrates, A., Blaes, O., Hungerford, A., & Fryer, C. L. 2005, ApJ, 632, 531 11

Strang, G. 1968, SIAM, J. Num. Anal., 5, 506 16

Straumann, N. 1989, in Particle Physics and Astrophysics, ed. H. Mitter & F. Widder (Berlin: Springer-Verlag), 79 141

Tassoul, J.-L. 1978, Theory of Rotating Stars (Princeton, New Jersey: Princeton University Press) 49, 50, 116

Thompson, C. 2000, ApJ, 534, 915 127

Thompson, T. A., Burrows, A., & Meyer, B. S. 2001, ApJ, 562, 887 152

Thompson, T. A., Burrows, A., & Pinto, P. A. 2003, ApJ, 592, 434 8, 43, 63

Tubbs, D. L. 1979, ApJ, 231, 846 145

Tubbs, D. L. & Schramm, D. N. 1975, ApJ, 201, 467 141, 144

Wang, C., Lai, D., & Han, J. L. 2006, ApJ, 639, 1007 124

Wang, L., Baade, D., Höflich, P., & Wheeler, J. C. 2003, ApJ, 592, 457 8

Wang, L., Howell, D. A., Höflich, P., & Wheeler, J. C. 2001, ApJ, 550, 1030 8

Wang, L., Wheeler, J. C., Höflich, P., et al. 2002, ApJ, 579, 671 8

Wilson, J. R. 1985, in Numerical Astrophysics, ed. J. M. Centrella & R. L. Bowers (Boston: Jones and Bartlett), 422 7

Winkler, P. & Petre, R. 2006, ApJ, submitted, astro-ph/0608205 8, 11, 129

Woodward, P. R., Porter, D. H., & Jacobs, M. 2003, in ASP Conf. Ser. Vol. 293: 3D Stellar Evolution, ed. S. Turcotte, S. Keller, & R. Cavallo (San Francisco: Astron. Society of the Pacific), 45 9

Woosley, S. E., Pinto, P. A., & Ensman, L. 1988, ApJ, 324, 466 8, 25, 27, 29, 31, 48

Woosley, S. E. & Weaver, T. A. 1995, ApJS, 101, 181 26, 30, 48

Zou, W. Z., Hobbs, G., Wang, N., et al. 2005, MNRAS, 362, 1189 10, 61

A

Neutrino transport

A.1 Transport equation

We start from the equation of radiation transport in spherical symmetry

$$\frac{1}{c}\frac{\partial}{\partial t}I + \mu\frac{\partial}{\partial r}I + \frac{1-\mu^2}{r}\frac{\partial}{\partial \mu}I = S, \tag{A.1}$$

where $I = I(t, r, \epsilon, \mu)$ is the specific intensity, $S = S(t, r, \epsilon, \mu)$ is the source function, ϵ is the neutrino energy, $\mu = \cos\theta$ and θ is the angle between radiation propagation and radial direction. Solid angle integration yields the zeroth angular moment equation,

$$\frac{1}{c}\frac{\partial}{\partial t}J + \frac{1}{r^2}\frac{\partial}{\partial r}(r^2 H) \qquad = S^{(0)} \equiv \frac{1}{2}\int_{-1}^{+1} \mathrm{d}\mu\, S \tag{A.2}$$

with $\{J, H\}(t, r, \epsilon) := \frac{1}{2}\int_{-1}^{+1} \mathrm{d}\mu\, \mu^{\{0,1\}} I(t, r, \epsilon, \mu)$. Integration over energy leads to

$$\frac{\partial}{\partial t}E + \frac{1}{r^2}\frac{\partial}{\partial r}(r^2 F) = Q^+ - Q^- \tag{A.3}$$

with $\{E, F\}(t, r) := 4\pi \int_0^\infty \mathrm{d}\epsilon\, \{J/c, H\}(t, r, \epsilon)$ being energy density and energy flux, respectively. The source term has been split in an emission rate Q^+ and an absorption rate $Q^- = \kappa_\mathrm{a} cE$, which is proportional to the energy density. The *flux factor* is defined as the ratio of flux to energy density,

$$f(r, t) := F(r, t) \,/\, cE(r, t). \tag{A.4}$$

In neutrino transport simulations solving the full Boltzmann equation (see e.g. Buras et al. 2003, 2006a,b) this quantity shows only little short-time variability during most phases of the supernova evolution. Therefore $\partial f/\partial t = 0$ is an acceptably good approximation. With $L := 4\pi r^2 F = 4\pi r^2 f cE$ one can now rewrite Eq. (A.3) as

$$\frac{\partial}{\partial t}L + c_\mathrm{eff}\frac{\partial}{\partial r}L = 4\pi\, r^2\, c_\mathrm{eff}\, \{Q^+ - Q^-\}, \tag{A.5}$$

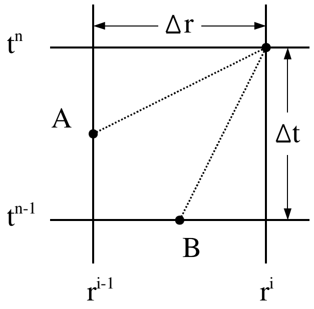

Figure A.1: The solution at (r^i, t^n) is computed from the data at a point $(r^\star, t^\star)$ located on the same characteristic line. Depending on the grid spacing, Δr, the time step, Δt, and the effective speed of neutrino propagation, $c_{\rm eff}$, either point A or point B must be used. The solution there can be obtained by interpolation in time or space, respectively.

where an effective speed of neutrino propagation has been introduced as $c_{\rm eff} := cf$. Provided $c_{\rm eff}$ were known, the solution of Eq. (A.5) requires considerably less effort than the numerical integration of Eq. (A.1). For vanishing source terms Q^+ and Q^- the neutrino energy or number density is just advected along characteristics $r(t) = r_0 + c_{\rm eff}\, t$. Although $c_{\rm eff}$ depends through $f(r,t)$ on the solution of the transport problem (Eq. A.4), neutrino transport calculations in the neutrino-decoupling layer of forming neutron stars reveal that it can be well fitted by a r-dependent function which depends on the steepness of the density profile (see Janka 1990, 1991b). Assuming further that the (medium-dependent) coefficients Q^+ and $\tilde\kappa \equiv \kappa_{\rm a}/f = 4\pi r^2 Q^-/L$ are constant between two points (r,t) and $(r^\star, t^\star)$, which are connected by a characteristic line, i.e.,

$$r^\star = r - c_{\rm eff}\,(t - t^\star), \tag{A.6}$$

Eq. (A.5) can be integrated analytically to yield

$$\begin{aligned} L(r,t) &= L(r^\star, t^\star)\, \mathrm{e}^{-\tilde\kappa c_{\rm eff}\,(t-t^\star)} \\ &+ \frac{4\pi Q^+}{\tilde\kappa^3} \Big\{ [1 - \mathrm{e}^{-\tilde\kappa c_{\rm eff}\,(t-t^\star)}]\,[1 + (\tilde\kappa r^\star - 1)^2] \\ &+ \tilde\kappa c_{\rm eff}\,(t-t^\star)[2\tilde\kappa r^\star + \tilde\kappa c_{\rm eff}\,(t-t^\star) - 2] \Big\}, \end{aligned} \tag{A.7}$$

where $L(r,t)$ and $L(r^\star,t^\star)$ are the luminosity values at both ends of the characteristic line.

We use Eq. (A.7) to construct a numerical scheme to solve Eq. (A.5) in the general case: We assume that the luminosity is known at the cell interfaces of a one-dimensional radial grid for a time t^{n-1}, and that the cell-averaged values of the quantities needed to compute the emission rate Q^+ and absorption coefficient $\tilde\kappa$ are also known for that time. As a further simplification we do not allow neutrinos to propagate in negative radial direction (actually this is granted by defining a non-negative function for the flux factor, see Sect. A.2). Then the luminosities at $t^n = t^{n-1} + \Delta t$ for each zone interface (starting at the innermost zone) can be computed using Eq. (A.7). In doing so we have to distinguish between two cases (see Fig. A.1): If $c_{\rm eff}\Delta t > \Delta r$, we can use point A as the starting point of the integration, $(r^\star, t^\star) = (r_{i-1}, t_A)$. The luminosity at this point is derived from a linear interpolation between $L(r_{i-1}, t^{n-1})$ and $L(r_{i-1}, t^n)$ (which is already known, as we are integrating outwards). If $c_{\rm eff}\Delta t \le \Delta r$, we use point B, the luminosity at this point being given by a linear interpolation between $L(r_{i-1}, t^{n-1})$ and $L(r_i, t^{n-1})$.

For time integration we use a predictor-corrector method: The transport routine is called two times. In the first (predictor) step the luminosities, emission rates and absorption coefficients of the last time step $[L^{n-1}, Q^{n-1}, \kappa^{n-1}]$ are used to compute preliminary values $(\tilde Q^n, \tilde\kappa^n)$ for the neutrino-medium coupling at the next time level. In the second (corrector) step the final values $[L^n, Q^n, \kappa^n]$ are calculated using $[L^{n-1}, \frac{1}{2}(Q^{n-1} + \tilde Q^n), \frac{1}{2}(\kappa^{n-1} + \tilde\kappa^n)]$ as input.

Equation (A.5) is solved not only for the energy luminosity $L = L_e$, but also for the number luminosity $L_n = 4\pi r^2 F_n = 4\pi r^2 fcn$ (n is the particle density and f is assumed to be the same flux factor as for the energy transport). Furthermore the equation has to be integrated for three neutrino types, ν_e, $\bar{\nu}_\mathrm{e}$, and ν_x (the latter denoting ν_μ, $\bar{\nu}_\mu$, ν_τ, and $\bar{\nu}_\tau$, which are treated identically). In the following we will use indices $\nu \in \{\nu_\mathrm{e}, \bar{\nu}_\mathrm{e}, \nu_x\}$ and $\alpha \in \{e, n\}$ to distinguish between these different cases.

In the 2D case the neutrino transport is assumed to proceed only radially, i.e. lateral components of the neutrino flux are ignored and Eq. (A.5) is integrated independently on different radial "rays", i.e. in radial direction for every lateral zone of the polar coordinate grid. Total luminosities of the star are obtained by summing up the flux densities $L/4\pi r^2$ for all angular cells (at a given radius r), appropriately weighting them with the corresponding surface elements.

A.2 Neutrino distribution function

To calculate the source terms in Eq. (A.5) or (A.7) we have to make an assumption about the neutrino energy spectrum, i.e. about the energy dependency of the specific intensity, which for particle energy and particle number is linked with the particle distribution function $f_{D,\nu}$ in the following way:

$$I_{\nu,\{n,e\}}(t, r, \epsilon, \mu) = \left(\frac{\epsilon^{\{2,3\}}}{(hc)^3}\right) c\, f_{\mathrm{D},\nu}(t, r, \epsilon, \mu), \tag{A.8}$$

where the exponent of 2 applies for number transport and the exponent of 3 for energy transport, corresponding to the indices n and e, respectively, of I_ν. We assume that $f_{\mathrm{D},\nu}$ can be written as product of a Fermi-Dirac distribution function,

$$f_{\mathrm{FD}}(x, \eta) = \frac{1}{1 + \exp(x - \eta)}, \tag{A.9}$$

and an angle-dependent function g_ν,

$$f_{D,\nu}(r, t, \epsilon, \mu) = g_\nu(r, t, \mu)\; f_{\mathrm{FD}}\left(\frac{\epsilon}{k_\mathrm{B} T_\nu(r, t)}, \eta_\nu(r, t)\right), \tag{A.10}$$

where in general the spectral temperature and degeneracy parameter, T_ν and η_ν, are different from the matter temperature and equilibrium degeneracy parameter.

Furthermore we assume that η_ν is just a function of the optical depth τ_ν:

$$\eta_\nu(\tau_\nu) = \eta_{\mathrm{eq},\nu}\,(1 - \mathrm{e}^{-\tau_\nu}) + \eta_{0,\nu}\,\mathrm{e}^{-\tau_\nu}, \tag{A.11}$$

where $\eta_{\mathrm{eq},\nu}$ is the equilibrium degeneracy parameter and $\eta_{0,\nu}$ is a chosen value as typically found in detailed transport calculations for $\tau_\nu \to 0$. The values for the different neutrino types are (cf. Janka 1991b; Janka & Hillebrandt 1989; Myra & Burrows 1990; Keil et al. 2003):

$$\begin{aligned} \eta_{\mathrm{eq},\nu_\mathrm{e}} &= (\mu_\mathrm{e} + \mu_\mathrm{p} - \mu_\mathrm{n})/k_\mathrm{B}T, & \eta_{0,\nu_\mathrm{e}} &\equiv 3, \\ \eta_{\mathrm{eq},\bar{\nu}_\mathrm{e}} &= -\eta_{\mathrm{eq},\nu_\mathrm{e}}, & \eta_{0,\bar{\nu}_\mathrm{e}} &\equiv 2, \\ \eta_{\mathrm{eq},\nu_x} &= 0, & \eta_{0,\nu_x} &\equiv 0. \end{aligned} \tag{A.12}$$

With η_ν defined, T_ν can now be calculated from the local average neutrino energy, which is computed from $L_{e,\nu}$ and $L_{n,\nu}$ as

$$\begin{aligned}\langle\epsilon_\nu\rangle &= L_{e,\nu}/L_{n,\nu} = E_\nu(r,t)/n_\nu(r,t) \\ &= \frac{\int_0^\infty \mathrm{d}\epsilon\ \int_{-1}^{+1}\mathrm{d}\mu\ I_{e,\nu}(r,t,\epsilon,\mu)}{\int_0^\infty \mathrm{d}\epsilon\ \int_{-1}^{+1}\mathrm{d}\mu\ I_{n,\nu}(r,t,\epsilon,\mu)} \\ &= k_\mathrm{B}T_\nu\,\mathcal{F}_3(\eta_\nu)/\mathcal{F}_2(\eta_\nu) \end{aligned} \tag{A.13}$$

with the Fermi integrals defined by

$$\mathcal{F}_n(\eta) \equiv \int_0^\infty \mathrm{d}x\ x^n\, f_\mathrm{FD}(x,\eta) \tag{A.14}$$

Thus the energy-dependent part of $f_{\mathrm{D},\nu}$ is fully defined. The angle-dependent part is related to the flux factor by

$$f_\nu = F_\nu/cE_\nu = \frac{\int_{-1}^{+1}\mathrm{d}\mu\ \mu I_\nu}{\int_{-1}^{+1}\mathrm{d}\mu\ I_\nu} = \frac{\int_{-1}^{+1}\mathrm{d}\mu\ \mu g_\nu(\mu)}{\int_{-1}^{+1}\mathrm{d}\mu\ g_\nu(\mu)} = \langle\mu_\nu\rangle. \tag{A.15}$$

To solve Eq. (A.5) only f_ν is needed, not the angle-dependent function $g_\nu(\mu)$. Far outside of the neutrinosphere, f_ν is approaching the *vacuum solution*. The latter can be derived under the assumption that neutrinos are emitted isotropically from the sharp surface of a sphere with radius R_ν, which is located at a distance r from the observer. In this case the flux factor is

$$f_{\nu,\mathrm{vac}} = \frac{1}{2}\left[1+\sqrt{1-(R_\nu/r)^2}\,\right]. \tag{A.16}$$

$f_{\nu,\mathrm{vac}}$ approaches 1 for $r \to \infty$ *(free streaming limit)* and $f_{\nu,\mathrm{vac}} = 1/2$ at the neutrinosphere. In a more realistic situation the neutrinosphere is not a sharp surface but a layer with finite thickness in which neutrinos gradually decouple from the stellar medium. In detailed transport calculations $f_\nu(R_\nu)$ is therefore found to be about 1/4. (see e.g. Janka & Hillebrandt 1989; Janka 1990). How fast f_ν approaches $f_{\nu,\mathrm{vac}}$ (with declining optical depth) depends on the steepness of the density gradient at the neutrinosphere (Janka 1990). Inside the neutrinosphere detailed transport calculations show that the flux factor behaves roughly like $f_\nu \propto \tau_\nu^m$ with $m < 0$.

Taking all this into account, the following function constitutes a good approximation for the flux factors from detailed transport calculations (Janka 1991b, 1990):

$$f_\nu(\tau_\nu) = \begin{cases} \dfrac{\frac{1}{2}[1+D]}{1+(1+D)(1-D^2)^{(n-1)/2}}, & \text{if} \quad \tau_\nu < \tau_{\nu,1}, \\ 1/4\,(\tau_\nu/\tau_{\nu,1})^m, & \text{if} \quad \tau_\nu > \tau_{\nu,1}. \end{cases} \tag{A.17}$$

Here $D = \sqrt{1-(R_\nu/r)^2}$, the neutrinosphere radius is defined by $\tau_\nu(R_\nu) = \tau_{\nu,1}$ and we adopt $\tau_{\nu,1} = 1.1$. The power-law index m is chosen such that $f_\nu(10) = 1/25$, and n is defined by a local power-law fit of the density profile around the neutrinosphere, $\rho(r) \propto r^{-n}$. A higher value of n therefore means a steeper density gradient.

A.3 Optical depth

Knowledge of the optical depth is necessary to evaluate Eqs. (A.11) and (A.17). For this purpose it is sufficient to compute τ_ν approximately by considering only the most relevant neutrino processes and assuming that the neutrino spectrum is given by the spectrum for local thermodynamic equilibrium. This means that instead of Eq. (A.10) we use

$$f^{\rm eq}_{{\rm D},\nu}(\epsilon_\nu, r) = f_{\rm FD}\left(\frac{\epsilon_\nu}{k_{\rm B}T(r)}, \eta_{{\rm eq},\nu}(r)\right) \tag{A.18}$$

with $\eta_{{\rm eq},\nu}$ and T instead of η_ν and T_ν.

The “transport optical depth” is defined as the integral

$$\tau_{{\rm t},\nu}(r) = \int_r^\infty {\rm d}r' \langle\kappa_{{\rm t},\nu}\rangle(r') \tag{A.19}$$

of the energy-averaged “transport opacity” (i.e. the opacity which is relevant for momentum transfer), $\langle\kappa_{{\rm t},\nu}\rangle(r)$ (see, e.g., Straumann 1989; Burrows & Thompson 2004). In the following, all neutrino interactions included in evaluating the opacity are calculated without final-state lepton blocking, unless otherwise stated.

The most important opacity-producing reactions are scattering off nucleons (n,p) and nuclei (Z_j, A_j), where $j = 1, 2, \ldots$ denotes the considered nuclear species, and absorption by neutrons and protons in case of $\nu_{\rm e}$ and $\bar\nu_{\rm e}$, respectively. Thus one can write

$$\langle\kappa_{{\rm t},\nu}\rangle = \langle\kappa^{\rm a}_\nu\rangle + \sum_{i\,\in\,\{{\rm n,p},A_j\}} \langle\kappa^{{\rm s},i}_{{\rm t},\nu}\rangle. \tag{A.20}$$

Here the (neutrino-flavour independent) scattering opacities are to lowest order in neutrino energy over nucleon rest mass (i.e., without effects of nucleon recoil, thermal motions, and weak-magnetism corrections):

$$\langle\kappa^{\rm s,p}_{{\rm t},\nu}\rangle = \frac{1}{6}\left[\frac{5}{4}\alpha^2 + (C_V - 1)^2\right]\frac{\sigma_0}{(m_{\rm e}c^2)^2}\,\langle\epsilon^2_\nu\rangle\; n_{\rm p}, \tag{A.21}$$

$$\langle\kappa^{\rm s,n}_{{\rm t},\nu}\rangle = \frac{5\alpha^2+1}{24}\frac{\sigma_0}{(m_{\rm e}c^2)^2}\,\langle\epsilon^2_\nu\rangle\; n_{\rm n}, \tag{A.22}$$

$$\begin{aligned}\langle\kappa^{{\rm s},A_j}_{{\rm t},\nu}\rangle &= \frac{1}{6}A_j^2[C_A - 1 + \frac{Z_j}{A_j}(2 - C_A - C_V)]^2 \\ &\quad\times\frac{\sigma_0}{(m_{\rm e}c^2)^2}\,\langle\epsilon^2_\nu\rangle\; n_{A_j},\end{aligned} \tag{A.23}$$

for scattering off protons, neutrons, and nuclei with number densities $n_{\rm p}$, $n_{\rm n}$, and n_{A_j}, respectively (see, e.g., Freedman et al. 1977; Straumann 1989; Burrows & Thompson 2004). The absorption opacities for $\nu_{\rm e}$ and $\bar\nu_{\rm e}$ are

$$\begin{aligned}\langle\kappa^{\rm a}_{\nu_{\rm e}}\rangle &= \frac{1}{4}(3\alpha^2+1)\frac{\sigma_0}{(m_{\rm e}c^2)^2}\; n_{\rm n} \\ &\quad\times\;\left(\langle\epsilon^2_{\nu_{\rm e}}\rangle + 2\Delta\langle\epsilon_{\nu_{\rm e}}\rangle + \Delta^2\right)\,\Theta(\langle\epsilon_{\nu_{\rm e}}\rangle),\end{aligned} \tag{A.24}$$

$$\begin{aligned}\langle\kappa^{\rm a}_{\bar\nu_{\rm e}}\rangle &= \frac{1}{4}(3\alpha^2+1)\frac{\sigma_0}{(m_{\rm e}c^2)^2}\; n_{\rm p} \\ &\quad\times\;\left(\langle\epsilon^2_{\bar\nu_{\rm e}}\rangle^\star + 2\Delta\langle\epsilon_{\bar\nu_{\rm e}}\rangle^\star + \Delta^2\langle\epsilon^0_{\bar\nu_{\rm e}}\rangle^\star\right).\end{aligned} \tag{A.25}$$

(see Tubbs & Schramm 1975; Bruenn 1985).

Here $\sigma_0 = 4G_{\rm F}^2 m_{\rm e}^2\hbar^2/\pi c^2 = 1.76\times 10^{-44}\,{\rm cm}^2$ (with the Fermi coupling constant $G_{\rm F}$), $\Delta = 1.2935\,{\rm MeV}$ is the rest mass difference of neutrons and protons, $\alpha = 1.254$, $C_A = \frac{1}{2}$, $C_V = \frac{1}{2} + 2\sin^2\theta_{\rm W}$, and $\sin^2\theta_{\rm W} = 0.23$.

In deriving Eqs. (A.21) – (A.25) (as well as for all rates and source terms given below) the electron and positron rest masses are ignored ($m_\mathrm{e}c^2 \ll \epsilon_\nu$) and nucleons and nuclei are assumed to have infinite rest masses ($m_{\mathrm{n,p},A_j}c^2 \gg \epsilon_\nu$) and to be nondegenerate. For electrons, phase space blocking is included in Eq. (A.25) by the factor

$$\Theta(\langle\epsilon_\nu\rangle) = 1 - f_\mathrm{FD}\left(\frac{\langle\epsilon_\nu\rangle + \Delta}{k_\mathrm{B}T}, \eta_{\mathrm{e}^-}\right), \tag{A.26}$$

which accounts for the fact that a significant fraction of the possible final electron states may be occupied. Phase space blocking can be neglected in $\kappa^\mathrm{a}_{\bar\nu_\mathrm{e}}$ (Eq. A.25), because the positrons are non-degenerate.

The neutrino energy moments are (generalising Eq. A.13) given by

$$\langle\epsilon_\nu^n\rangle = (k_\mathrm{B}T_\nu)^n \frac{\mathcal{F}_{2+n}(\eta_\nu)}{\mathcal{F}_2(\eta_\nu)}, \tag{A.27}$$

$$\langle\epsilon_\nu^n\rangle^\star = (k_\mathrm{B}T_\nu)^n \frac{\mathcal{F}_{2+n}(\eta_\nu - \Delta/k_\mathrm{B}T_\nu)}{\mathcal{F}_2(\eta_\nu)}, \tag{A.28}$$

and for evaluating Eqs. (A.21)–(A.25) to compute $\tau_{\mathrm{t},\nu}$ (Eq. A.19) for use in Eq. (A.17), we take $\eta_\nu = \eta_{\mathrm{eq},\nu}$ and $T_\nu = T$.

In contrast, Eq. (A.11) is evaluated with the “effective optical depth for equilibration”,

$$\tau_\nu(r) = \int_r^\infty \mathrm{d}r' \langle\kappa_{\mathrm{eff},\nu}\rangle(r'), \tag{A.29}$$

where the effective opacity is defined as

$$\langle\kappa_{\mathrm{eff},\nu}\rangle = \sqrt{\langle\kappa_\nu^\mathrm{a}\rangle \times \langle\kappa_\nu^\mathrm{a} + \kappa_{\mathrm{t},\nu}^\mathrm{s}\rangle}. \tag{A.30}$$

Here the spectrally averaged absorption opacity, $\langle\kappa_\nu^\mathrm{a}\rangle$, is taken to include neutrino-pair annihilation to $\mathrm{e}^\pm$-pairs (Eq. 2.18), which is assumed to be the most important reaction for producing $\nu_x\bar\nu_x$ pairs. Both $\langle\kappa_\nu^\mathrm{a}\rangle$ and $\langle\kappa_\nu^\mathrm{a} + \kappa_{\mathrm{t},\nu}^\mathrm{s}\rangle$ are evaluated for the “true” (not the local equilibrium) neutrino spectrum (i.e. for the spectral temperature T_ν and the spectral degeneracy η_ν instead of T and $\eta_{\mathrm{eq},\nu}$) by employing the source terms from the neutrino transport solution of the last time step.

A.4 Source terms

Solving Eq. (A.7) requires the knowledge of the emission rates, $Q^+_{\nu_i}$, and absorption coefficients, $\tilde\kappa_\nu = \kappa_\nu^\mathrm{a}/f_\nu$, which appear in this equation. Since Eq. (A.7) is used to determine the number fluxes, $L_{n,\nu}$, and luminosities, $L_{e,\nu}$, of all neutrinos and antineutrinos $\nu \in \{\nu_\mathrm{e}, \bar\nu_\mathrm{e}, \nu_x\}$, the source terms need to be calculated for the neutrino number, as well as energy. In the following, all these neutrino source terms are derived without taking into account final-state lepton blocking, unless otherwise stated. As in Eq. (A.30), κ_ν^a is defined to include the contributions from the β-processes, Eqs. (2.16) and (2.17) for ν_e and $\bar\nu_\mathrm{e}$, as well as those of $\mathrm{e}^+\mathrm{e}^-$ pair annihilation (Eq. 2.18). The absorption coefficient κ_ν^a can be computed from the corresponding neutrino absorption rate by

$$\kappa_\nu^\mathrm{a} = Q_\nu^- 4\pi r^2 f_\nu / L_\nu = (Q_\nu^\mathrm{a} + Q_{\nu\bar\nu}^\mathrm{ann})\, 4\pi r^2 f_\nu / L_\nu. \tag{A.31}$$

For the number transport the neutrino absorption and emission rates (in units of number per cm^3 per second) by charged-current β-reactions between leptons and nucleons can be written with our approximations for the neutrino distribution function and the appropriate statistical weights for the leptons as follows:

$$\begin{aligned}
\mathcal{R}^{\mathrm{a}}_{\nu_\mathrm{e}} &= \sigma c \frac{L_{e,\nu_\mathrm{e}}\, n_\mathrm{n}}{4\pi r^2 c f_{\nu_\mathrm{e}}} \frac{\langle\epsilon^2_{\nu_\mathrm{e}}\rangle + 2\Delta\langle\epsilon_{\nu_\mathrm{e}}\rangle + \Delta^2}{\langle\epsilon_{\nu_\mathrm{e}}\rangle}\, \Theta(\langle\epsilon_{\nu_\mathrm{e}}\rangle), && \text{(A.32)}\\
\mathcal{R}^{\mathrm{a}}_{\bar\nu_\mathrm{e}} &= \sigma c \frac{L_{e,\bar\nu_\mathrm{e}}\, n_\mathrm{p}}{4\pi r^2 c f_{\bar\nu_\mathrm{e}}} \frac{\langle\epsilon^2_{\bar\nu_\mathrm{e}}\rangle^\star + 2\Delta\langle\epsilon_{\bar\nu_\mathrm{e}}\rangle^\star + \Delta^2\langle\epsilon^0_{\bar\nu_\mathrm{e}}\rangle^\star}{\langle\epsilon_{\bar\nu_\mathrm{e}}\rangle}, && \text{(A.33)}\\
\mathcal{R}^{\mathrm{e}}_{\nu_\mathrm{e}} &= \frac{1}{2}\sigma c\, n_\mathrm{p}\, n_{\mathrm{e}^-}\, [\langle\epsilon^2_{\mathrm{e}^-}\rangle^\star + 2\Delta\langle\epsilon_{\mathrm{e}^-}\rangle^\star + \Delta^2\langle\epsilon^0_{\mathrm{e}^-}\rangle^\star], && \text{(A.34)}\\
\mathcal{R}^{\mathrm{e}}_{\bar\nu_\mathrm{e}} &= \frac{1}{2}\sigma c\, n_\mathrm{n}\, n_{\mathrm{e}^+}\, [\langle\epsilon^2_{\mathrm{e}^+}\rangle + 2\Delta\langle\epsilon_{\mathrm{e}^+}\rangle + \Delta^2], && \text{(A.35)}
\end{aligned}$$

where $\sigma = \frac{1}{4}(3\alpha^2+1)\sigma_0/(m_\mathrm{e}c^2)^2$ and the electron (positron) number density is

$$n_{\mathrm{e}^\mp} = \frac{8\pi}{(hc)^3}\,(k_\mathrm{B})^3 \mathcal{F}_2(\pm\eta_{\mathrm{e}^-})\,. \qquad \text{(A.36)}$$

The electron and positron energy moments are given by

$$\begin{aligned}
\langle\epsilon^n_\mathrm{e}\rangle =& (k_\mathrm{B}T)^n\, \frac{\mathcal{F}_{2+n}(\eta_\mathrm{e})}{\mathcal{F}_2(\eta_\mathrm{e})}, && \text{(A.37)}\\
\langle\epsilon^n_\mathrm{e}\rangle^\star =& (k_\mathrm{B}T)^n\, \frac{\mathcal{F}_{2+n}(\eta_\mathrm{e} - \Delta/k_\mathrm{B}T)}{\mathcal{F}_2(\eta_\mathrm{e})}. && \text{(A.38)}
\end{aligned}$$

The annihilation and production rates of neutrino number in e$^+$e$^-$ pair reactions are given by (adapted from Schinder et al. 1987; see also Janka 1991a and Janka 1991b, and references therein):

$$\begin{aligned}
\mathcal{R}^{\mathrm{ann}}_\nu &= \frac{\sigma_0 c}{(4\pi r^2 c)^2}\frac{L_{n,\nu}L_{n,\bar\nu}}{\langle\epsilon_\nu\rangle\langle\epsilon_{\bar\nu}\rangle}\left\{\frac{2}{9}\frac{\Phi(f_\nu,\chi_\nu)}{f_\nu f_{\bar\nu}}\frac{\mathcal{C}^2_{\mathrm{A}\nu}+\mathcal{C}^2_{\mathrm{V}\nu}}{(m_\mathrm{e}c^2)^2}\langle\epsilon_\nu\rangle\langle\epsilon_{\bar\nu}\rangle\right.\\
&\quad \left. +\frac{1}{6}\frac{1-f_\nu f_{\bar\nu}}{f_\nu f_{\bar\nu}}(2\mathcal{C}^2_{\mathrm{V}\nu}-\mathcal{C}^2_{\mathrm{A}\nu})\right\}, && \text{(A.39)}\\
\mathcal{R}^{\mathrm{prod}}_\nu &= \frac{1}{18}\frac{\sigma_0 c}{(m_\mathrm{e}c^2)^2} n_{\mathrm{e}^-}n_{\mathrm{e}^+}\left\{(\mathcal{C}^2_{\mathrm{A}\nu}+\mathcal{C}^2_{\mathrm{V}\nu})\langle\epsilon_{\mathrm{e}^-}\rangle\langle\epsilon_{\mathrm{e}^+}\rangle\right.\\
&\quad \left. +\frac{3}{4}(m_\mathrm{e}c^2)^2(2\mathcal{C}^2_{\mathrm{V}\nu}-\mathcal{C}^2_{\mathrm{A}\nu})\right\}. && \text{(A.40)}
\end{aligned}$$

These rates hold for neutrinos ν or antineutrinos $\bar\nu$ of all flavours. In Eq. (A.31), $\mathcal{R}^{\mathrm{a}}_\nu$ and $\mathcal{R}^{\mathrm{ann}}_\nu$ have to be used instead of Q^{a}_ν and Q^{ann}_ν for computing the absorption coefficient for the number transport. In Eq. (A.39), $\Phi(f_\nu,\chi_\nu)$ is a geometrical factor,

$$\Phi(f_\nu,\chi_\nu) = \frac{3}{4}\left[1 - 2f_\nu f_{\bar\nu} + \chi_\nu\chi_{\bar\nu} + \frac{1}{2}(1-\chi_\nu)(1-\chi_{\bar\nu})\right], \qquad \text{(A.41)}$$

where we express the variable Eddington factor χ_ν in terms of the flux factor f_ν (Eq. A.4) using a statistical form, which was derived by Minerbo (1978) on grounds of maximum entropy considerations (for photons or nondegenerate neutrinos, as assumed here):

$$\chi_\nu = \langle\mu^2_\nu\rangle = \frac{1}{3} + \frac{0.01932\, f_\nu + 0.2694\, f^2_\nu}{1 - 0.5953\, f_\nu + 0.02625\, f^2_\nu}. \qquad \text{(A.42)}$$

The weak coupling constants in Eqs. (A.39) and (A.40) are given by

$$\mathcal{C}_{\mathrm{A}\nu} = \begin{cases} +\frac{1}{2} & \text{for } \nu \in \{\nu_\mathrm{e}, \bar{\nu}_\mathrm{e}\}, \\ -\frac{1}{2} & \text{for } \nu \in \{\nu_\mu, \bar{\nu}_\mu, \nu_\tau, \bar{\nu}_\tau\}, \end{cases} \tag{A.43}$$

$$\mathcal{C}_{\mathrm{V}\nu} = \begin{cases} +\frac{1}{2} + 2\sin^2\theta_\mathrm{W} & \text{for } \nu \in \{\nu_\mathrm{e}, \bar{\nu}_\mathrm{e}\}, \\ -\frac{1}{2} + 2\sin^2\theta_\mathrm{W} & \text{for } \nu \in \{\nu_\mu, \bar{\nu}_\mu, \nu_\tau, \bar{\nu}_\tau\}. \end{cases} \tag{A.44}$$

The source term which describes the rate of change per unit of volume in the evolution equation of the electron lepton number of the stellar medium is

$$Q_\mathrm{N} = \dot{Y}_\mathrm{e}\, n_\mathrm{b} = (\mathcal{R}^\mathrm{a}_{\nu_\mathrm{e}} - \mathcal{R}^\mathrm{e}_{\nu_\mathrm{e}}) - (\mathcal{R}^\mathrm{a}_{\bar{\nu}_\mathrm{e}} - \mathcal{R}^\mathrm{e}_{\bar{\nu}_\mathrm{e}}). \tag{A.45}$$

The source terms which account for the absorption and emission of energy through ν_e and $\bar{\nu}_\mathrm{e}$ are computed in analogy to Eqs. (A.32) – (A.35) as

$$Q^\mathrm{a}_{\nu_\mathrm{e}} = \sigma c \frac{L_{e,\nu_\mathrm{e}}\, n_\mathrm{n}}{4\pi r^2 c f_{\nu_\mathrm{e}}} \frac{\langle\epsilon^3_{\nu_\mathrm{e}}\rangle + 2\Delta\langle\epsilon^2_{\nu_\mathrm{e}}\rangle + \Delta^2\langle\epsilon_{\nu_\mathrm{e}}\rangle}{\langle\epsilon_{\nu_\mathrm{e}}\rangle}\, \Theta(\langle\epsilon_{\nu_\mathrm{e}}\rangle), \tag{A.46}$$

$$\begin{aligned} Q^\mathrm{a}_{\bar{\nu}_\mathrm{e}} &= \sigma c \frac{L_{e,\bar{\nu}_\mathrm{e}}\, n_\mathrm{p}}{4\pi r^2 c f_{\bar{\nu}_\mathrm{e}}} \\ &\times \frac{\langle\epsilon^3_{\bar{\nu}_\mathrm{e}}\rangle^\star + 3\Delta\langle\epsilon^2_{\bar{\nu}_\mathrm{e}}\rangle^\star + 3\Delta^2\langle\epsilon_{\bar{\nu}_\mathrm{e}}\rangle^\star + \Delta^3\langle\epsilon^0_{\bar{\nu}_\mathrm{e}}\rangle^\star}{\langle\epsilon_{\bar{\nu}_\mathrm{e}}\rangle}, \end{aligned} \tag{A.47}$$

$$Q^\mathrm{e}_{\nu_\mathrm{e}} = \frac{\sigma c}{2}\, n_\mathrm{p}\, n_{\mathrm{e}^-} \left[\langle\epsilon^3_{\mathrm{e}^-}\rangle^\star + 2\Delta\langle\epsilon^2_{\mathrm{e}^-}\rangle^\star + \Delta^2\langle\epsilon_{\mathrm{e}^-}\rangle^\star\right], \tag{A.48}$$

$$Q^\mathrm{e}_{\bar{\nu}_\mathrm{e}} = \frac{\sigma c}{2}\, n_\mathrm{n}\, n_{\mathrm{e}^+} \left[\langle\epsilon^3_{\mathrm{e}^+}\rangle + 3\Delta\langle\epsilon^2_{\mathrm{e}^+}\rangle + 3\Delta^2\langle\epsilon_{\mathrm{e}^+}\rangle + \Delta^3\right]. \tag{A.49}$$

The annihilation or production of energy in neutrinos (ν) by $\mathrm{e}^+\mathrm{e}^-$ pair reactions is given as (Janka 1991a)

$$\begin{aligned} Q^\mathrm{ann}_\nu &= \frac{\sigma_0 c}{(4\pi r^2 c)^2} \frac{L_{e,\nu} L_{e,\bar{\nu}}}{\langle\epsilon_\nu\rangle\langle\epsilon_{\bar{\nu}}\rangle} \left\{ \frac{2}{9} \frac{\Phi(f_\nu, \chi_\nu)}{f_\nu f_{\bar{\nu}}} \frac{\mathcal{C}^2_{\mathrm{A}\nu} + \mathcal{C}^2_{\mathrm{V}\nu}}{(m_\mathrm{e}c^2)^2} \langle\epsilon^2_\nu\rangle\langle\epsilon_{\bar{\nu}}\rangle \right. \\ &\left. + \frac{1}{6} \frac{1 - f_\nu f_{\bar{\nu}}}{f_\nu f_{\bar{\nu}}} (2\mathcal{C}^2_{\mathrm{V}\nu} - \mathcal{C}^2_{\mathrm{A}\nu}) \langle\epsilon^2_\nu\rangle \right\}, \end{aligned} \tag{A.50}$$

$$\begin{aligned} Q^\mathrm{prod}_\nu &= \frac{1}{36} \frac{\sigma_0 c}{(m_\mathrm{e}c^2)^2} n_{\mathrm{e}^-} n_{\mathrm{e}^+} \\ &\times \left\{ \left[\langle\epsilon^2_{\mathrm{e}^-}\rangle\langle\epsilon_{\mathrm{e}^+}\rangle + \langle\epsilon^2_{\mathrm{e}^+}\rangle\langle\epsilon_{\mathrm{e}^-}\rangle\right] (\mathcal{C}^2_{\mathrm{A}\nu} + \mathcal{C}^2_{\mathrm{V}\nu}) \right. \\ &\left. + \frac{3}{4} (m_e c^2)^2 \left[\langle\epsilon_{\mathrm{e}^-}\rangle + \langle\epsilon_{\mathrm{e}^+}\rangle\right] (2\mathcal{C}^2_{\mathrm{V}\nu} - \mathcal{C}^2_{\mathrm{A}\nu}) \right\}. \end{aligned} \tag{A.51}$$

For annihilation of antineutrino ($\bar{\nu}$) energy, $\langle\epsilon^2_\nu\rangle$ has to be replaced by $\langle\epsilon^2_{\bar{\nu}}\rangle$ and $\langle\epsilon_\nu\rangle$ has to be exchanged with $\langle\epsilon_{\bar{\nu}}\rangle$ in Eq. (A.50), while the production of ν and $\bar{\nu}$ was assumed to be symmetric and both rates are given by Eq. (A.51).

Also in scattering processes energy can be exchanged between neutrinos and the stellar medium. For scattering off e^- or e^+, using the rates of Tubbs & Schramm (1975), and ignoring electron

Table A.1: Weak coupling constants for ν and $\bar{\nu}$ scattering off e^+ or e^- (cf. Eq. A.52). C_3^{x} stands for $C_3^x = (C_\mathrm{A}-1)^2 - (C_\mathrm{V}-1)^2$, $C_\mathrm{A} = \frac{1}{2}$, $C_\mathrm{V} = \frac{1}{2} + 2\sin^2\theta_\mathrm{W}$, and ν_x can be ν_μ or ν_τ.

	C_1	C_2	C_3
$\nu_\mathrm{e}\mathrm{e}^-$	$(C_\mathrm{V}+C_\mathrm{A})^2$	$(C_\mathrm{V}-C_\mathrm{A})^2$	$C_\mathrm{A}^2 - C_\mathrm{V}^2$
$\nu_\mathrm{e}\mathrm{e}^+$	$(C_\mathrm{V}-C_\mathrm{A})^2$	$(C_\mathrm{V}+C_\mathrm{A})^2$	$C_\mathrm{A}^2 - C_\mathrm{V}^2$
$\bar{\nu}_\mathrm{e}\mathrm{e}^-$	$(C_\mathrm{V}-C_\mathrm{A})^2$	$(C_\mathrm{V}+C_\mathrm{A})^2$	$C_\mathrm{A}^2 - C_\mathrm{V}^2$
$\bar{\nu}_\mathrm{e}\mathrm{e}^+$	$(C_\mathrm{V}+C_\mathrm{A})^2$	$(C_\mathrm{V}-C_\mathrm{A})^2$	$C_\mathrm{A}^2 - C_\mathrm{V}^2$
$\nu_x\mathrm{e}^-$	$(C_\mathrm{V}+C_\mathrm{A}-2)^2$	$(C_\mathrm{V}-C_\mathrm{A})^2$	C_3^x
$\nu_x\mathrm{e}^+$	$(C_\mathrm{V}-C_\mathrm{A})^2$	$(C_\mathrm{V}+C_\mathrm{A}-2)^2$	C_3^x
$\bar{\nu}_x\mathrm{e}^-$	$(C_\mathrm{V}-C_\mathrm{A})^2$	$(C_\mathrm{V}+C_\mathrm{A}-2)^2$	C_3^x
$\bar{\nu}_x\mathrm{e}^+$	$(C_\mathrm{V}+C_\mathrm{A}-2)^2$	$(C_\mathrm{V}-C_\mathrm{A})^2$	C_3^x

phase space blocking in the final reaction channels, the following spectrally averaged expression for the energy transfer rate per unit of volume can be derived (see Janka 1991b):

$$\begin{aligned} Q_{\nu\mathrm{e}} \quad = \quad & \frac{1}{12}(C_1 + \frac{1}{6}C_2)\frac{\sigma_0 c}{(m_\mathrm{e}c^2)^2} n_\mathrm{e} \frac{L_{e,\nu}}{4\pi r^2 c f_\nu \langle\epsilon_\nu\rangle} \\ & \Bigg\{ \Big[\langle\epsilon_\nu^2\rangle(\langle\epsilon_\mathrm{e}\rangle + \frac{3}{4}m_\mathrm{e}c^2) - \langle\epsilon_\nu\rangle\langle\epsilon_\mathrm{e}^2\rangle \Big] \\ & + \frac{3}{8}\frac{C_3}{C_1 + \frac{1}{3}C_2}(m_\mathrm{e}c^2)^2 \Big[\langle\epsilon_\nu\rangle - \frac{\langle\epsilon_\mathrm{e}^2\rangle}{\langle\epsilon_\mathrm{e}\rangle} \Big] \Bigg\}, \end{aligned} \qquad \text{(A.52)}$$

where e can be e^+ or e^- and ν stands for neutrinos or antineutrinos of all flavours and the constants C_1, C_2, C_3 for the different combinations are listed in Table A.1. The term $3m_\mathrm{e}c^2/4$ in the bracket results from a merge of the rate expressions for the limits of relativistic and non-relativistic electrons. In the latter case the neutrino-electron scattering cross section is proportional to $\epsilon_\nu/(m_\mathrm{e}c^2)$ for $\epsilon_\nu \gg m_\mathrm{e}c^2$ (cf. Sehgal 1974).

Every transfer by neutrino-nucleon scattering, which is only “nearly conservative”, is taken into account following Tubbs (1979). The corresponding rate is (see Janka 1991b):

$$\begin{aligned} Q_{\nu\mathrm{N}} = & \frac{1}{4}\frac{\sigma_0 c}{(m_\mathrm{e}c^2)^2}\mathcal{C}_\mathrm{N}\mathcal{E}_\mathrm{N}\frac{n_\mathrm{N}}{m_\mathrm{N}c^2}\left\{\langle\epsilon_\nu^4\rangle - 6T\langle\epsilon_\nu^3\rangle\right\} \\ & \times \frac{L_{e,\nu}}{4\pi r^2 c f_\nu \langle\epsilon_\nu\rangle} \end{aligned} \qquad \text{(A.53)}$$

with

$$\mathcal{C}_\mathrm{N}\mathcal{E}_\mathrm{N} = \begin{cases} \frac{2}{3}[(C_\mathrm{V}-1)^2 + \frac{5}{4}\alpha^2] & \text{for N = p,} \\ \frac{1}{6}(1+5\alpha^2) & \text{for N = n.} \end{cases}$$

The symbol ν stands again for neutrinos and antineutrinos of all flavours. Also scattering contributions are included in the energy generation rate Q^+ and absorption coefficient $\tilde{\kappa}$ used in Eq. (A.7). Considering scattering as an absorption process followed immediately by an emission process, we add the net energy exchange rates $Q_{\nu\mathrm{e}^-}$, $Q_{\nu\mathrm{e}^+}$, $Q_{\nu\mathrm{p}}$ and $Q_{\nu\mathrm{n}}$ to Q_ν^- (used for computing $\tilde{\kappa}_\nu$ in Eq. A.7) when the rates are positive (i.e. in case of energy transfer from neutrinos to the stellar gas), and the absolute values of $Q_{\nu\mathrm{e}^-}$, $Q_{\nu\mathrm{e}^+}$, $Q_{\nu\mathrm{p}}$ and $Q_{\nu\mathrm{n}}$ to Q_ν^+ otherwise. The total neutrino energy source term to be used in the gas energy equation including the contributions from ν_e and $\bar{\nu}_\mathrm{e}$ absorption and emission, $\nu\bar{\nu}$ pair production, and all scattering reactions is

$$\begin{aligned} Q_\mathrm{E} &= \sum_{\nu\,\in\,\{\nu_\mathrm{e},\bar{\nu}_\mathrm{e}\}} (Q_\nu^\mathrm{a} - Q_\nu^\mathrm{e}) + \sum_{\nu\,\in\,\{\nu_\mathrm{e},\nu_\mu,\nu_\tau\}} \left(Q_{\nu\bar{\nu}}^\mathrm{ann} - Q_{\nu\bar{\nu}}^\mathrm{prod}\right) \\ &+ \sum_{\nu\,\in\,\{\nu_\mathrm{e},\nu_\mu,\nu_\tau,\bar{\nu}_\mathrm{e},\bar{\nu}_\mu,\bar{\nu}_\tau\}} \left(Q_{\nu\mathrm{e}^+}^\mathrm{s} + Q_{\nu\mathrm{e}^-}^\mathrm{s} + Q_{\nu\mathrm{p}}^\mathrm{s} + Q_{\nu\mathrm{n}}^\mathrm{s}\right), \end{aligned} \tag{A.54}$$

where $Q_{\nu\bar{\nu}}^\mathrm{ann} = Q_\nu^\mathrm{ann} + Q_{\bar{\nu}}^\mathrm{ann}$ and $Q_{\nu\bar{\nu}}^\mathrm{prod} = Q_\nu^\mathrm{prod} + Q_{\bar{\nu}}^\mathrm{prod}$.

In practise, however, the lepton number source term Q_N as well as the energy source term for the hydrodynamics part of the code is not computed from Eq. (A.45) and (A.54), respectively, but from the luminosity change between points (r^i, t^n) and $(r^\star, t^\star)$ (cf. Fig. A.1). The source terms $\tilde{Q}_\mathrm{N}^i$ and $\tilde{Q}_\mathrm{E}^i$ for a grid cell i at time level t^n are then given by

$$\tilde{Q}_\mathrm{N}^i = \frac{L_n^\mathrm{diff}(r^i, t^n) - L_n^\mathrm{diff}(r^\star, t^\star)}{\Delta V_i}, \tag{A.55}$$

$$\tilde{Q}_\mathrm{E}^i = \frac{L_e^\mathrm{tot}(r^i, t^n) - L_e^\mathrm{tot}(r^\star, t^\star)}{\Delta V_i}, \tag{A.56}$$

where $\Delta V_i = \frac{4\pi}{3}(r_i^3 - r^{\star 3})$ is the part of the cell volume crossed by the characteristic line between (r^i, t^n) and $(r^\star, t^\star)$, L_e^tot is the sum of the luminosities of neutrinos and antineutrinos of all flavours, and L^diff is the difference between the ν_e and $\bar{\nu}_\mathrm{e}$ number fluxes, $L_{\nu_\mathrm{e},n} - L_{\bar{\nu}_\mathrm{e},n}$. Equations (A.55) and (A.56) work well as a description of the neutrino sources in the gas equations only, if the neutrino fluxes do not exhibit a large degree of variability on the radial and temporal scales of the r-t cells. This, however, is reasonably well fulfilled in the context considered in this work.

Finally, the outgoing neutrino fluxes transfer also momentum to the stellar fluid. To account for this, we include a momentum source term Q_M which enters the Euler equation of the hydrodynamics solver. It is sufficient to include only the most important reactions, by which neutrinos transfer momentum, i.e. ν_e and $\bar{\nu}_\mathrm{e}$ absorption on n and p, respectively, and the scattering processes of ν and $\bar{\nu}$ of all flavours off nucleons and nuclei (pair processes and electron/positron scattering can be safely ignored). For a neutrino or antineutrino ν, the corresponding rate (in units of erg/cm^4) is

$$Q_\mathrm{M}^\nu = \frac{L_{e,\nu}}{4\pi r^2 c} \left(\frac{\langle \kappa_\nu^\mathrm{a} \epsilon_\nu \rangle}{\langle \epsilon_\nu \rangle} + \sum_{i \in \{\mathrm{p},\mathrm{n},A_j\}} \frac{\langle \kappa_{\mathrm{t},\nu}^{\mathrm{s},i} \epsilon_\nu \rangle}{\langle \epsilon_\nu \rangle} \right), \tag{A.57}$$

where the first term in the sum is relevant only for ν_e and $\bar{\nu}_\mathrm{e}$. The energy averages of the scattering transport opacities, $\kappa_{\mathrm{t},\nu}^{\mathrm{s},i}$, and of the absorption opacities, κ_ν^a, all weighted by the neutrino energy, are given by

$$\langle \kappa^{\mathrm{s,p}}_{\mathrm{t},\nu}\epsilon_\nu\rangle = \frac{1}{6}\left[\frac{5}{4}\alpha^2+(C_\mathrm{V}-1)^2\right]\frac{\sigma_0}{(m_\mathrm{e}c^2)^2}\langle\epsilon_\nu^3\rangle n_\mathrm{p}, \tag{A.58}$$

$$\langle \kappa^{\mathrm{s,n}}_{\mathrm{t},\nu}\epsilon_\nu\rangle = \frac{5\alpha^2+1}{24}\frac{\sigma_0}{(m_\mathrm{e}c^2)^2}\langle\epsilon_\nu^3\rangle n_\mathrm{n}, \tag{A.59}$$

$$\langle \kappa^{\mathrm{s},A_j}_{\mathrm{t},\nu}\epsilon_\nu\rangle = \frac{1}{6}A_j^2\left[C_\mathrm{A}-1+\frac{Z_j}{A_j}(2-C_\mathrm{A}-C_\mathrm{V})\right]\frac{\sigma_0}{(m_\mathrm{e}c^2)^2}\langle\epsilon_\nu^3\rangle n_{A_j}, \tag{A.60}$$

$$\begin{aligned}\langle \kappa^{\mathrm{a}}_{\nu_\mathrm{e}}\epsilon_{\nu_\mathrm{e}}\rangle =& \frac{1}{4}(3\alpha^2+1)\frac{\sigma_0}{(m_\mathrm{e}c^2)^2}\\ &\times\left(\langle\epsilon_{\nu_\mathrm{e}}^3\rangle+2\Delta\langle\epsilon_{\nu_\mathrm{e}}^2\rangle+\Delta^2\langle\epsilon_{\nu_\mathrm{e}}\rangle\right)\Theta(\langle\epsilon_{\nu_\mathrm{e}}\rangle),\end{aligned} \tag{A.61}$$

$$\begin{aligned}\langle \kappa^{\mathrm{a}}_{\bar\nu_\mathrm{e}}\epsilon_{\bar\nu_\mathrm{e}}\rangle =& \frac{1}{4}(3\alpha^2+1)\frac{\sigma_0}{(m_\mathrm{e}c^2)^2}\\ &\times\left(\langle\epsilon_{\bar\nu_\mathrm{e}}^3\rangle^\star+3\Delta\langle\epsilon_{\bar\nu_\mathrm{e}}^2\rangle^\star+3\Delta^2\langle\epsilon_{\bar\nu_\mathrm{e}}\rangle^\star+\Delta^3\langle\epsilon_{\bar\nu_\mathrm{e}}^0\rangle^\star\right).\end{aligned} \tag{A.62}$$

The energy moments $\langle\epsilon_\nu^n\rangle$ and $\langle\epsilon_\nu^n\rangle^\star$ are given in Eqs. (A.27) and (A.28). They are calculated using the nonequilibrium neutrino spectral parameters T_ν and η_ν. The momentum source term in the equation of gas motion then reads

$$Q_\mathrm{M} = \sum_{\nu\in\{\nu_\mathrm{e},\nu_\mu,\nu_\tau,\bar\nu_\mathrm{e},\bar\nu_\mu,\bar\nu_\tau\}} Q_\mathrm{M}^\nu \tag{A.63}$$

It was not included in the simulations presented in this work, but will be taken into account in future calculations.

The implementation of the source terms $\tilde{Q}_\mathrm{N}$, $\tilde{Q}_\mathrm{E}$, and Q_M into the framework of our PPM hydrodynamics code was discussed in detail by Rampp & Janka (2002) and Buras et al. (2006a).

We finish by pointing out that the approximative neutrino transport scheme developed here employs two basic assumptions, which are radical simplifications of the true situation:

1. In deriving Eq. (A.7) from the transport equation we assumed that the flux factor $f(r,t)$ is a *known* function, although it is actually dependent on the solution of the transport problem (see Eq. A.4). Equation (A.7) certainly has the advantage of analytic simplicity, but also has a severe disadvantage: The source terms can be very large and the numerical use requires a very fine grid zoning at high optical depths. The cell size should fulfill the constraint that the optical depth of the cell stays around unity or less. Moreover, the implementation of the source terms in (A.7) and the medium sources (Eqs. A.55, A.56) is not symmetric and the numerical scheme does not strictly conserve the total lepton number and total energy of neutrinos plus gas.

2. For treating the spectral dependence, we made the assumption that the neutrino phase space distribution function can be factorised into a product of an angle-dependent function g_ν and an energy-dependent term, which we assume to be of Fermi-Dirac shape. This certainly constrains the spectral shape, but the factorisation also implies that the flux-factor is assumed not to be an energy-dependent quantity. This in turn means that the mean energy of the neutrinos flux, $\langle\epsilon_\nu\rangle_\mathrm{flux}\equiv L_{e,\nu}(r,t)/L_{n,\nu}(r,t)$ is identical with the mean energy of the local neutrino density, $\langle\epsilon_\nu\rangle_\mathrm{local}\equiv E_\nu(r,t)/n_\nu(r,t)$. This is certainly a problematic simplification in view of the fact that the neutrino interactions with the stellar medium are strongly energy-dependent.

Nevertheless, the described neutrino transport treatment represents a practical approximation which is able to reproduce basic features of more detailed transport solutions and yields agreement with those even beyond the purely qualitative level.

B

Explosion energy

The explosion energy of neutrino-driven supernovae consists of two major contributions. The first is the recombination energy of the matter in the gain layer at the onset of the explosion. This matter consists of free nucleons and alpha particles at the time the explosion starts. Almost all of this mass (except for some fraction in the downflows, which is accreted onto the neutron star) ends up in a dense shell behind the expanding shock. As the shock propagates outward, the temperature in this expanding shell decreases and the matter recombines to α-particles and later to nuclei.

Figure B.1 displays the available recombination energy of the matter in the gain layer at the time of the explosion,

$$E_{\mathrm{rec}}^{\mathrm{gain}}(t_{\mathrm{exp}}) = \int_{\text{gain layer}} \epsilon_{\mathrm{rec}}(r, t_{\mathrm{exp}})\, \mathrm{d}V . \tag{B.1}$$

Here $\epsilon_{\mathrm{rec}}(r,t)$ denotes the density of recombination energy available when matter consists of nucleons, α-particles and some mass fraction of heavy nuclei,

$$\epsilon_{\mathrm{rec}}(r,t) = B_{\mathrm{h}}\, n_{\mathrm{h}}^{\mathrm{max}}(r,t) - \left(B_\alpha\, n_\alpha(r,t) + B_{\mathrm{h}}\, n_{\mathrm{h}}(r,t)\right) , \tag{B.2}$$

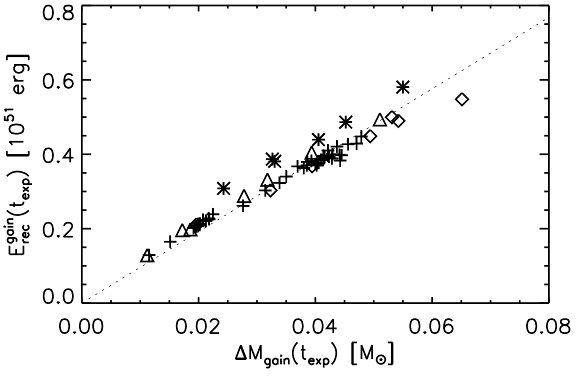

Figure B.1: Available recombination energy, $E_{\mathrm{rec}}^{\mathrm{gain}}$, as a function of the mass in the gain layer, ΔM_{gain}, at the time of explosion for the models of Tables 3.1–3.3. The slope of this approximately linear relation corresponds to about 5 MeV per baryon (dotted line).

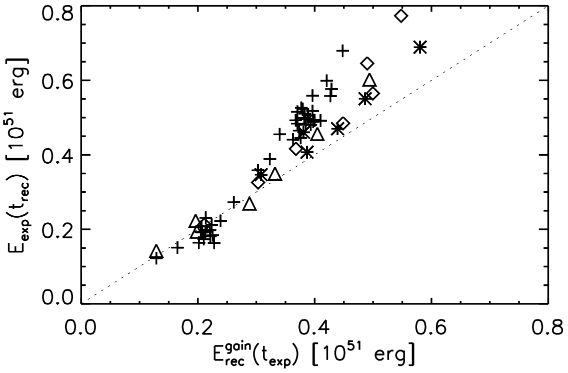

Figure B.2: Explosion energy after the recombination of the ejecta, $E_{\rm exp}(t_{\rm rec})$, as a function of the available recombination energy in the gain layer at the onset of the explosion, $E_{\rm rec}^{\rm gain}(t_{\rm exp})$, for the models of Tables 3.1–3.3. For low explosion energies the two quantities agree well.

with $B_{\rm h}$ and B_α being the binding energies of a representative heavy nucleus ($Z_{\rm h}, A_{\rm h} = N_{\rm h} + Z_{\rm h}$) from the iron group (as assumed in our equation of state) and of α-particles, respectively, and $n_{\rm h}^{\rm max} = \min(\, n_{\rm p}^{\rm tot}/Z_{\rm h},\, n_{\rm n}^{\rm tot}/N_{\rm h}\,)$ and $n_{\rm h}$ are the maximum and current number densities, respectively, of this heavy nucleus when $n_{\rm p}^{\rm tot}$ and $n_{\rm n}^{\rm tot}$ are the total (bound+free) number densities of protons and neutrons.

Figure B.1 shows that for all models of Tables 3.1–3.3 $E_{\rm rec}^{\rm gain}(t_{\rm exp}) \approx N_{\rm b}^{\rm gain}(t_{\rm exp}) \times 5\,{\rm MeV}$, when $N_{\rm b}^{\rm gain}$ is the total number of baryons in the gain layer. This means that due to the partial assembly of free n and p in α-particles at the time of explosion, about 5 MeV (instead of $>$ 8 MeV) remain available for being released by recombination during the subsequent expansion and cooling.

This recombination is essentially complete when the shock has reached a radius of 3000 km (recombination to α-particles happens even much earlier). We denote this time by $t_{\rm rec}$. Figure B.2 demonstrates that the explosion energy at time $t_{\rm rec}$, $E_{\rm exp}(t_{\rm rec})$, roughly equals the available recombination energy, $E_{\rm rec}^{\rm gain}(t_{\rm exp})$, at the onset of the explosion. This means that neutrino heating essentially has the effect of lifting the total energy of mass elements in the gain layer close to zero (i.e., $\epsilon_{\rm tot} = \epsilon_{\rm kin} + \epsilon_{\rm int} + \epsilon_{\rm grav} \approx 0$) and thus makes this matter unbound and enables its expansion in the gravitational potential of the forming neutron star. The excess energy of this matter at time $t_{\rm rec}$, i.e. $E_{\rm exp}(t_{\rm rec})$, is provided by the recombination of nucleons to α-particles and finally to iron-group nuclei. Only in case of higher explosion energies, $E_{\rm exp}(t_{\rm rec})$ is clearly larger than $E_{\rm rec}^{\rm gain}(t_{\rm exp})$ (Fig. B.2). In this case neutrino heating in the gain layer is stronger and the heating time scale of the matter there shorter than the expansion time scale when the shock begins to accelerate outwards. Therefore neutrinos are able to deposit “excess energy” in the ejecta before this matter has moved out of the region of strong heating.

The second contribution to the explosion energy comes from the neutrino-driven baryonic wind which sets in after the surroundings of the nascent neutron star have been cleaned from the initially heated gas. Indeed this wind is an important energy source at “late” times. To demonstrate this, we compare the time derivative of the explosion energy, $\mathrm{d}E_{\rm exp}/\mathrm{d}t$, with the wind power, $L_{\rm wind}$, and the net energy loss/gain rate $L_{\rm shock}$ at the shock (Fig. B.3). The curve for $\mathrm{d}E_{\rm exp}/\mathrm{d}t$ in Fig. B.3 is calculated as the numerical derivative of the energy integral

$$E_{\rm exp}(t) = \int_{V^+} \epsilon_{\rm tot}(r,t)\mathrm{d}V, \tag{B.3}$$

where the integration is performed over the volume V^+, in which the total energy $\epsilon_{\rm tot}(r,t)$ is

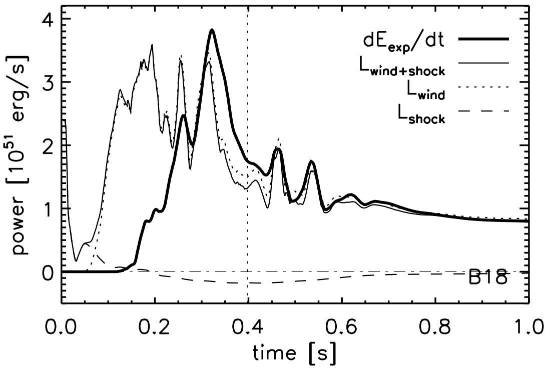

Figure B.3: Evolution of the time derivative of the explosion energy ($\mathrm{d}E_{\mathrm{exp}}/\mathrm{d}t$, thick solid) for Model B18. Also shown are the wind power at a radius of 200 km (L_{wind}, dotted), the energy loss/gain rate at the shock by $\mathcal{P}\mathrm{d}V$ work and swept-up matter (L_{shock}, dashed), and the sum of the latter two quantities ($L_{\mathrm{wind+shock}}$, thin solid). $L_{\mathrm{wind+shock}}$ agrees well with $\mathrm{d}E_{\mathrm{exp}}/\mathrm{d}t$ for $t > t_{\mathrm{rec}}$ (right of the vertical line).

positive (see also Eq. 3.8). For $t > t_{\mathrm{rec}}$ this volume fills the region between an inner boundary at $r \approx 200\,\mathrm{km}$ and the shock (except for some parts of the accretion downflows, where ϵ_{tot} may still be negative).

The explosion energy is subject to changes by $\mathcal{P}\mathrm{d}V$-work performed at, and by energy fluxes through the boundaries of V^+, in particular by the wind, whose power is given by the surface integral

$$L_{\mathrm{wind}} = \oint_{r=200\,\mathrm{km}} (\epsilon_{\mathrm{tot}} + \epsilon_{\mathrm{rec}} + \mathcal{P})\ \max(v_r, 0)\,\mathrm{dS}. \tag{B.4}$$

This expression takes into account the total energy ($\epsilon_{\mathrm{tot}} = \rho e_{\mathrm{tot}}$ with e_{tot} defined by Eq. 3.9) of the wind material streaming through the inner boundary radius into V^+, the energy that will be set free at larger radii by recombination (Eq. B.1), as well as the work performed by pressure forces. Here we have neglected effects due to downflows by omitting contributions to the surface integral from zones with negative radial velocity.

The change of the explosion energy due to energy flow through the outer boundary of V^+ (i.e., the shock), is given by the net energy loss/gain rate

$$L_{\mathrm{shock}} = \oint_{r=R_{\mathrm{s}}(\theta)^+} [(\epsilon_{\mathrm{tot}} + \epsilon_{\mathrm{rec}} + \mathcal{P})\, v_r\ + (\epsilon_{\mathrm{tot}} + \epsilon_{\mathrm{rec}})\, \dot{R}_{\mathrm{s}}]\,\mathrm{dS}. \tag{B.5}$$

The integration has to be performed over a surface located slightly upstream of the shock. Compared to Eq. (B.4) an additional term arises here from the motion of the shock, which propagates with a local velocity $\dot{R}_{\mathrm{s}}(\theta)$.

Figure B.3 shows that these two terms explain the evolution of $\mathrm{d}E_{\mathrm{exp}}/\mathrm{d}t$ for $t > t_{\mathrm{rec}}$, i.e.

$$\mathrm{d}E_{\mathrm{exp}}/\mathrm{d}t \approx L_{\mathrm{wind}} + L_{\mathrm{shock}} \tag{B.6}$$

holds at late times, and the thin and thick solid lines in Fig. B.3 almost coincide. Note also that $L_{\mathrm{wind}} \gg |L_{\mathrm{shock}}|$. This is true for all our models, and therefore the increase of the explosion energy after about 0.5 s post bounce is (almost exclusively) associated with the time-integrated wind power (see Fig. B.4).

The relative importance of the two major constituents of the explosion energy that we have discussed here, i.e., the nuclear recombination energy of the matter in the gain layer and the

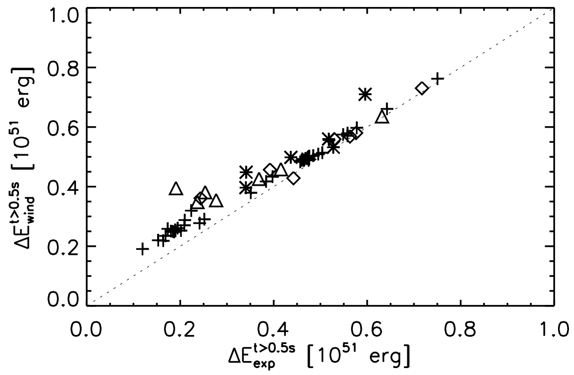

Figure B.4: Relation between the increase of the explosion energy between $t = 0.5\,\mathrm{s}$ and $t = 1\,\mathrm{s}$, $\Delta E_{\rm exp}^{t>0.5\,\rm s}$, and the integrated wind power during this time interval, $\Delta E_{\rm wind}^{t>0.5\,\rm s}$, for the models of Tables 3.1–3.3.

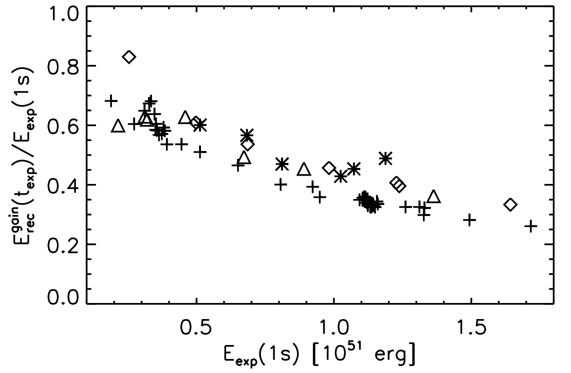

Figure B.5: Ratio of the recombination contribution to the total explosion energy 1 s after core bounce, $E_{\rm rec}^{\rm gain}(t_{\rm exp})/E_{\rm exp}(1\,\rm s)$, as a function of $E_{\rm exp}(1\,\rm s)$ for the models of Tables 3.1–3.3. For low-energy models the recombination contribution dominates, whereas for higher explosion energies the wind contribution becomes more important.

integrated power of the neutrino-driven wind, varies with the explosion energy. In our “standard boundary contraction” models the fraction of the explosion energy provided by recombination drops from about 70% for the low-energy models to about 30% for the model with $E_{\rm exp}(1\,\rm s) \approx 1.5\times10^{51}$ erg (Fig. B.5). This fraction declines because the wind power is proportional to a higher power of the luminosity ($L_{\rm wind} \propto L_\nu^\alpha$ with $\alpha \approx 3$; Thompson et al. 2001) and although the mass in the gain layer at the onset of the explosion scales linearly with the boundary luminosity (Fig. 3.11).

For the “rapid boundary contraction” cases the wind contribution is even more important, e.g. for Model W12F-c $E_{\rm rec}^{\rm gain}(t_{\rm exp})/E_{\rm exp}(1\,\rm s) \approx 0.2$, i.e. about 80% of the explosion energy are generated by the neutrino-driven wind. For a fixed boundary luminosity the wind power is higher in this case than for the “standard boundary contraction”, because $L_{\rm wind}$ increases with decreasing neutron star radius (see e.g. Thompson et al. 2001). However, $\Delta M_{\rm gain}(t_{\rm exp})$, and thus also $E_{\rm rec}^{\rm gain}(t_{\rm exp})$, are similar for models with “standard” and “rapid” boundary contraction and the same $L_{\rm ib}$. This is so because two effects compensate each other roughly: On the one hand the density at a given radius r in the gain layer is lower for a faster contraction ($\rho^{\rm r}(r, t_{\rm exp}^{\rm r}) < \rho^{\rm s}(r, t_{\rm exp}^{\rm s})$, where r and s denote the rapid and standard contraction cases, respectively), but on the other hand also the gain radius is smaller and thus located in a region of higher density, $\rho^{\rm r}(R_{\rm g}^{\rm r}, t_{\rm exp}^{\rm r}) > \rho^{\rm s}(R_{\rm g}^{\rm s}, t_{\rm exp}^{\rm s})$.

At $t = 1\,\mathrm{s}$, when we stopped most of our simulations, the explosion energy is still increasing (see, e.g., Fig. 3.20). Yet, with the subsequent drop of the core luminosity (we assume a $t^{-3/2}$ behaviour at $t > t_L$, see Eq. 2.27) also the wind power, which is proportional to L_ν^α (see above), must decline strongly. Therefore the explosion energy will grow only moderately. In case of the long-time simulation B18-lt it rose from 1.14×10^{51} erg at $t = 1\,\mathrm{s}$ to 1.43×10^{51} erg at $t = 2\,\mathrm{s}$, and reached 1.46×10^{51} erg by the end of the simulation at $t = 3.6\,\mathrm{s}$.

C

Hydrodynamics in an accelerated frame of reference

In an inertial frame of reference the hydrodynamic equations are given by

$$\frac{\partial \rho}{\partial t} + \nabla \cdot (\rho \vec{v}) = 0, \tag{C.1}$$

$$\rho \left(\frac{\partial \vec{v}}{\partial t} + (\vec{v} \cdot \nabla)\vec{v} \right) + \nabla \mathcal{P} = \rho \vec{g}, \tag{C.2}$$

$$\frac{\partial \rho E}{\partial t} + \vec{\nabla} \cdot ((\rho E + \mathcal{P})\ \vec{v}) = \vec{v} \cdot \rho \vec{g}, \tag{C.3}$$

where ρ is the density, $\vec{v}$ is the velocity, $\mathcal{P}$ is the pressure, $\vec{g}$ is the gravitational acceleration and $E = \epsilon + v^2/2$ is the sum of internal energy, ϵ, and kinetic energy, ϵ_{kin}, per unit mass.

Let AF be a frame of reference that coincides with an inertial frame IF at time $t = 0$ and accelerates with a constant rate a in z-direction, $\vec{a} = a\vec{e}_z$. The Cartesian coordinates of both frames are then related by

$$(x', y', z', t') = (x, y, z - at^2/2, t) \tag{C.4}$$

(primed quantities are used for the accelerated frame), which implies that

$$\partial z'(x, y, z, t)/\partial t = -at \quad \text{and} \quad \partial z(x', y', z', t')/\partial t' = at. \tag{C.5}$$

For density, pressure, velocity, kinetic energy and gravitational acceleration the following relations hold:

$$\begin{aligned}
\rho'(x', y', z', t) &= \rho(x, y, z, t), \\
\mathcal{P}'(x', y', z', t) &= \mathcal{P}(x, y, z, t), \\
\vec{v}'(x', y', z', t) &= \vec{v}(x, y, z, t) - at\vec{e}_z \\
\epsilon'_{\text{kin}}(x', y', z', t) &= \epsilon_{\text{kin}}(x, y, z, t) - v_z^2/2 + (v_z - at)^2/2, \\
\vec{g}'(x', y', z', t) &= \vec{g}(x, y, z, t) - a\vec{e}_z.
\end{aligned} \tag{C.6}$$

From relations (C.4)–(C.6), it is easy to see that the equation of mass conservation (C.1) does not change in the accelerated frame. The momentum equation in this frame is

$$\rho' \left(\frac{\partial \vec{v}'}{\partial t} + (\vec{v}' \cdot \vec{\nabla}')\vec{v}' \right) + \vec{\nabla}' \mathcal{P}' - \rho \vec{g}' = -at\rho \left(\frac{\partial v_x}{\partial z} \vec{e}_x + \frac{\partial v_y}{\partial z} \vec{e}_y \right).$$

Note that in contrast to Eq. (C.2) there is now an additional term on the right hand side, which affects the momentum components perpendicular to the direction of acceleration. Thus for instance the x-component of the time derivative of the velocity is

$$\frac{\partial v'_x}{\partial t} = -\left(v'_x \frac{\partial v'_x}{\partial x'} + v'_y \frac{\partial v'_x}{\partial y'} + v'_z \frac{\partial v'_x}{\partial z'} \right) - \frac{1}{\rho'} \frac{\partial \mathcal{P}'}{\partial x'} + g'_x - at \frac{\partial v_x}{\partial z}, \tag{C.7}$$

where the additional (rightmost) term is negligible compared to $v'_z \, (\partial v'_x / \partial z')$, as long as $|at| \ll |v_z|$.

Similarly, it can be shown that the additional terms arising in the energy equation (C.3) for an accelerated frame of reference are of order t^2 and can also be neglected, as long as $|at| \ll |v_z|$ holds.

Within a typical time step Δt of a supernova simulation (of order 10^{-6} s) the condition $|a\Delta t| \ll |v_z|$ is satisfied, because the maximum neutron star accelerations are of $\mathcal{O}(10^8\,\mathrm{cm/s^2})$, and hence $|a\Delta t| = \mathcal{O}(100\,\mathrm{cm/s})$, which is much smaller than the relevant velocities in the simulations, which are of $\mathcal{O}(10^6\mathrm{cm/s})$. Thus a solution of the inertial frame hydrodynamics equations with the simple replacement $\vec{g} \rightarrow \vec{g}' = \vec{g} - \vec{a}$ should yield an excellent approximation to the solution of the hydrodynamic equations in the accelerated frame.

Unfortunately, in the present problem the neutron star acceleration, and hence the instantaneous acceleration of the frame, $\vec{a}(t)$, is not known a priori, because it is coupled to the solution of the hydrodynamic problem during a considered time step. Therefore we need to make use of an operator-splitting approach, in which we first ignore the acceleration of the frame of reference and simply solve the inertial frame hydrodynamics equations (just using the gravitational acceleration $\vec{g}$). We can then compute the current value of $\vec{a}(t)$, which is assumed to be constant over the time step, using momentum conservation: The sum of the momenta of the neutron star core, $\vec{P}_{\mathrm{core}}$, and the matter on the numerical grid, $\vec{P}_{\mathrm{grid}}$, is conserved and initially zero, so that $\Delta \vec{P}_{\mathrm{core}} = -\Delta \vec{P}_{\mathrm{grid}}$. We can then use the relation

$$\vec{a}(t^n) = -\frac{\vec{P}_{\mathrm{grid}}(t^n) - \vec{P}_{\mathrm{grid}}(t^{n-1})}{M_{\mathrm{core}}\,\Delta t} \tag{C.8}$$

to determine the acceleration in this time step. Finally we take the effects of the global acceleration of our frame into account in a second step, by adding

$$-\vec{a}(t^n)\,\Delta t \equiv -\Delta \vec{v}^{\,n}_{\mathrm{core}} \tag{C.9}$$

to the hydrodynamic velocity in each zone of the grid, in essence performing a Galilei transformation to an instantaneous inertial frame in which the neutron star is again at rest.

Danksagungen

Dank gebührt an erster Stelle meiner Mutter, meinem Bruder und dessen Freundin, die aus so manchem Wochenende einen gesellschaftlichen und kulinarischen Höhepunkt machten und mich dazu befähigten, trotz numerischer Probleme und karger Mensa-Kost die folgende Woche zu überstehen.

Meinen beiden Betreuern Hans-Thomas Janka und Ewald Müller gilt ein ganz besonderer Dank. Sie haben mir ein Thema gestellt, das sich als überaus interessant, anspruchsvoll und ergiebig herausgestellt hat, und sie haben mich bei der Bearbeitung dieses Themas kompetent und engagiert unterstützt. Thomas, der den grössten Teil der Betreuung übernommen hat, war mit unermüdlichem Einsatz bemüht, das Projekt voranzubringen. In vielen intensiven Diskussionen mit ihm konnten schwierige Probleme aus dem Weg zu geräumt werden. Auch Ewald verstand es, mich immer wieder auf die richtige Spur zu bringen und zu motivieren.

Konstantinos Kifonidids danke ich für zahlreiche interessante Diskussionen, Hilfe bei Parallelisierung und Optimierung und vor allem dafür, dass er sich durch meine Paper-Drafts gequält hat. Ich danke Thierry Foglizzo, dessen Studien diese Arbeit wesentlich beeinflusst haben und der mir immer wieder geduldig erklärt hat, was in meinen Simulationen eigentlich passiert. Tomek Plewa danke ich dafür, dass er für mich einen unangenehmen Fehler im Hydrocode entfernt hat. Auch Robert Buras und den übrigen Mitgliedern der Hydro-Gruppe danke ich für viele Diskussionen und nützliche Hinweise.

Ich danke `himiko`, `spa`, `psi`, `sam` und `jump` für fleissiges Rechnen und ich danke auch allen, die für die Administration dieser Computersystem an den Rechenzentren in Garching und Jülich zuständig waren. Dem Cray-Cyber-Projekt des Vereins für historische Computer in München danke ich für Rechenzeit auf einer historischen Cray Y-MP EL (Baujahr 1991), ohne die ich ein nicht weniger historisches, aber wichtiges Fortran-Programm nicht zum Laufen gebracht hätte. Auch den Systemadministratoren am MPA möchte ich danken, vor allem Norbert Grüner, mit dem zusammen ich vier Jahre lang die Webseiten des Institutes gepflegt habe.

Schliesslich möchte ich noch allen danken, die dafür gesorgt haben, dass die Arbeit am MPA nicht nur interessant war, sondern auch sehr viel Spass gemacht hat. Stellvertretend möchte ich hier nur meine Büromitbewohner Tobias, Martin und Almudena nennen.

Und zum Schluss möchte ich mich bei allen für ihr Interesse bedanken, die mich die letzten Jahre immer wieder mit folgender Frage begrüsst haben: “Wann gibst du jetzt eigentlich ab?” — sie müssen sich etwas neues einfallen lassen.

Curriculum Vitae

Name:		Leonhard Scheck
Geburtsdatum:		25.6.1973
Geburtsort:		Murnau
Schulbildung:	1980–1984	Grundschule Murnau
	1984–1992	Staffelsee-Gymnasium, Murnau
Wehrdienst:	1992/1993	Funker, Kemmel-Kaserne, Murnau
Studium:	11/1993–08/2000	Allgemeine Physik, Technische Universität München
	10/1995	Diplom-Vorprüfung
	10/1995-08/2000	Hauptstudium, Spezial-/Wahlfächer: Astrophysik, Teilchen-Astrophysik, Numerische Mathematik
	09/1999-08/2000	Diplomarbeit am Max-Planck-Institut für Astrophysik Titel: *“Untersuchungen zur Langzeitentwicklung relativistischer, extragalaktischer Jets”* Betreuer: Dr. Ewald Müller
	08/2000	akademischer Grad “Diplom-Physiker (Univ.)”
	seit 02/2001	Promotion in Allgemeiner Physik Technische Universität München und Max-Planck-Institut für Astrophysik Titel der Dissertation: *“Parametric studies of Hydrodynamic Instabilities in the Supernova Core by Two- and Three-Dimensional Simulations”* Betreuer: Dr. Hans-Thomas Janka und Dr. Ewald Müller